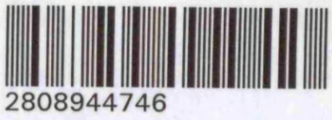

UNIVERSITY OF LONDON THESIS

Degree PhD Year 2006 Name of Author FRANCHETTA Matteo

EXPERIMENTAL AND TRANSIENT COMPUTATIONAL FLUID DYNAMIC ANALYSIS OF VEHICLE UNDERHOOD IN HEAT SOAK

Matteo Franchetta

Department of Mechanical Engineering

University College London

May 2006

Submitted in partial fulfilment of the requirements for the Degree of

Doctor of Philosophy

ProQuest LLC
789 East Eisenhower Parkway
P.O. Box 1346
Ann Arbor, MI 48106-1346

Abstract

Simulation-based analyses of underhood compartments are proving to be crucially important in a vehicle development program, reducing test work and time-to-market. While Computational Fluid Dynamics (CFD) simulations of steady forced flows have demonstrated reliable, studies of transient natural convective flows in engine compartments under thermal soak are not yet carried out due the high computing demands and lack of validated work. The present work assesses the practical feasibility of applying the CFD tool at the initial stage of a vehicle development programme for investigating the thermally-driven flow in an engine bay.

A typical vehicle underhood was reproduced in half-scale for laboratory investigations. Surface temperatures of components, airflow patterns induced by the buoyant forces as well as the spatial distribution of the air temperature were measured under both steady and transient thermal conditions. Temperature mappings were obtained with thermocouples whereas airflow magnitudes and directions were determined with Particle Image Velocimetry (PIV) instrumentation. The detailed measurements were used as reference for validating the corresponding CFD simulations carried out with the software VECTIS. Experimental and numerical data correlated well in steady state, both quantitatively and qualitatively.

A computation procedure that enables pseudo time-marching simulations to be performed with significantly reduced CPU time usage, in comparison to traditional fully-conservative transient simulations, was also developed. The methodology used a unique combination of CFD solver parameters to overcome the computationally challenging problem of solving for momentum transport in time-marching mode and for a long period of physical time. The procedure was successful in providing a detailed and time-accurate flow and thermal simulation of the underhood model during transient cooling. Such simulation would not have been practically feasible with a standard transient simulation. A reduction in CPU processing time in excess of 90% was achieved with good correlation between the CFD predictions and the experimental data.

Declaration

I hereby declare that the work presented in this thesis is solely my own work and that to the best of my knowledge the work is original except where otherwise indicated by reference to other authors. No part of this work has been submitted for any other degree or diploma.

Matteo Franchetta

May 2006

Acknowledgements

A Ph.D. research is regarded a lonely and isolating experience, yet results are not possible without the personal and practical support of numerous people. The author wishes to thank everyone that has provided help and assistance during the research and particularly the staff of the UCL Mechanical Engineering Department.

This dissertation would not have been possible without the expert guidance of my supervisor, Dr. William K. O. Suen. Not only was he readily available, he always had a word of advice and encouragement throughout the research. His verbal and written comments have been always extremely perceptive, helpful, and appropriate. Special thanks to Dr. Paul A. Williams who has followed my work in the most productive way with a balanced diet of friendly encouragement and practical help.

My appreciation also goes to Ricardo Vehicle Engineering for their financial support and helpful advices during the course of the project. Special gratitude is owed to Thomas Bancroft for his continuous assistance with the computational side of the work. Acknowledgements are also due to the UCL Graduate School for the scholarship granted.

I am forever indebted to my parents for their understanding and encouragement when it was most required and for having supported my undergraduate studies in the first place. A special thanks goes to Stefania, whose love, patience and encouragement enabled me to complete this work.

Of course, despite all the assistance provided by Dr. Suen and others, I alone remain responsible for the content of the following, including any errors or omissions, which may unwittingly remain.

Table of Contents

List of Tables

Chapter 2

Chapter 3

Chapter 4

Chapter 5

Chapter 6

Appendices

List of Figures

Chapter 1

Chapter 2

Chapter 3

Chapter 4

Chapter 5

Chapter 6

Appendices

Nomenclature

Latin Symbols		units
Cr	Courant number	[–]
c_μ	Coefficient of dissipation, c_μ=0.09	[–]
c_p	Specific heat at constant pressure	[J kg^{-1} K^{-1}]
dt	Time separation (between PIV pulses or camera exposure)	[μs]
ds	Spatial separation (PIV tracers)	[pixel]
d	Diameter	[m]
e	Error	[–]
E	Constant expressing wall roughness, E=9.8 smooth wall	[–]
g	Gravitational acceleration	[m s^{-2}]
g_s	Grid spacing (cell size)	[m]
Gr	Grashof number, $Gr = g\beta(T_\infty - T_w)L^3 / \nu^2$	[–]
H	Absolute enthalpy, $H = c_p T + \frac{1}{2} U_i U_i$	[J kg^{-1}]
h	Heat transfer coefficient	[W m^{-2} K^{-1}]
k	Turbulent kinetic energy, $k = 1/2 \cdot u_1^{\,2}$	[m^2 s^{-2}]
k_f	Fluid thermal conductivity or diffusivity	[W m^{-1} K^{-1}]
L	Characteristic length or length scale	[m]
L_t	Turbulent length scale	[m]
l	Length	[m]
n	Number of items (measurements) in a statistical sample	[–]
Nu_L	Nusselt number, hL / k_f	[–]
p	Pressure	[Pa]
P	Sublayer resistance factor, $P = 9.0 \cdot [(\sigma_l / \sigma_t) - 1] \cdot (\sigma_l / \sigma_t)^{-1/4}$	[–]
Pe	Péclet number, $Re \cdot Pr$	[–]
Ph	Peak height of highest correlation peak	[–]
$Ph_{\min}$	Background noise level in correlation plane	[–]
Pr	Prandtl number, $Pr = \nu / \alpha = c_\rho \mu / k$	[–]
q	Magnitude of value being compared	[–]
q_H	Heat flux	[W m^{-2}]
R	Gas constant for air, R = 287.05	[J kg^{-1}K^{-1}]
Ra	Rayleigh number, $g\beta\Delta TL^3 / \alpha\nu$	[–]
Re	Reynolds number, Re = Ul / ν	[–]

r	Grid refinement ratio, $r_{12} = g_{S2} / g_{S1}$	[–]
St	Stanton number, $St = Nu / RePr$	[–]
s_x	Sample standard deviation	[–]
$s_{\bar{x}}$	Sample standard deviation of the mean	[–]
T	Temperature	[K] or [°C]
T^+	Near-wall temperature profile, $T^+ = c_p \rho (T - T_w) u_\tau / q$	[–]
t	Time	[s]
Δt	Timestep size	[s]
t_s	Student's t-distribution, $t_s = (\bar{x} - \mu_p) / (s\sqrt{n})$	[–]
U_i	Local averaged velocity with (U, V, W) components	[m s^{-1}]
$u(t)$	Flow velocity	[m s^{-1}]
u	Tangential fluid velocity	[m s^{-1}]
u^+	Dimensionless fluid velocity, $u^+ = u / u_\tau$	[m s^{-1}]
u_t	Turbulent velocity scale	[m s^{-1}]
u_τ	Frictional velocity, $u_\tau = \sqrt{\tau_w / \rho}$	[m s^{-1}]
V	Volume	[m^3]
V_{pt}	Particle velocity (ref. flow tracer settling velocity)	[m s^{-1}]
x_i	Spatial co-ordinate with (x, y, z) components	[m]
$\bar{x}$	Sample mean	[–]
y^+	Mesh-dependent wall distance, $y^+ = (y \cdot u_\tau) / v$	[m]
Z	General empirical constant (zero-equation model)	[–]

Greek Symbols

		units
α	Thermal diffusivity, $\alpha = k / \rho \cdot c_p$	[W m^{-1} K^{-1}]
β	Volumetric thermal expansion coeff., $= -(1/\rho) + (\partial \rho / \partial T)_p$	[K^{-1}]
δ_{ij}	Kronecker delta (δ_{ij}=1 for i=j, δ_{ij}=0 for $i \neq j$)	[–]
ε	Rate of dissipation of turbulent kinetic energy	[J kg^{-1} s^{-1}]
ϕ	General variable or scalar parameter	[–]
Γ_ϕ	Diffusion coefficient for general variable, ϕ	[kg m^{-1} s^{-1}]
κ	Von Karman's constant, $\kappa \approx 0.419$ in law of wall	[–]
λ	Wavelength	[ηm]
μ	Dynamic (molecular) viscosity	[kg m^{-1} s^{-1}]
μ_t	Turbulent or eddy viscosity (diffusivity)	[kg m^{-1} s^{-1}]

μ_p	Population mean	[–]
ν	Kinematic viscosity, $\nu = \mu / \rho$	[$m^2 s^{-1}$]
ρ	Density	[$kg m^{-3}$]
σ	Standard deviation	[–]
σ_t	Turbulent Prandtl number (=0.9 in VECTIS)	[–]
σ_l	Laminar Prandtl number (user-supplied, σ_l =0.7 by default)	[–]
τ	Relaxation time (ref. flow tracer)	[s]
τ_w	Wall shear stress	[$N m^{-2}$]
τ_{ij}	Stress tensor	[$N m^{-2}$]
ω	Turbulence frequency	[Hz]

Superscripts/Subscripts

—	Overbar: mean value
+	Profile
0	Reference condition
f	Relative to fluid
FS	Full scale
CFD	Corresponding to VECTIS solution
conv	Convection contribution
crit	Critical value
EXP	Corresponding to laboratory measurements
H	Relative to enthalpy
i, j	Covariant indices, i, j =1, 2, 3
max	Maximum or peak
min	Minimum or lowest
p	Constant pressure
pt	Relative to particle (PIV tracer)
rad	Radiation contribution
RS	Reduced scale
w	Relative to wall or surface
∞	Relative to surroundings (i.e. free stream)
ϕ	Corresponding to general variable or fluid quantity, ϕ

Acronyms

A/C	Air Conditioning system
AOI	Area of Interrogation
ATF	Automatic Transmission Fluid
CAD	Computer Aided Design
CCD	Charge Coupled Device
CFD	Computational Fluid Dynamics
CHT	Conjugate Heat Transfer
cHTC	convective Heat Transfer Coefficient
DDE	Dynamic Data Exchange
DNS	Direct Numerical Simulation
ECU	Electronic Control Unit
EGR	Exhaust Gas Re-circulation
FFT	Fast Fourier Transform
GCI	Grid Convergence Index
HTC	Heat Transfer Coefficient
HVAC	Heating Ventilation Air Conditioning
IntWinS	Interrogation Window Size
LES	Large Eddy Simulation
LRN	Low Reynolds Number turbulence model
LSV	Laser Speckle Velocimetry
Nd:YAG	Neodymium:Yttrium Aluminum Garnet laser
N-S	Navier-Stokes equations
PAS	Power Assisted Steering
PID	Proportional Derivative Integral
PISO	Pressure Implicit with Splitting of Operators algorithm
PIV	Particle Image Velocimetry
PTFE	PolyTetraFluoroEthylene
PTU	Programmable Timing Unit
RANS	Reynolds-Averaged Navier Stokes
RMS	Root Mean Square
RNG	Re-Normalisation Group turbulence model
RPM	Recursive Projector Method
RSM	Reynolds Stress turbulence Model
SIMPLE	Semi-Implicit Method for Pressure-Linked Equations algorithm
STM	System Thermal Model
TTL	Transistor-Transistor Logic
UTM	Underhood Thermal Management
urf	under relaxation factor

Published Papers

The following papers have been published as a results of this research:

Franchetta, M., Suen, K. O., Williams, P. A., Bancroft, T. G. [2004]: Measurement and Prediction of Natural Convection in Automotive Underhood Model, *2004 International Mechanical Engineering Conference*, Kuwait City, Kuwait. Published on "*Recent Advances and Applications in Heat and Mass Transfer (Part 1)*", Editors M. H. Al-Hajeri, A. F. Al-Mudhaf and M. E. Eleshaky, pp. 150-167, Kuwait Society of Engineers.

Franchetta, M., Suen, K. O., Williams, P. A., Bancroft, T. G. [2005]: Investigation into Natural Convection in an Underhood Model under Heat Soak Condition, *Proceedings of 2005 SAE World Conference*, Detroit, USA, SAE Paper No. 2005-01-1384.

Franchetta, M., Bancroft, T. G., Suen, K. O. [2005]: Efficient Computation Method for Transient CFD Simulation of a Typical Vehicle Underhood, *Proceedings of 2005 European Ricardo Software Conference*, Frankfurt, Germany.

Franchetta, M., Bancroft, T. G., Suen, K. O. [2006]: Fast Transient Simulation of Vehicle Underhood in Heat Soak, *Proceedings of 2006 SAE World Conference*, Detroit, USA, SAE Paper No. 2006-01-1606.

Franchetta, M., Suen, K. O., Bancroft, T. G. [2006]: Pseudo-Transient Analysis of Underbonnet Compartment during Thermal Soak, Journal of Automotive Engineering, Proceeding of the Institution of Mechanical Engineers (Part D). *Pending publication.*

Chapter 1

INTRODUCTION AND LITERATURE SURVEY

1.1 BACKGROUND AND MOTIVATION

The engine compartment of a passenger vehicle, also referred to as the underhood, is most frequently located at the front and can house in excess of hundred elements including powertrain, electrical, suspension and exhaust components. The tight packaging of a typical modern underhood environment is shown in Figure 1.1.

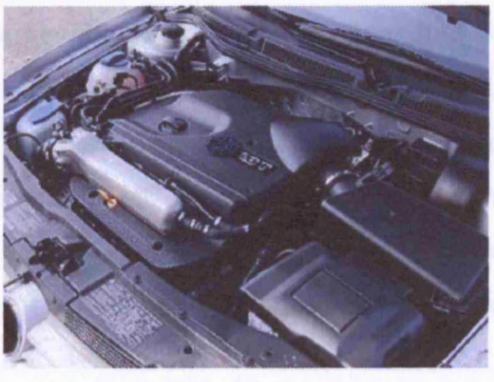

Figure 1.1 – Tightly-packaged engine compartment of a modern passenger vehicle.

Cooling Airflow – All modern passenger cars require the cooling system to deliver sufficient quantity of air to all the components/systems in the underhood at all operating conditions. It is a common practice to let the cooling air enter the engine compartment at a point on the vehicle body shell where high static pressure prevails and to let it flow out at a location of low pressure (*ram effect*). The air inlets (numbered as 1 and 2 in Figure 1.2) are usually located directly above and below the bumper while the outlet apertures are placed underneath the car, where the static

pressure is low. From the front apertures, the air flows through the air duct to the "cooling pack" module that combines the AC compressor (4), the radiator (5) and the oil cooler (7). Modern underhood designs have also a fan (6) placed downstream the radiator to "draw" air through it. The air from the fan flows around the engine block (8) before discharging to ambient near the front axle (9).

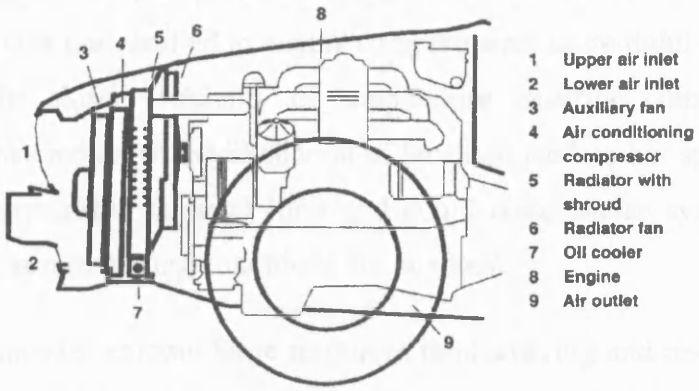

Figure 1.2 – Cooling air system in a vehicle with front engine installation (section along centreline) [Hucho 1998].

Figure 1.3 shows a schematic side view of the flow patterns in the engine bay for two typical operating conditions. At high road speed the air flows uniformly through the cooling pack and discharges through the outlet by blending with the flow underneath the vehicle. If the ram effect is zero, such as during idling, the cooling airflow is determined entirely by the performance of the fan and by buoyancy effects (due to warm-up) within the compartment. Incoming air is drawn into the underhood from the front or the bottom, depending if the fan is operating, with different effects on the internal flow development and on its overall cooling performance.

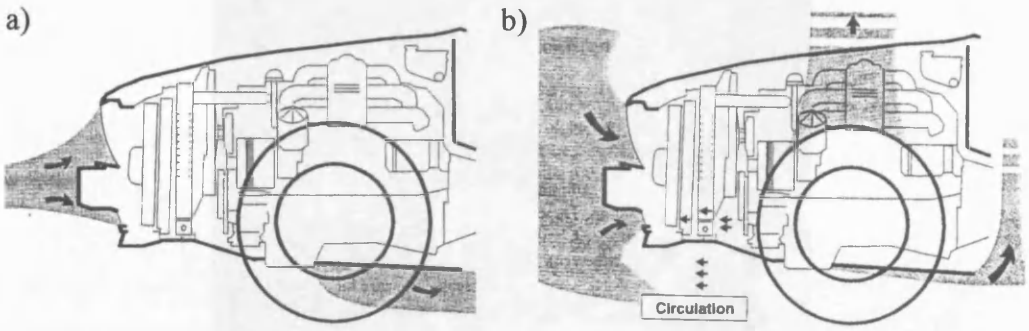

Figure 1.3 – Underhood airflow during: (a) full-load operation and (b) idle condition. Internal and external flow circulation [Hucho 1998].

Underhood Thermal Management – Stringent engine emission requirements have necessitated that catalytic converters be packaged within the engine bay. As a result, exhaust system components have become the primary sources of heat into the underhood with surface temperatures reaching up to 900K when the engine is at its maximum power output. In addition, the combination of increased styling restrictions, greater cooling requirements, additional electronics, noise insulation and extra safety features has resulted in engine compartments more tightly packaged than in the past. The closer proximity of temperature sensitive components to the damaging heat has increased the likelihood of localised surface hot spots. These may be above the permissible material limit and could compromise system durability, especially when severe driving conditions are common.

Automotive companies commit large resources in identifying and resolving thermal-related issues under the hood, such as cooling of engine, overheating of electronic modules, heat transfer to auxiliary parts and airflow distribution. Underhood Thermal Management (UTM) investigations allow engineers to improve the integrity and performance of all the auxiliary parts in the engine bay, avoiding the need for major changes in the final stages of a vehicle development programme.

UTM has become a topic of increased interest, as evidenced by the recent surge of activities in the literature. The need to perform investigations on prototypes to determine valid thermal strategies is increasing with each new generation of vehicles. Currently, analyses rely heavily on expensive and time-consuming wind tunnel and in-territory testing (Figure 1.4) and on the expertise of the engineers.

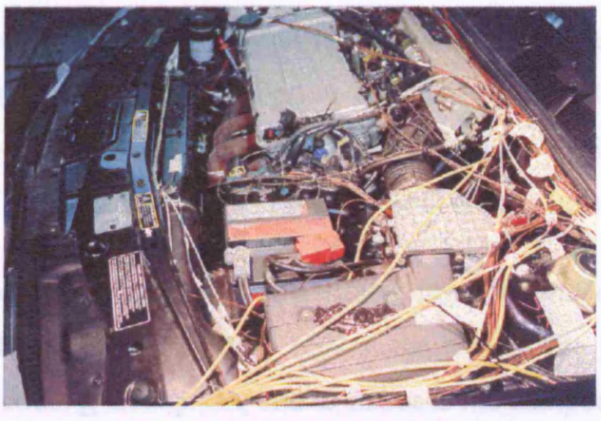

Figure 1.4 – Engine bay instrumented with temperature and pressure sensors for in-territory testing [Ricardo UK Ltd 2000].

The common industrial practice is to investigate the engine compartment under worst-case operating thermal conditions, such as:

- Vehicle at maximum velocity (*Vmax*) (i.e. sustained high heat load with strong inlet ram airflow)
- Idling (i.e. weak fan-driven airflow, potential re-circulation of hot air)
- Heat soak (i.e. engine key-off, fan-driven airflow limited to a short period or not possible, natural convection)
- Hill Climb with trailer tow (i.e. high heat load, weak airflow mainly fan-driven)

Targets that must be achieved by successful underhood thermal management are: fluid[1] temperatures within limits to enhance component and system performance while preventing fluid degradation; component temperatures below recommended limit to avoid malfunctions or failure; cool air to engine intakes to maximise engine power output. These can be met by optimising the airflow through the cooling pack (i.e. cooling pack size, layout, sealing/shrouding, inlet aperture sizing), the airflow over auxiliary components (i.e. location of components, enhancement of heat rejection from exhaust system and catalysts, prevention of hot air re-circulation over electronics and plastics) and the air intake system (i.e. location and size of inlets to avoid ingestion of hot air and system over-heating). These are achieved by:

1) Insulation of components with internal heat source, e.g. braided fibreglass sleeving on Exhaust Gas Recirculation (EGR) tubes [AEI 2000].

2) Insertion of heat shields (aluminised reflective material) between components and external heat sources. This option is usually adopted for parts that are adjacent to the exhaust manifolds and for battery cables (particularly temperature sensitive), and intends to provide protection from radiant heat.

3) Use of alternative materials for manufacturing the underhood components. Advanced materials enable both to reduce the size of the parts, consequently increasing the cooling flow paths, and to increase the components' heat resistant

[1] Coolant fluid, oil, Power-Assisted Steering (PAS) fluid, Automatic Transmission Fluid (ATF).

capability [Kleet *et al.* 2000]. An example is polyamide, which is currently being integrated into engine bays especially for the manufacture of inlet manifolds [Dutmer 2003]. Nevertheless, new materials are still at risk of degradation when exposed to heat spikes or during thermal soak [AEI 2000]. They must therefore be implemented together with other thermal protection measures.

4) Re-location of the components. This is typically difficult to accomplish unless it is performed early in the vehicle development cycle when the component packaging is evolving and some flexibility is available. It is also possible only if reliable information on the thermal environment and on peak operating temperatures is available early in the design phase.

Computational Fluid Dynamics – To reduce the number of prototype-based physical tests and the associated costs, numerical analyses have been introduced in the initial stages of development programmes. Underhood simulations with Computational Fluid Dynamics (CFD) software have proven an attractive alternative to the empirical investigations for component design, selection and system integration [Baker *et al.* 1997]. They allow early identification of potential thermal problems, and subsequent development of appropriate protection strategies and better underhood packaging configurations. As an additional benefit, CFD simulations can also act as a guide for instrumentation setup: when physical tests are carried out on prototypes, later in the development cycle, the planning of the number and positions of the thermocouples on the test property can be directed by the thermal maps obtained from the numerical simulations.

Encouraging results were obtained in the past with steady-state simulations of forced flows in underhoods [e.g. Haidar and Draper 1998, Butler and Stevens 1999]. These replicated the thermal condition at Vmax, Idle and Hill Climb with trailer-tow. Sample airflow and temperature predictions from a steady-state CFD analysis are shown Figures 1.5 and 1.6.

Figure 1.5 – Air velocity predictions in a typical underhood (top and side views along centreline) [Ricardo UK Ltd 2000].

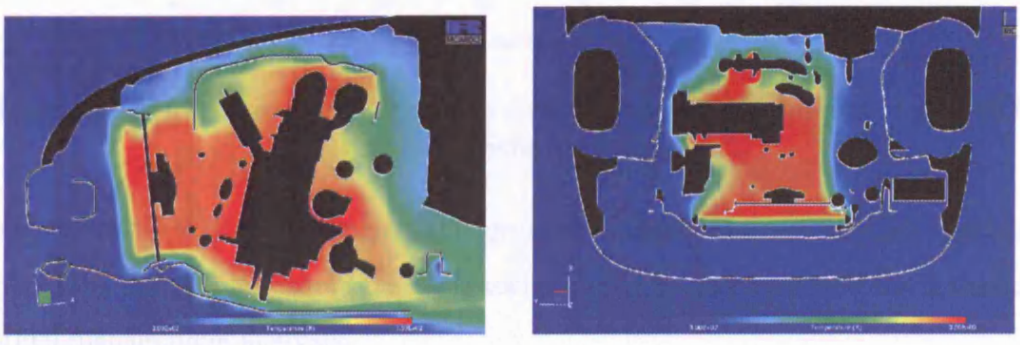

Figure 1.6 – Air temperature predictions [Ricardo UK Ltd 2000].

The CFD approach, however, has not yet been extended to model thermal conditions such as the "Heat Soak" (or "Thermal Soaking"). In such operating condition the engine bay is characterised by a strong interaction between the thermal state of system components and the developing flow field. The flow patterns are buoyancy-induced and inherently unstable. Furthermore, the period of interest is generally long: underhood environments are commonly investigated while cooling down for approximately 30 minutes, with components experiencing high temperatures especially during the first 10 minutes, as shown in Figure 1.7. Running a long transient CFD simulation solving for mass, momentum and energy necessitates extremely high computational resources and a long CPU processing time. The increasing demands on automotive companies to reduce product development time and respond to market trends more quickly makes such thermal conditions currently unfeasible to be investigated numerically.

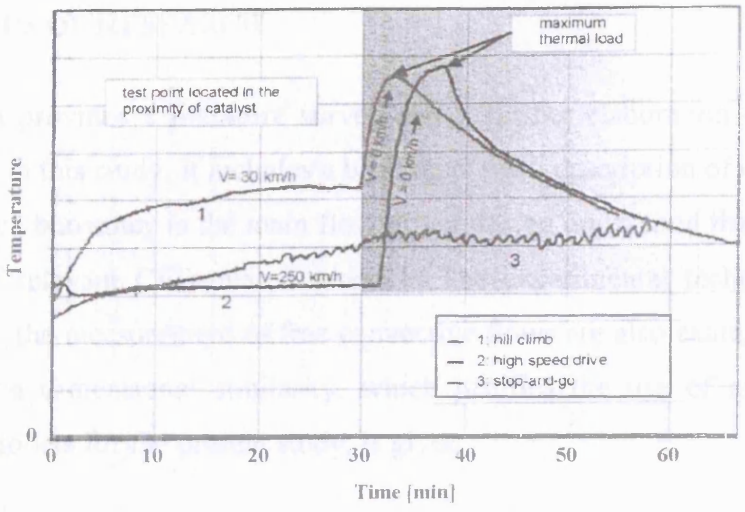

Figure 1.7 – Underhood thermal state at different operating conditions followed by heat soak [Schuster 2003].

Strong interest exists in reducing the processor time required for time-marching simulations in order to enable the CFD technique to be implemented for underhood thermal management analysis.

Scope of the Work – The present work investigates the surface temperature distribution and the thermally-driven airflow patterns within a vehicle underhood under heat soak. A half-scale compartment containing heated metal blocks representing the heat input of the engine, gearbox and turbocharger of a typical passenger vehicle is examined both experimentally and computationally and during both steady and transient conditions. The laboratory investigations consist of temperature measurements of surfaces and air planes, and optical measurements of airflow magnitude and direction. The simulations are performed with the commercially-available CFD software, VECTIS, which was provided by the automotive engineering company sponsoring the work, Ricardo UK Ltd.

The first part of the study is aimed to establish the accuracy of VECTIS in simulating natural convective flows by comparing experimental and computational steady-state results. Subsequently, a methodology able to reduce the CPU runtime currently required for CFD transient simulations is investigated. The proposed computational procedure is developed based on a combination of solver and modelling parameters and does not require the numerical algorithms of the software to be modified.

1.2 STATUS OF RESEARCH

This section provides a literature survey and a further elaboration of the subjects investigated in this study. It includes a brief theoretical description of convective heat transfer, since buoyancy is the main flow driver during underhood thermal soak, and a review of relevant CFD-related research. The experimental techniques that are available for the measurement of free convective flows are also examined. Finally, a discussion on dimensional similarity, which justifies the use of an under-scaled laboratory models for the present study, is given.

1.2.1 Convective Heat Transfer

In the diversity of studies related to heat transfer, considerable effort has been directed to the convective mode, in which the relative motion of the fluid provides a mechanism for energy and, for a concentration difference, mass transfer [Burmeister 1993]. Natural convection represents a limit on the heat transfer rate and this becomes a very important consideration for problems in which other means for heat rejection are neither possible nor practical.

Natural convective flows result from the interaction of the density difference with the gravitational field and are invariably linked with and dependent on the temperature and concentration fields. As such, the motion that arises is not known at the onset and has to be determined from consideration of the heat and mass transfer processes coupled with fluid flow mechanisms. Furthermore, the velocity magnitudes of free convective flows are usually very small, in the order of 10^{-1} m/s, and therefore the experimentation and the analysis of processes involving buoyant fluids are generally complicated. Special techniques and methods have been devised in the past by researchers for obtaining valuable information on flow characteristics and on heat and mass transfer rates. These are reviewed in the following paragraphs.

In convection heat transfer there exist thermal boundary layers where thermal energy is transferred between regions of different temperature. For a thermal boundary layer to develop, a temperature difference between the surface (T_w) and the surroundings (T_∞) must exist. By equating the heat conducted by the fluid away from the wall

surface to the same heat transfer expressed in terms of a convective Heat Transfer Coefficient (cHTC), h, the following relation is obtained [Lienhard *et al.* 2002]:

$$\underbrace{-k_f \left.\frac{\partial T}{\partial y}\right|_{y=0}}_{\text{conduction into the fluid}} = h(T_w - T_\infty) \tag{1.1}$$

The cHTC is not a property of the fluid but it is an experimentally determined parameter whose value depends on all the variables that influence convection, such as the surface geometry, the nature and properties of the fluid and the bulk fluid velocity. Based on Newton's law of cooling, the dimensionless Nusselt number (ratio of convection to fluid conduction heat transfer) can be determined. This is based on the characteristic dimension of the body under consideration:

$$\left.\frac{\partial\left(\frac{T_w - T}{T_w - T_\infty}\right)}{\partial(y/L)}\right|_{y/L=0} = \frac{hL}{k_f} = Nu_L \tag{1.2}$$

Nusselt number correlations are a valid method to estimate the heat transfer rate from a surface. These are generally determined empirically and are available in most heat transfer textbooks.

The equations describing the motion of natural convective fluids are conservation of mass and conservation of momentum. The heat transfer effects are described by conservation of thermal energy. The set of governing equations are generally expressed in coupled elliptic partial differential form and are, therefore, of considerable complexity. These are presented in Chapter 3 together with the numerical approach used for the simulations documented in this thesis.

1.2.2 Computational Fluid Dynamic Research

A review of the available numerical methods for the solution of flows characterised by convection heat transfer follows. Past simulation studies that are relevant to the present work are also discussed. Although the CFD software employed for this study does not give complete freedom on the choice of the turbulence closure model for the

calculations, a brief review of the relevant literature research is presented. This is to aid the discussion of the computational results given in Chapters 4 and 6, where alternative turbulence modelling approaches have been proposed to improve the CFD prediction accuracy. Finally, previous attempts to reduce the simulation time for transient analyses are reviewed.

Types of CFD Models – The governing equations of fluid motion are not amenable to analytical solution in almost all practical situations due to the 3-D structure, possible unsteadiness and often-complex boundary conditions. Numerical techniques must therefore be employed; these have been developed in a wide variety.

Semi-empirical models based on the boundary layer and turbulence hypotheses with mass, momentum and energy conservation have been derived to determine the characteristics of convective flow from heat sources and to predict the vertical temperature stratification and contaminant distribution in rooms [Morton 1956]. These models yield relatively simple steady-state solutions, enabling broad estimations of the thermal condition and contaminant dispersion in compartments to be made.

The applicability of the semi-empirical relations is often restricted to simple geometries and the resulting flow field resolution is generally low [Loomans 1998]. For more detailed flow information the full Navier-Stokes (N-S) equations and the equation for conservation of energy must be solved. Such numerical approach is employed in CFD, which is based on the discretisation of the governing equations in space (and in time). Different CFD numerical approaches exist. These are often categorised according to the way in which the dynamics of eddies in a turbulent flow is addressed.

Direct Numerical Simulation (DNS) fully resolve the set of N-S equations down to the smallest turbulence scales and it is free from any modelling approximation [Moin and Spalart 1987]. Such complete computation places severe requirements on the temporal and spatial resolution of the vortex length scales of the flow field. Indeed, the instantaneous range of scales in turbulent flows increases rapidly in proportion to the Reynolds number (in the order of $Re^{9/4}$ [Nieuwstadt 1993]). As such, DNS cannot be currently applied to practical engineering flow problems (mostly turbulent), since

an extremely fine grid resolution and a small timestep (DNS solves inherently in time-marching fashion) is required [Stathopoulos 2002]. Two alternative numerical methods have been devised to tackle more effectively the unsteady flow problems associated with natural convection: Large Eddy Simulation (LES) and Reynolds-Averaged Navier-Stokes (RANS).

LES solves directly for the transient behaviour of the large-scale turbulence motion but approximates the small-scale structures, which remain spatially under-resolved. To distinguish small-scale and large-scale eddies, a filtering process is carried out on the governing equations to preserve only the equations modelling the evolution of large-scale turbulence [Peng 1998]. The fine-scale structures are indirectly accounted for by a sub-grid eddy-viscosity model [Musser *et al.* 2001]. This numerical method is intrinsically time-dependent and its computing cost is not far from DNS since a sufficiently fine mesh and a small timestep are required to capture all the essential spatial and time-dependent turbulent scales. Within the capacity and speed of present computers, the LES approach is mainly employed for the solution of simple geometries and for specific investigations of flow turbulent fluctuations [Emmerich and McGrattan 1998].

In many engineering applications, such as the one examined in this study, it is often of interest to detect mean flow properties rather than the instantaneous flow fluctuations. The use of statistical methods introduces a viable alternative approach for calculating time-averaged flow quantities: the RANS numerical method. The RANS formulation is based on the solution of the Navier-Stokes equations after all stochastic turbulent fluctuations have been averaged out. Calculations are possible on relatively coarse meshes and at steady state, with consequent savings in computational processing time. If a transient solution is desired, quasi-steady solutions can be calculated on a series of sequential time steps. The main drawback of the RANS method is that the averaging process introduces unknown correlations in the governing equations that must be numerically accounted for with a turbulence "closure" model. Most notably, the inclusion of turbulence models in the fluid dynamic computation leads to sources of error in the flow predictions, the assessment of which requires experimental validation [Yang 2004].

Underhood and Natural Convection Simulations – To date, only few studies have fully investigated with CFD the vehicle underhood space and its component packaging design with consideration to thermal development and cooling airflow management. Jan *et al.* [2000] demonstrated the use of an adaptive Cartesian mesh for accurate front-cooling airflow predictions and the feasibility of building local geometric models of an underhood to understand its thermal environment. Schuster *et al.* [2003] also discussed the application of "model-modularisation" and combined the experimental and numerical practices in order to resolve the temperature development in the exhaust tunnel of a concept vehicle. More recently, Yang and co-researchers [2004] have modelled the cooling airflow rates and the hot flow re-circulation at idle, when only the cooling fans are operating. Bendell [2005] investigated the thermal development of a production vehicle underfloor during trailer towing conditions. Fortunato *et al.* [2005] have performed a full steady-state 3-D analysis of a vehicle during the hill climb operating condition and correlated successfully the surface temperatures with test data.

In general, the practice adopted by automotive engineers and researchers consists of solving the complex flow patterns in an engine compartment with a 3-D steady-state CFD analysis and of calculating the thermal condition with a 1-D system thermal model (e.g. Butler and Stevens [1999], Stevens *et al.* [1999]). The steady-state computations, only applicable to the solution of forced airflows, serve to determine local heat transfer coefficients and air velocities. The data is then transferred to the thermal model that provides a 1-D network description of the whole underhood system environment by calculating the temperature of components and, given pressure loss and flow rate data, the thermal effects from the internal flow of cooling circuits. The information obtained has been used to rapidly assess thermal issues, assisting packaging studies and the provision of heat shielding to sensitive components (e.g. Skea *et al.* [2003]).

Other underhood-related CFD studies in the literature also only address forced fluid flows. Examples are the simulations of the airflow through the heating-ventilation & air-conditioning (HVAC) module (e.g. Cho *et al.* [1997], Chen [1997]) and in the passenger cabin compartment (e.g. Ishihara *et al.* [1991], Aroussi and Aghil [2000]). Only very recently, Weidmann *et al.* [2005] have investigated the buoyancy-induced

flow field and the convective heat transfer in an engine bay, although with a computational model having a very simplified geometry and boundary conditions. The study consisted of comparing measurements of surface temperatures taken on Teflon™ blocks representing the engine and auxiliary underhood parts with numerical predictions obtained by coupling CFD with a 1-D code. The laboratory model was immersed in a water bath to establish well-defined boundary conditions and a heat source located below the modelled components was used to trigger the convective fluid patterns. Although the agreement between simulations and experiments was found to be satisfactory by the authors, it is deemed that the experimental setup and the prescribed thermal boundary conditions were far from being realistic.

With the exception of the work of Weidmann *et al.*, a lack of CFD investigations on buoyant flows for automotive applications was recognised. CFD studies of convective flows in compartments with inlet/outlet openings are predominantly related to building ventilation because of the practical difficulties that exist in acquiring valuable experimental data in environments with large geometric scale (e.g. Gosman *et al.* [1980], Nielsen [1998a], Gladstone and Woods [2001]). Even though the final application is different, the past research on building ventilation was found to be relevant to the present study, in particular with reference to the setup of mesh grids and boundary conditions, and to the choice of turbulence modelling. Building ventilation has the same governing features that characterise the cooling airflow around an engine in heat soak state, namely: flow predominantly driven by buoyancy forces (natural or mixed convection); continuous exchange between the interior and the external ambient air; unsteady flow in most cases, with time-variable boundary conditions; heat transfer transported simultaneously by conduction, convection and thermal radiation; temperature field requiring the simultaneous solution in solids and surrounding fluids (i.e. conjugate heat transfer problem). The buoyant flows in engine compartments are however generated by much higher temperature and density differences because of the intense heat sources.

Ramos *et al.* [2002] described a numerical procedure for analysing 3-D natural convection in rooms. It involves the solution of the incompressible Navier-Stokes equations, the equation of state, the turbulence energy conservation and the

dissipation rate of turbulence energy. In setting up the boundary conditions, the researchers did not extend the fluid domain outside the modelled room. The flow was instead linked to the outdoor conditions using "free" boundaries, which prescribed a constant pressure equal to the atmospheric value taken sufficiently far from the inlet and outlet openings. The necessity of well-defined boundary conditions to obtain a reliable account of the natural convective processes was discussed also by Janssen and Berckmans [1997], who performed simulations on test rooms.

The paper by Jaroš *et al.* [2001] on a solar-heated room characterised by natural convection proposes the use of the Oberbeck-Boussinesq approximation [Worthy 2003] to numerically treat the buoyancy forces. The algorithm simplifies the treatment of density variation by replacing the density difference in the fluid model with a linear relationship between density and temperature. Since the volumetric thermal expansion coefficient, β, is given by

$$\beta = -\frac{1}{\rho}\left(\frac{\partial \rho}{\partial T}\right)_p \quad \text{or} \quad \beta \approx -\frac{1}{\rho}\frac{(\rho_\infty - \rho)}{(T_\infty - T)} \tag{1.3}$$

the density variations can be transformed into temperature ones:

$$(\rho_\infty - \rho) \approx \rho \cdot \beta \cdot (T - T_\infty) \tag{1.4}$$

Jaroš *et al.* implemented the Oberbeck-Boussinesq approximation to re-formulate the buoyancy source term in the CFD momentum equations modelling the fluid transport. The source term was re-written as:

$$S_{B,i} \approx -\rho_0 \cdot \beta \cdot (T - T_0) \cdot g_i \tag{1.5}$$

The coupling of momentum and energy equations became in this way direct and the numerical solution less computationally intensive and more convergent, a key consideration in CFD.

Mann and Haigis [2000] aimed to establish an efficient and a reliable procedure for predicting the air circulation in the compartment of a commuter train. A full-scale mock-up of a passenger compartment was built and experimentally examined. Temperature and velocity profiles as well as the overall heat balance were simulated

and then compared with experimental data. The occurrence of free and forced convection demonstrated to be particularly challenging for the numerical simulation and a completely converged solution could not be achieved with a steady state CFD solver. Due to the moderate Reynolds numbers and the effects of buoyancy, the flow field exhibited an unstable behaviour (velocity fluctuations in a range 0.1-0.2 m/s) with ever changing large vortex structures. The authors concluded that the fluctuations did not have a significant effect on the steady temperature field while a time dependent solution did not provide significant additional information to warrant the increased CPU resource effort.

Turbulence Modelling – Several studies exist that validate CFD predictions of convective flows in ventilated indoor spaces (e.g. [Nielsen *et al.* 1979, Papakonstantinou *et al.* 2003, Posner *et al.* 2003, Lee and Awbi 2004]), but they have been mainly carried out for simple geometries. Only few researchers (e.g. Mistriotis *et al.* [1997] and Howell and Potts [2001]) have examined environments containing flow obstacles. CFD software packages have exhibited limitations in simulating complex indoor flows. In geometrically complicated compartments, with shapes that favour flow re-circulation and obstacles that promote flow separation, a detailed turbulence modelling is indispensable. It is the reliability, sensitivity and validity of the turbulence models that are the main sources of concern in literature.

The most widely used model to compute the dissipation rate of turbulent kinetic energy is the standard eddy-viscosity ($k-\varepsilon$) model. Robustness, CPU economy and reasonable accuracy for a wide range of turbulent flows explain its popularity for industrial applications. However, turbulence closure models based on the ε-equation are known to predict the onset of flow separation too late and generally to under-predict its size [Rodi 1991]. As a consequence, the accuracy of the flow predictions tends to reduce with increasing complexity of the investigated geometry. A further deficit of the standard $k-\varepsilon$ model is that it is based on the assumptions of isotropic turbulence (turbulent fluctuations are the same in all directions) and flow with large Reynolds number; it therefore provides satisfactory accuracy when no regions of anisotropy and relatively strong velocity fields exist in the fluid domain [Loomans 1998]. The model has also shown in some cases to yield too a large turbulent diffusivity (viscosity) [Taskinen 2004].

An important issue for processes characterised by convective heat transfer is the numerical treatment of the turbulence in the region close to solid walls. The near-wall flow formulation determines the accuracy of the wall shear stress and wall heat transfer predictions and has a strong influence on the correct simulation of flow separation. The $k-\varepsilon$ model does not fully solve the flow transport in the boundary layer, which is instead approximated with analytical wall functions. The validity of the wall functions has been queried for flow fields as observed in rooms and ventilated compartments [Baker and Kelso 1990, Weidmann *et al.* 2005].

Launder and Sharma [1974] developed the Low-Reynolds-Number (LRN) model for improved prediction of turbulence localised on surfaces. Its main characteristic is that the transport process in the laminar sub-layer is fully resolved in contrast to k-epsilon models. On the other hand, LRN models require a finer grid in the near-wall zone to capture the rapid variation of the flow variables [Gunnar and Hellstrom 2005] and, correspondingly, a larger number of grid nodes in the computational mesh. Computer-storage and processing requirements are distinctively higher than for solutions employing wall functions.

The $k-\omega$ turbulence model of Wilcox [1988] also does not involve the calculation of empirical functions to bridge the gap between the fully-turbulent region and the viscous sublayer but it does requires the boundary layer to be discretised with a denser grid mesh. The model has been validated for complex, three-dimensional shear flows and has shown to be superior to ε -type models for computing flows with adverse pressure gradients [Sotiropoulos and Ventikos 1998].

The above two-equation models use the Boussinesq viscosity approximation to simplify the governing flow transport equations. The turbulent stresses are assumed equal to the product of an eddy viscosity and a mean strain rate (formulation given in Chapter 3). The approximation is not valid when the turbulent transport or non-equilibrium effects are important. Reynolds Stress Models (RSM), possibly the highest level of turbulence closure currently feasible for CFD simulations, have been developed with no such approximate relation. However, the larger computational costs due to the solution of six additional transport equations and the lower numerical stability are the practical drawbacks when compared to eddy viscosity models.

Literature is filled with tests and comparisons between different turbulence models for various applications. Chen [1995] compared different versions of the standard k-epsilon model to predict indoor airflow patterns. The *RNG* version (Re-normalization Group $k-\varepsilon$ model [Yakhot and Orszag 1986]) gives good predictions by accounting with damping functions for the low velocities of the indoor airflows. Muller and Renz [1998] demonstrated that the LRN model gives the best overall agreement with measured data for displacement ventilation set-ups. However, the work also showed that the standard $k-\varepsilon$ model and a simplified Reynolds-stress model did not differentiate much in the quality of the final airflow predictions. Similar conclusions were obtained by Nielsen [1998b], who established that the use of alternative versions of the $k-\varepsilon$ model results in flow simulations very similar to the ones obtained when employing LRN models. The higher computing demands of LRN models, which translate to longer processing times, are therefore not always justified. The use of computing-intensive models should be limited to specific studies on flow transport close to solid boundaries and not generally extended to industrial applications, which are often driven by time constraints.

Transient Simulation Strategies – Despite the continuous and steady growth in computational power realised in the last three decades, the simulation of three-dimensional unsteady flows is still, for most cases, a computationally intensive task. Transient CFD analyses require computations to be carried out with very small timesteps, of the order of 1×10^{-3} second, to comply with the strict convergence criteria that are necessarily set on the discretised Navies-Stokes equations for solution accuracy and stability. Consequently, thermal processes with a long timescale are currently impossible to simulate within a timeframe that is acceptable for engineering product development programmes.

Strong interests exist to make time-dependent simulations more affordable. Previous attempts to reduce the CPU runtime of transient CFD simulations have fallen into three main categories. These focussed on:

1) Increasing the hardware capacity
2) Increasing the efficiency of the numerical algorithms
3) Simplifying the modelled problem

The first approach is somehow implicit to the advances of computer technology, which embrace all aspects of modern engineering. The need for larger amounts of computational power is in fact partially mitigated by the ever-increasing performance capabilities of modern computers. Furthermore, the recent development of simulation codes, which are now able to partition the investigated domain into an arbitrary number of sub-domains, have led to the evolution of the *parallel processing* technique (e.g. [Neves 1988] and [Nobile and Onesti 1995]). Code parallelisation allows the distribution of the CFD computation across multiple computer processors (linked into *hardware clusters*) maintaining both CPU and memory scalability. Large simulations that exceed the capacity of individual computers can therefore be tackled.

The speed of the parallel supercomputers that are nowadays available can in principle handle any type of transient simulation in a reasonable timeframe, provided that the memory demands are met [Hucho 1998]. However, such machines are usually installed at national institutions and are not accessible for general use.

Researchers have been very much interested in the development of more efficient numerical algorithms to solve the time-accurate Navier-Stokes equations. Pitkanen *et al.* [1999], for instance, have succeeded in reducing the processing time of time-dependent computations (applied to the simulation of centrifugal compressors) by implementing the *dual-time stepping* scheme of Jameson [1991]. The developed algorithm resolves the flow transport iteratively by explicit time stepping until a steady state is reached at every physical timestep; this enables to carry out the computations on relatively large time steps, thus increasing the temporal progression of the solution. Gortz and Moller [2004] have further refined the algorithm by implementing into the flow solver the Recursive Projector Method (RPM) devised by Schroff and Keller [1993]. The RPM algorithm is a combined explicit-implicit method that enhances the convergence of the steady iterative loop during the dual-time stepping computations. The overall processing time for time-accurate simulations of turbulent unsteady flows was found to reduce by a factor of 2, but the effects on the accuracy of the predictions were not reported.

Despite the success of new numerical algorithms in reducing the computational efforts for transient CFD simulations, the practical savings in the CPU turnaround time are still far from practical requirements. This is why most of the time dependent CFD analyses that can be found in the open literature have been focussed upon the approach of simplifying computation itself. This was obtained, for example, by reducing the geometric complexity of the investigated model (and of the corresponding mesh grid), by implementing approximated or empirical expression as boundary conditions, by adopting simplified numerical models or by employing 1-D system codes for the solution of the thermal interactions of solid models with the flow field.

Asghari [2001] proposed the use of simplified heat-transfer-coefficient relations to investigate the time-dependent thermal variations of an electronic module. The method was based on the prescription of approximated cHTCs values, expressed as a linear function of the wall temperature, as boundary conditions for the model. The cHTCs were determined with various steady-state computations performed at different power-dissipation levels and solving only for the energy equation of the fluid domain. The method was found to reduce the time of the computations by a factor of 10 by sparing the need of solving the heat balance on the walls. Only a 5% loss in prediction accuracy compared with a standard transient simulation was reported. However, the methodology required a significant number of steady-state runs upfront the transient simulation to determine the cHTCs quantities (for the various boundaries and at different thermal conditions). Such procedure would therefore practically cancel out any saving in CPU runtime gained during the transient computations.

A similar technique was developed by ThermoAnalytics Inc. [2003a] and integrated in the thermal modelling software RadTherm™. Boundary information (convection coefficient and film temperature) generated with multiple steady-state runs is imported and interpolated at distinctive time steps during 1-D transient calculations in order to yield a complete thermal solution with reduced processing time. The result of the simulation is strictly a temperature distribution map at the wall of the investigated model with no characterisation of the flow field domain.

An alternative approach consists of simplifying the numerical formulation of CFD software, for example by adopting a less computing-demanding turbulence closure formulation. Yazhuo [2002] and Srebric *et al.* [1999] implemented a zero-equation turbulence model for the simulation of indoor airflows. The model was based on a single algebraic function expressing the flow turbulent viscosity, without requiring the solution of additional differential transport equations. Mathematically, the eddy-viscosity was calculated using the following empirical relation [Chen and Xu 1998]:

$$\mu_t = Z \cdot \rho_{air} \cdot U \cdot L_t \tag{1.6}$$

where L_t is a length scale taken as the mean flow distance from the closest solid surface (e.g. mean boundary layer thickness), U is the local mean flow velocity and Z is an empirical constant that depends on the air properties and on the compartment geometry (Chen and Xu [1998] suggested a value of 0.03874 for indoor ventilation airflows).

Equation (1.6) is based on a single length scale characterising the model under scrutiny. Consequently, the algebraic function would grossly approximate the eddy viscosity of turbulent flows in geometric configurations consisting of more than one solid element or heat source, such as in the engine bay investigated in this study. Furthermore, the results obtained by Yazhuo [2002] indicated that the performance of the zero-equation model was poor even for simple models when compared to the $k-\varepsilon$ prediction accuracy, although it may be acceptable for concept design purposes. Srebric *et al.* [1999] reported predictions of air velocities and temperature distribution acceptably close to measurements but empirical temperatures were used as boundary conditions, thus greatly reducing, a-priori, potential modelling errors. Both studies stated savings in computational time of the order of 50% compared to solutions obtained with more traditional turbulence models.

In general, the literature survey indicated that no effective methodology yet exists to perform in a reasonable timeframe detailed time-dependent simulations of complex flow fields. The larger hardware capacity of modern computers has only recently permitted to transiently investigate temperature and velocity profiles with CFD, but only for short time periods (e.g. [Ghani *et al.* 2002]). Coupled flow and thermal

fields have proven even more difficult to compute, unless a large CPU parallel processing architecture was employed. Relatively accurate and efficient predictions were at best obtained with the fluid dynamic solver linked to a 1-D thermal modelling code (e.g. as tested by Negrao [1997] for natural ventilation in buildings). All the attempts to reduce the CPU runtime have demonstrated relatively small savings and often at the expense of marked losses in prediction accuracy. The need for an alternative methodology, enabling time-accurate CFD simulations to be performed with greatly reduced processing time, was identified.

1.2.3 Experimental Research

A literature review was carried out to assess the experimental work performed to-date by researchers in the field of natural convection, both to aid the choice of appropriate experimental equipment/techniques and also to anticipate possible technical difficulties during the measurements.

Empirical investigations on convective heat transfer have been primarily carried out on geometrically simple enclosures. Scaled laboratory mock-ups have been employed for easiness of manufacture, lower cost and because they allow meticulous analyses to be performed. Representative literature is summarised below together with a discussion on dynamic similarity for scaled test models. Different techniques were utilised in the past, from investigations of surface temperature distributions to more demanding analyses of flow patterns and flow turbulence.

Natural Convection Investigations – The temporal development of convective flows has been almost exclusively investigated in enclosures with simple geometric configurations. These were often set up with horizontal or vertical walls heated/cooled by constant heat fluxes or with isothermal boundaries (e.g. [Olson and Glicksman 1991], [Khalifa and Abdullah 1999], [Vargas *et al.* 2002]). The main objective of the studies was to determine the correlations of the mean convective Nusselt number as a function of the Grashof number. Very few researches examined the influence of inlet/outlet openings on free convective flow patterns. Detailed studies were prevented by the difficulties in acquiring relevant quantitative data in large scale (the research is predominantly related to building ventilation) and in establishing dynamic similarity with scaled models.

A difficulty generally recognised by researchers is the achievement of the idealised boundary conditions traditionally sought for CFD data comparison and validation (e.g. essentially adiabatic surfaces or constant heat fluxes). As pointed out by Launder [2002], controllable boundary properties are particularly cumbersome and usually do not correspond to the actual experimental requirements or do not match the conditions set in the CFD test case. Ince and Launder [1989, 1995] managed to improve the quality of the comparisons between experimental and CFD results by increasing the insulation on the external boundaries of their laboratory model and specifying them as adiabatic walls in the computational representation.

Awbi and Hatton [1999] measured the convective heat transfer coefficients on internal room surfaces and correlated the results with the corresponding data available in literature for CFD boundary specification. The study demonstrated that the use of inaccurate heat transfer coefficients in CFD has a significant influence on the calculated conduction losses/gains and on the heat transfer between surfaces and air. The need to determine the coefficients numerically, rather than specifying their values at fixed conditions, was recognised.

Dynamic Similarity – Investigations carried out on models with reduced scale possess various advantages over a full-scale analysis. Examples are the possibility of systematically studying the influence of certain parameters isolated from all other variables affecting the phenomenon or the possibility of observing rapidly varying phenomena which elude actual observation [Jaluria 1998].

The problem that arises for scaled models is the legitimacy of extending the results of the measurements to different geometric scales. The theory of similarity, based on dimensional analysis, must be employed to determine the factors that govern a given system and to establish dynamic similarity. This approach is widely used in fluid mechanics and in studies of heat and mass transfer. If dynamic similarity exists, the results from the model may be applied quantitatively to determine the prototype behaviour [Enquist and Earsome 1996].

Dynamic similarity requires that the forces acting on two models with different geometric scale are in the same direction at corresponding locations and that their magnitudes are related by a constant factor [Incropera and DeWitt 2001]. Geometric

and kinematic similarities must also exist. Thermal similarity demands the temperature profiles of a thermal system to be geometrically similar at corresponding times [Wosnitza 2002]. This is often complicated and involves a degree of approximation since several different mechanisms usually arise in a typical thermal system. Radiative transport, temperature-dependent properties of the materials and heat sources have been found to be difficult to model because of the often non-linear variations with temperature [Jaluria 1998].

From the criteria of similarity for a viscid fluid in motion, the similitude condition for natural convective flows result in the conservation of the Grashof and Prandtl numbers, which are usually grouped together as the Rayleigh number, defined below.

Grashof number $$Gr = \frac{g\beta(T_\infty - T_w)L^3}{\nu^2} \tag{1.7}$$

Prandtl number $$Pr = \frac{c_\rho \mu}{k} = \frac{\nu}{\alpha} \tag{1.8}$$

Rayleigh number $$Ra = Gr \cdot Pr \tag{1.9}$$

The Rayleigh number is commonly employed to characterise natural convective flows and it is defined as the product of the Grashof number, which describes the relationship between buoyancy and inertia forces in a fluid, and the Prandtl number, which relates the viscosity of a fluid to its temperature. It should be usefully recognised that a one-dimensional laminar flow persists when its Rayleigh number is below a critical value, which mainly depends on the geometry of the heated component. Generally, when the Rayleigh number exceeds the value of 2000, the fluid begins to "roll". For Rayleigh numbers in the range of 10^5 to 10^7 the flow becomes susceptible to small disturbances such as multiple stationary transverse vortices: the fluid is characterised by instability or "soft" turbulence [South and Witten 1998]. For Rayleigh numbers above 10^8–10^9, an aperiodic (chaotic) turbulent motion exists. Such condition is usually denoted as "hard" turbulence because it is characterised by gently flowing regions punctuated by small regions of violent flow and temperature swings [South and Witten 1998].

Buoyancy dominated flows have been studied mainly in sub-scale enclosures. In order to match the Rayleigh number of the full-scale counterparts, fluids alternative to air have been employed because of their different (much higher) density. Scaled models have been reproduced with water [Bejan *et al.* 1981, Berlandier *et al.* 1989] or gases, such as the R114 [Olson *et al.* 1990]. Nevertheless, it appears that none of the works in literature was able to simultaneously match the Prandtl, Rayleigh and Reynolds numbers of the reduced and full-scale systems. Even though some good agreement has been possible for *Pr* and *Ra* alone, the lack of full dynamic similarity has made the data from the investigated models difficult to extrapolate [Olson *et al.* 1990].

A group of researchers in Cambridge University developed scaling relations based on experiments carried out utilising the density difference of salt in fresh water to generate buoyancy forces [Linden *et al.* 1990, Baker and Linden 1991]. The "salt-bath" technique allowed the researchers to match the full-scale value of the Reynolds and Peclet numbers to achieve dynamic similarity for turbulent flows. The modelling technique and the related mathematical formulation were however questioned by Howell and Potts [2001], who studied experimentally the temperature stratification within an enclosure. The researchers demonstrated that the distribution of temperature in a full-scale room could not be realistically described by the salt-bath method since it neglects the heat diffusion and thermal radiation effects. In particular, as the kinematic viscosity of water is only about $1/10^{th}$ that of air and the diffusivity of salt in water is less than $1/10{,}000^{th}$ that of heat in air, the technique of Linden *et al.* would be strictly suitable only for modelling flows where diffusion of heat is insignificant: salt diffuses too slowly in water to represent the diffusion of heat in air.

An alternative technique, using electrolytically-generated fine hydrogen bubbles to replicate a buoyancy-driven fluid, was tested by Chen *et al.* [2001]. Experiments on displacement natural ventilation induced by two types of buoyancy sources, a point source and a line source, showed that the ventilation and stratification phenomena could be successfully modelled with the "fine-bubble" technique. However, it was also shown [Yang 2004] that hydrogen bubbles tend to accumulate in the

experimental rig giving rise to unrealistic flow fields if reduced scale models are used.

Boulard *et al.* [1999] investigated the air streams and the temperature distribution generated by buoyancy forces in a naturally-ventilated and scaled greenhouse heated by the floor (Figure 1.8). The relation between the geometrical and thermal characteristics of the reduced- and full-scale models was simply taken as the equality in Rayleigh numbers. By equating Ra_{RS} to Ra_{FS} the following relation was derived:

$$L_{FS} / L_{RS} = (\Delta T_{RS} / \Delta T_{FS})^{0.33} \tag{1.10}$$

The researchers calculated that for a 2 degrees air temperature difference between the inside and the outside of the greenhouse, a 16°C difference was required to be established to reproduce the actual convective pattern in the scaled rig without distortion ($L_{FS} / L_{RS} = 2$). The results were however not compared with full-scale measurements and the validity of the similarity criterion was therefore not proved.

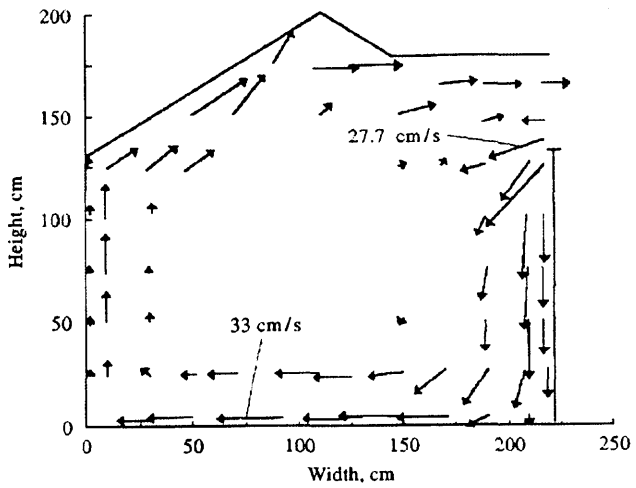

Figure 1.8 – Measured velocities in single-sided ventilated greenhouse model [Boulard *et al.* 1999].

Baturin [1972] stated that there exist domains of auto-similarity within which a thermal phenomenon is independent of the individual criteria of similarity. By comparing the temperature and velocity fields in a building in realistic conditions and in a model at 1/20 scale, the author established that for a Rayleigh number ranging from 2×10^7 to 2×10^{13}, the free convective motion of a fluid is independent of

its linear dimension and the temperature of the heat source. In other words, if the Rayleigh numbers of the full- and sub-scale models are within the above range, thermal processes can be studied on scaled models with the only requirements for geometric similarity and identity of boundary properties. Baturin also stated that the results of other researchers (not referenced in his work) established that the condition of auto-similarity can be extended for $Ra \geq 4\times10^5$, i.e. also for airflows in soft turbulence regime.

Sase *et al.* [1984] and Mistriotis *et al.* [1997] referred to the above conclusions to analyse the buoyant flow in a scaled greenhouse model with an electrically heated floor. Since the Rayleigh number of the model was 6×10^8 and the corresponding full-scale value was 6×10^{11} (width of the model taken as the characteristic length), the condition for thermal similarity was considered automatically satisfied and only geometric similarity was established between the models.

Based on the above results, the heated components in the underhood compartment studied in this work were set at a temperature corresponding to the average condition a full-scale engine-bay in thermal soak: engine and gearbox at approximately 130°C and turbocharger/exhaust at 400°C. The Rayleigh number of the model, calculated as the volume-weighted average of the Rayleigh numbers of the heated blocks (Appendix B), was 1.8×10^7. The thermal similarity of the laboratory model with its full-scale counterpart ($Ra=1.4\times10^8$) was taken as automatically satisfied since the Rayleigh numbers were well above 4×10^5. Only similarity in geometry and boundary condition was prescribed.

Alternative scaling solutions could arguably have been chosen. Water could have been used as the working fluid, but buoyancy forces modelled by salinity differences might have failed to correctly represent the airflow motion. Complete similarity in Rayleigh numbers could otherwise have been attempted; however, owed to the cubic relation between Ra and its characteristic length scale, the temperature of the underhood components would have been unrealistically high (e.g. turbocharger block temperature $\approx$ 1000°C). Since the purpose of the experimental investigation was to acquire data for CFD validation and not to accurately replicate the actual thermal development of the buoyant flow in a full-scale engine-bay, the scaling issues were

not further examined. The laboratory model was therefore designed to be identical to the computational model and set with identical initial thermal boundary conditions, as required for a valid data comparison.

Temperature Measurement Instrumentation – Different experimental techniques have been used in the past to measure the thermal state of solid bodies and fluids.

Infrared thermography has been widely employed for building ventilation studies (e.g. [Wisniewski *et al.* 1998]). The technique consents to monitor the temperature distribution of walls bounding the flow domain.

A differential interferometer was used by Ramesh and co-researchers [2001] to determine the cHTC values across the surfaces of an enclosure from the fringe deflections measured on the interferogram. The technique could not however provide any quantitative information of the flow temperature stratification within the enclosure.

Optical tomography, using data obtained from holographic or Mach-Zehnder interferograms, is a technique that has received particular attention in the past (e.g. [Zhang and Ruff 1994], [Soller and Wenskus 1994], [Mishra *et al.* 1999]). Holographic-type interferometry has even enabled the reconstruction of the 3-D temperature field in an enclosure via a tomographic spatial comparison of two wavefronts, recorded as holograms at two different times. The application of this technique to the measurement of convective flows in compartments faces however specific challenges, as highlighted by Zhang and Ruff [1994]. These include limited view angle, which directly affects the accuracy of any reconstruction produced by a tomographic de-convolution algorithm, and refractive index effects associated with 3-D flows, which generally prevent the use of a measured wall temperature as a direct reference of the fringe order. Realising the potential of this experimental method to obtain data with sufficiently high spatial resolution has also posed significant practical problems.

Thermo-sensitive tracer particles (e.g. micro-capsulated liquid crystal particles) were employed for the simultaneous measurement of flow velocities and temperatures by Wozniak *et al.* [1994, Kobayashi *et al.* [1992] and Tanasawa [1995]. Temperature

distribution maps were obtained from the colour intensity of the particle images. The images could also be used to determine the velocity distribution of the flow by comparing the space travelled by the particles in successive recordings. However, the technique ideally suits only investigations with liquid as the working fluid.

A widely used experimental approach for measuring temperature is by means of thermocouples connected to a data logging unit. Examples are the works of Rasmus [1996] and Zhang *et al.* [1999], who determined the air temperature stratification in a livestock building environment. By using a relatively large number of sensors, the authors were able to fully characterise thermally the air plumes.

The use of thermocouples was deemed to be the most practical and feasible temperature measurement method to investigate the underhood model and it was thereby selected for the experimental analysis of this study.

Flow Measurement Instrumentation – Various methods exist for the measurement of flow fields around heated bodies. A categorisation of the available techniques is possible by distinguishing their operating principle [Loomans 1998]:

- *Visualisation techniques* – These techniques make part of or the whole flow pattern visible (e.g. smoke wires, laser sheet, and tuft) enabling to resolve the topology of the flow field. However, quantitative data cannot usually be derived or they are strongly dependant on the interpretation of the experimentalist.

- *Heat-transfer techniques* – They are based on the transfer of thermal energy from a heat source to the flowing fluid. The quantity of transferred energy is a measure for the flow velocity. Heat transfer techniques, an example being hotwire anemometry, require the insertion of a physical probe in the laboratory model. Commercially-available sensors are also usually designed for single point measurements and for air velocities higher than 0.2 m/s. They would not be suitable, therefore, for the complete characterisation of a convective airflow in an engine compartment.

- *Time-of-flight techniques* – Either the time interval between the upstream injection of a tracer and its downstream detection or the displacement of a tracer

during a time interval is measured. Sonic pulses, heat pulses, ions or solid particles can act as tracers. Examples are sonic anemometry and particle velocimetry. Apart from high instrument cost and low ease-of-operation, sonic anemometry has a number of characteristics which render it less favourable for the present research, the most important being the distortion of the flow caused by the probe head itself [Mortensen and Hojstrup 1995].

- *Doppler Effect techniques* – Flow velocities are determined from changes in the propagation of light waves through the fluid. The waves are scattered by particles in the fluid causing a frequency shift (*Doppler shift*) of the emitted wave. An example is Laser-Doppler Anemometry (LDA). Although non-intrusive, LDA does not allow extracting extensive information on the spatial structure of the flow as it is point-wise [Posner 2001], i.e. the flow velocity is only determined at single spatial locations within the measurement volume.

An essential requirement for the optical measurements in this study was to obtain accurate two-dimensional quantitative information of the airflow patterns without any physical instrumentation intrusion. This is possible by illuminating and measuring the fluid with a laser.

One of the laser techniques employed in the past for investigating natural convective flows is laser sheet tomography (e.g. [Stickland *et al.* 1996]). Laser tomography images are obtained by illuminating with a sheet of light the flow field seeded by a fine powder (milk powder) or dye; since the intensity of the reflected light is proportional to the concentration of the seeding particles in the flow, a qualitative impression of the 2-D flow structure and turbulence intensity level can be derived. Monochrome images, which are produced to obtain a false colour representation of the concentration distribution within the fluid, allow graphical comparisons with CFD to be carried out. Quantitative information is generally difficult to obtain because of the difficulty in calibrating the colour of the processed images with the concentration of seeding in the fluid.

Laser Speckle Velocimetry (LSV) and low- and high-image-density Particle Image Velocimetry (PIV) were developed to investigate complex flow structures. In LSV, dense particles are seeded into the flow and are illuminated by a laser light sheet to

form laser speckle images. By analysing the double-exposure images using Yang's fringe method of interrogation [Stetson *et al.* 1975], the speckle displacement information is extracted and velocity data is obtained.

Pickering and Halliwell [1984] and Adrian [1984] established high-image-density PIV as an improvement on LSV to overcome the practical difficulty of high-density particle seeding. The PIV technique, essentially a time-of-flight method, is based on the comparison of two images, separated in time, taken of light-scattering particles injected into the flow medium (Figure 1.9). A continuous or pulsed laser beam, which is usually shaped by cylindrical optics, produces a sheet of light that illuminates a cross-section of the flow field. Photographic film or a CCD camera is used to capture two consecutive images of the light scatter through this plane. Pathline lengths of all the particle tracers in the flow field can be then calculated and the velocity information derived from knowledge of the time separation between the images. The recorded data is usually de-convoluted using a correlation function (auto or cross correlation) that yields a complete two-dimensional velocity vector field from the acquired images.

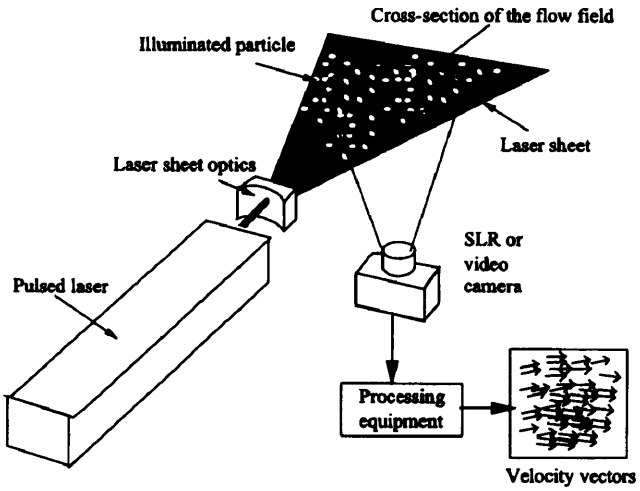

Figure 1.9 – Schematic of PIV operation [Chan 1999].

The requirements for the PIV tracer particles are to track the flow accurately (linear system theory [Westerweel 2000]), not to contaminate the test chamber and not to be hazardous. Zhao *et al.* [1999] conducted full-scale room measurements using helium bubbles in air. Other tracers have also been used in the past, e.g. micro-sized liquid

droplets or oxygen bubbles [Ma *et al.* 1995]. An extensive review of tracer and seeding particles for image velocimetry is given by Melling [1997].

The main drawback of the PIV technique is that the size of the investigated area is usually small (few centimetres squared), being limited by the velocity of the flow, the speed and resolution of the camera and by the quality of the flow field illumination. Measurements on a 1×1.5 m^2 area were attempted by Muller and Renz [1996] but required a very expensive instrumentation with a 23W Argon-Ion laser.

Particle image velocimetry has been widely employed for instantaneous mapping of whole flow domains in compartments and modern developments in digital image processing and optical instruments have made the image acquisition, process, and the analysis automatic and quantitative. It was therefore deemed as the most appropriate technique for the optical measurements of this study.

1.2.4 Summary

The following was established from the literature survey:

1. Numerical simulation is a valuable tool for engineering design and with the continuous increase in computational power the reliance on numerical simulations for airflow and thermal prediction will also increase. Despite recent advances in CFD many issues remain unresolved. The specification of realistic and well-defined boundary conditions for the accurate prediction of natural convective flows in complex environments is one of them.

2. One of the main difficulties with CFD in its present state is turbulence modelling. In particular, the application of wall functions to resolve boundary layer flows limits the accuracy of the simulations because of the approximations in the formulation of wall shear stress, average dissipation and generation rate of turbulent kinetic energy. The accurate treatment of near-wall flows with low-Reynolds number models and the increase of grid refinement are currently restricted by the high computing requirements.

3. Very few CFD studies have concentrated on transient natural convective flows related to automotive applications. With reference to the underhood space,

interest in literature is recent and numerical studies have been mostly performed with steady-state computations modelling forced airflows. The thermal state of engine compartments has also been typically resolved with 1-D models rather than with complete 3-D simulations. There is a general indication that experimental validation studies on buoyant flows are necessary, together with novel calculation methods able to reduce the computing time currently required to perform transient CFD analyses. Processes characterised by continually changing flows and with a long time period of interest (e.g. engine compartments in heat soak) will then become feasible for simulation-based investigations, reducing vehicle development times and costs.

4. Few authors have researched methodologies able to reduce the CPU runtime for transient CFD simulations. The tested strategies were based on modelling simplifications that noticeably affected the accuracy of the predictions. A strong interest exists for novel and alternative methods/procedures enabling fast detailed analyses of time-dependent processes.

5. Literature highlights a general difficulty in the construction of representative scaled models of ventilated compartments due to the range of physical driving forces that govern the flow field. Buoyant, inertial and viscous forces all contribute to the developing flow and complete dynamic and geometric similarity with the full-scale prototype has not been successful. It has been shown, however, that for $GrPr \geq 4\times10^5$ a thermal phenomenon is independent of the individual criteria of similarity. The condition of "auto-similarity" was considered met in the present study since the Rayleigh numbers of the underhood model and its full-scale prototype were in the range $2\times10^6 < GrPr < 2\times10^8$.

6. The use of thermocouples logging onto a dedicated processing unit has proved, in a wide range of past studies, to be a simple yet reliable quantitative thermal measurement technique. Particle image velocimetry emerged from the literature survey as the most suitable non-intrusive whole-field optical technique for measuring convective flow patterns.

1.3 RESEARCH OBJECTIVES

The main objectives of the PhD research are:

1. Validate the CFD simulation of a natural convective flow against experimental measurements, while gaining a better understanding of the buoyant flow patterns developing in a vehicle underhood under thermal soak.

2. Develop a numerical strategy to reduce the CPU processing time currently required for fully conservative transient simulations.

The first objective will be tackled firstly by investigating empirically the buoyancy-driven airflow patterns and the spatial temperature distributions within a simplified half-scaled underhood model. The analysis will give a qualitative insight into the airflow patterns induced by buoyancy in an underhood compartment. Quantitative data will then be collected for comparison with the CFD simulations, which will be performed in steady-state with the software package VECTIS [Ricardo UK Ltd 2004]. The comparison between experimental and computational data will quantify the accuracy of the CFD software and permit to address the reasons for discrepancy. Such experimental characterisation and validation work on natural convection, applied to a vehicle underhood compartment (even if simplified in its geometry) is not believed to have been reported before in literature.

A reliable computational procedure able reduce the computing time of a typical fully conservative transient simulation will also be researched. The methodology will be tested on simple geometries and then employed to simulate the transient thermal and flow development within the underhood model. The new computation methodology will aim to provide time-accurate predictions in agreement with the experimental data so as to be implemented with confidence by a typical engineering analysis group.

1.4 OUTLINE OF THE THESIS

The thesis is divided into seven chapters. The apparatus and techniques used for the experimental investigation are presented in Chapter 2. The characteristics of the laboratory rig are described together with the procedures followed during the measurements. Data uncertainty is also addressed.

In Chapter 3, the transport equations governing the convective airflow in a vehicle underhood are formalised and their numerical implementation in CFD is discussed. The geometry and boundary conditions of the modelled compartment are also described. A sensitivity analysis is performed to optimise the CFD solver parameters and the results are discussed in the chapter.

The main characteristics of the natural convection flow patterns observed in the laboratory model are documented in Chapter 4. The detailed comparison between experimental and numerical data in steady thermal conditions is reported. The accuracy of the CFD predictions is assessed based on the agreement with the laboratory measurements. Both numerical and experimental errors are accounted for during the data comparison and are discussed in the chapter.

The second part of the thesis presents the work carried out to define a method for less computing-intensive CFD transient simulations. Chapter 5 describes the numerical tests performed with different methodology variants on geometric models with different degrees of simplification. The results are examined against the baseline full transient simulation data.

A comparison between the time-marching CFD predictions for the underhood model during transient cooling and the transient data recorded from experimental investigations is contained in Chapter 6. The underhood model proved a good validation test case for the proposed "fast transient" methodology. The efficiency and accuracy of the calculation procedure is assessed.

The last chapter of the thesis contains a summary of the research and draws the main conclusions. Necessary further work is also proposed.

Chapter 2

EXPERIMENTAL SETUP AND PROCEDURE

2.1 PRELIMINARY REMARKS

Experimental investigations were carried out to characterise qualitatively and quantitatively the airflow pattern and the temperature field in the underhood laboratory model and to provide data for comparison with CFD simulations.

Steady-state investigations were performed when the buoyant flow reached a quasi-steady condition within the compartment, i.e. when the time variation of the temperature on the block surfaces was not significant (time-averaged temperatures varied only with position). Repeated measurements were taken and the data was averaged.

Transient measurements were taken while the underhood components were cooling down from set thermal conditions. Temperatures were recorded continuously for 30 minutes while flow measurements were taken in replicates at pre-set time intervals and successively ensemble averaged.

Particle image velocimetry emerged as the optimal non-intrusive optical technique for mapping the flow velocities whereas temperature measurements required direct instrumentation with thermocouples. The following paragraphs describe the geometric configuration and the features of the laboratory model, the set-up of the instrumentation and the procedures followed for recording the data. Measurement uncertainty is also discussed.

2.2 EXPERIMENTAL SETUP

Laboratory Underhood Model Configuration

An enclosure representing a vehicle engine-bay was constructed in a 1:2 scale (compartment base of 0.57 m × 0.56 m, maximum compartment height of 0.40 m). The scaling size was chosen compromising between the preservation of the thermal and flow conditions in full-scale and the requirements of the PIV instrumentation. The first requirement restrained from using a smaller geometric scale as it would have hindered the dynamic similarity with a full-scale underhood (Rayleigh number less than 4×10^5); the latter restricted the model to be manufactured in a larger size because PIV observational areas are necessarily very small (few centimetre squares) for a satisfactory vector resolution. A high image resolution was particularly necessary for post-processing the PIV data of this study because natural convection is characterised by very low flow velocities.

The overall geometry of the experimental model was simplified in its shape for easiness of manufacturing but the characteristic geometric features, typical of a front-engine sport saloon vehicle, were conserved. Figures 2.1 to 2.3 depict the physical boundaries of the model superimposed on the slice views of a typical underhood environment (blue lines represent the outline of the compartment boundaries and red lines define the boundaries of the engine, gearbox and turbocharger).

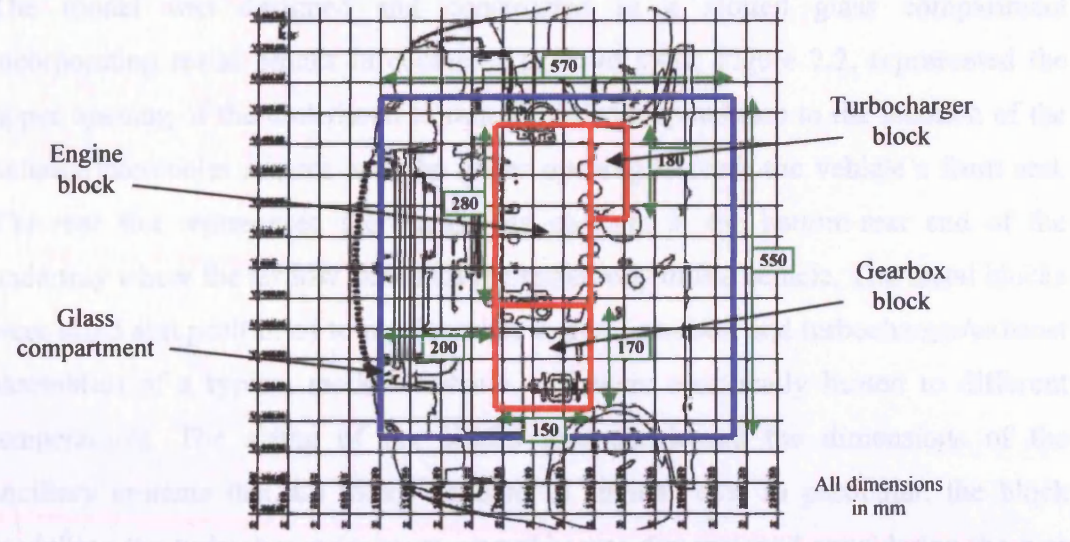

Figure 2.1 – Top view of physical boundaries of laboratory model superimposed on the slice view of a typical underhood configuration.

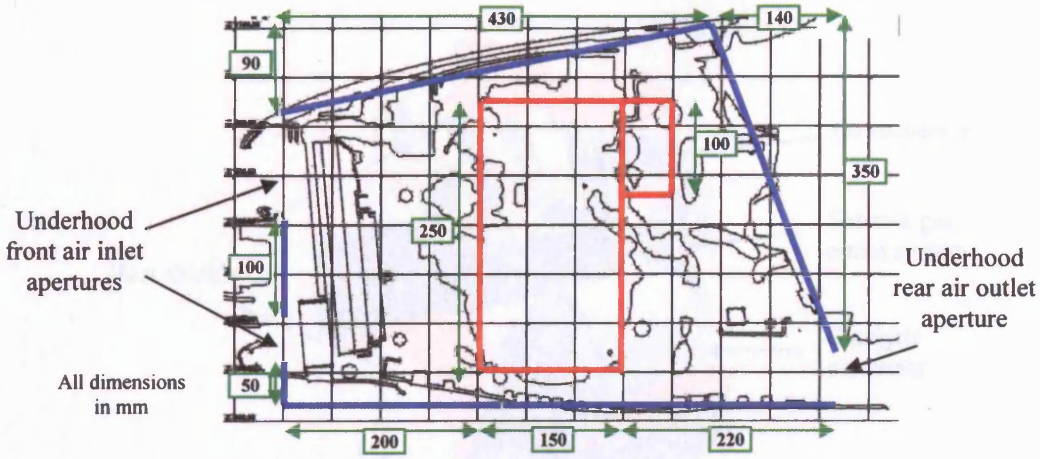

Figure 2.2 – Side view of physical boundaries of laboratory model superimposed on the slice view of a typical underhood configuration.

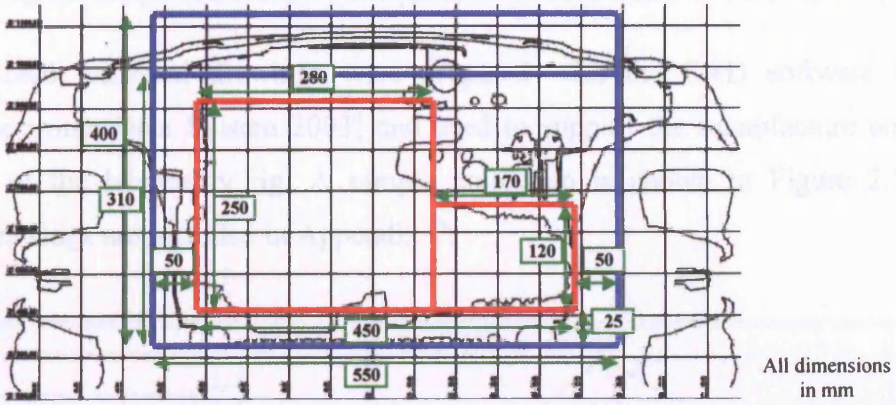

Figure 2.3 – Front view of physical boundaries of laboratory model superimposed on the slice view of a typical underhood configuration.

The model was designed and constructed as a slotted glass compartment incorporating metal blocks in contact. The front slots, Figure 2.2, represented the upper opening of the underhood to ram air, in correspondence to the location of the radiator/intercooler system, and the lower opening beneath the vehicle's front end. The rear slot represented the engine-bay aperture at the bottom-rear end of the undertray where the airflow exits into the underbody of the vehicle. The metal blocks were sized and positioned to represent the engine, gearbox and turbocharger/exhaust assemblies of a typical modern vehicle, and were electrically heated to different temperatures. The sizing of the blocks also considered the dimensions of the ancillary systems that are today standard in engine bays. In particular, the block modelling the turbocharger/exhaust assembly was dimensioned considering the size of a typical turbocharger with a close-coupled catalyst (Figure 2.4).

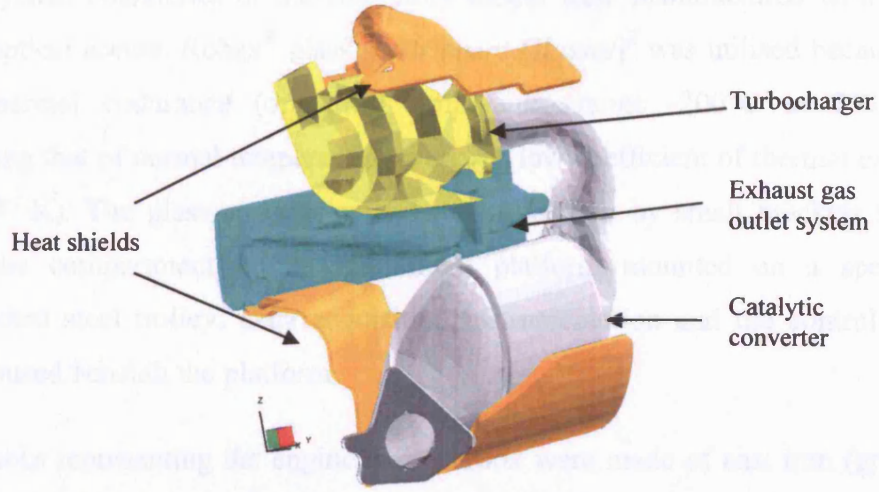

Figure 2.4 – Reference CAD model of a turbocharger with close-coupled catalyst used for sizing the simplified block in laboratory model (courtesy of Ricardo UK).

Two-dimensional technical drawings were prepared with the CAD software I-DEAS™ [Electronic Data System 2003] and used to support the manufacture and construction of the laboratory rig. A sample collection is shown in Figure 2.5. Additional drawings are included in Appendix C.

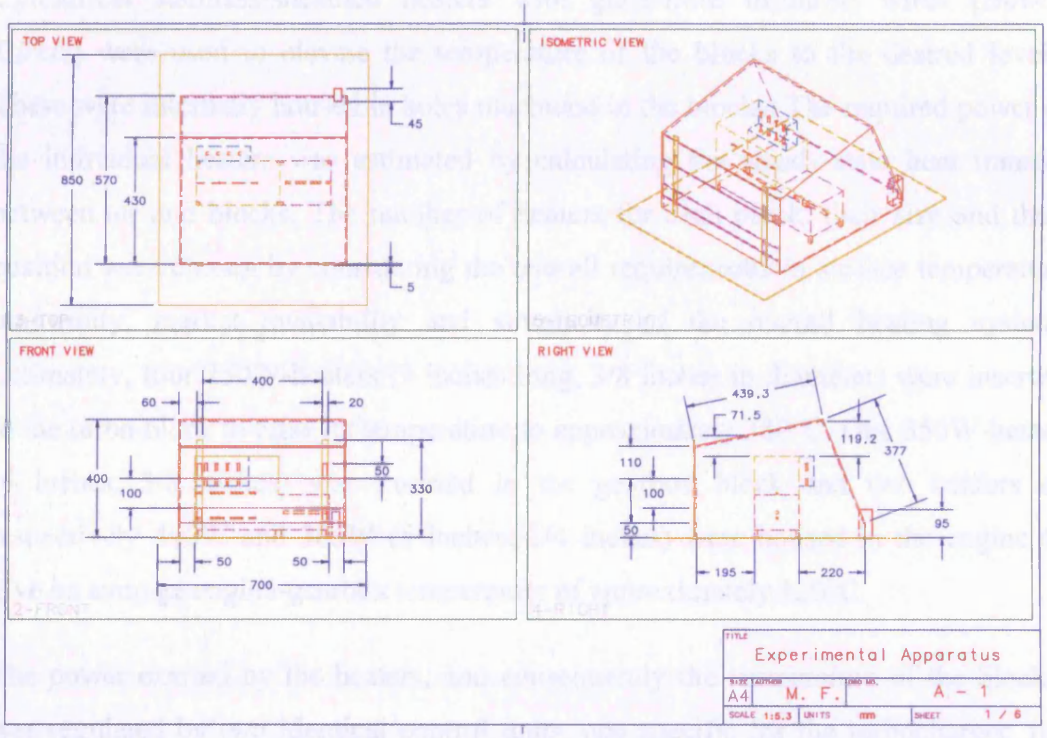

Figure 2.5 – CAD technical drawing of laboratory model (all dimensions in mm).

The physical boundaries of the laboratory model were manufactured with glass to allow optical access. Robax® glass [*Instrument Glasses*][2] was utilised because of its high thermal endurance (operating temperature range -200°C to 750°C), far exceeding that of normal tempered glass and its low coefficient of thermal expansion (1.6×10^{-7}/K). The glass surfaces were held in position by small brackets that also fixed the compartment on an aluminium platform mounted on a specifically constructed steel trolley. Data acquisition instrumentation and the controller units were housed beneath the platform.

The blocks representing the engine and gearbox were made of cast iron (grey type, grade 250) and had flat surfaces. For ease of manufacture, the engine was made of three separate but geometrically identical blocks positioned one over the other. The turbocharger block was cut into shape from an aluminium slag (aluminium alloy, type 6082) and was positioned on the side of the engine block with screws. It was however separated from the engine surface by a 5mm-thick insulating pad made from Duratec750® [*RS Components Ltd*].

Cylindrical stainless-sheathed heaters with glass-fibre insulated wires [*Hawco Direct*] were used to elevate the temperature of the blocks to the desired levels. These were internally housed in holes machined in the blocks. The required power of the individual heaters was estimated by calculating the steady-state heat transfer between air and blocks. The number of heaters for each block, their size and their position were chosen by considering the overall requirements in surface temperature uniformity, market availability and simplicity of the overall heating system. Ultimately, four 250W-heaters (3 inches long, 3/8 inches in diameter) were inserted in the turbo block to raise its temperature to approximately 380°C. One 350W-heater (6 inches, 3/8 inches) was inserted in the gearbox block and two heaters of respectively 400W and 305W (5 inches, 1/4 inches) were housed in the engine to give an average engine-gearbox temperature of approximately 120°C.

The power exerted by the heaters, and consequently the temperature of the blocks, was regulated by two identical control units, one specific for the turbocharger, the

[2] Henceforth, the companies that manufactured or supplied the materials or the instrumentation used for the experimental study will be referenced in square brackets with italic font. A complete list can be found in the *Reference* section of this thesis.

other regulating the temperature of both the engine and gearbox. Figures 2.6 and 2.7 show respectively the diagram of the wiring circuit and a 2-D drawing of the control unit box shown as constructed. The power controllers were of the configurable type [BS-1000 Series, *Hawco Direct*] with Proportional-Derivative-Integral (PID) control architecture, thus with system response amenable to fine-tuning.

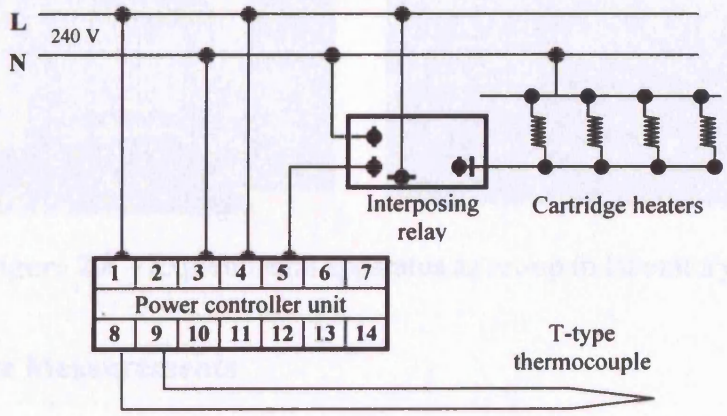

Figure 2.6 – Wiring circuit for heater's power control unit.

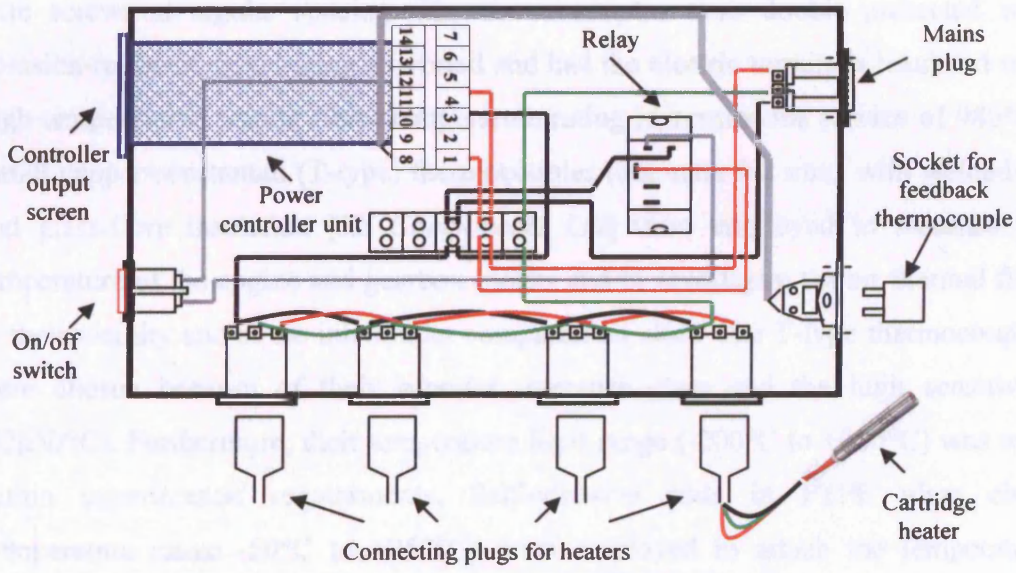

Figure 2.7 – Top view of custom-made power control unit box.

In order to maintain the thermal convection patterns stable and reproducible, the underhood model was installed in a relatively large and still room (2.5 m high, 2.5 m wide and 5.5 m long), as shown in Figure 2.8. No heating and cooling devices were

employed for controlling the ambient air, which, however, was not expected to significantly affect the thermal conditions in the compartment.

Figure 2.8 – Experimental apparatus as set-up in laboratory.

Temperature Measurements

The temperature of the turbocharger surfaces was quantified with nickel-chromium/nickel-aluminium (K-type) sensors [*Omega Engineering Ltd*] attached with screws at regular spacing. The thermocouples were double protected with abrasion-resistant nickel-alloy overbraid and had the electric terminals insulated with high temperature ceramic fibre (temperature rating in continuous service of 980°C). Small copper/constantan (T-type) thermocouples (diameter 0.2 mm) with welded tip and glass-fibre insulation [*RS Components Ltd*] were employed to measure the temperature of the engine and gearbox blocks and to investigate the air thermal field in their vicinity and at the inlet/outlet compartment slots. The T-type thermocouples were chosen because of their superior tolerance class and the high sensitivity (42μV/°C). Furthermore, their temperature limit range (-200°C to +350°C) was well within experimental requirements. Self-adhesive pads in PTFE glass cloth (temperature range -50°C to +250°C) were employed to attach the temperature sensors onto the block surfaces, as shown in Figure 2.9.

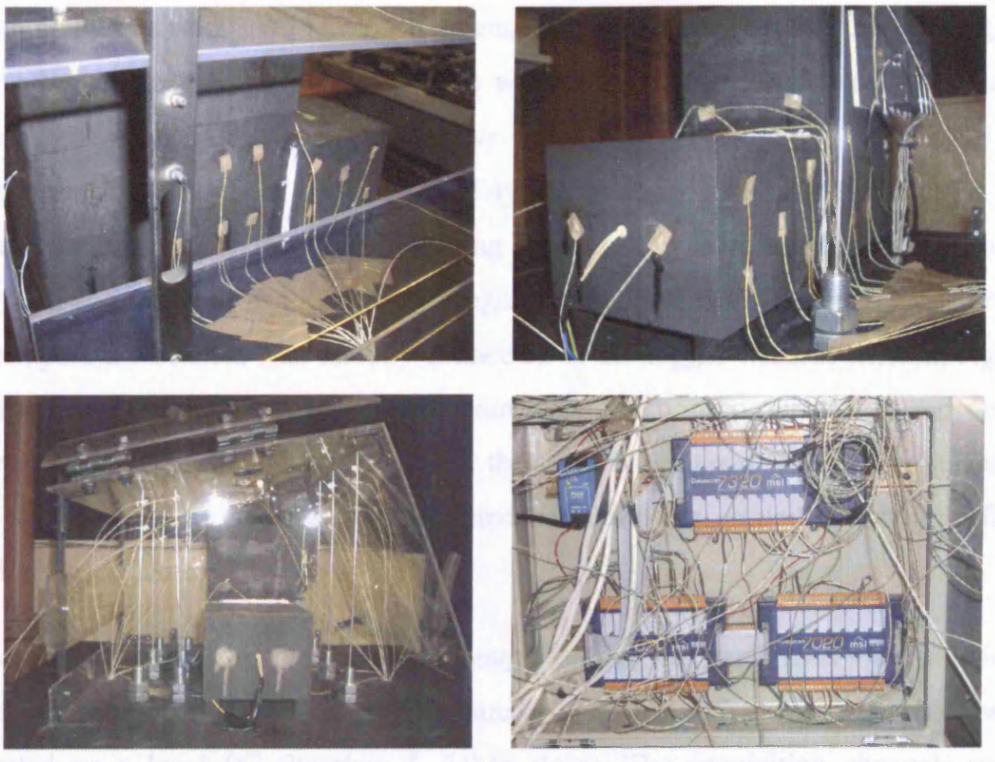

Figure 2.9 – Thermocouple and logging instrumentation.

Thin supporting rods, visible in Figure 2.9, were manufactured for positioning the thermocouples across parallel planes within the compartment, thus providing temperature readings of the fluid domain. The rods had a series of 0.2 mm holes to allow fitting and protruding of the sensors at specific spatial locations. Above the heated blocks, the thermocouples were glued to thin threads with their ends attached to the upper glass boundary.

The sensors used to map the air thermal state were shielded to minimise reading errors from heat radiation. Shielding was provided with tiny foils (approximately 2×2 mm^2 area) positioned in front of the thermocouple tips. They were mounted parallel to the flow direction, where possible, to prevent obstruction to the buoyant flow. The measurements were also repeated without screening to check the effectiveness of the shielding setup; if necessary the foils were re-positioned and re-oriented.

The measurement accuracy of the thermocouples was determined using the reference value of a precision thermometer (accuracy ±0.5°C). The calibrated accuracy stated by the manufacturer was confirmed to be ±1.5°C for the K-types and ±0.5°C for the T-types.

All temperatures were sampled at a frequency of 1Hz and recorded with a datalogger before being processed. Data acquisition was performed by an external Datascan® 16-bit processor [*Measurement Systems Ltd*] with a sensitivity of 0.625μV (resolution of ±0.02°C for both K- and T-type thermocouples). The system was set up in a multiplexer architecture providing a 48-channel capability by means of a main unit connected to two modules through an expansion bus. The field wiring from the temperature sensors was directly connected to the logger without external signal conditioning; all the necessary linearization, cold junction compensation and noise filtering were performed automatically by the acquisition board. The data acquisition unit was allowed to stabilise in a powered condition for around one hour before readings were taken.

Monitoring and recording of the thermocouple output was performed via a software specific to the logging unit [Dalite Software, *Measurement Systems Ltd*], which was executed on a local PC (Pentium I, 64Mb Ram). The acquisition channels were individually configured and the logging rate programmed (1 Hz). The software allowed real time monitoring of the temperature condition in the compartment via a Dynamic Data Exchange (DDE) interface and stored the data in a file format suitable for importing into a spreadsheet package. A sample of the processed recordings is given in Figures 2.10 and 2.11.

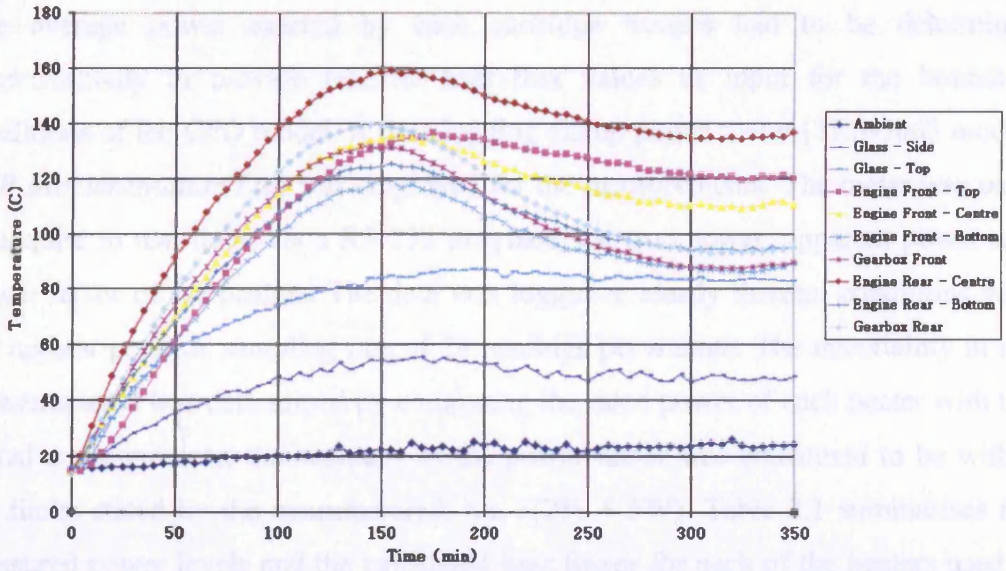

Figure 2.10 – Sample of processed thermal data for engine and gearbox blocks during heating towards steady state.

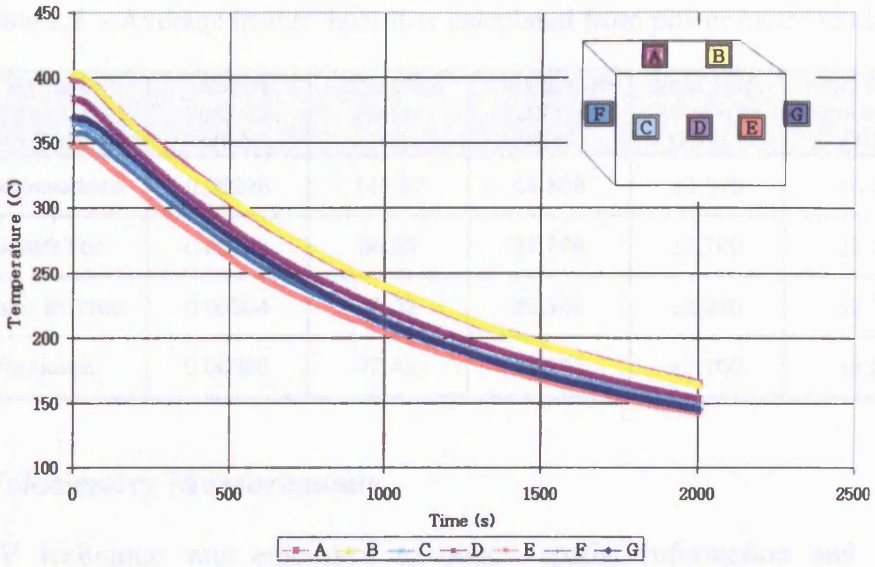

Figure 2.11 – Sample of processed thermal data for turbocharger block during cooling (position of sensors on the block shown).

Each set of measurement consisted of approximately 40 thermocouple recordings at different spatial locations. Several investigations were required to reconstitute the complete temperature field in the underhood. The temperatures were recorded for approximately 5 hours during heating up to reach steady state (Figure 2.10), for 1 hour at steady conditions and for 30 minutes during cooling down of the blocks.

Heater Power Output Measurements

The average power exerted by each cartridge heaters had to be determined experimentally to provide realistic heat flux values as input for the boundary conditions of the CFD model. A data-logging clamp power meter [TES-3063 model, *ATP Instrumentation Ltd*] was employed for the measurements. The meter was used to acquire in real-time, via a RS-232 interface, the true power, apparent power and power factor of the heaters. The data was logged at steady thermal conditions with the highest possible sampling rate of 20 readings per minute. The uncertainty in the measurements was determined by comparing the rated power of each heater with the actual measurements; the accuracy of the power meter was confirmed to be within the limits stated by the manufactured, i.e. ±(2% + 5W). Table 2.1 summarises the measured power levels and the calculated heat fluxes for each of the heaters used in the underhood model.

Table 2.1 – Average heater' heat flux calculated from power meter reading.

Heater Location (wrt Block)	Heater Surface (m^2)	Measured Power (W)	Calculated Heat Flux (W/m^2)	Heat Flux Accuracy (W/m^2)	Heat Flux Accuracy (%)
Turbocharger	0.00228	145.57	**63,800**	±3,500	±5.5
Engine Top	0.00253	95.58	**37,700**	±2,700	±7.2
Engine Bottom	0.00304	85.32	**28,100**	±2,200	±7.8
Gearbox	0.00380	72.42	**19,100**	±1,700	±8.9

Flow Velocimetry Measurements

The PIV technique was employed to obtain spatial information and velocity distribution of the buoyant flow in the laboratory compartment.

Figure 2.12 depicts schematically the typical arrangement of a PIV instrumentation system. A particle-laden flow is illuminated twice by a sheet of laser light produced by cylindrical optics and the displacements of the particles are recorded as either a double-exposed image or a pair of single-exposed images. The recorded displacement field is measured locally across the whole area of interrogation (AOI), scaled by the image magnification and then divided by the known laser pulse separation ($t_2 - t_1$) to obtain the flow velocity from sub-areas of the image (or *interrogation windows*). Statistical correlation techniques then evaluate the particle image matching and the flow velocity vectors. The result is a complete 2-D velocity vector field for the investigated flow region.

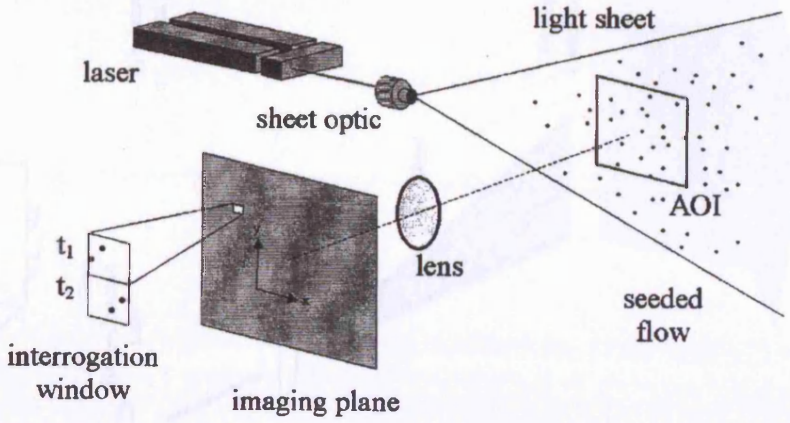

Figure 2.12 – Typical setup of PIV instrumentation for 2-D flow analysis [LaVision 2002a].

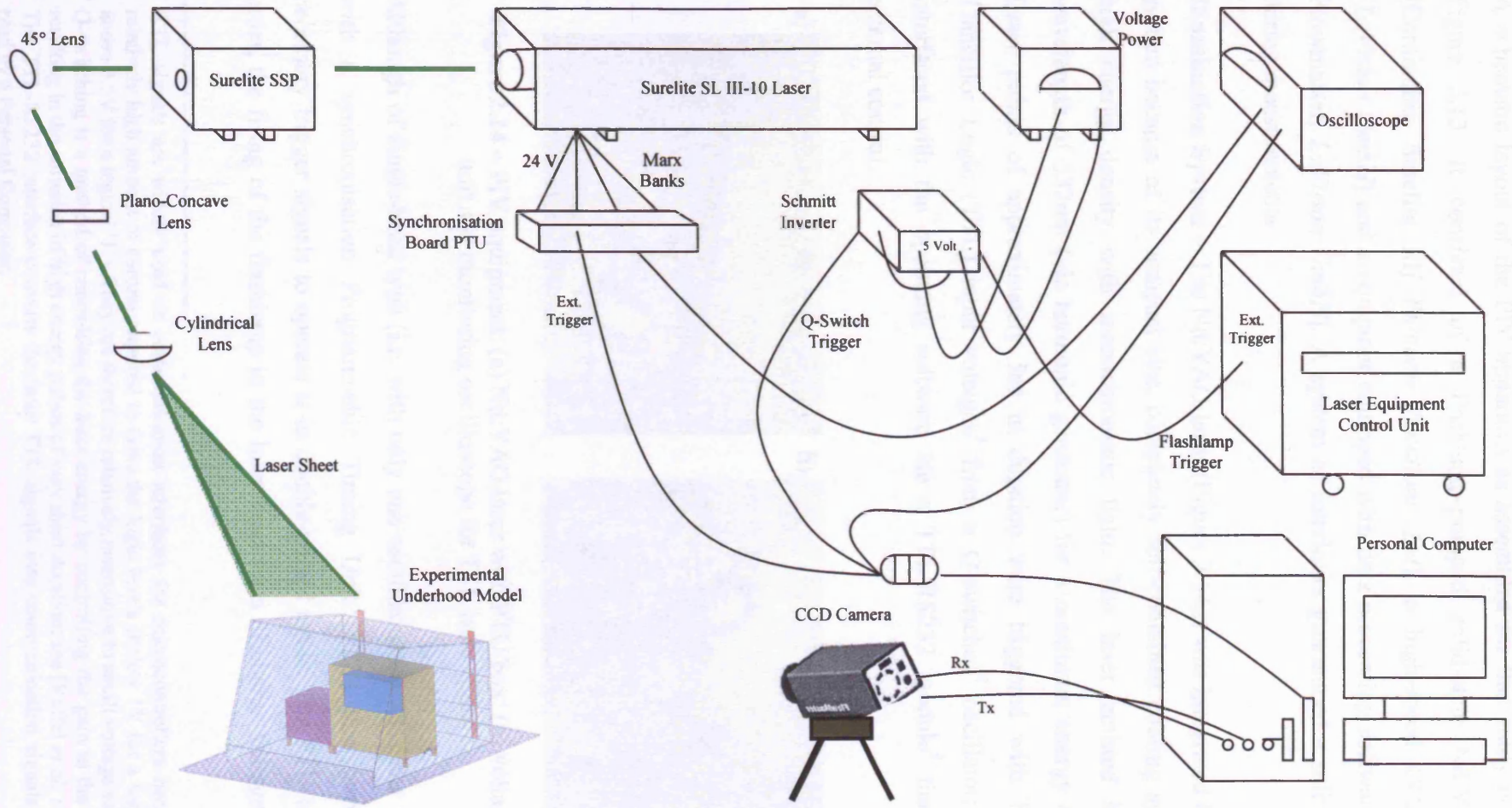

Figure 2.13 – Schematic diagram of PIV instrumentation as set-up for the laboratory investigations.

A schematic layout of the PIV apparatus as assembled for this study is shown in Figure 2.13. It consisted of a flashlamp-pumped solid-state Nd:YAG laser [Continuum Surelite III, *Photonic Solutions Ltd*], a high-speed CCD camera [*LaVision GmbH*] and a computer equipped with data-processing software [DaVis-Flowmaster, *LaVision GmbH*]. A system of interlocks guaranteed a safe operation during measurements.

Illumination System – The Nd:YAG laser (Figure 2.14a) was integrated in the PIV system because of its compact size, completely self-contained cooling system and high energy density with monochromatic light. The laser emitted light at a wavelength of 532nm (via harmonic generator) for a maximum energy of 425mJ. Laser pulses of approximately 5ns in duration were triggered with Transistor-Transistor Logic (TTL) input voltages[3] from a Q-switched[4] oscillator; this was interfaced with the operating software via a TTL/RS232 module[5] that enabled external control.

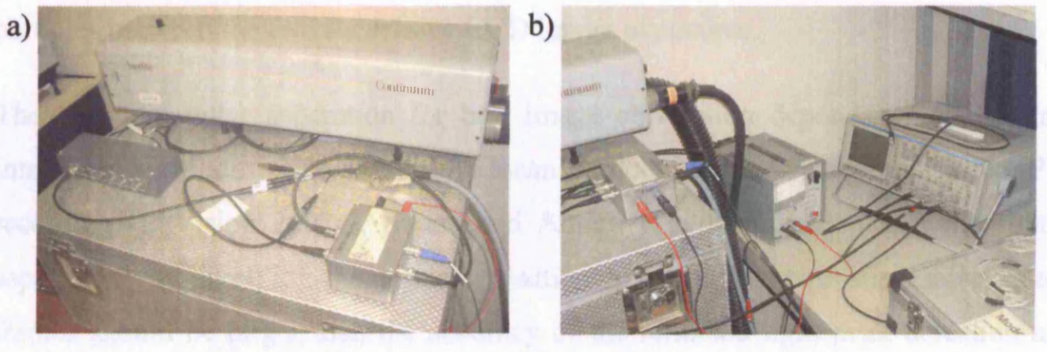

Figure 2.14 – PIV equipment: (a) Nd:YAG laser with PTU box; (b) voltage input unit and monitoring oscilloscope for TTL laser signals.

Although of single-head type (i.e. with only one oscillator rod), the laser was fitted with a synchronisation Programmable Timing Unit (PTU) that provided the necessary trigger signals to operate it in double-pulsed mode. The PTU tracked, in order, the firing of the flashlamp in the laser head (at a discharge voltage 1.78kV),

[3] TTL signals are widely used as communication interfaces for microcontrollers because of the relatively high amount of current required to drive the logic levels (below 1V for a logical '0' and above 3.5V for a logical '1'). They are therefore relatively insensitive to small voltage variations.

[4] Q-switching is a method of controlling the laser energy by controlling the gain in the laser cavity resulting in the emission of high energy pulses of very short duration; see [Raffel *et al.* 1998].

[5] The TTL-RS232 interface converts the laser TTL signals into communication signals that can be read by a Personal Computer.

the Q-switch trigger of the first Marx bank[6] at a pre-selected delay (i.e. first laser pulse) and the Q-switch trigger of the second Marx bank at a pre-set time interval (i.e. second laser pulse).

The time between the two laser pulses, dt, was adjusted manually by modifying the timing of the Q-Switch triggers. The operation was rendered possible by displaying on the screen of a 20MS/s–20MHz digital oscilloscope [1604-type, *L&T Gould*, Figure 2.14b] the flashlamp optical pulse (acquired with a photodiode) and the Q-switch voltage signals, all plotted on a timescale. Every adjustment on the temporal position of the laser flashes within the single flashlamp energy curve could therefore be monitored, thus allowing for a precise setup and guaranteeing pulses with similar power output.

The value of dt practically defined the separation between the two exposures of the PIV image recording. Hence, for a given flow velocity and factor of magnification, the selected pulse interval determined the spatial distance, ds, travelled by the particles between the two successive CCD image exposures.

The optimum pulse separation for best image correlation depends on the desired interrogation window size and on the mean particle image displacement in the PIV recording [LaVision 2002a]. Keane and Adrian [1990] suggested that the spatial separation (in pixel) of the particle position between the two successive image frames should be larger than the accuracy of the reflected light peak detection and smaller than a quarter of the selected interrogation window size (in pixel), i.e. $0.1\text{pixel} < ds < 1/4$ IntWinS. As a guideline, LaVision [2002a] recommends a mean particle image shift (i.e. tracer displacement) in the range of 3 to 5 pixels.

In this study, the Q-switches were triggered with a dt of 200μs to record images with adequate particle displacement. The laser was therefore fired at the temporal extremes of the flashlamp energy curve as shown in Figure 2.15.

[6] Marx banks consist of a number of capacitors charging in parallel and switching in series to achieve very high voltage pulses.

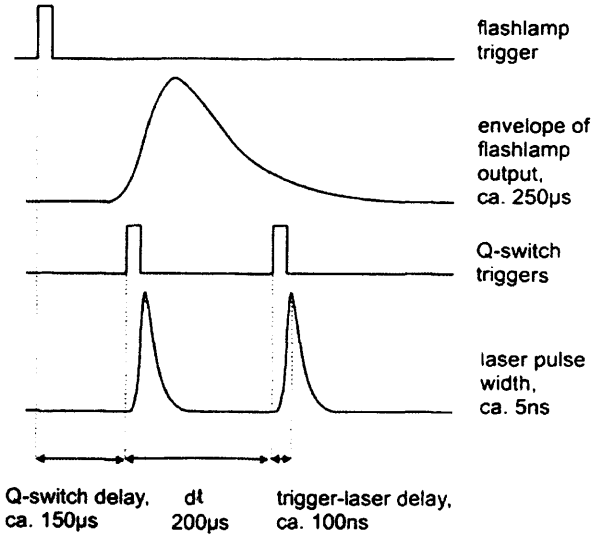

Figure 2.15 – Double-pulse triggering within single flashlamp cycle (adapted from [LaVision 2002a]).

The selected pulse separation was the best possible value that could be used, considering:

- The generally very low particle mean shift that was observed, which was a direct consequence of the low velocities of the natural convective flow.

- The limits in camera resolution, which restricted from investigating the flow on larger interrogation areas. In fact, as the minimum pixel array required to describe a single tracer particle is of 2-by-2 pixels in size [Chang *et al.* 2004], the area of interrogation had to be necessarily small (average size was of 40×30 mm^2) to ensure a satisfactory resolution. On the other hand, the size of the particle tracers could not be increased, in order to guarantee that the flow streamlines were followed with minimal slip (further discussed below).

- The intrinsic limits of the laser's single-oscillator configuration, i.e. the time between the two successive laser pulses could not be controlled independently as it would be possible with a double-oscillator laser.

The chosen Q-switch trigger interval restricted the total energy available per pulse. As shown in Figure 2.16 [Continuum 1995b], double-pulsing with a separation of 200µs (largest possible interval when firing during the same flashlamp discharge) resulted in individual pulse energies 15% of the maximum energy available in single

pulse operation. The total energy of both pulses was therefore 0.3×425mJ or 127.5mJ. Nevertheless, with the use of highly reflective laser sheet optics (to avoid any additional energy loss from the laser beam), the power of the emitted light was found to be satisfactory for illuminating the seeded flow: the intensity of the reflections from the particle tracers was adequate for both image correlation and vector processing.

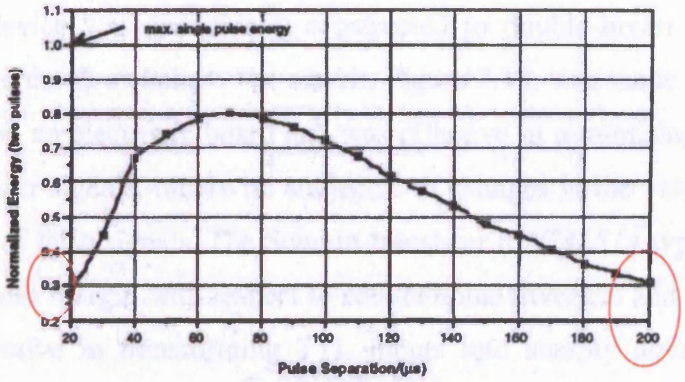

Figure 2.16 – Laser energy versus separation for double-pulse operation [Continuum 1995b].

The mean particle shift measured from the acquired images ranged between 1.5 and 2 pixels, depending on the investigated area (i.e. the image size and the velocity of the illuminated flow). It was deduced that the "optimal" particle shift of 5 pixels could be obtained using a *dt* of approximately 600μs. During the setting of the laser triggering timing, an attempt in increasing the laser separation and hence the particle shift was made by firing a single laser pulse in each of two successive flashlamp discharges, as schematically described in Figure 2.17.

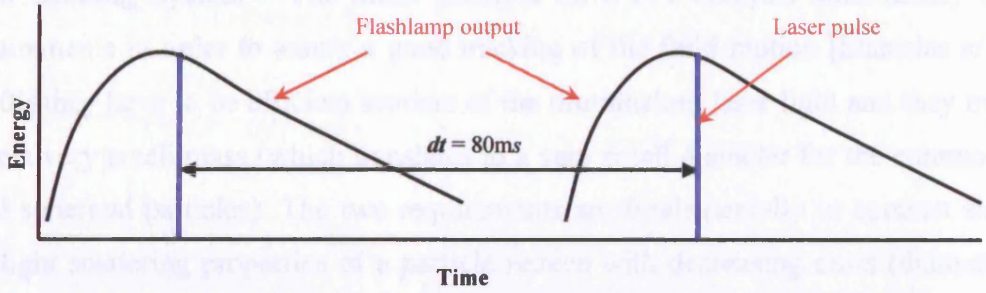

Figure 2.17 – Single-pulse operation at 12.5Hz.

However, since the laser had a set frequency of operation of 12.5Hz, the temporal separation between two successive and identical flashlamp discharges was inevitably of 80ms, i.e. 130 times larger than required (600μs). At the same time, the field of view could not be increased by such a factor due to aforementioned requirements in image spatial resolution. As a result, the recorded images did not correlate because of a complete out-of-plane loss of tracers.

An electronic device was specifically constructed to double-invert the TTL laser signals triggering the Q-switches. The circuit, Figure 2.18, was made with a Schmitt transistor built on an electronic board and was effective in minimising the electrical noise of the trigger signals, otherwise subjected to changes in the voltage amplitude and thus at risk of false signals. The Schmitt transistor (*SN74LS14* type) was chosen for its greater noise margin with respect to conventional inverters and because it was particularly effective in transforming TTL inputs into sharply defined, jitter-free output signals.

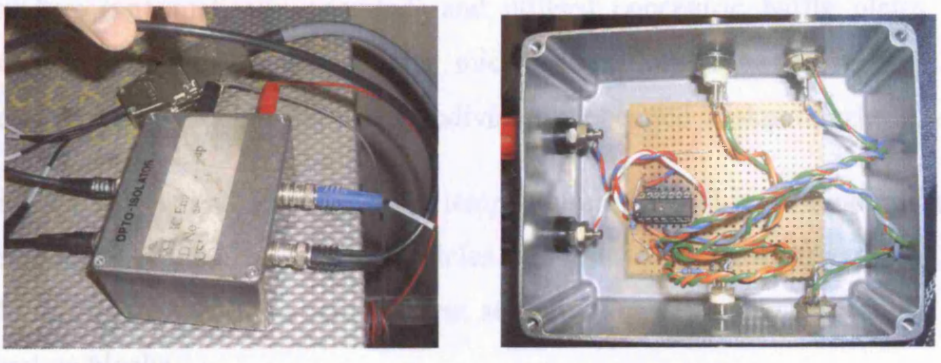

Figure 2.18 – Schmitt-inverter circuit box.

Flow Seeding System – The tracer particles for a PIV analysis must satisfy two requirements in order to assure a good tracking of the fluid motion [Stanislas *et al.* 2000]: they have to be efficient scatters of the illuminating laser light and they must have a very small mass (which translates to a very small diameter for the commonly used spherical particles). The two requirements are fundamentally in contrast since the light scattering properties of a particle reduce with decreasing mass (diameter); thus a compromise had to be sought in this study. The evaluation of the terminal settling velocity of a particle under gravity enabled to determine if the tracers would follow the air streamlines without excessive slip. The settling velocity is the

minimum velocity the flow must have in order to transport (as a suspended load) a particle. This should be ideally negligible compared to the actual flow velocity in order to ensure neutrally-buoyant PIV tracers. Stokes' drag law [Posner 2001] can be used to calculate the terminal settling velocity of spherical tracers:

$$u_{\infty} = \frac{g d_{pt}^2 \left(\rho_{pt} - \rho_f\right)}{18 \mu_f} \tag{2.1}$$

For measuring the underhood flow, vegetable oil droplets (organic corn oil) were employed as tracers because good light scatters, non-toxic, easily atomised and cheap. Owing to the very large density difference with air, the oil was atomised in droplets with diameter of approximately 1μm. The resulting settling velocity was 0.026 mm/sec (Appendix E), therefore, as required, of negligible magnitude.

The particles were produced using a liquid droplet seeder [LS-10 model, *Scitek Consultants*]. The device (Figure 2.19a) was connected to an air compressor via a control box (pneumatically operated) and utilised concentric baffle plates in its reservoir to atomise the liquid. The microscopic droplets were released with controllable and repeatable size by ten individually operated Laskin nozzles[7].

The low flash point and decomposition temperature of the oil was found not to be a critical factor because the seeded particles did follow the flow streamlines when introduced in the underhood compartment and rarely came in contact with the high-temperature blocks.

a) b)

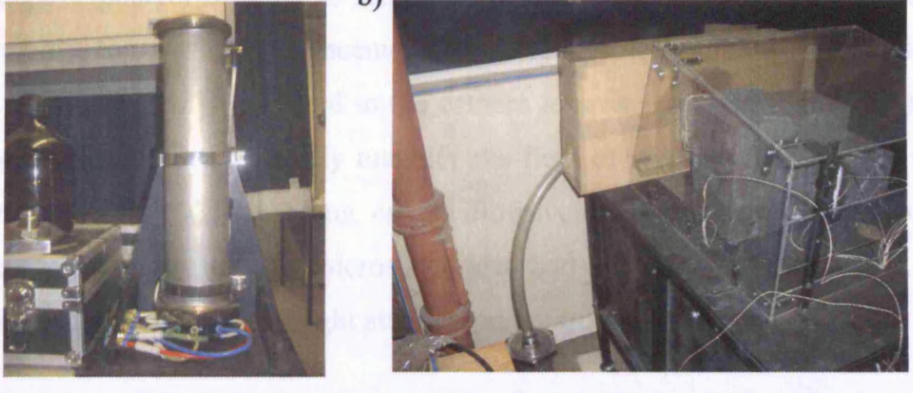

Figure 2.19 – PIV equipment: (a) liquid droplet seeder with Laskin Nozzles; (b) purpose-made inlet box connected to seeder.

[7] Technical details on the design and operation of Laskin atomisers are given by Melling [1997].

An "inlet box" connected to the seeder via a plastic tube (Figure 2.19b) was incorporated into the overall PIV system and placed at the compartment air inlet opening. The box ensured a stable seeding concentration aiming at creating a uniform distribution in the compartment. This resulted in a higher statistical correlation of the particle displacements within each PIV interrogation zone (i.e. high signal to noise ratio). Moreover, the inlet box avoided introducing the particles directly from the seeder at a finite velocity, thus minimising any disturbances to the natural convective flow: the seeding firstly accumulated in the box and was then "vented out" by the convective air motion developing in the underhood.

Image Acquisition System – The PIV imaging instrumentation was arranged with the largest velocity component of the observed flow field parallel to the light sheet (i.e. maximum flow velocity in the observed plane) and camera viewing direction normal to the light sheet. Such arrangement minimised the occurrence of systematic errors that would affect the flow mapping [LaVision 2002b].

The 12-bit CCD camera [3S-type, *LaVision GmbH*] was mounted on a tripod and fitted with a gear head for fine adjustments and calibration. Care was taken to adjust the light intensity during the recordings to avoid camera chip saturation: light reflections from metallic parts in and close to the observed area (i.e. block and K-type thermocouples sensors) were minimised by having the areas painted matt-black.

The camera was shuttered synchronously with the laser and the in-plane spatial displacement of the seeded particles was recorded in two 1280×1024 pixel images with single-exposure. In order to increase the spatial resolution of the images, and consequently the particle displacements, a long-distance microscope [Model K2, *Infinity Photo-Optical*] was fitted to the camera lens as shown in Figure 2.20a. The microscope was used to optically magnify the field of view by a factor that ranged between 1.25X to 3X, depending on the flow velocities in the investigated area. Besides the focusing ring, the microscope also had a built-in iris diaphragm, which allowed for depth of field and light attenuation control.

The dimension of the light sheet was regulated through the choice of optical lenses (shape and characteristics focal point) and by changing their relative distance. A combination of two plano-concave lenses (one at 45°) with 25 mm focal length,

placed in parallel with a positive cylindrical lens with 156 mm focal length [*Photonic Solutions Plc*], was used. The first lens was effectively turning the projected laser beam by 90° and had a reflectance of 99.5%. The lenses were mounted on a traversing system that allowed for their easy displacement to the required position (Figure 2.20b). The dimensions of the light sheet were modified in relation to the required size of the investigation area, which varied among the different observed regions. It was however always focused into a 1 mm thickness at the control area. This value was found to give the best compromise between maximum droplet illumination and minimum out-of-plane loss of particles.

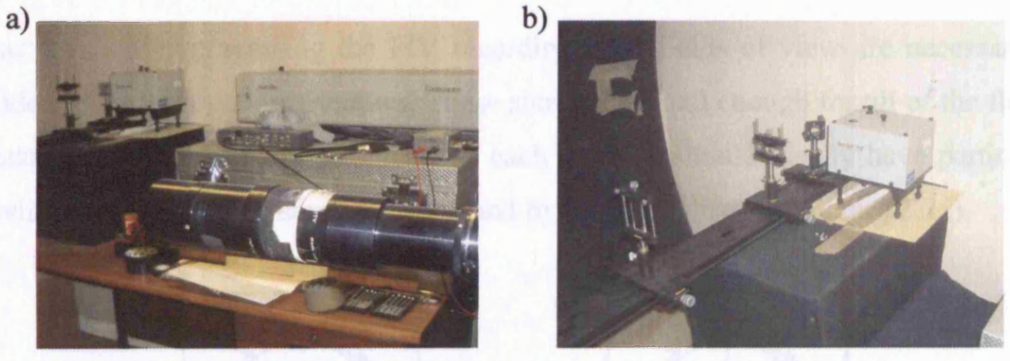

Figure 2.20 – PIV equipment: (a) long-distance microscope; (b) arrangement of lenses for laser light sheet.

Image Processing and Data Analysis – The evaluation of the flow structures essentially depends on the way the images are recorded. One possibility is to record the scattered light of both illuminations in one frame and then to evaluate the two exposures with *auto-correlation*. The other possibility is to record the scattered light from the illuminations in two separate frames (double frame/double exposure) and use the *cross-correlation* algorithm.

The information from the auto-correlation is ambiguous and not conclusive unless some a-priori information about the observed flow direction is available [LaVision 2002a]. With auto-correlation it is impossible to detect the sign of the particle displacement because it is unknown which particle is illuminated by the first and which by the second laser pulse. On the other hand, the cross-correlation is able to resolve both flow directions and intensities. However, a double-shuttered camera with a frame transfer faster than the delay between the laser pulses is necessary to

record the two separate images. This requirement has restricted its use in the past as recordings were almost exclusively performed with photographic film.

The fast electronic shutter of the CCD camera employed in this study and the relatively large pulse separation that was specified enabled the recording of the illuminated underhood flow with two separate images and thus the evaluation of the air velocities with cross-correlation. Because the second frame acquired by the camera could not be shuttered (as the first frame was being transferred to the camera register), a bandpass filter was used in front of the lens to avoid different background light intensities in the images.

When evaluating/processing the PIV recordings, the fields of view are necessarily divided into interrogation windows. These should be small enough for all of the flow structure to be statistically sampled, i.e. each window should ideally have particles moving uniformly in the same direction and by the same distance (Figure 2.21).

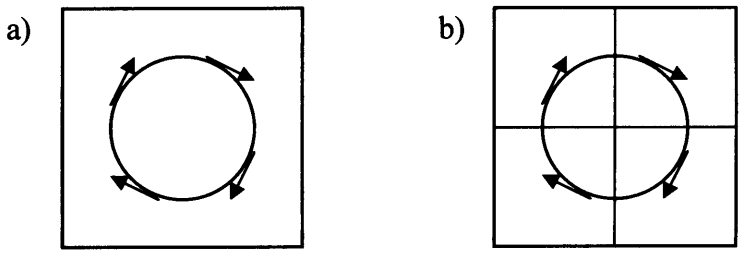

Figure 2.21 – Interrogation window size: (a) size too large to permit statistical sampling of particles; (b) correct size for evaluating flow vectors.

The cross-correlation algorithm operates on the light intensities inside each interrogation window. The procedure consists of computing the Fast Fourier Transform (FFT) of a single window, squaring it and performing the inverse-FFT. The highest correlation peak found is then taken as the displacement vector, ds. Consequently, only one vector per interrogation area is evaluated. Figure 2.22 illustrates schematically the spatial cross-correlation of two particle images with the displacement vector being calculated between corresponding interrogation areas.

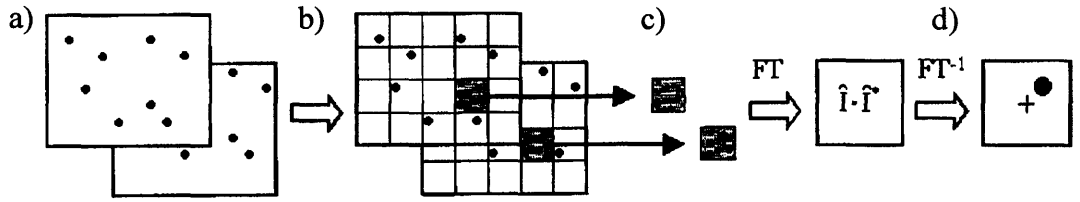

Figure 2.22 – Cross-correlation evaluation procedure: (a) double-frame/double-exposure; (b) images subdivided in interrogation windows; (c) windows evaluated with FFT-based algorithm; (d) highest correlation peak (shown as a dot) taken as displacement vector [LaVision 2002a].

The selection of an adequate size for the interrogation windows is a critical factor in PIV data processing. In this study, the velocity vectors were evaluated using an adaptive multi-pass algorithm with decreasing size. The algorithm performed a first evaluation pass with an initial interrogation windows size of 64×64 pixels and calculated a reference vector field; the cross-correlation was then performed on a 32×32 pixel mesh and the vectors calculated in the first pass were used as the best-choice particle shifts for the second pass. In this manner, the particle displacements were adaptively improved and more accurate and reliable vectors were determined. The production of erroneous (or *spurious*) vectors was also significantly reduced when compared to evaluations performed on windows with fixed sizes.

The images were processed on a dedicated PC unit (Intel® Xeon™, 2GHz) through the PIV software package DaVis [*LaVision GmbH*]. In addition to light intensity peak detection and localisation, algorithms were utilised for vector post-processing, i.e. to eliminate spurious vectors, fill up holes in the measured velocity field and to smooth measurement noise in the data. In particular, three numerical techniques were implemented in the data analysis to refine the velocity plots:

1) A 3×3 kernel median filter was applied to the two-component velocity matrices to discard estimates showing abrupt changes in velocity magnitude. The mean vector velocity augmented by two times the standard deviation was chosen as the cut-off value. Vectors with higher and lower velocities were therefore recognised as spurious and deleted. A *Q-factor* was also used as a post-processing criterion for eliminating questionable vectors below a pre-set ratio-threshold of 1.5. The *Q-factor* is the relative ratio between common image correlation backgrounds and it is defined as [LaVision 2002a]:

$$Q_{factor} = \frac{Ph_1 - Ph_{min}}{Ph_2 - Ph_{min}} > 1.5 \qquad (2.2)$$

where Ph_{min} is the lowest peak value in the correlation plane while Ph_1 and Ph_2 are the peak heights of the first and second highest correlation peaks. It is easily inferred from Equation (2.2) that the higher the *Q-factor* value, the higher would be the confidence in the vector.

2) An interpolation function was implemented at the post-processing stage to replace the spurious vectors by filling the gaps with a weighted average of the surrounding vectors. The algorithm also estimated velocity vectors in the drop out regions. It was in fact observed that, due to the model geometry and the flow conditions, the tracers did not always completely fill the field of view, even after their concentration in the compartment was significantly increased. Interpolation errors were reduced by testing the effect of different algorithm parameters on the processed vector plots, such as reducing the threshold of velocity gradient.

3) A 3×3 vector-smoothing filter was employed to reduce noise in the final processed plots and improve the graphical presentation for CFD comparison.

Figure 2.23 shows the result of implementing the post-processing functions for the flow region investigated in the vicinity of the turbocharger block.

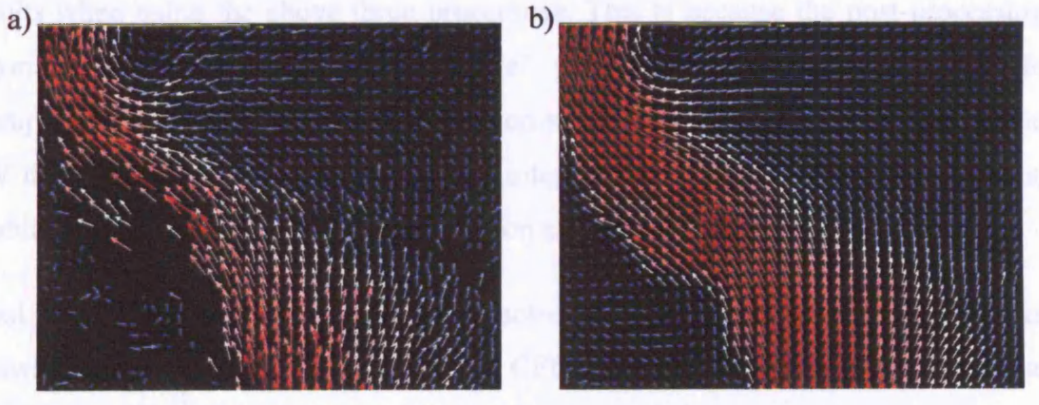

Figure 2.23 – PIV image post-processing: (a) flow field vector plot; (b) post-processed vector plot.

Appendix F contains the results of a sensitivity analysis carried out to assess the effects of the post-processing algorithms on the final vector plots and the

consequences of using different data-handling procedures. The sensitivity analysis was performed on the first 10 images acquired under steady-state conditions for two representative flow regions: at the outlet of the compartment (Figures F1–F4) and above the turbocharger (Figures F5–F8). The quantitative data presented in Figures F1 and F5 clearly demonstrates that the interpolating and smoothing functions had only small effects on the final plots: the mean image vector velocities were almost identical. On the other hand, the algorithms eliminating the spurious vectors were considered essential to obtain a reliable representation of the flow structure and accurate maximum flow velocity values.

Figures F2 to F4 and F6 to F8 in Appendix F compare three different methods for averaging the vector data:

1. The images were averaged into a single one that was then cross-correlated into a vector plot and finally post-processed.

2. The images were singularly cross-correlated into separate vector plots and then averaged. The resulting vector plot was then post-processed.

3. The images were singularly cross-correlated and separately post-processed. The resulting post-processed vector plots were then averaged.

No substantial and consistent difference was observed in the computed velocity results when using the above three procedures. This is because the post-processing algorithms were based on "conservative" parameters, which resulted in little manipulation of the vectors. The third option was however chosen for processing the PIV data because it could be more easily integrated into a "batch" type of analysis, enabling a fully automated vector calculation and image post-processing.

Finally, quantitative information was extracted from the post-processed vector plots allowing the subsequent comparison with CFD predictions (Chapters 4 and 6). The data consisted of minimum, maximum and average flow velocity. The software also evaluated the standard deviation from the mean velocity after averaging the data.

2.3 EXPERIMENTAL PROCEDURE

The experimental observations and the computational simulations were carried out simultaneously and each of them was used to refine the set-up of the other. This course of action allowed modifications/corrections of the geometry and boundary conditions to be made throughout the testing timeframe to both the laboratory and the computational models. An example was the measurement of the temperature of the underhood base that consented to identify an incorrect boundary condition specified in the CFD model. The base of the compartment was initially approximated as being isothermal (at ambient conditions) but VECTIS predicted in its vicinity a lower air temperature than measured (i.e. the surface was behaving as a "heat sink"). The issue was resolved by refining the approximation using adiabatic thermal conditions at the boundary. The use of the power meter during experimental investigations also was beneficial as it enabled the actual laboratory heat flux values to be prescribed as heat sources in the CFD model. On the other hand, the results of early simulations made possible both the identification of "interesting" flow patterns within the compartment volume, allowing the planning for effective PIV observations, and the strategic positioning of the thermocouples.

Tables 2.2 and 2.3 summarise the thermal tests and the PIV measurements performed. Schemes showing the position of the temperature sensors and of the areas investigated with PIV are presented in Appendix D.

2.3.1 Thermocouple Measurements

Measurements with thermocouples were carried out to obtain the surface temperature distribution of the three blocks in the laboratory model, the airflow temperature in their vicinity and the air temperature stratification at the inlet and outlet apertures of the compartment.

A data-handling program was written within Matlab™ [Mathworks 1999] to facilitate quantitative comparisons with CFD simulation results. The program interpolated between measured data points and produced 2-D contour maps, as further described in Chapter 4.

Table 2.2 lists the set-up and objectives sought for each set of measurements. Investigations denoted as *Test A* and *Test B* were aimed in characterising the surface temperature of the blocks. As shown in Appendix D (Figures D1, D2 and D3), the thermocouples were located at regular spacing (distributed on all block surfaces in *Test A* and located so as to obtain a higher resolution in the proximity of the interfaces between the blocks in *Test B*). The co-ordinate position of the temperature sensors was recorded and inputted into the Matlab™ data files for post-processing the corresponding contour plots. During *Test C* (Figure D4), 38 thermocouples were spread within the compartment volume in order to measure the overall thermal state of the solid surfaces and the air planes. The sensor used in *Tests D* and *E* mapped the thermal state around the blocks and at the compartment openings.

A number of thermocouples were kept fixed to the surfaces of the blocks throughout the recordings to ensure that the heating conditions were consistent among the various tests. Moreover, the measurements in tests *A* and *C* were repeated to verify, and thereafter guarantee, instrumentation repeatability and preservation of the sensors' accuracy.

Table 2.2 – Test plan for the temperature measurements.

TEST NAME	DESCRIPTION	NUMBER OF THERMOCOUPLES	TEST OBJECTIVES	HEATER OPERATION
THERMAL - TEST A1	*Blocks* - Overall Thermal State (Steady)	7 K-type on turbocharger, 28 T-type on engine and gearbox, 2 T-type for ambient air	Record the overall steady-state surface temperature distribution for comparison with CFD data	Heaters ON and controlled to fixed temperature (steady-state)
THERMAL - TEST A2	*Blocks* - Overall Thermal State (Transient)	As Test A1	Overall transient (during cooling) surface temperature distribution for comparison with CFD data	Heaters OFF. Blocks cooling down
THERMAL - TEST B1	*Blocks* - Thermal State Engine-Turbo (Steady + Transient)	7 K-type on turbocharger, 30 T-type on engine upper surfaces (7 of which fixed as Test A), 2 T-type for ambient air	Localised temperature distribution on upper surfaces for comparison with transient CFD data	Heater ON to fixed temperature and then OFF for cooling down the blocks
THERMAL - TEST B2	*Blocks* - Thermal State Engine-Gearbox (Steady + Transient)	7 K-type on turbocharger, 30 T-type on engine lower surfaces and gearbox (7 of which fixed as Test A), 2 T-type for ambient	Localised temperature distribution on bottom surfaces for comparison with transient CFD data	Heater ON to fixed temperature and then OFF for cooling down the blocks
THERMAL - TEST C1	*Airflow* - Overall Thermal State (Steady)	7 K-type on turbo, 7 T-type on eng/gbx (fixed as Test A), 6 T-type on glass, 17 T-type on rods (air temp), 1 T-type for ambient	Overall air temperature stratification within compartment for comparison with steady CFD	Heaters ON and controlled to fixed temperature (steady-state)
THERMAL - TEST C2	*Airflow* - Overall Thermal State (Transient)	As Test C1	Air temperature stratification within compartment during cooling for comparison with transient CFD	Heaters OFF. Blocks cooling down
THERMAL - TEST D1	*Airflow* - Inlet/Outlet Thermal State (Steady)	7 K-type on turbocharger, 7 T-type on eng/gbx blocks (as Test A), 23 T-type at inlet/outlet slots, 2 T-type for ambient air	Air temperature stratification at inlet/outlet openings for comparison with steady CFD	Heaters ON and controlled to fixed temperature (steady-state)
THERMAL - TEST D2	*Airflow* - Inlet/Outlet Thermal State (Transient)	As Test D1	Air temperature stratification at inlet/outlet during cooling for comparison with transient CFD	Heaters OFF. Blocks cooling down
THERMAL - TEST E1	*Airflow* - Temperature Stratification (Steady)	7 K-type on turbo, 7 T-type on eng/gbx blocks (as Test A), 23 T-type on rods around blocks (air temp), 2 T-type for ambient	Air temperature distribution next to the block surfaces for comparison with steady CFD data	Heaters ON and controlled to fixed temperature (steady-state)
THERMAL - TEST E2	*Airflow* - Temperature Stratification (Transient)	As Test E1	Air temperature distribution next to the block surfaces during cooling for comparison with transient CFD	Heaters OFF. Blocks cooling down

Figure 2.24 depicts a sample of the processed experimental results at selected locations within the underhood during transient cooling. As shown, the natural cooling of the blocks was recorded from steady conditions. The observed cooling rates are similar to the ones depicted in the highlighted area of Figure 2.25, which represents the in-territory (field) test results of a typical full-scale engine-bay under heat soak condition, followed by a hot start to idle. The thermal data of Figure 2.25 is to a certain extent complicated by the operation of the cooling fan, the speed of which was controlled by the Electronic Control Unit (ECU) depending on the engine coolant temperature[8]. As a consequence, the data plotted in the figures cannot strictly be compared in quantitative terms, even if only the portion of the field measurements with fan off is considered. Moreover, the laboratory underhood geometry was simplified and various typical engine-bay elements, e.g. the heat exchangers in front of the vehicle, were not modelled in the analysis presented in this thesis. Nevertheless, the temperature trends shown are indicative of the thermal similarity that was realised.

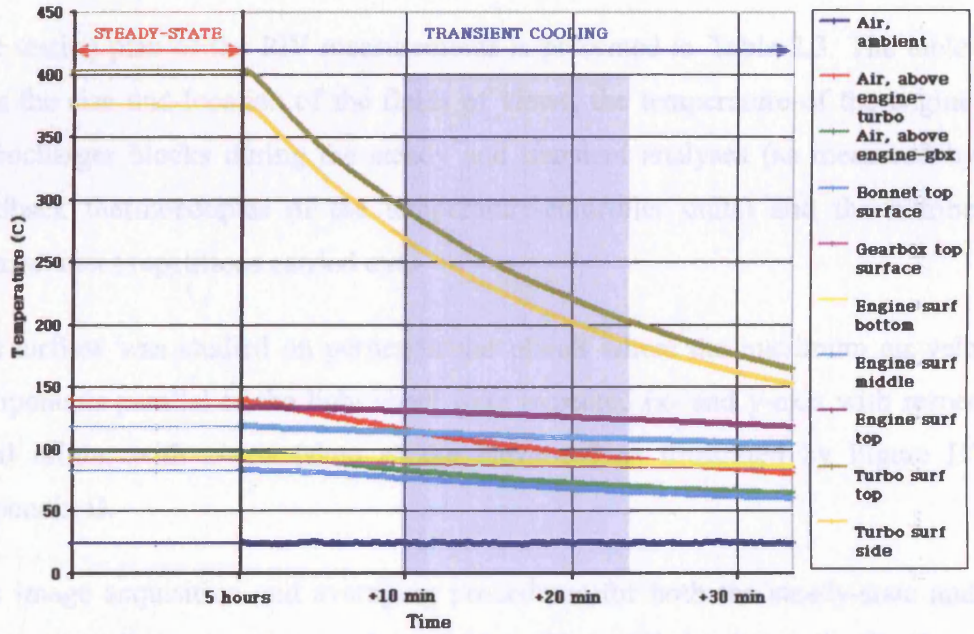

Figure 2.24 – Selection of laboratory underhood thermal data at steady-state condition followed by transient cooling.

[8] During key-off soak, the cooling fans come on generally at half speed if the temperature of the engine coolant rises above a pre-set value and run until the ECU "live time" expires, which is a function of the battery energy consumption.

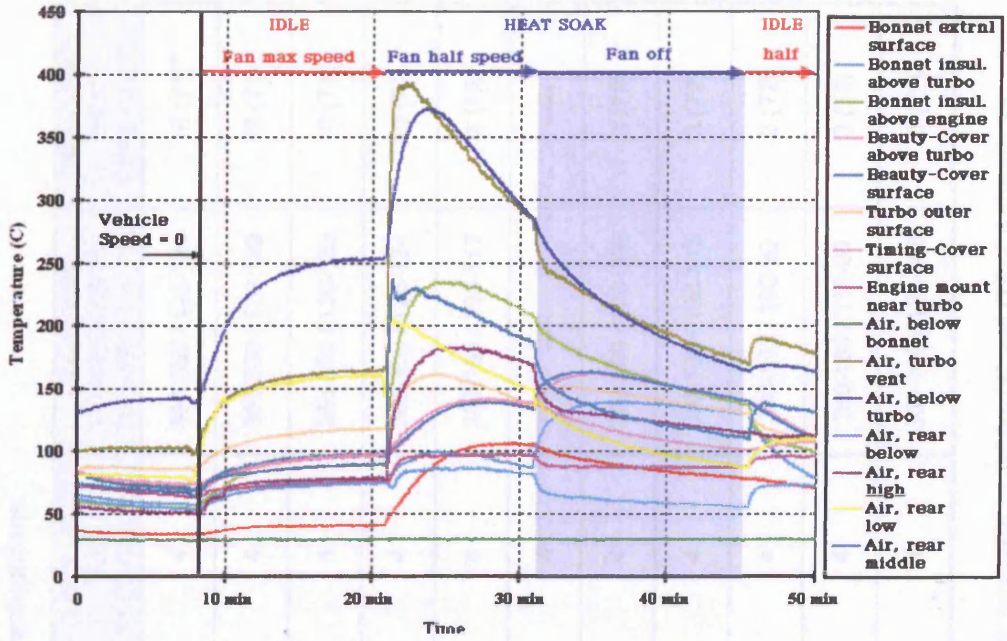

Figure 2.25 – Full-scale underhood in-territory thermal data. The operation of the cooling fan is indicated (courtesy of Ricardo UK Ltd).

Particle Image Velocimetry Measurements

The testing plan of the PIV measurements is presented in Table 2.3. The table also lists the size and location of the fields of views, the temperature of the engine and turbocharger blocks during the steady and transient analyses (as measured by the feedback thermocouples of the temperature-controller units) and the number of measurement repetitions carried out.

The airflow was studied on perpendicular planes where the maximum air velocity components parallel to the light sheet were expected (x- and y-axis with respect to local origin, with z-axis taken as the elevation) as illustrated by Figure D7 in Appendix D.

The image acquisition and averaging procedures for both the steady-state and the transient analyses are presented in Tables G1 to G3 in Appendix G. For each investigated plane, 60 images were taken at a rate of one image per second (1Hz) in steady conditions; the measurements were repeated at four different times. The final processed steady-state vector plots represented therefore the average of the 240 images recorded per plane.

Table 2.3 – Test plan for flow velocimetry investigations.

TEST NAME	PLANE	LOCATION	AREA (mm^2)	STEADY-STATE TEMPERATURES Turbo/Engine (°C)	STEADY -STATE TEST REPETITIONS	TRANSIENT TEMPERATURES Turbo/Engine (°C)	TRANSIENT TEST REPETITIONS
PIV – TEST 1X	X – Z	Above Engine, edge	29.97 × 22.60	365 / 123	4	365-350 / 125-124	10 (*T1*)[#]
PIV – TEST 2Y	Y – Z	Above Engine, centre	38.87 × 30.13	365 / 135	4	365-350 / 130-129	10 (*T1*)
PIV – TEST 3X	X – Z	Above Turbo, edge	37.20 × 27.40	365 / 130	4	365-350 / 130-129	10 (*T1*)
PIV – TEST 4Y	Y – Z	Above Turbo, centre	38.87 × 30.13	365 / 123	4	365-350 / 125-124	10 (*T1*)
PIV – TEST 5X	X – Z	Top of Rig, above turbo	35.75 × 27.00	360 / 125	4	360-165 / 125-117	3 (*T2*)[#]
PIV – TEST 6X	X – Z	Below Turbo, edge (3 areas)	32.72 × 24.72	364 / 125	4	-----	-----
PIV – TEST 7X	X – Z	Above Gearbox	32.86 × 24.83	362 / 129	4	360-190 / 120-105	3 (*T2*)
PIV – TEST 8Y	Y – Z	Above Gearbox	41.80 × 31.58	360 / 125	4	360-160 / 130-115	3 (*T2*)
PIV – TEST 9X	X – Z	Outlet, centre	46.69 × 35.28	360 / 125	4	360-153 / 100-90	3 (*T2*)
PIV – TEST 10Y	Y – Z	Outlet, side	50.32 × 38.02	360 / 120	4	360-150 / 110-90	3 (*T2*)
PIV –TEST 11X	X – Z	Inlet	31.16 × 27.32	360 / 125	4	360-160 / 130-105	3 (*T2*)

[#] *T1* and *T2* refer to the measurement procedures followed during transient investigation. These are presented in Tables G2 and G3 of Appendix G.

For the transient analysis, two different data acquisition procedures were adopted. For the areas investigated with the *T1* method (Table G2), 12 images were taken at 5s intervals for a period of 1 minute and the measurements were repeated for a total of 10 times. The PIV results consisted therefore of 12 ensemble-averaged flow field vector plots obtained at regular intervals from steady condition for a total cooling time of 1 minute. On the other hand, the cooling of the underhood was studied for 30 minutes when the *T2* procedure was employed (Table G3): images were taken at every second within five 15s-windows at pre-set time intervals. The measurements were repeated 3 times (sets A, B and C in Table G3) and the results were then averaged.

2.4 Experimental Errors and Uncertainties

An important aspect of the experimental design was to recognise potential sources of measurement error in order to devise strategies that minimised their impact on the results. Table 2.4 summarises the sensitivity, resolution and the accuracy of the temperature and flow velocimetry instrumentation employed.

Table 2.4 – Accuracy of experimental instrumentation.

INSTRUMENTATION FOR THERMAL INVESTIGATIONS			
	Sensitivity	Resolution	Accuracy
K-type TC	41μV/°C	0.25 °C	±1.5°C or ±0.0065T
T-type TC	42μV/°C	0.10 °C	±0.5°C or ±0.0045T
Datalogger	0.625μV	16 bit - 0.02 °C	---
Temp Controller	0.625μV	0.02 °C	±0.02% rdg + 0.01%range
Power Meter	---	10W	±(2% + 5W)

INSTRUMENTATION FOR FLOW VELOCIMETRY INVESTIGATIONS			
	Sensitivity	Resolution	Accuracy
Image Scaling	---	0.5mm	±3.6% of mean velocity
PIV Processing (Appendix F)	---	---	±6.3% of mean velocity

On average, the temperature recordings were affected by an error of approximately ±5%, mainly due to the relatively poor accuracy of the thermocouples at high temperatures. The accuracy of the power controller, which indirectly regulated the steady temperature of the blocks, was not critical for the quality of the measurements. On the other hand, the relatively high uncertainty affecting the measurements with the power meter would have influenced the accuracy of the steady-state CFD predictions as the simulations were based on prescribed heat flux boundary conditions.

A relatively high measurement uncertainty also affected the PIV data. However, most of the potential sources of errors were difficult to quantify, being of systematic type and functions of both the experimental conditions and of the algorithms used for the particle-displacement detection. Indeed, many researchers (e.g. Huang *et al.* [1997] and Bolinder [1999]) have indicated that the determination of the measurement errors is one of the main challenges in the application of PIV. This is owed to the generally complex instrumentation and to the large effort that is required for a "piece by piece" validation of the flow field results.

The sources of error potentially affecting the PIV data recorded in this study were:

- Random errors due to noise in the recorded images
- Bias errors arising from the process of computing the signal peak location to sub-pixel accuracy
- Gradient error resulting from rotation and deformation of the flow within an interrogation spot leading to loss of correlation
- Tracking error resulting from the inability of few particles atomised in larger diameters to follow the flow without slip
- Human errors in the calibration of the scaling of the images

Some of the errors were minimised by careful selection of experimental conditions. For example, consideration was devoted in the setting of the parameters reducing the correlated signal to noise ratio, e.g. lens choice, camera set-up, image intensity

distribution variation and surface reflections. Other sources were inherent to the nature of the correlation in PIV and could not be eliminated. For example, although the flow field was homogenously seeded, the location of the correlation peak could be influenced by random correlations between tracer droplets not belonging to the same pair of frames. In addition, bias errors could have resulted from a phenomenon called "peak locking" [Prasad 2001]. Peak locking occurs when the size of the tracer is too small (<1.5 pixels) and a sub-pixel curve fitting is employed to determine the location of the correlation peak in sub-sample areas (interrogation windows). Such curve fit causes a bias of the signal peak location towards discrete values of displacement (i.e. the magnitudes of the evaluated particle image displacement translate to integer values) [Chen and Katz 2005, Gui and Wereley 2003].

The field of views were scaled manually using a ruler bar focused in the plane of the light sheet. The potential systematic error affecting the calculated flow vector magnitudes due to wrong calibration of the flow images was quantified by carrying out a sensitivity analysis. It emerged that a ±1 mm deviation in the size of the field of views translated in a ±3.65% error for the mean air velocity calculated in the region.

Although the overall uncertainty actually affecting the PIV measurements could not be exactly quantified, a better confidence was established on the accuracy of the data by statistical sampling and averaging. This procedure, further discussed in Chapter 4, permitted the reduction of the random errors associated with the measurements.

2.5 CLOSURE

The features of the experimental investigation carried out on a simplified half-scale laboratory underhood model have been presented in this chapter. The investigations aimed to characterise the natural convective airflow pattern and the temperature field in order to:

- Gain a better understanding of the thermal processes during thermal soak
- Provide data for comparison with CFD simulation results

The experimental model constructed has been described together with the instrumentation employed for the investigations. Thermocouples were used for measuring the temperature of block surfaces and air planes. The data was recorded using a bespoke logging unit and was processed using a specific program written in Matlab™. A power meter was also employed to determine the power exerted in the blocks by the cartridge heaters in order to provide realistic boundary conditions to the computational model. Particle image velocimetry enabled to obtain spatial information about the velocity components of the buoyant flow. From a combination of different measured regions, qualitative information on the three-dimensional structure of the flow in the compartment could be obtained. The sources of errors potentially affecting the measurements have been discussed.

Chapter 3

COMPUTATIONAL FLUID DYNAMIC ANALYSIS

3.1 PRELIMINARY REMARKS

In order to realise a numerical simulation for fluid flow and heat transfer in a compartment, such as the underhood of a vehicle, three aspects must generally be accounted for. These include a mathematically well-posed numerical method, a suitable turbulence model and physically well-defined and consistent boundary conditions. The basic physical governing laws of convective fluids can be described by a set of non-linear partial differential equations, expressing conservation of mass, momentum and energy. These are not amenable to solution by analytical approaches and thus require the adoption of a numerical method in order to obtain a discrete representation of the continuous solution in space and time.

The simulations presented in this study were carried out with the CFD software VECTIS using a Conjugate Heat Transfer (CHT) calculation procedure. The thermal state of the heated elements and the characteristics of the airflow patterns inside the compartment were predicted by taking into account all three modes of heat transfer.

The present chapter describes VECTIS's numerical formulation and solution algorithm, the turbulence model employed, the characteristics of the computational underhood geometry and its associated mesh, and the boundary conditions that were specified for the analysis. The selected solver parameters for the steady-state and transient computations are also discussed. Finally, potential CFD numerical errors and uncertainties are addressed.

3.2 DESCRIPTION OF CFD SOFTWARE VECTIS

VECTIS is a computational fluid dynamic code developed by Ricardo Software Ltd. [2004a, 2004b]. The software calculates the velocity vectors of three-dimensional, time-dependent, compressible or incompressible flows by solving the governing transport equations via numerical differencing schemes. It also determines the thermal state of any solid components within the fluid domain by solving the energy balances. The structure of the software package, e.g. the links between the individual program modules that govern a simulation in VECTIS from domain discretisation to data post-processing, is described in Appendix A.

This section contains a mathematical description of the equations and numerical algorithms employed for the simulations of this study. The governing equations are given in a differential Cartesian tensor notation with covariant indices[9]. Any variable or mathematical sign that is not specifically clarified is defined in the nomenclature of the thesis. The formulation of the two turbulence models available in VECTIS is also presented in order to aid the discussion of the CFD results given in Chapter 4 (steady-state results) and Chapter 6 (transient results). Finally, the simulation procedure for a CHT-type computation is described.

3.2.1 Reynolds-Averaged Navier-Stokes (RANS) Equations

The unsteady RANS conservation equations, describing the flow transport phenomena and governing the heat transfer of the investigated CFD model, can be written in a generic conservation form [Ricardo Ltd 2004b]:

$$\underbrace{\frac{\partial \phi}{\partial t}}_{\text{Time Derivative}} + \underbrace{\frac{\partial}{\partial x_i}(U_i \phi)}_{\text{Advection}} = \underbrace{\frac{\partial}{\partial x_i}\left(\Gamma_\phi \frac{\partial \phi}{\partial x_i}\right)}_{\text{Diffusion}} + \underbrace{S_\phi}_{\text{Source Term}} \tag{3.1}$$

where ϕ is a generic variable representing a fluid quantity, the upper-case U_i is the local mean velocity vector that has components (U, V, W) in the Cartesian directions x_i (i=1,2,3), Γ_ϕ is the diffusion coefficient and S_ϕ is the source term affecting the

[9] An index (i or j) runs from 1 to 3, a single index implies a vector component (i.e. $U_i = U, V, W$), two equal indices implies summing over the indices (i.e. $\tau_{ii} = \tau_{11} + \tau_{22} + \tau_{33}$) and two different indices denotes a matrix (i.e. $a_{ij} = A$ in matrix notation).

fluid properties (e.g. an external force or internal heat generation). Equation (3.1) is based on the advection-diffusion balance with the terms representing, respectively, the transient, advection, diffusion and physical source transport phenomena.

Fluid properties, such as velocity and pressure, are conveniently time-averaged in the RANS formulation by Reynolds decomposition [Nieuwstadt 1993]. The mean component and the time-dependent fluctuations of the fluid quantities are separated; since the fluctuations (or perturbations) can generally be considered truly random (i.e. with their time-average equal to zero), they are neglected in the numerical formulation of the flow governing equations. Figure 3.1 shows the instantaneous turbulent airflow velocity, *u(t)*, separated in components by Reynolds decomposition.

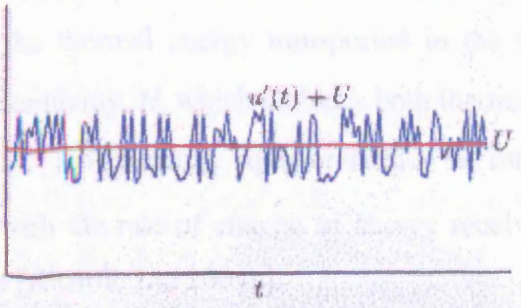

Figure 3.1 – Velocity in a point for a turbulent flow, *u(t)*; mean component, *U*, separated from fluctuating component, *u'(t)* [Hemph 2003].

Continuity Equation – In the total mass balance (continuity) equation, ϕ corresponds to the flow density, ρ, and both diffusion and source terms are equal to zero. The equality between the time rate of change of density in the modelled region and the net flow of mass into the region is written as [Ricardo Ltd 2004b]:

$$\frac{\partial \rho}{\partial t} + \frac{\partial}{\partial x_i}(\rho U_i) = 0 \qquad (3.2)$$

Momentum Equation – The momentum conservation equation equates the change of momentum of a particle to the sum of forces acting on it. In the RANS formulation, ϕ represents the three components of U_i, and Equation (3.1) becomes [Segal *et al.* 1996]:

$$\frac{\partial}{\partial t}(\rho U_j)+\frac{\partial}{\partial x_i}(\rho U_i U_j)=\frac{\partial}{\partial x_i}(\tau_{ij}-\rho\overline{u_i u_j})-\frac{\partial(p+\rho k)}{\partial x_i}+S_{B,i} \qquad (3.3)$$

where p is the mean pressure, k is the turbulent kinetic energy, the buoyancy force is added as a source term (i.e. $S_{B,i}=-\rho\beta\cdot\Delta T\cdot g_i$, from Boussinesq's approximation), and the diffusion term is characterised by the Reynolds stress (for turbulent flows), $\rho\overline{u_i u_j}$, and the stress tensor τ_{ij}, which is calculated from

$$\tau_{ij}=\mu\left(\frac{\partial U_i}{\partial x_j}+\frac{\partial U_j}{\partial x_i}\right) \qquad (3.4)$$

Energy Equation – The temperature field in the modelled fluid domain can be described by solving the thermal energy transported in the flow. The variable ϕ equates to the absolute enthalpy, H, which includes both thermal enthalpy and kinetic energy ($H=c_pT+\frac{1}{2}U_iU_i$). The energy equation relates the rate of change of energy within a fluid region with the rate of change of energy received by heat and work transfer. It is written as [Ricardo Ltd 2004b]:

$$\frac{\partial}{\partial t}(\rho H)+\frac{\partial}{\partial x_i}(\rho U_i H)=\frac{\partial p}{\partial t}+\frac{\partial}{\partial x_i}\left(\Gamma_H\frac{\partial H}{\partial x_i}-\rho\overline{u_i' H}\right)+q_W+q_{rad} \qquad (3.5)$$

where Γ_H is the turbulent diffusivity, q_W and q_{rad} are, respectively, the heat flux through the wall and the energy contribution from radiation, and $-\rho\overline{u_i' H}$ is the turbulent scalar flux for the enthalpy, which is a diffusion term that results from the time-averaging process.

Equation of State – In total, six dependent variables (U, V, W, ρ, p and T) are contained, before averaging, in the above five transport equations. The equation of state for an incompressible fluid is added to close the set. Assuming perfect gas behaviour, this is written as:

$$p=\rho RT \qquad (3.6)$$

Turbulent scalar fluxes, such as the Reynolds heat-flux vector, are solved by the eddy-viscosity models with the gradient-diffusion hypothesis of Daly and Harlow [1970]. These are formulated as:

$$-\rho\overline{u_i'H} = \Gamma_t \frac{\partial T}{\partial x_j} \tag{3.8}$$

where Γ_t is the turbulent scalar diffusivity (also expressed as μ_t / σ_t, where σ_t is the turbulent Prandtl number).

The unknown quantity in Equations (3.7) and (3.8) is the turbulent viscosity, μ_t. This can be described, from dimensional arguments, by the characteristic velocity scale, V_t, and the characteristic length scale, L_t, of the turbulent fluctuations of the modelled flow [Peng 1998]:

$$\mu_t = c_\mu V_t L_t \tag{3.9}$$

where c_μ is the coefficient of dissipation.

Different turbulence models provide different formulae to define the two scales of fluctuation. The two-equation models available in VECTIS define them by the turbulent kinetic energy, k, and its dissipation rate, ε:

$$L_t = \frac{k^{3/2}}{\varepsilon} \text{ and } V_t = k^{1/2}, \text{ where } \varepsilon = \nu \frac{\partial u_i}{\partial x_j} \frac{\partial u_j}{\partial x_i}$$

The turbulent viscosity is thus taken as an isotropic property of the flow that changes with time and position and it is calculated from:

$$\mu_t = c_\mu \rho \frac{k^2}{\varepsilon} \tag{3.10}$$

with c_μ = 0.09 [Launder and Spalding 1974].

The computation of the turbulent viscosity requires two additional equations in the RANS formulation to express the transport of both k and ε (e.g. as given by

Launder and Sandham [2002]). The turbulence energy and dissipation transport equations comprise several empirically-determined coefficients which take different values in the standard and in the *RNG* formulations of the $k-\varepsilon$ model. The coefficients physically regulate the responsiveness of the model to the effects of flow strain, streamline curvature, flow separation, re-attachment and re-circulation [Ricardo Ltd 2004b]. The *RNG* version further differentiates from the traditional $k-\varepsilon$ model for a non-linear source term contained in the transport equations that has been shown to improve the prediction of turbulence kinetic energy in regions characterised by large strain rates [Zhou *et al.* 1997].

Wall Functions – Eddy-viscosity models are effective in calculating the turbulent transport of a free stream flow, in which the inertia forces are much greater than the viscous forces (high Reynolds number). However, at wall boundaries, where velocities approach zero, the viscous forces will be equal in order of magnitude to the inertia forces, or even larger. Therefore, the near-wall effects (wall shear stress, convective heat transfer coefficient, turbulence energy, etc.) must be modelled separately. VECTIS adopts the wall function method, also known as the logarithmic *Law of the Wall* [Tennekes and Lumley 1972].

Experimental and mathematical 2-D analyses have shown that the near wall region can be sub-divided into three layers [Gunnar and Hellstrom 2005]. The innermost layer, the so-called *viscous* sub-layer, where the flow is almost laminar and where the (molecular) viscosity plays a dominant role in momentum and heat transfer. The *logarithmic* or *outer* layer, further away from the wall, where inertia forces are dominant and the turbulent flow is considered being fully developed. Finally, there exists a region between the viscous sub-layer and the logarithmic layer, known as the *buffer* or *transition* region, where both viscous and inertia forces are effective and of equal importance.

The Law of the Wall uses empirical formulae to efficiently bridge the gap between the viscous and the fully-developed layers of the boundary layer (the latter is modelled by the $k-\varepsilon$ transport equations). Its formulation is based on the dimensionless fluid velocity at the first grid node next the boundary, i.e. $u^+ = u/u_\tau$,

where u is the tangential fluid velocity, $u_\tau = \sqrt{\tau_w / \rho}$ is the friction velocity and τ_w is the wall shear stress. The value of u^+ is assumed to be purely a function of the dimensionless wall distance y^+, which is defined by:

$$y^+ = \rho u_\tau y / \mu \tag{3.11}$$

where y is the distance of the first grid node from the wall and is equal to half the size of the corresponding mesh cell (since all flow variables are assumed to be located at the cell centre).

The value of the y^+ practically informs the CFD software what equations to use to resolve the flow velocity and heat transfer at the surfaces of the model. The velocity profile in near-wall cells is in fact expressed by [Tennekes and Lumley 1972]:

$$u^+ = y^+; \qquad y^+ \le y_V^+ \tag{3.12}$$

$$u^+ = \frac{1}{\kappa}\ln(Ey^+); \qquad y^+ > y_V^+ \tag{3.13}$$

where κ is the von Karman's constant (= 0.419), E is an empirical constant expressing the wall roughness (= 9.79, in VECTIS, for smooth walls) and y_V^+ represents the edge of the viscous sub-layer (= 11.6 in VECTIS). Accordingly, if the y^+ values are lower than 11.6, the velocity profile is determined from the laminar stress-strain relationship of Equation (3.12), otherwise the flow is assumed to be in the transition sub-region and the velocity calculated with the logarithmic function of Equation (3.13).

Given the Reynolds's analogy between momentum and energy transfer, as found in the Stanton number ($St = Nu / RePr$), the temperature profile at the wall is calculated in VECTIS with an analogous formulation [Ricardo Ltd 2004b]:

$$T^+ = \sigma_t(u^+ + P) \tag{3.14}$$

where $T^+ = c_p \rho (T - T_w) u_\tau / q$, σ_t is the turbulent Prandtl number and P is the "sub-layer resistance factor", which is a function of both the laminar and turbulent Prandtl numbers of the flow (defined in the nomenclature).

In local equilibrium, where $k = u_\tau^2 / \sqrt{c_\mu}$, the wall shear stress is expressed by

$$\tau_w = \frac{\rho k_p^{1/2} c_\mu^{1/4} \kappa u}{\ln(E y^+)} \tag{3.15}$$

and is added as a source term in the momentum equations for near-wall cells. The heat flux for near-wall cells is entered as the source term in the energy equation and is calculated from (for $y^+ > y_V^+$):

$$q = \frac{\mu c_p y^+ (T - T_w)}{\sigma_t \left(\frac{1}{\kappa} \ln(E y^+) + P \right) y} \tag{3.16}$$

The local heat transfer coefficient at a wall is then computed from $h = q / (T - T_w)$.

The use of the wall functions removes the need of employing a fine mesh to explicitly resolve the flow profile in the boundary layer and it is therefore computationally efficient. However, the formulation is based on a set of implicit assumptions about the flow and the accuracy of the solution depends on how well these are met in any particular application. The assumptions are [Ricardo Ltd 2004b]:

- The flow is essentially one-dimensional, such that gradients of velocity and scalar quantities are normal to the wall.
- Shear stress in the boundary layer is uniform and equal to the value at the wall; the effects of pressure gradients are therefore small.
- Turbulence is in local equilibrium (the production of turbulence balances its dissipation).
- The turbulent length scale varies linearly with the distance from the wall.

Furthermore, a great care is required from the user when allocating the mesh nodes next to the walls of the computational model. The size of the near-wall grid cells is indeed the main factor affecting the value of the y^+ and thus the accuracy of the numerical solution of the boundary layer effects. The cells should not be too large (e.g. $y^+ > 60$) or the software will be including viscous effects in the flow regions outside the transition boundary layer; on the other hand, they should not be too small (e.g. $y^+ < 5$) to avoid modelling the transient sub-layer with the $k-\varepsilon$ formulation, i.e. as being fully turbulent. The acceptable size of the near-wall cells is not fixed as it also depends on the Reynolds number of the flow: the minimum allowable y^+ value decreases as the friction velocity decreases. A sensitivity analysis was carried out in this study to investigate the effects that different wall mesh refinements had on the flow and thermal underhood predictions. The results of the analysis are presented and discussed in Section 3.4.1.

3.2.3 Radiation Model

Simulations in VECTIS can include the effects on temperature distributions due to not only convection and conduction, but also radiation. Thermal radiation between different surfaces in a flow domain is calculated in VECTIS via a separate program module, which is based on the diffuse radiation theory formulation [Mahan 2002]. The distribution of the radiated heat to surrounding surfaces is derived from the value of view factors, which are calculated on selected "patches" discretising the surfaces of the modelled solid elements. Only wall-to-wall radiation is calculated in VECTIS, with the air between the surfaces assumed to have no interaction. The mathematical formulation of the radiation module and the coupling of its calculation procedure with the CFD solver are described in Appendix A.

3.2.4 Numerical Scheme and Solution Algorithms

The fundamental equations governing the conservation of mass, momentum and energy are firstly discretised by VECTIS on a structured Cartesian mesh defined by the user and then solved fully-implicitly, with the coupling between variables and non-linear effects incorporated using iterative or predictor-corrector algorithms. The calculations are iterated at each timestep until a specific convergence tolerance is met

by the transient solver or iterated towards a steady state from the input conditions for steady computations. This section summarises VECTIS's numerical scheme and the specific solver algorithms implemented for the simulations carried out in this study.

Discretisation – The Finite Volume method [Chung 2002] is used in VECTIS to obtain a discrete representation of the continuous solution in space, and, for transient computations, in time, from the set of differential equations governing flow motion and heat transfer.

Fluid and solid domains are divided into a contiguous set of non-overlapping control volumes (cells) with the influence of external factors specified at the boundaries. The grid is of non-body-fitted structured Cartesian type, which greatly simplifies the grid generation and reduces computing stored memory in comparison to the body-fitted alternatives of either structured hexahedral or unstructured tetrahedral grids [Ye *et al.* 1999]. All the variables are stored at the geometric centre of each cell (*collocated* variable distribution rather than *staggered*) and any transport variable is integrated over the neighbouring cell centres. The Gauss Divergence Theorem [Kreyszig 1999] is used to express the convection and diffusion terms as a balance of the net in-flux through the cell surfaces [Ricardo Ltd 2004b].

Differencing Scheme – A bounded high-order scheme is used to determine cell face values from the properties at neighbouring cell centres. The scheme operates by blending a first-order *hybrid* scheme [Spalding 1972] and a second-order *oscillation-free* scheme [Watkins 1989], which guarantees higher approximation accuracy [Ricardo Ltd 2004b]. In order to avoid locally non-limited[10] solutions, typically of oscillatory character, the hybrid scheme, in turn, is set to switch between a *central* differencing scheme with a second-order accuracy if the Peclet number ($=Re \cdot Pr$) of the flow is less than 2 and an *Upwind* differencing scheme with a first-order accuracy for an higher Peclet number.

Solver Algorithms – For time marching calculations, all the discretised equations are solved at each time step to a pre-set convergence margin. All the mesh values are

[10] The solution is said to be non-limited when the solution value in a computational point is non-bounded by the solution values in the surrounding points, which influence the point. A central difference discretisation may, for cell Reynolds numbers or cell Peclet numbers exceeding 2, lead to solutions increasingly non-physical and/or diverging [Michelsen 1995].

solved simultaneously, for each equation, in an implicit solution fashion, such that the timestep size is determined by the coupling between the variables and non-linearities rather than by a Courant type limit on the solution propagation speed through the mesh, as with an explicit scheme [Anderson 1995]. The calculation of steady-state solutions follows the same procedure, although the variables are under-relaxed between iterations to control stability and convergence.

An iterative approach, from an initial guessed flow field, is necessary to determine the separated but coupled flow field variables from the governing equations. The numerical solution is in fact complicated by the pressure source term in the momentum equation since the pressure field cannot be determined from a separate equation. A pressure-velocity algorithm, which couples the solutions of the momentum and continuity equations, is implemented in VECTIS. The momentum equation is solved with the existing pressure field to yield a predicted velocity field that, in general, does not satisfy the continuity. The predicted velocity field is then used to determine the mass flow imbalance in each cell, which in turn is used to solve either a pressure or a pressure-correction equation. The velocity field is finally updated explicitly via the momentum equation for a combined pressure-velocity solution that represents an improved solution to the coupled continuity-momentum system.

Two different algorithms were selected in this study among those available in VECTIS for coupling momentum and continuity equations. The SIMPLE (Semi-Implicit Method for Pressure Linked Equations) scheme [Patankar 1980] was chosen for the steady computations. The algorithm iterated the transport equations until convergence was reached and it was supplemented with a relaxation technique to stabilise the solution (user-controlled parameters). For time-marching calculations, all equations were iterated at each timestep using the PISO (Pressure Implicit with Splitting of Operators) algorithm [Issa 1986]. The scheme was based on an additional pressure and velocity correction equation, which was computed before updating the momentum predictor. A more consistent approximation to the final solution before the successive iteration, was thus obtained during the transient simulations.

Convergence – The stability of the numerical solution was monitored during the computations through several criteria: the mass and heat conservation had to be balanced, the residuals of the discretised conservation equations (difference between the left- and right-hand sides of the equations after substitution of the approximate solution from the iterative coupling) had to steadily decrease and the change in field values between iterations had to be very small. The procedure allowed the identification, early during the analysis, of any incorrect solver parameters or boundary conditions.

3.2.5 Conjugate Heat Transfer Computations

A coupled fluid-solid heat transfer simulation performed with a single CFD software is today the requisite for accurate flow and thermal simulations. In VECTIS, this type of simulation is possible by implementing the Conjugate-Heat-Transfer (CHT) calculation procedure. The basic mode of operation is as follows:

1. Separate computations, or *processes*, are set up for each modelled CHT domain (solid or fluid). Each domain is set up with an individual mesh structure within a global co-ordinate system that is common between all the CHT processes.
2. A hierarchy of processes is established whereby one CHT model starts up other models participating to the CHT computation, and each can in turn start up other processes (a parent-child relationship).
3. The wall boundaries of each model participating to the CHT computation are identified in their respective input file as "external" boundaries; these exchange temperature and heat transfer coefficient values with the boundaries of the conjugated models.
4. The CFD computations are started and each process exports its boundary information to an external global file that establishes all the CHT thermal links. Thereafter, the solution of the temperature fields proceeds at a time-step level (or per iteration number with the steady solver), with the conjugated models exchanging the thermal boundary data through geometrically-linked surface patches until a solution convergence is reached.

3.3 CONSTRUCTION OF CFD SIMULATION

3.3.1 Computational Model and Mesh

The geometry and dimensions of the underhood laboratory rig were exactly reproduced using the CAD software I-DEAS™ [Electronic Data Systems 2003]. The holes in the blocks housing the cartridge heaters were also precisely replicated in their location and dimension, as shown on the right hand side of Figure 3.2.

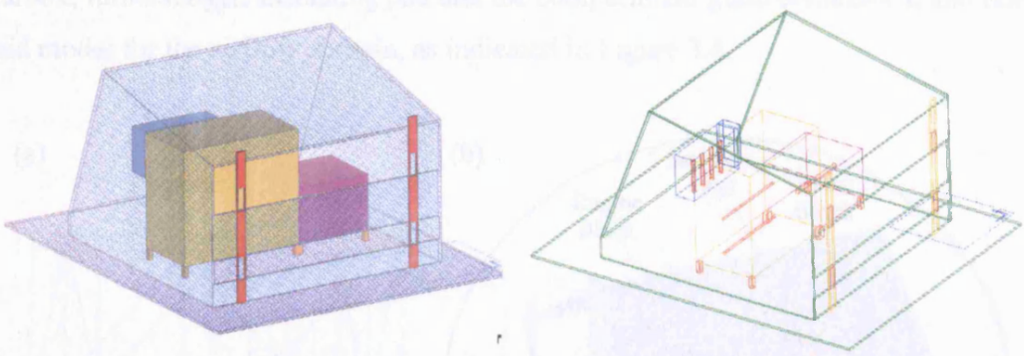

Figure 3.2 – Underhood CAD geometry.

The underhood compartment was modelled in a computational chamber (Figure 3.3) to obviate the need of applying specific boundary conditions in the regions of the openings to the ambient environment. The chamber had the same dimensions of the experimental room, thereby large enough to minimise possible temperature and pressure influences on the convective flow inside the engine bay.

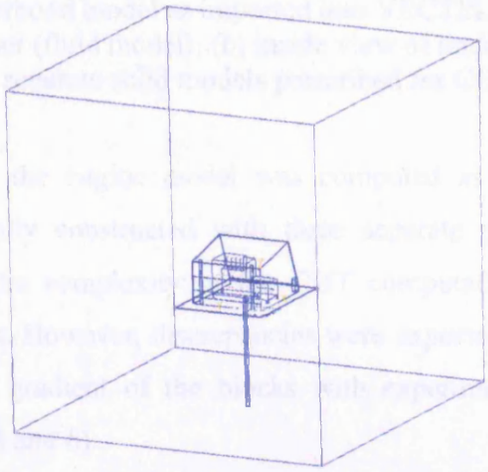

Figure 3.3 – Computational chamber prescribing the air domain of the investigated geometry.

The column shown in Figure 3.3 between the underhood model and the chamber bottom surface was added to the model as an expedient to avoid ambiguities during the mesh generation process. By joining the solid domains, the volumes of the solid underhood elements were prevented from being meshed in VECTIS as fluid by default.

The computational processes participating to the conjugate heat transfer simulation consisted of five separate solid models, representing respectively the engine, gearbox, turbocharger, insulating pad and the compartment glass boundaries, and one fluid model for the airflow domain, as indicated in Figure 3.4.

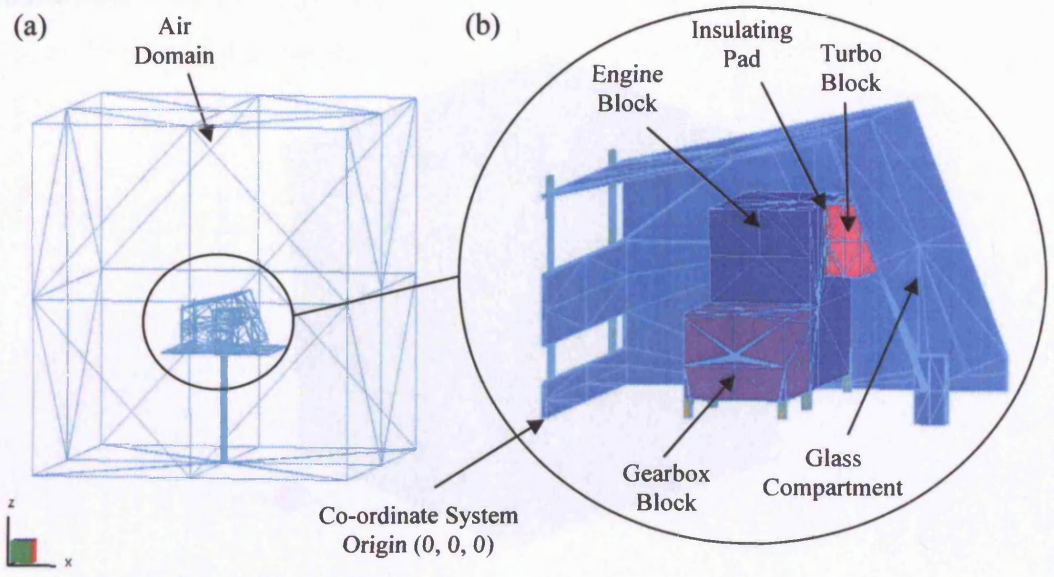

Figure 3.4 – Underhood model as imported into VECTIS: (a) global view of computational chamber (fluid model); (b) inside view of underhood geometry with indication of the separate solid models prescribed for CHT computations.

It is emphasised that the engine model was computed as a single solid block, although it was actually constructed with three separate metal parts. This was necessary to reduce the complexity of the CHT computations and, in turn, the processor requirements. However, discrepancies were expected when comparing the predicted temperature gradient of the blocks with experimental data (correlation presented in Chapters 4 and 6).

A structured Cartesian mesh was constructed for each CHT domain after the underhood CAD model was imported into VECTIS in a triangulated surface format (Figure 3.4). The mesh density was primarily controlled by defining the size of the "global mesh", which is shown in Figure 3.5. The spacing of the mesh lines in each of the three co-ordinate directions was defined to be non-uniform in order to concentrate more cells in the regions where higher flow and thermal gradients were expected. Consequently, the outer regions of the computational chamber were discretised with relatively larger cells. The same global mesh that was defined for the air domain was employed for discretising the solid domains, in order to enhance the CHT mapping (i.e. the grid cells coupling of the different CHT domains at the boundaries).

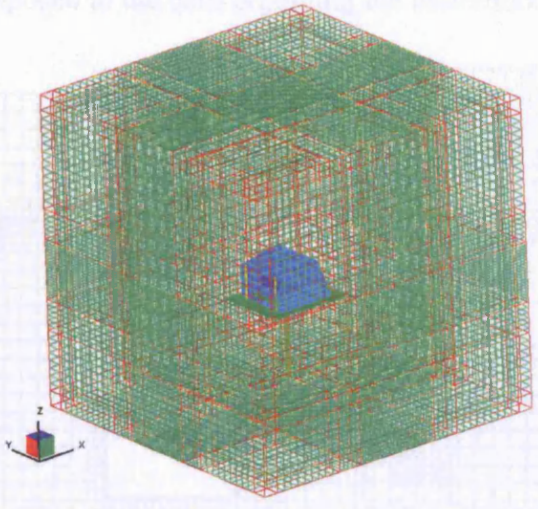

Figure 3.5 – Structured global mesh of underhood model defined for generation of Cartesian grid.

The mesh cells are generated in three stages by VECTIS: firstly, all global hexahedral cells that lie entirely outside the CFD model are eliminated; then the remaining cells are sub-divided, or "refined", near the boundaries in order to approximate the shape of the modelled domain; finally, the refined cells are truncated to conform exactly to the original boundary. The amount of cell refinement near the boundaries is controlled by the "refinement depth" parameter, which dictates how many times a global cell is cut into 2 during the mesh generation.

The level of cell refinement defined for the boundaries of the underhood model varied according to the specific CHT domain being discretised and the thermal

gradient expected on each surface. Overall, the amount of refinement that was prescribed ranged from a value of 1 to 3, where depth 1 sub-divided the global cells into 2×2×2 refined cells, depth 2 into 4×4×4 cells and depth 3 into 8×8×8 cells. The refinement algorithm also enabled the control of the cell size gradation towards the boundaries through the "blending distance" parameter. In this study, the parameter was either set equal to 0 at the surfaces of the solid CHT domains (no cell refinement propagation from the boundary to the surrounding cell layers), or -1 at the surfaces of the fluid domain (refinement depth of surrounding cells taken by VECTIS to be 1 unit lower than that specified for near-wall cells), where higher definition was required to calculated the wall heat transfer and to resolve the boundary layer turbulence. Figure 3.6 presents a slice view of the air domain mesh that evidences the level of refinement imposed to the cells adjoining the underhood boundaries.

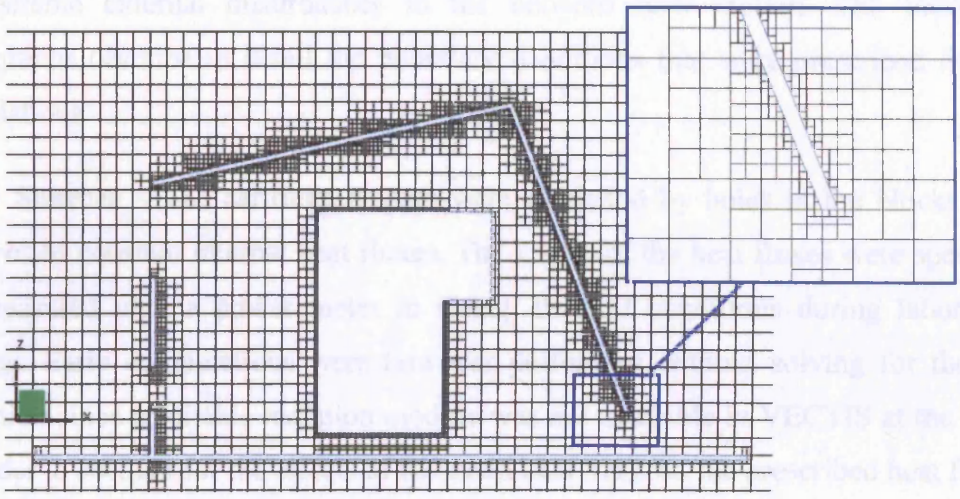

Figure 3.6 – 2-D view of mesh for air domain as generated by VECTIS. The cell refinement next to the glass boundaries is magnified (depth = 3, blending = -1).

After several attempts with different mesh densities (determined from the combination of global mesh sizes and cell refinement depths), the simulations were based on approximately 740,000 cells for the air domain and a total of approximately 230,000 cells for the solid models (15,907 cells for the engine block, 5,542 cells for the gearbox, 5,852 cells for the insulating pad, 7,152 cells for the turbocharger and 191,560 cells for the compartment). The mesh density was investigated as presented in Section 3.4.1 and was regarded as the optimal compromise between a denser grid, associated with a longer CPU runtime, and a less dense grid, associated with a marked deterioration of flow and thermal predictions (and also of graphical

resolution, which would hinder the data correlation with PIV measurements). The final size of the cells (side length) ranged from a minimum of 2.5 mm, for the refined cells at the walls, to 20 mm, for the cells discretising the air domain outside the underhood compartment.

3.3.2 Boundary Conditions

The thermal natural ventilation under the hood depends on the spatial distribution of the sensible heat sources and on their intensity. The accurate modelling of the thermal convective process required that the characteristics of the heat sources as well as the properties of the materials in which heat propagates were precisely defined. Moreover, appropriate inlet and outlet flow conditions had to be specified to correctly model the actual condition of the investigated flow field and to avoid undesirable external disturbances to the buoyant flow motion. The following paragraphs describe in detail the boundary conditions that were prescribed for the simulations.

Heat Sources – The cartridge heaters were modelled by holes in the blocks with prescribed constant internal heat fluxes. The values of the heat fluxes were specified as measured with a power meter in steady thermal conditions during laboratory testing. Early computations were however performed without solving for thermal radiation since a suitable radiation module was not available in VECTIS at the time. In order to account for the effects of radiation heat transfer, the prescribed heat fluxes were initially reduced based on the estimated radiation heat losses from the blocks, which were determined with the software RadTherm™ [ThermoAnalytics 2003b].

RadTherm™ is a thermal analysis program that allows multimode heat transfer and one-dimensional fluid flow simulations. In this study, a CAD surface description of the underhood was entered in the code with prescribed material and surface properties; these were assigned to various groups of surface elements and then combined into thermal nodes by the program. RadTherm™ computed the temperature of the model surfaces (Figure 3.7) with an implicit solution to the finite-difference equations derived from the thermal properties of each node and their radiation exchange. The calculations for radiation heat transfer were based on the area, emissivity, temperature and on the view factors of the surfaces, which were

assumed of diffuse-grey type. The view factors were calculated using a single-plane variant algorithm of the hemi-cube method [Cohen and Wallace 1993, Curran *et al.* 1995]. Heat transfer by conduction and convection were also predicted.

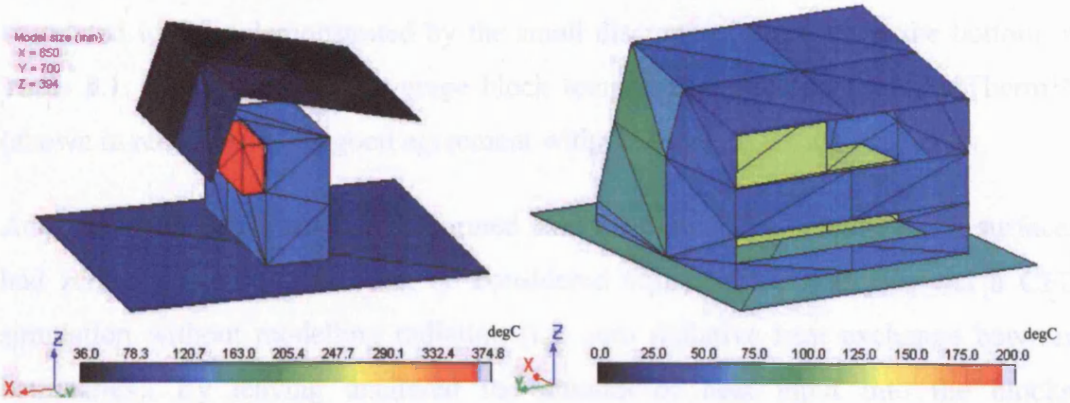

Figure 3.7 – Sample of steady-state thermal mapping for underhood model as simulated with RadTherm™ (part of the glass surfaces removed for clarity).

Preliminary calculations were performed to determine the net conduction, convection and radiation heat transfers of the underhood blocks and their resulting average temperature. The simulations were setup so as to replicate the experimental conditions: the heat load in the blocks was specified as measured in laboratory, the emissivity of the block surfaces was assumed equal to 0.9 (black painted surfaces) and the emissivity of the glass surfaces was set to 0.95. The results of the computations are presented in Table 3.1. The proportion of heat lost by each block due to radiation is tabulated as a percentage of the heat input.

Table 3.1 – Prediction of heat transfer and temperature of blocks based on heat input as measured by power meter.

	TURBO	ENGINE	GEARBOX
Heat Input into Blocks (W)	582.28	180.90	72.42
Predicted Net Conduction (W)	-89.53	26.25	44.06
Predicted Net Convection (W)	-125.39	-79.73	-49.91
Predicted Net Radiation (W)	-367.31	-127.40	-66.56
Percentage Radiation Loss from Blocks	**63%**	**70%**	**92%**
Predicted Average Block Temperature (°C)	372.67	129.43	125.87
Calculated Net Convection (W)	-127.87	-80.34	-45.91
Difference in Convection data	-1.98%	-0.76%	8.02%

In order to assess the validity of the numerical calculations, in general, and the accuracy of the underhood model as it was defined in RadTherm™, in particular, the convective heat loss from the model surfaces was also calculated analytically (see Appendix B) and compared to computational predictions. The two sets of data correlated well, as demonstrated by the small discrepancies shown at the bottom of Table 3.1. Furthermore, the average block temperatures predicted by RadTherm™ (shown in red) provided a good agreement with the laboratory measurements.

Additional computations were performed with the assumption that the block surfaces had zero emissivity, which can be considered equivalent of carrying out a CFD simulation without modelling radiation (i.e. zero radiative heat exchange between boundaries). By leaving unaltered the amount of heat input into the blocks, unrealistically high temperatures in the underhood enclosure were predicted. When the heat load in the blocks was reduced by the previously predicted amount of radiated heat ("percentage radiation loss" in Table 3.1), the blocks were instead predicted to remain approximately in the original temperature state.

The results of the simulation are presented in Table 3.2. As a consequence of setting the emissivity of the blocks to zero, the average temperatures of the underhood elements were calculated to closely correspond to the values given in Table 3.1. It was therefore inferred that the effects of radiation heat transfer could be satisfactorily approximated in the underhood model by reducing the heat input in the blocks. More generally, the heat load approximation could be implemented in any similar CFD analysis to reduce hardware demands by completely obviating the need of modelling radiation heat transfer.

Table 3.2 – Prediction of heat transfer and temperature of blocks based on reduced heat input and zero surface emissivity.

	TURBO	ENGINE	GEARBOX
Reduced Heat Input into Blocks (W)	203.80	54.27	7.24
Predicted Net Conduction (W)	-71.36	21.54	40.87
Predicted Net Convection (W)	-132.44	-75.86	-48.14
Predicted Net Radiation (W)	0.00	0.00	0.00
Predicted Average Block Temperature (°C)	382.48	126.55	123.18
Temperature Difference with Table 3.1	2.6%	-2.3%	-2.2%

The reduced values of the heat fluxes to be specified as boundary conditions in the underhood CFD model were calculated based on the surface area of the modelled heaters (Table 3.3). The heat fluxes for the engine block are shown in the table respectively for the top and the bottom heater embedded in its volume.

Table 3.3 – Calculated reduced heat flux of underhood heaters for boundary condition specification in CFD.

	TURBO	ENG TOP	ENG BOTTOM	GEARBOX
Heat Input into Blocks (W)	582.28	95.58	85.32	72.42
% Radiation Loss from Blocks	63	70	72	92
Reduced Heat Input (W)	215.44	26.76	23.89	5.79
Heater Surface (m^2)	0.00228	0.00253	0.00304	0.00380
Reduced Heat Flux (W/m^2)	23,575	11,160	8,300	1,540

Material Properties – The realistic simulation of conduction heat transfer was favoured by the possibility in VECTIS to directly specifying the material properties of the solid domains (i.e. density, specific heat and thermal conductivity). Specifically, the properties of *grey cast iron (grade 250)* were entered for the engine and the gearbox blocks, *6082-aluminium alloy* for the turbo block, *Robax® glass* for the compartment boundaries and *Duratec® plastic* for the insulating pad. However, the less-than-ideal contact between the blocks in the laboratory setup, despite the use of conductive paste to minimise the air gaps in the interfaces, could not be properly modelled. An excessively complicated computation with additional CHT solid elements would in fact be required to specifically model the thermal effects of the air-gap (further discussed in Chapter 4).

Inlet/Outlet Boundaries – The control volume of the computational chamber was limited by a total pressure-type boundary set in correspondence to the bottom surface and by a constant mass flow rate boundary at the upper surface. The pressure-type boundary was chosen to account for the changes in density of the fluid domain within the computational chamber. Since pressure-type boundaries are known to potentially lead to solution instability [Yang *et al.* 2003], being strongly dependent on the calculated flow condition, it was specifically set at the bottom of the chamber where no flow re-circulation was expected (contrary to the top surface which would be affected by the buoyant plume). It was coupled with a top boundary having a

constant mass flow rate with uniform profile of -0.001kg/s (outflow), thus low enough to practically prescribe still ambient condition in the chamber. The inlet/outlet air velocities were automatically computed by VECTIS to satisfy the continuity (mass conservation) equation.

Wall-Type Boundaries and Initial Conditions – Wall surfaces participating to the CHT computations were all identified as "external" boundaries. Model surfaces not exchanging thermal information, such as the base of the compartment (i.e. vehicle under-tray) and the laboratory rig mountings (i.e. steel strips holding firmly the laboratory compartment and exactly reproduced with CAD), were set as adiabatic walls. The reference air density was specified as 1.16 kg/m^3, and the initial air temperature and pressure conditions were set to 300 K and 1 bar, respectively.

3.4 SET-UP OF NUMERICAL SIMULATIONS

CFD users are required to anticipate the flow characteristics, select appropriate modelling techniques (e.g. turbulence model, boundary conditions, etc.), construct an appropriate mesh grid, choose the parameters controlling the execution of the CFD code, ensure that the solution is converged, assess the simulation data and diagnose any abnormal result. This procedure presents many opportunities for poor decisions that would inevitably introduce errors in the final numerical predictions.

In this study, the effects that solver parameters (i.e. under-relaxation and multigrid factors), grid density (i.e. number of cells, cell refinement, distance of near-wall grid points) and choice of turbulence model (i.e. $k-\varepsilon$, *RNG*-$k-\varepsilon$ or none) have on the CFD results were investigated with a parametric/sensitivity analysis. The results enabled the identifications of the optimal parameters and modelling technique for accurate steady and transient simulations of the underhood model.

3.4.1 Sensitivity Analysis

The sensitivity analysis was carried out on a small and geometrically simple test configuration and on the underhood model itself.

Analysis on Simple Test Case – The simple test model enabled an investigation into the effects of the "global" solution parameters (i.e. independent of the modelled geometry) to be completed in a relatively short timeframe. The steady-state convergence factors and the turbulence models available in VECTIS were examined. The test case consisted of two solid elements of different dimensions and material properties (cast iron and aluminium alloy) in contact. These were placed in a computational chamber, as shown in Figure 3.8, and were solved with a steady-state CHT simulation. A constant heat flux boundary condition was prescribed at the bottom surface of the larger block (coloured in blue in Figure 3.8a) while the rest of the wall boundaries were set to exchange thermal properties with the surrounding air. The inlet and outlet flow conditions, at the top and bottom surfaces of the computational chamber, were set as for the computations of the underhood (Section 3.3.2).

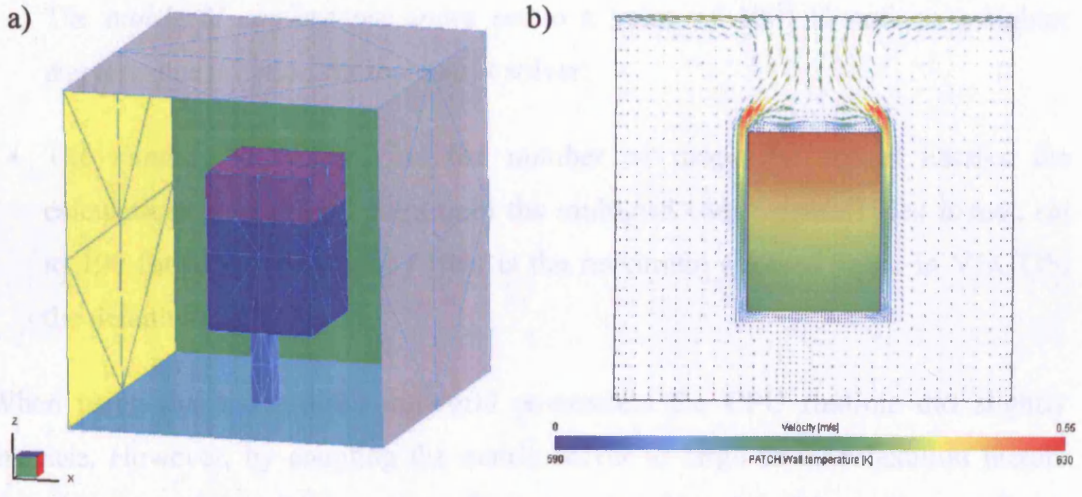

Figure 3.8 – Sensitivity analysis: (a) geometric configuration of test case; (b) sample slice view of airflow solution at steady state.

Initial computations were directed to establish the optimal parameters for the under-relaxation technique, which is used for improving the stability of a computation, particularly in solving steady-state problems. Under-relaxation works by limiting the amount that a variable changes from one iteration to the next and it is expressed through specific factors (referred to as *under-relaxation factors*, or *urf*), which can range between 0 (solution does not change at all between iterations) and 1 (solution is completely re-computed at each iteration). The results of the analysis evidenced, as expected, that small *urf*, while ensuring stable computations, also slowed down the

iterative solution process and consequently the progression of the simulation. On the other hand, large *urf* moved quickly the iterative process forward and the numerical solution converged faster towards the steady condition. It was determined that under-relaxation factor as high as 0.99 are optimal for simulating natural convective flow, assuming the numerical solution remains stable throughout the computation. In addition, it was found that the stability of the solution could be enhanced by a two-level Matrix solver (available in VECTIS), i.e. a Multigrid iterative solver scheme for the pressure equation [Ricardo Ltd 2004b]. The iterative solver performs the numerical calculations on a nested sequence of grids of varying size, with the solution on the coarser grids enabling the damping the low-frequency numerical errors [Hutchinson and Raithby 1986]. The following multigrid parameters showed to provide a stable numerical solution when under-relaxation factors of 0.99 were used to speed up its convergence:

- The *multigrid convergence index* set to a value of 10^{-10} to enforce a tighter convergence criterion for the matrix solver.

- The *number of sweeps*, i.e. the number of times the solver iterates the calculations at each grid point until the multigrid convergence index is met, set to 100 for improved stability (this is the maximum allowed value in VECTIS; the default value being 5).

When using the above strict multigrid parameters the CPU runtime did slightly increase. However, by coupling the matrix solver to large under-relaxation factors the processing time of the computations was overall reduced by a factor of 100 compared to the default VECTIS solver parameters. However, it is usefully pointed out that the under-relaxation values would need to be reduced for more complex geometric flow configurations (e.g. a typical underhood compartment), as their numerical solutions are more prone to numerical instabilities.

Further analysis was performed to examine the effects of grid density and choice of turbulence modelling. The fluid domain of the test case was discretised with four different meshes varying in number of cells and wall refinement. Three mathematical representations were employed to describe the airflow: a fully turbulent regime solved with either the standard $k-\varepsilon$ model or the *RNG* variant, and a laminar

regime with no numerical solution for turbulence. The twelve different modelling combinations and the results of the simulations (predicted average temperatures of the fluid and solid domains) are presented in Table 3.4.

Table 3.4 – Results of sensitivity analysis for different variants of simple test case.

Variant A – Low grid density, unrefined walls	Mesh Characteristics		Predicted Average Temperature (K)		
	Cell No.	y^+ range	Laminar	k–ε	*RNG* k–ε
AIR	12,404	$0.4<y^+<1.4$	308.28	308.13	308.14
BLOCK 1	30,863		578.52	585.59	587.13
BLOCK 2	22,680		584.66	592.02	593.55
Variant B – Medium grid density, unrefined walls	**Mesh Characteristics**		**Predicted Average Temperature (K)**		
	Cell No.	**y^+ range**	**Laminar**	**k–ε**	***RNG* k–ε**
AIR	15,613	$0.3<y^+<0.9$	308.52	308.43	308.42
BLOCK 1	30,863		592.08	628.39	628.67
BLOCK 2	22,680		598.82	635.46	635.47
Variant C – Medium grid density, refined walls	**Mesh Characteristics**		**Predicted Average Temperature (K)**		
	Cell No.	**y^+ range**	**Laminar**	**k–ε**	***RNG* k–ε**
AIR	29,447	$0.2<y^+<0.8$	307.93	307.92	307.80
BLOCK 1	30,863		594.50	597.10	597.20
BLOCK 2	22,680		601.22	603.79	603.83
Variant D – High grid density, unrefined walls	**Mesh Characteristics**		**Predicted Average Temperature (K)**		
	Cell No.	**y^+ range**	**Laminar**	**k–ε**	***RNG* k–ε**
AIR	116,603	$0.1<y^+<0.5$	307.29	307.58	307.48
BLOCK 1	30,863		585.40	617.89	619.42
BLOCK 2	22,680		591.90	624.60	625.90

The table shows that the predicted air temperatures tend to slightly reduce in value as the mesh density was progressively increased. The Grid Convergence Index (GCI) was calculated in order to determine if the calculations were asymptotically reaching a unique solution with refining grids [Peng *et al.* 1997]. Based on the Richardson extrapolation method [Sorensen and Nielsen 2003], the CGI is written as:

$$CGI = F_s \left| \frac{F_2 - F_1}{1 - r_{12}^p} \right| \tag{3.17}$$

where F_1 and F_2 are two separate solution quantities (e.g. predicted temperatures) on two grids with different size and r_{12} is the grid refinement ratio ($r_{12} = g_{S2} / g_{S1}$, where g_{s1} is the number of cells for the finer grid and g_{s2} for the coarser grid) with p representing the order of convergence (i.e. $p = 2$ for a "second-order" solution). F_s

is a factor of safety that is commonly taken as 3 for comparisons between two grids and 1.25 for comparisons over three or more grids [Roache 1994].

Figure 3.9 plots the CGI for the test case (based on the air temperature) with respect to the variation of the mesh density of the fluid domain. The CFD computations are clearly seen to be asymptotically reaching a grid-independent solution regardless of the numerical treatment used for turbulence. From the gradient of the lines in Figure 3.9, it is inferred that complete grid-independence could be obtained by discretising the fluid domain with more than 150,000 cells.

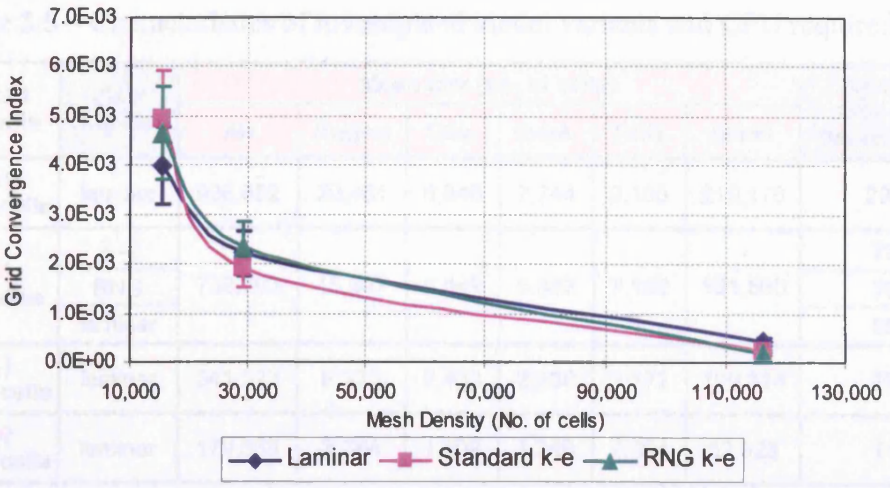

Figure 3.9 – Variation of grid convergence index as a function of the mesh size for the simple test case.

Table 3.4 shows that higher block temperatures were obtained when air turbulence was solved. However, the characteristic Rayleigh number of the model (approximately equal to 4×10^4) suggested that the actual flow regime next to the model boundaries was predominantly laminar. The turbulence models adopted the wall functions (from the Law of the Wall) to compute the flow properties in the near-wall cells. Although the y^+ values were very small, and a laminar flow condition was correctly assumed at the walls ($y^+<11.6$), the approach erroneously computed the wall heat transfer coefficients because a fully developed turbulent flow was assumed outside the boundary layer (for the cells contiguous to the first grid point). Consequently, the differences in prediction accuracy given by standard and the *RNG* version of the $k-\varepsilon$ model could not be established.

Analysis on Underhood Model – The analysis on the simple test case revealed that the mesh quality is crucial for accurate heat transfer modelling. A similar sensitivity analysis was therefore also carried out on the underhood geometry.

Table 3.5 presents the characteristics of the four different model variants investigated. The underhood model (*Variant B*) was solved either by prescribing full laminar flow conditions or with the $k-\varepsilon$ and the *RNG* turbulence models. The mesh density was then increased by 25% (*Variant A*), decreased by both 50% (Variant C) and 75% (Variant D), and solved with the airflow assumed laminar.

Table 3.5 – Characteristics of investigated model variants and CPU requirements.

Model Variants	Flow regime	Mesh size (no. of cells)						Processor time per iteration (s)
		Air	Engine	Gbx.	Insul.	Turb.	Glass	
(A) +25%cells	laminar	938,862	20,461	6,846	7,744	9,105	219,176	290
(B) Baseline	k–ε	738,703	15,907	5,542	5,852	7,152	191,560	78
	RNG							79
	laminar							65
(C) -50% cells	laminar	341,523	8,975	2,433	2,730	3,372	100,314	29
(D) -75% cells	laminar	179,668	3,784	1,508	1,386	2,364	52,923	11

Table 3.5 also lists the processor time required to complete each numerical iteration. Hardware demands were distinctively higher when the effects of turbulence fluctuations were modelled; no clear difference was observed between solving the flow with the standard $k-\varepsilon$ model or with its RNG variant, although the latter was expected to increase the processing time by up to 30% because of the additional terms in its formulation [Zhou et al. 1997]. The runtime to complete the simulations was found to be exponentially proportional to the number of cells in the mesh.

The steady-state flow velocities and the thermal predictions are presented in Table 3.6. The average air velocities were extracted from a vertical (z-y) plane at the centre of the fluid domain. The average y^+ values, calculated at the boundaries of the solid CHT components, are also listed. The thermal predictions obtained with the standard $k-\varepsilon$ model were similar to measurements and close to the predictions assuming a laminar flow in the compartment. The results were consistent with the "soft"

turbulence regime, which was expected to characterise the underhood flow since the characteristic Rayleigh number was 2.2×10^6. Although the y^+ values were small, the first cells near the walls were arguably correctly computed inside the viscous sub-region of the boundary layer due to the very low Reynolds number of the flow.

Table 3.6 – Results of sensitivity analysis for underhood geometry.

Model Variants	Flow regime	Avg. y^+ size	Predicted Average Temp. (°C)				Flow Velocity (m/s)	
			Air	Eng.	Gbx	Turbo	max. in z-y plane*	avg. in z-y plane*
(A) +25%cells	laminar	1.942	39.1	119.8	112.9	372.1	0.7021	0.1148
(B) Baseline	k–ε	2.218	36.0	113.9	106.9	359.9	0.5890	0.0700
	RNG		51.4	121.2	113.5	367.2	0.6373	0.0913
	laminar		39.4	119.4	112.1	369.9	0.7115	0.1189
(C) -50% cells	laminar	2.441	38.0	115.0	108.2	368.7	0.5624	0.0780
(D) -75% cells	laminar	2.937	34.8	108.4	101.3	361.3	0.4703	0.0798

* z-y plane located at x=0.38 (close to turbocharger side surface)

On the other hand, the *RNG* $k-\varepsilon$ model estimated much higher average block temperatures and mean flow velocities in the compartment than measured. A possible reason is that its formulation (specifically, the empirical coefficients and the additional non-linear term appearing in the turbulence transport equations) is specific for flow with large strain rates; the model would consequently tend to reduce the turbulence in the compartment through increased turbulent energy dissipation. The predicted higher temperature of the block surfaces, compared to the $k-\varepsilon$ solution, could be similarly justified (lower convective heat dissipation).

The accuracy of the laminar predictions converged towards near grid-independence as the mesh was discretised with a larger number of cells. Figure 3.10 plots the GCI variation based on the average of the predicted block temperatures. The analysis confirmed that the mesh size of model *Variant B* was the most appropriate for the computations of this study. The extended CPU runtime necessary to solve a 25% larger mesh (*Variant A*) would not be justified by the very small improvement in prediction accuracy. On the other hand, the results suggested that mesh grids with a relatively low number of cells (e.g. *Variant C*) yield acceptable flow and thermal

information and, given the high runtime savings, they could be a viable option for preliminary design studies.

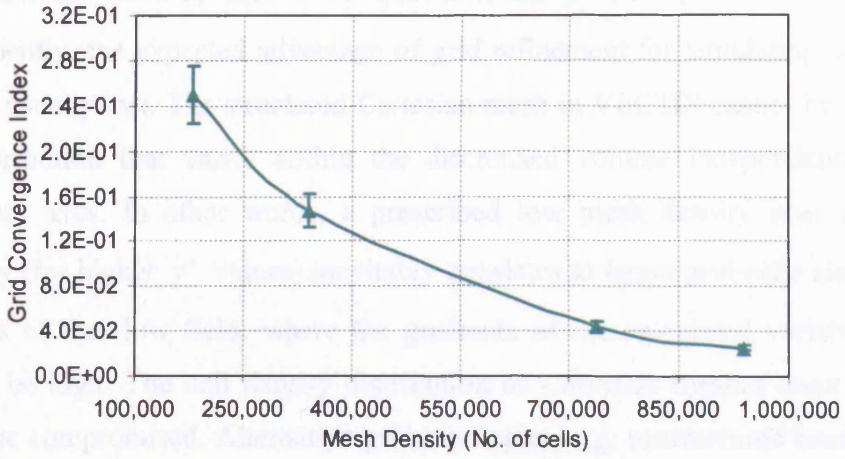

Figure 3.10 – Variation of grid convergence index as a function of the mesh size for underhood model.

A graphical comparison between the steady-state flow predictions obtained with the smallest and the largest of the investigated mesh densities (Variant A and D) is shown in Figure 3.11. Although the solution with the smaller mesh was observed to lose in vector resolution, the flow patterns in the compartment were predicted with a qualitative accuracy similar to the high-density solution.

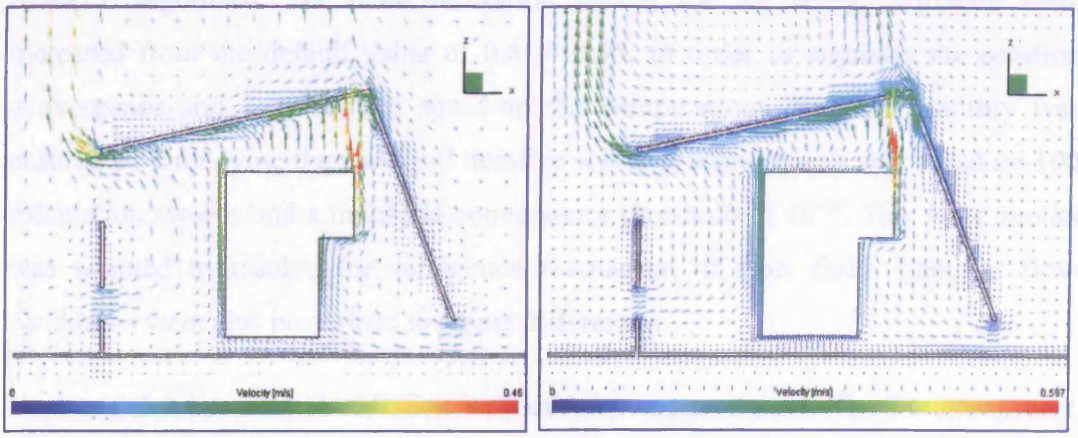

Figure 3.11 – Graphical comparison of flow predictions obtained with model variants *A* and *D*.

The grid dependency check gave a good indication of the best mesh quality for the underhood model, but it was also realised that it failed to recognise the main requirement of the wall function approach, i.e. a correct near-wall grid distribution.

Higher mesh densities and consequently higher grid refinements at the boundaries have usually a detrimental effect on the accuracy of the heat transfer predictions (the wall functions generally held to be applicable for $y^+ \geq 30$ [Ricardo Ltd 2004b]). Consequently, the expected advantage of grid refinement for simulating convective flows is usually lost. The structured Cartesian mesh in VECTIS cannot be set with a cell distribution that varies within the discretised volume independently of the coordinate axes. In other words, a prescribed low mesh density near a specific boundary (for higher y^+ values) inevitably translates to larger grid cells also at other locations of the flow field, where the gradients of the calculated variables might actually be high. The cell density distribution of Cartesian meshes must therefore always be compromised. Alternative grid topologies (e.g. unstructured hexahedral or unstructured tetrahedral cells) are more suited for optimising the cell sizes for both accurate and efficient computations (although their set-up is more laborious) but are not available as choice in VECTIS.

3.4.2 Steady-State Simulations

The steady-state simulations were carried out with the solid and fluid domains thermally conjugated. Momentum and continuity equations were coupled with the SIMPLE algorithm. The under-relaxation factors for the energy equation were increased from the default value of 0.6 to 0.95, in order to augment the solution convergence and consequently speed-up the computations. Solution stability was ensured by employing the multigrid iterative solver scheme, which was based on 100 calculation sweeps and a multigrid convergence threshold of 10^{-10}. The $k-\varepsilon$ model was adopted to resolve the turbulence fluctuation of flow field. Laminar flow conditions were also prescribed to assess differences.

Heat transfer by thermal radiation was initially not modelled. The boundary heat fluxes were instead specified with reduced values, as previously discussed. However, as a suitable radiation model became available as part of the VECTIS software package, at a later stage of the research programme, the steady-state simulations were repeated including the modelling of radiation heat transfer; the heat fluxes in the blocks were then specified exactly as determined from the measurements. An emissivity of 0.99 was specified for the blocks (matt black paint) and 0.91 for the

compartment (glass). Table 3.7 show small percentage differences between the temperature predictions obtained by approximating and by fully modelling radiation. As expected, the boundaries of the underhood compartment were predicted to be at a higher temperature when solving radiation since the heat flux approximation could not model the heat absorbed by the glass as radiated from the block surfaces.

Table 3.7 – Average steady-state block temperatures predicted with and without VECTIS's radiation model.

CHT Solid Domain	Predicted Average Temperature (K)		Difference (%)
	Without Radiation (compensated by heat flux reduction)	With Radiation	
Air	312.18	312.42	0.08
Engine	385.21	398.34	3.41
Gearbox	379.97	392.33	3.25
Turbo	634.03	639.86	0.92
Glass	312.70	330.83	5.80

Computations began with quiescent flow conditions and uniform initial block temperatures. They were halted after approximately 5,000 solver iterations when the temperatures and velocities computed at the monitoring cells reached convergence (i.e. steady thermal state), as shown in the plot of Figure 3.12.

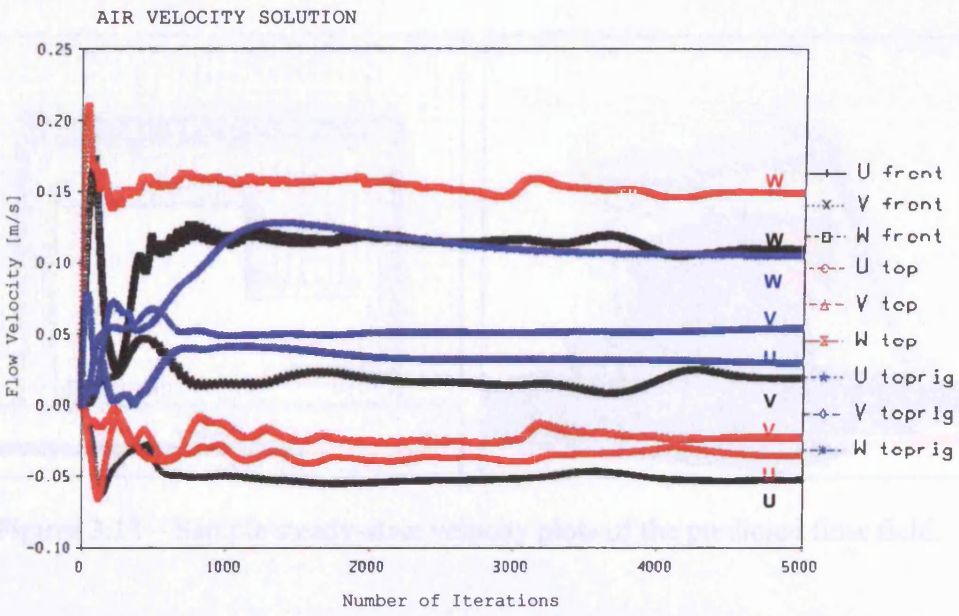

Figure 3.12 – Convergence of flow velocity solution (U, V, W components of velocity magnitude) as extracted from three different locations within the fluid domain (in front of heated blocks, above the engine and above bonnet).

The location of the monitoring cells was chosen so as to provide as much (useful) information as possible. Therefore, locations close to high temperature boundaries were avoided because the solution was likely to converge with little difficulty, being close to the driving force. Similarly, no monitoring point was placed in the core of flow recirculation regions because they would fail to properly represent the overall trend of the solution convergence. The monitoring cells also allowed continuous checking during computations of the value of the transport equation residuals, which were verified to be below 1×10^{-6} (absolute variation between iterations) before the simulation end-time was reached.

The processor time required to complete one steady-state iteration was about 90 seconds (95 seconds with the radiation model) on a Pentium IV, 2.40GHz, 1GB Ram. Approximately 125 hours were necessary, overall, to complete the analysis (132 hours with radiation model).

The post-processing software integrated into VECTIS's package was employed to visualise flow and thermal maps of the results and to extract from them quantitative information. Sample results showing the flow patterns predicted within the compartment and the temperature distribution on the block surfaces and air planes are shown in Figures 3.13 and 3.14.

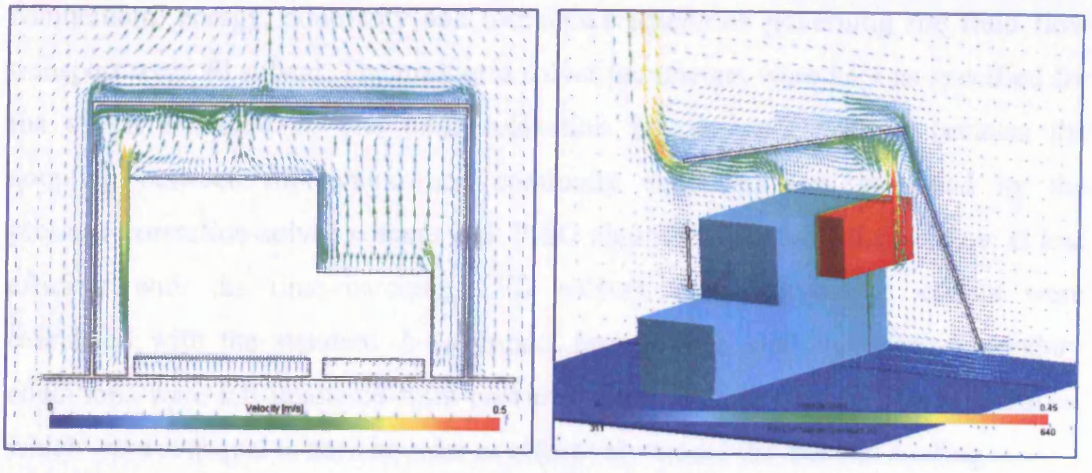

Figure 3.13 – Sample steady-state velocity plots of the predicted flow field.

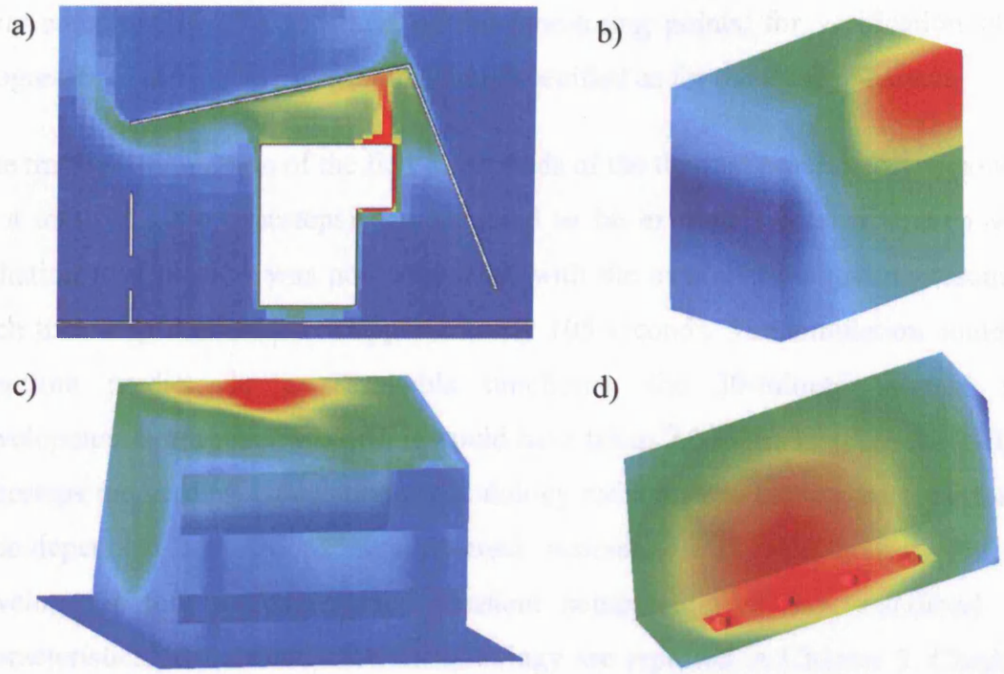

Figure 3.14 – Predicted steady temperature distribution for: (a) sample air plane across model; (b) engine block; (c) compartment boundaries; (d) turbocharger block. (Temperatures and dimensions not to scale).

3.4.3 Transient Simulations

The effects that natural cooling has, over a period of time, on the convective flow patterns and on the temperature of the blocks were investigated.

Momentum, energy, continuity and turbulence equations governing the fluid flow transport were all solved. The multigrid solver parameters were kept as specified for the steady simulations. The under-relaxation factors were not set because the coupling between momentum and continuity equations was governed by the pressure-correction-solver scheme with PISO algorithm (the SIMPLE scheme is less efficient with the time-marching CFD solver). Flow turbulence effects were calculated with the standard $k-\varepsilon$ model and relative wall treatment. Boundary conditions were left unaltered from previous simulations except for the heat fluxes, which were set equal to zero in order to effectively model the thermal cooling.

A convergence criterion of 10^{-6} was imposed on the time-dependent solution of the governing equations. The transient analysis was based on a timestep of 0.005 seconds and was re-started from the thermal condition determined with the steady-

state computation. The locations of the monitoring points, for verification of the progresses of the numerical solution, were specified as for the steady analysis.

The transient simulation of the first 10 seconds of the thermal process (corresponding to a total of 2000 timesteps) demonstrated to be extremely intensive even when radiation heat transfer was not calculated; with the available computing resources, each time step was solved in approximately 105 seconds. The simulation could not therefore predict, in a reasonable timeframe, the 30-minute thermal flow development during heat soak, as it would have taken 7,000 hrs to solve the 240,000 timesteps required. A calculation methodology reducing the simulation time for the time-dependent simulations was deemed necessary and was investigated and developed before performing the transient computation of the underhood. The characteristics of the calculation methodology are reported in Chapter 5. Chapter 6 discusses the transient CFD results obtained.

3.5 COMPUTATIONAL ERRORS AND UNCERTAINTIES

The sources of errors and uncertainties in the CFD predictions can be broadly divided into two distinct categories [Stern *et al.* 1999]: modelling and numerical. Modelling errors stem from the assumptions and approximations in the mathematical representation of the physical problem (such as geometry, mathematical equations, coordinate transformation, boundary conditions, turbulence models, etc.) and the incorporation of previous data (such as fluid properties) into the model. Numerical errors are associated with the numerical solution of the mathematical equations (such as discretisation, artificial dissipation, incomplete iterative and grid convergence, lack of conservation of mass, momentum, and energy, internal and external boundary non-continuity, computer round-off, etc.).

CFD errors are highly dependent on the specific application (i.e. geometry and boundary conditions). Usually, they cannot be completely eliminated but it is possible to determine and reduce them by testing different solution models or discretisation strategies [Roache 1997], as it was done in this study by performing parametric sensitivity analyses. The following is a list of the CFD errors that were recognised and investigated:

1) *Physical approximation errors* (or modelling errors) are due to the uncertainty in the formulation of the numerical models or to their deliberate simplification. The sensitivity study investigated the effects of using different turbulence models. Various boundary conditions were also tested, in particular for the inlet and outlet surfaces of the computational chamber, which were critical for correctly modelling the thermally driven flow in the compartment.

2) *Iterative convergence errors* exist because the iterative methods in the simulation must eventually have a termination point. In this study, the steady-state solution was ensured being fully converged and the transient computations were carried out with a strict convergence criterion, as previously reported. Potential convergence errors in the predictions were therefore considered as negligible.

3) *Discretisation errors* (or numerical errors) occur from the representation of the governing flow equations and other physical models, such as algebraic expressions in a discrete space and time domain (finite-volume formulation). A consistent numerical solution will approach the continuum representation of the equations with zero discretisation error when the number of grid points is increased and the size of the grid spacing tends to zero. Ideally, all CFD solutions should be independent of their mesh density but because of computer power restrictions and runtime requirements, this is practically impossible, at least for three-dimensional calculations [Sorensen and Nielsen 2003]. The requirement can be relaxed, while preserving confidence in the solution of the governing equations, by obtaining *grid-convergence*, which implies that the solution asymptotically approaches the exact solution (to the governing equations). Grid-independence for the underhood model was investigated as part of the sensitivity analysis.

4) *Computer round-off errors* develop with the representation of floating point numbers on the computer and depend on the accuracy at which these numbers are stored. As reasonably advanced computer resources were employed in this study, round-off errors were not considered significant when compared with other errors.

5) *Programming errors* are "bugs" or mistakes made in writing the CFD software. These types of errors are discovered by systematically performing verification

studies on the sub-programs of the codes or performing validation studies against experimental data. They are generally the responsibilities of the software developers. During the present study, it was found that the CHT procedure failed to correctly conserve energy across the interfaces of the thermally conjugated boundaries. Quantitative discrepancies of approximately 10% were noted by equating the heat balances of selected boundaries. The inaccuracy, which was caused by incorrect CHT meshing across the interfaces, was reported to Ricardo Software Ltd., which subsequently released a patch correcting the problem.

6) *Usage errors* are due to the application of the CFD software in a less-than-accurate or improper manner. These errors usually emerge when the condition of the flow is not known a-priori and therefore the conclusions drawn from the simulation may be incorrect even if a converged solution is obtained. No errors of this kind were evident for the simulations reported in this thesis. Usage errors, in the form of modelling and discretisation errors, were sometimes intentionally introduced within the calculation methodology developed to speed up the transient simulations (at the expense of losses in prediction accuracy). These are further discussed in Chapter 5.

3.6 CLOSURE

The present chapter has described the mathematical formulation, the numerical scheme and the solution algorithm of the software employed for the CFD investigations, VECTIS. Turbulence and radiation model formulations have also been introduced.

Steady and time-marching simulations were carried out using a conjugate heat transfer solution procedure that allowed for a realistic representation of the conduction, convection and radiation heat transfer in the modelled compartment. Model geometry, mesh characteristics and boundary conditions were described. The calculations were based on a finite-volume scheme and on the standard $k-\varepsilon$ model for dissipation of turbulent kinetic energy.

The grid density, turbulence modelling, wall function approach (range of y^+ values) and convergence parameters were investigated via a parametric analysis. The aim was to improve the overall accuracy of the CFD predictions.

The numerical setup of both the steady-state and transient solvers has also been presented. The transient calculations were noted to be excessively computing-intensive and did not permit the simulation of the flow and thermal conditions in the underhood for the complete timeframe of interest. A numerical methodology able to speed up the CPU runtime for time-marching computations was deemed necessary.

Finally, sources of numerical and modelling errors and uncertainties have been addressed. The grid convergence index was adopted to estimate the error between the calculated solution and the exact solution to the governing equations with respect to the number of cells in the mesh. It was determined that a nearly grid-independent solution of the underhood flow field was obtainable with a mesh of about 700,000 cells; the grid dependency check did not however take into account the near-wall grid requirements of the wall function for correct wall heat transfer predictions and therefore may not be fully realistic for natural convective flow simulations.

Chapter 4

DATA COMPARISON – STEADY-STATE

4.1 PRELIMINARY REMARKS

The accuracy of VECTIS in predicting surface and air temperature distributions and flow patterns in the underhood model is examined in this chapter. Numerical predictions obtained with the steady-state solver were compared with the measured data acquired after thermal equilibrium was established between the heated blocks and the surrounding flow.

The data correlation was performed on selected surfaces and air planes. All of the modelled blocks had at least one surface thermally investigated and the flow was studied in various x- and y-planes across the compartment. The 2-D regions were located with respect to the reference co-ordinate system shown in Figure 4.1

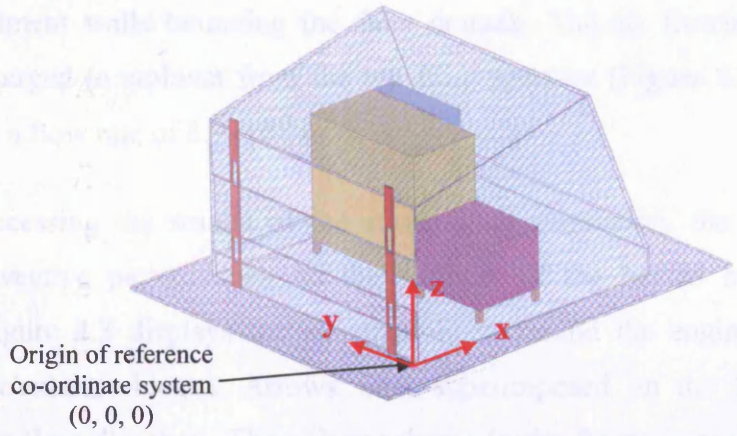

Figure 4.1 – Reference co-ordinate system locating in space the surfaces and the air planes examined.

The origin was fixed at one of the outer corners of the underhood (i.e. the y = 0, x = 0 and z = 0 planes corresponded, respectively, to the side, front and bottom surface of the compartment). Appendix D contains diagrams showing the locations of the thermocouples and of the fields of view.

4.2 UNDERHOOD FLOW FIELD CHARACTERISATION

Figure 4.2 depicts the flow fields as predicted on different perpendicular planes within the underhood volume. In particular, Figure 4.2a shows the results of the simulation on selected vertical y-z planes, Figure 4.2b on vertical x-z planes and Figure 4.2c on various horizontal x-y planes. By combining the predictions, the three-dimensional structure of the convective flow can be deduced qualitatively.

The introduction of the ambient air from both the front and the rear bottom openings of the compartment resulted in a horizontal flow just above the floor level (Figure 4.2b). The average inlet air velocities were very similar at both apertures and approximately equal to 0.07 m/s, with peak values of 0.12 m/s.

Within the enclosure, the convective strength of the air increased as it rose vertically next to the block surfaces towards the upper boundaries of the underhood. The air velocity reached its maximum value of 0.63 m/s in this region (Figure 4.2a, x = 0.40 m plane). Above the blocks, re-circulating vortices with diameter up to 50 mm were observed (as partly displayed in Figure 4.2b on the y = 0.35 m and the y = 0.47 m planes). Such characteristic flow patterns developed due to the geometric shape of the compartment walls bounding the flow domain. The air flowing in the upper layers discharged to ambient from the top front aperture (Figure 4.2b, y = 0.22 m plane), with a flow rate of 8.9×10^{-3} m^3/s.

By post-processing the results of the steady-state simulation, the features of the natural convective patterns next to the surfaces of the heated blocks could be deduced. Figure 4.3 displays the air streamlines around the engine, gearbox and turbocharger/exhaust blocks. Arrows were superimposed on the figure to better delineate the flow direction. The colour scheme in the figure is proportional to the temperatures of the air and surfaces (temperature scale given at the bottom).

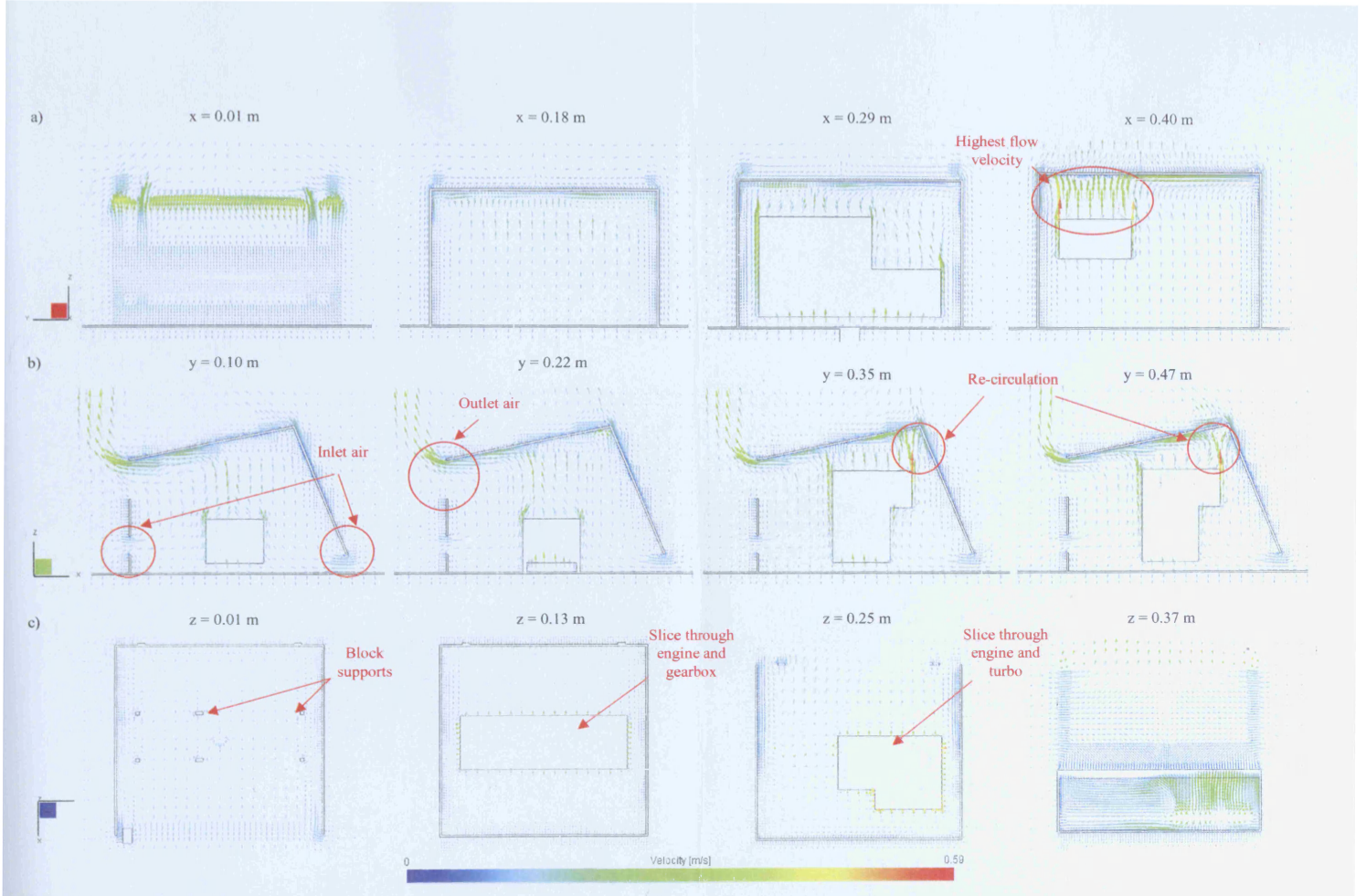

Figure 4.2 – Airflow patterns predicted within the underhood: 2-D views along (a) x-axis; (b) y-axis; (c) z-axis.

A distinctive flow path, directed towards the front opening of the engine compartment, can be observed above the gearbox. The path (or "duct" in UTM lexicon) was formed because the air motion was restricted from flowing above the engine and turbocharger blocks by the vortices developing at their edges.

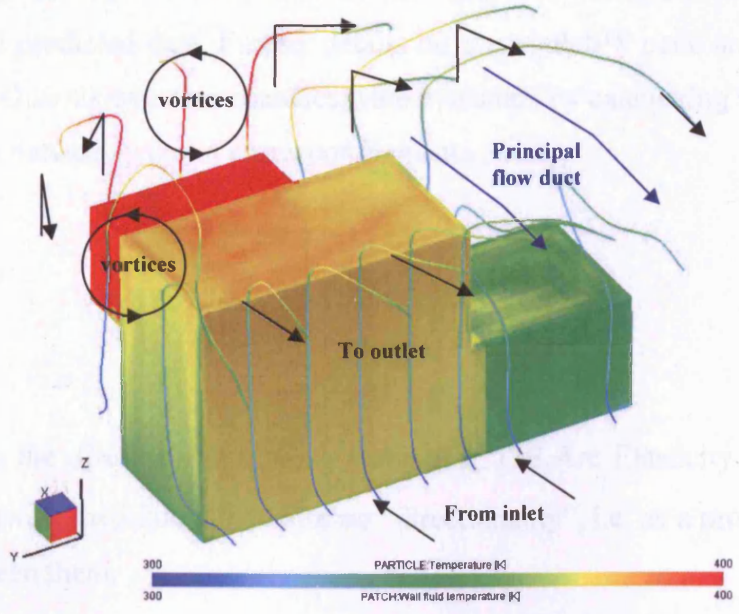

Figure 4.3 – Airflow patterns predicted above the heated blocks.

4.3 TEMPERATURE MEASUREMENTS VS. VECTIS PREDICTIONS

Both the predictions obtained by solving the underhood model with the heat flux approximation and by fully modelling radiation heat transfer were compared qualitatively and quantitatively with the measurements. The effects of employing the $k-\varepsilon$ turbulence model or prescribing the flow regime as fully-laminar were also examined.

The 2-D planes chosen for the data comparisons were characterised by various unique thermal features, such as vertical surface temperature distribution with low and high heat dissipation (front surfaces of engine and gearbox blocks, and rear surface of turbocharger), horizontal surface temperature distribution (upper surface of engine block), air temperature stratification next to heated blocks (air plane across underhood volume) and air temperature distribution across the outlet slot of the underhood.

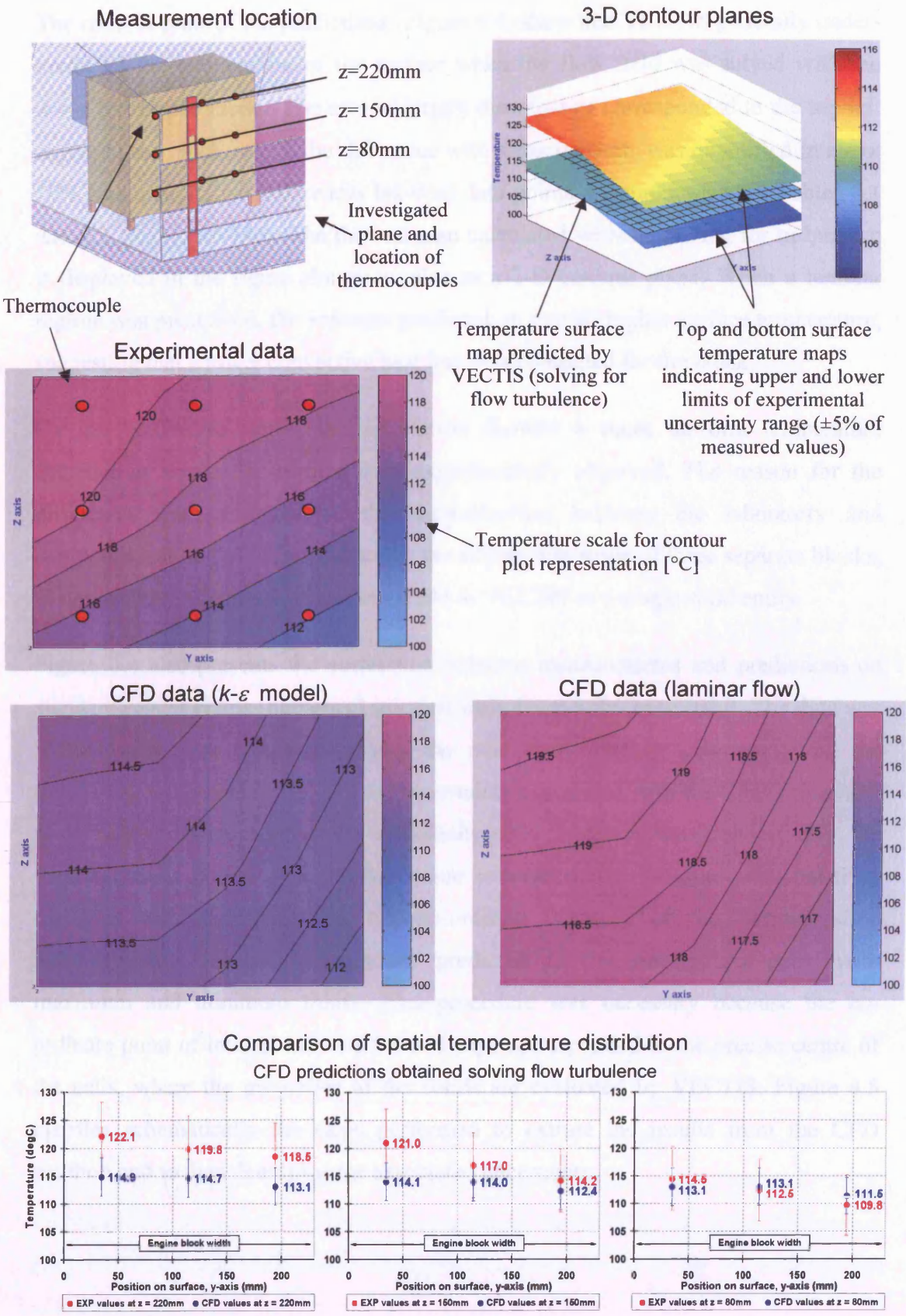

Figure 4.4 – Temperature comparison for engine's front surface (all data in degrees Celsius); Turbulent and laminar flow regimes.

The contour plots of the predictions (Figure 4.4) show that VECTIS generally under-predicted the temperature of the surface when the flow field was solved with the $k-\varepsilon$ turbulence model. The area of largest discrepancy corresponded to the top left region of the block, where the difference with measurements was quantified in about 10% (the quantitative differences between data points are summarised in Tables 4.1 and 4.2, pages 145-146). The thermal map calculated without solving for turbulence is displayed in the figure alongside, also as a 2-D contour plane. When a laminar regime was prescribed, the software predicted an overall higher surface temperature, suggesting that a lower convective heat loss was computed for the block.

On the qualitative terms, the simulation showed a more uniform temperature distribution across the surface than experimentally observed. The reason for the difference was attributed to the dissimilarities between the laboratory and computational model setups. Although the engine was made of three separate blocks, as described in Chapter 2, it was modelled in VECTIS as a single solid entity.

Figure 4.4 also presents the correlation between measurements and predictions on standard scatter charts (numerical solution with $k-\varepsilon$ turbulence only). The data was plotted with error bars representing the overall uncertainty associated with the measuring equipment (±5%) and the uncertainty associated with the CFD values due to the spatial discretisation of the air domain (±3% for this surface). Specifically, the CFD data was plotted as an average value between the temperature extracted from the grid cell of interest (at the co-ordinate location of the corresponding thermocouple) and the temperatures predicted in the surrounding cells, with maximum and minimum limits. This procedure was necessary because the co-ordinate point of interest may not have always corresponded to the precise centre of the cells, where the properties of the solids are evaluated by VECTIS. Figure 4.5 clarifies schematically the steps performed to extract the results from the CFD solution and to then determine the associated uncertainty.

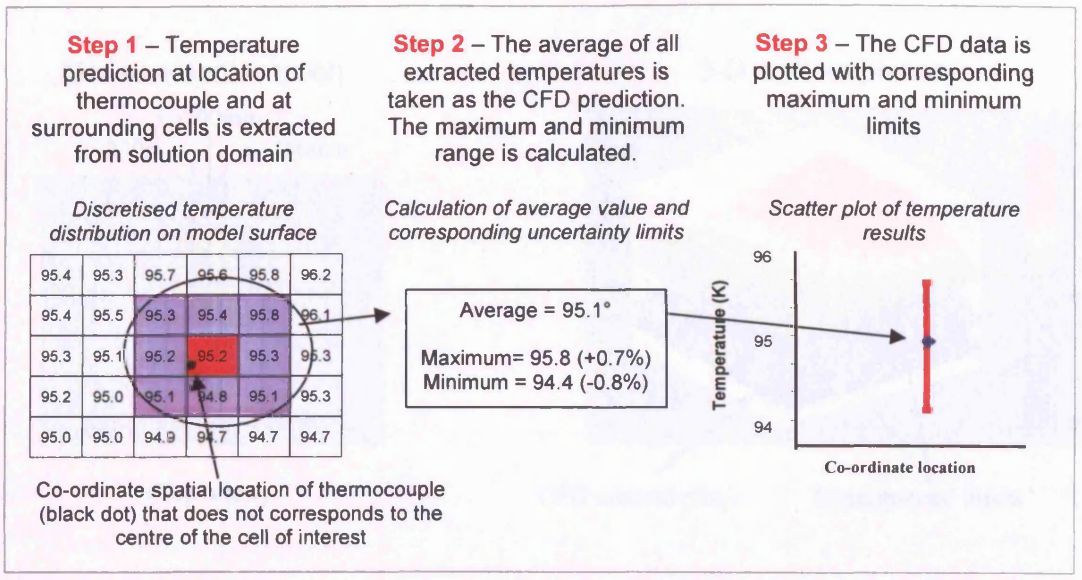

Figure 4.5 – Schematic of the procedure followed to extract the CFD temperature predictions and plot on scatter charts for comparison with experimental data.

The agreement between the two sets of data was regarded to be acceptable because the error bands in the scatter plot of Figure 4.4 overlapped. This was also established from the 3-D contour-plane representation (at the top of the figure), which showed that the simulated temperature distribution was mostly within the upper and lower limits of the overall experimental uncertainty range (i.e. ±5% of measured values).

Top Surface of Engine Block – The thermal distribution on the upper surface of the engine block was clearly influenced by the heat conducted from the turbocharger, which was at a distinctively higher temperature. The CFD results, presented in Figure 4.6, indicated that the effects of prescribing different regimes to the flow were relatively small on the thermal state of the surface.

The 2-D Matlab™ representations revealed that the qualitative variation in surface temperature was very well predicted. The quantitative agreement between the data points was however relatively poor, with the simulations clearly under-predicting the thermal condition of the surface. The overall thermal distribution within the engine was simulated to be more uniform than measured, therefore it was actually expected that relatively large temperature discrepancies would result at the top and bottom surfaces of the block.

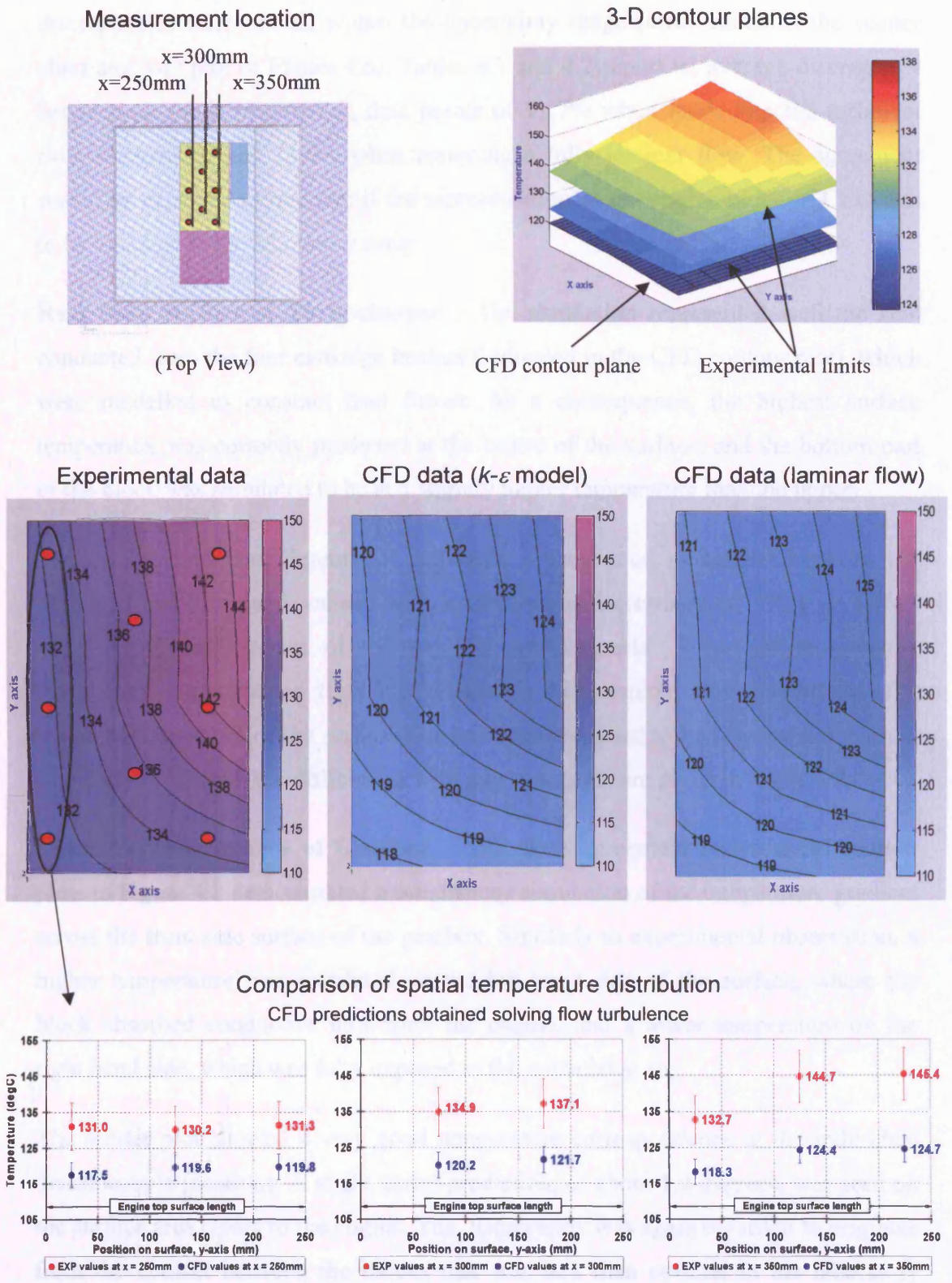

Figure 4.6 – Temperature comparison for engine's top surface (all data in degrees Celsius); Turbulent and laminar flow regime.

The overall simulation accuracy was not considered as satisfactory since the discrepancies were not all within the uncertainty range (error bands in the scatter chart and 3-D plot of Figure 4.6). Tables 4.1 and 4.2 report an average discrepancy between all the corresponding data points of 11.7% when modelling the turbulent flow fluctuations and 11.0% when assuming a fully laminar flow. The agreement would be expected to improve if the representation of the engine block in CFD was to be identical to the laboratory setup.

Rear Side Surface of Turbocharger – The simulation represented well the heat conducted from the four cartridge heaters (indicated in the CFD contour plot), which were modelled as constant heat fluxes. As a consequence, the highest surface temperature was correctly predicted at the centre of the surface, and the bottom part of the block was simulated to be at a slightly higher temperature than the upper.

The data comparison, Figure 4.7, indicated a very good agreement between the predicted and measured values, with a maximum discrepancy of 1% (i.e. 3.7°C) observed at the location of the top left thermocouple. A similar temperature distribution was obtained from the simulation with laminar flow conditions. The average temperature of the surface was however predicted to be few degrees higher. The CFD results and the differences with measurements are given in Table 4.2.

Front Vertical Surface of Gearbox – The close agreement between the contour plots in Figure 4.8 demonstrated a satisfactory simulation of the temperature gradient across the front side surface of the gearbox. Similarly to experimental observation, a higher temperature was simulated on the left hand side of the surface, where the block absorbed conductive heat from the engine, and a lower temperature on the right hand side, which was fully exposed to the convective air.

The scatter plot showed a very good temperature correspondence at the individual thermocouple locations. A slight under-prediction, of about 1.2 degrees, was seen on the surface area closer to the engine. The discrepancy was again regarded to originate from the contact between the blocks that was less than optimal in the laboratory setup (albeit the heat transfer was maximised with conductive paste) but was modelled as being ideal by VECTIS. The computation with laminar airflow over-predicted the condition determined from laboratory analysis by about 5°C.

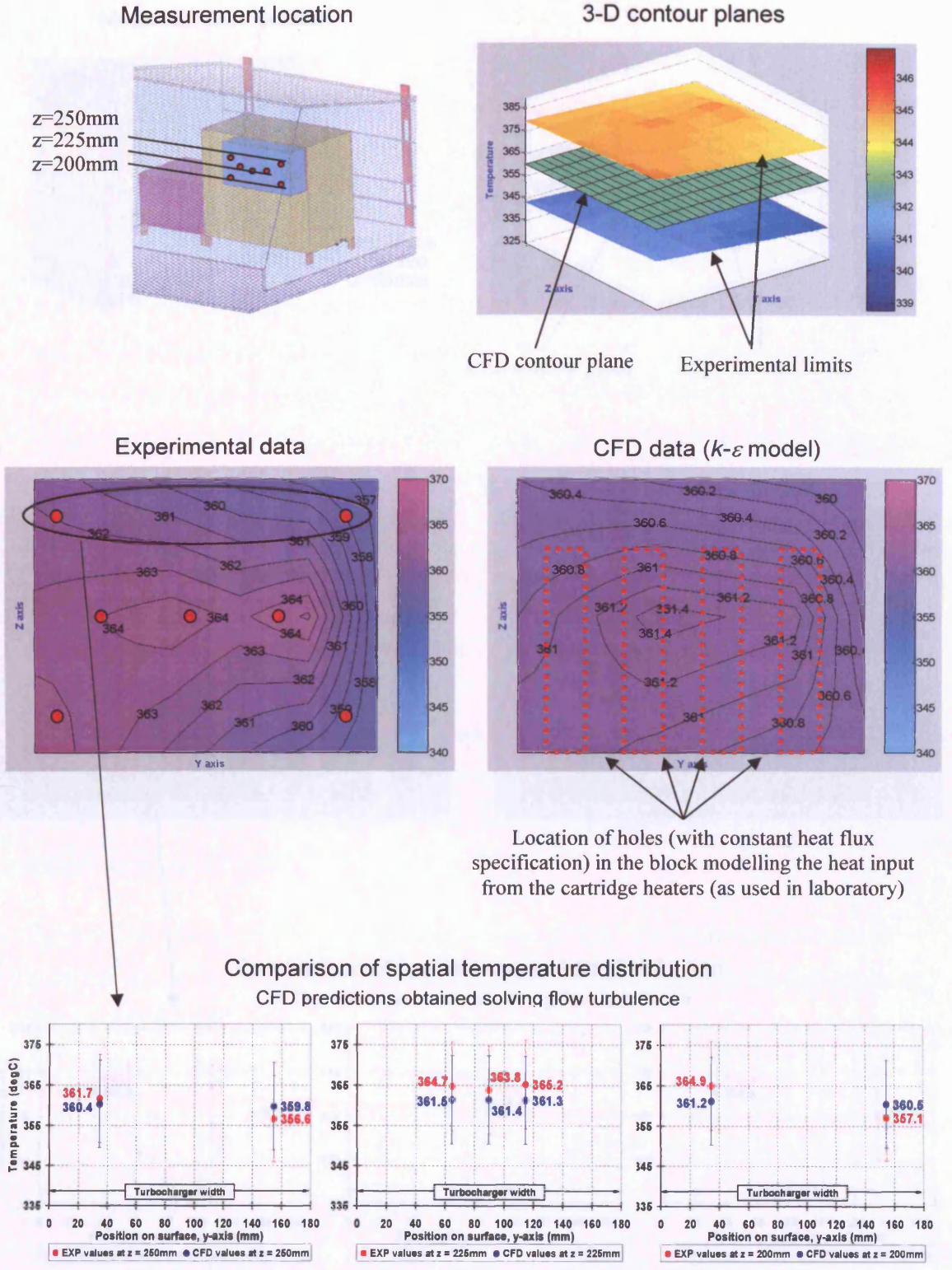

Figure 4.7 – Temperature comparison for turbocharger's rear surface (all data in degrees Celsius); Turbulent flow regime.

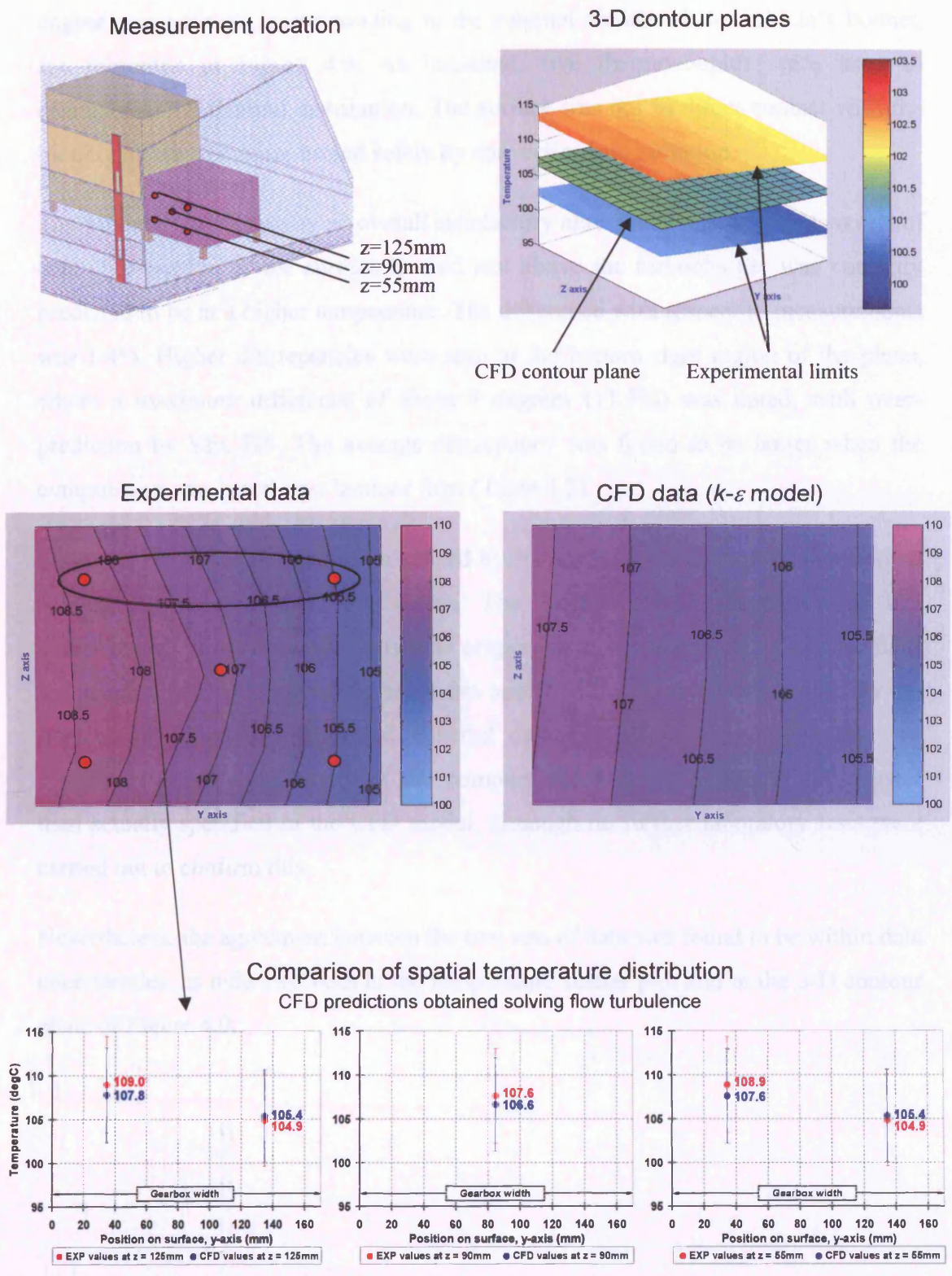

Figure 4.8 – Temperature comparison for gearbox's front surface (all data in degrees Celsius); Turbulent flow regime.

Top Surface of Compartment – The thermal maps for the top boundary of the engine compartment, corresponding to the external surface of the vehicle's bonnet, are presented in Figure 4.9. As indicated, five thermocouples were used to characterise the thermal distribution. The surface was not in direct contact with the blocks and was therefore heated solely by convection and radiation.

The Matlab™ plots display an overall satisfactory agreement between the two sets of data. The portion of the surface located just above the turbocharger was correctly predicted to be at a higher temperature. The difference with respect to measurements was 1.4%. Higher discrepancies were seen at the bottom right region of the plane, where a maximum difference of about 7 degrees (11.5%) was noted, with over-prediction by VECTIS. The average discrepancy was found to be larger when the computation was based on a laminar flow (Table 4.2).

The CFD error was thought to be caused by inaccurate specification of the thermal conductivity of the glass boundaries. The Robax™ type glass was in fact approximated to have similar physical properties to commercially-available high-temperature resistant tempered glasses. No specific information was provided by the supplier or found in specialised material databases. It was envisaged that the effective thermal conductivity of the compartment boundaries was slightly lower than actually specified in the CFD model, although no further laboratory tests were carried out to confirm this.

Nevertheless, the agreement between the two sets of data was found to be within data uncertainties, as indicated both in the temperature scatter plot and in the 3-D contour plane of Figure 4.9.

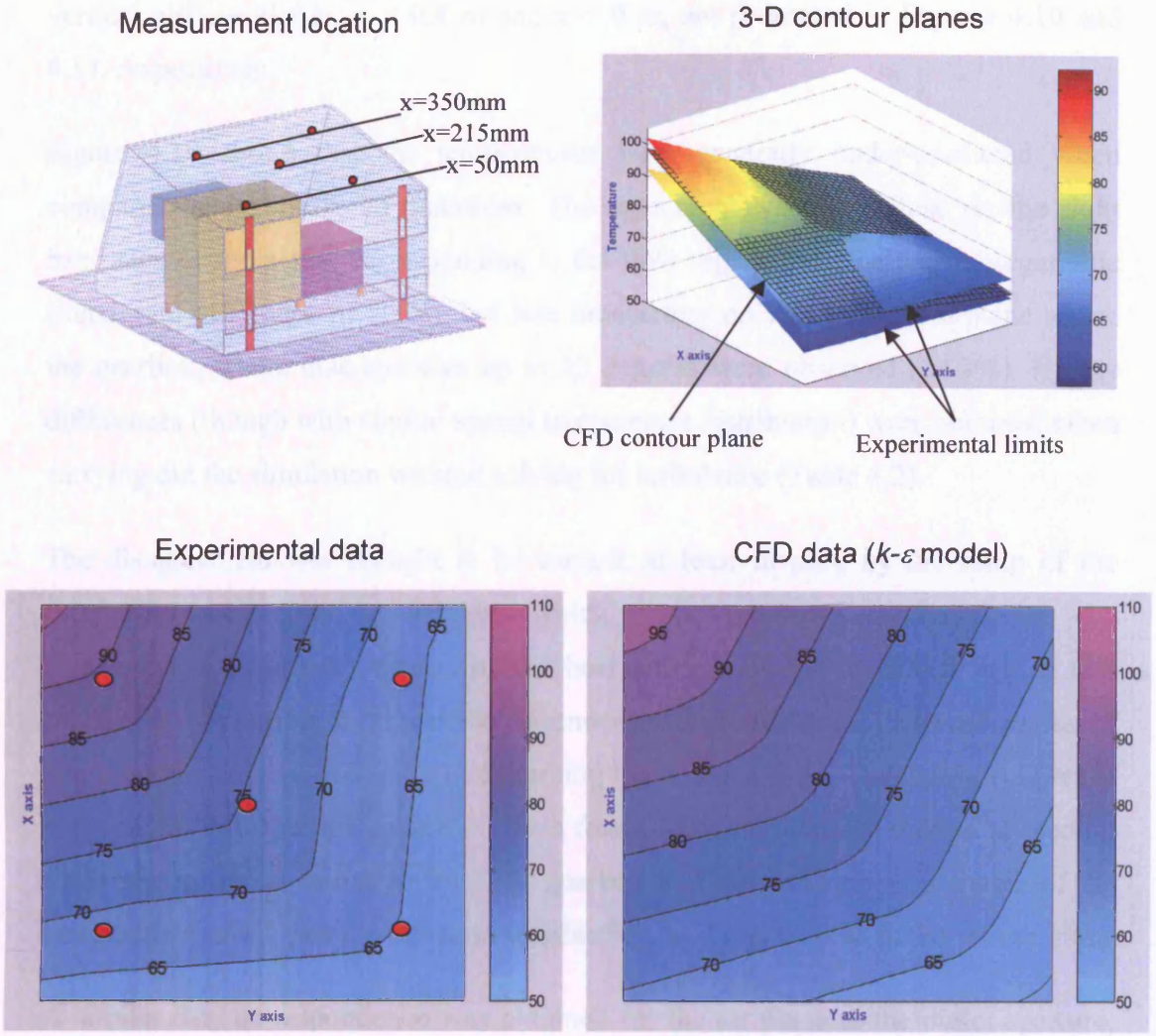

Figure 4.9 – Temperature comparison for bonnet's surface (all data in degrees Celsius); Turbulent flow regime.

Air Plane behind Blocks and At Outlet – The thermal stratifications across two vertical airflow planes, x = 0.4 m and x = 0 m, are presented in Figures 4.10 and 4.11, respectively.

Figure 4.10 shows that the temperatures were generally under-predicted when compared to the measured quantities. The agreement was very close on the right hand side of the plane, corresponding to the flow region near the turbocharger side (maximum difference of 2.4%), but less satisfactory on the side of the plane above the gearbox, where discrepancies up to 15 degrees were observed (14.9%). Higher differences (though with similar spatial temperature distribution) were obtained when carrying out the simulation without solving for turbulence (Table 4.2).

The disagreement was thought to be caused, at least in part, by the setup of the thermocouples' reflecting shields, which were employed to minimise the measurement uncertainty caused by the heat radiated by the blocks. It was in fact practically impossible to shield the thermocouples from all the different angles of emission of radiative heat without disturbing the buoyant flow. The thermocouples at the position indicted in Figure 4.10 were found to be particularly subject to reading uncertainties due to radiation from the gearbox and turbocharger. The match of the temperature values was nevertheless satisfactory, as it can be seen in the scatter plot.

A similar data correspondence was obtained for the air plane at the outlet aperture, Figure 4.11. In this region, the air temperature measurements were expected to be less susceptible to the effects of radiation because the sensors were not in close proximity of the block surfaces and especially because they were not directly exposed to the heat emitted by the turbocharger. The CFD results were overall in good qualitative and quantitative agreement with the measured data. The temperatures at the bottom of the plane were however over-predicted by 6 degrees, on average. Since the predictions with laminar flow showed a better correspondence with measurements (0.4°C average difference), it is likely that the turbulence model failed to correctly resolve the flow field next to the glass boundaries. This region was further examined with PIV, as presented in Section 4.4.1.

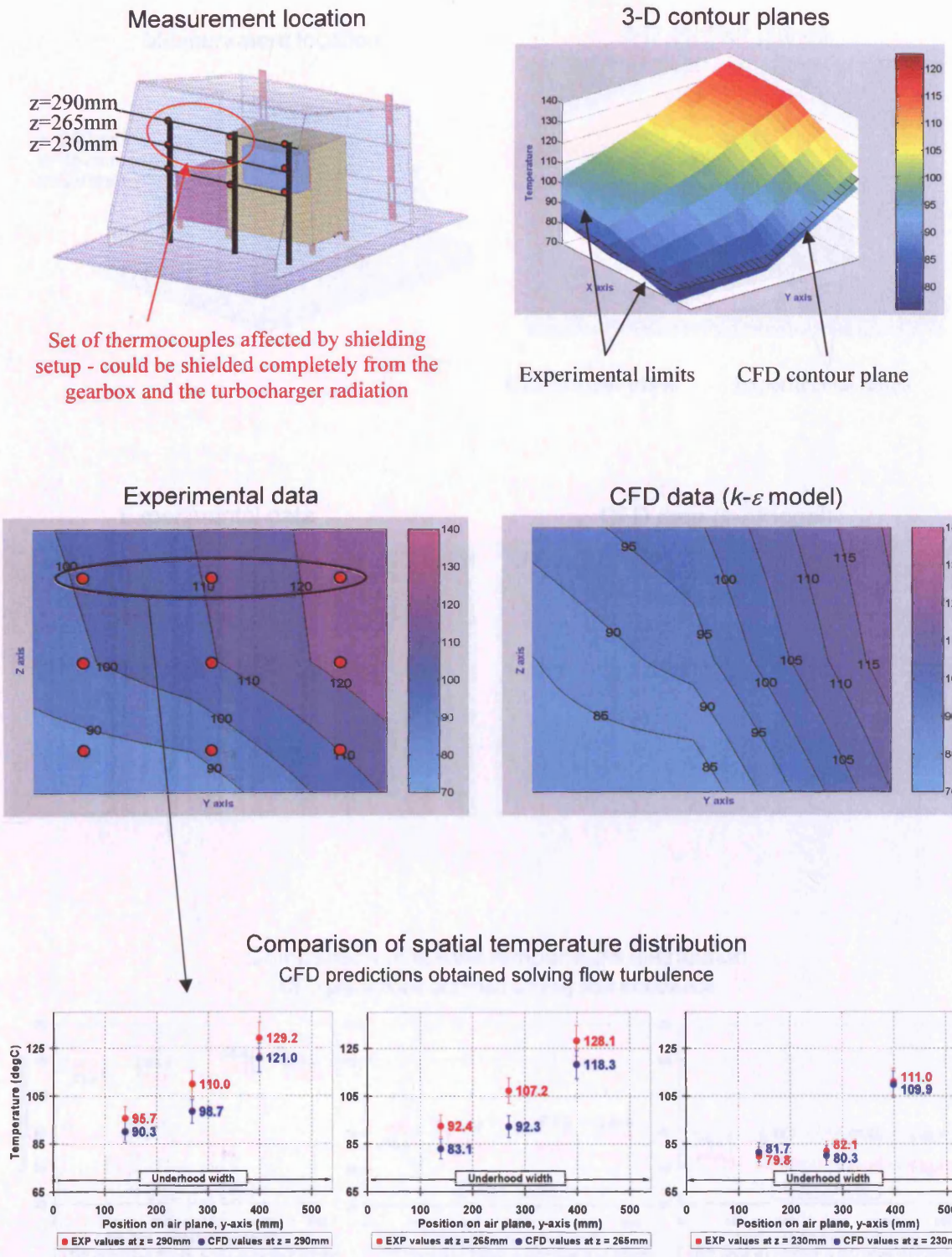

Figure 4.10 – Temperature comparison for the rear air plane (all data in degrees Celsius); Turbulent flow regime.

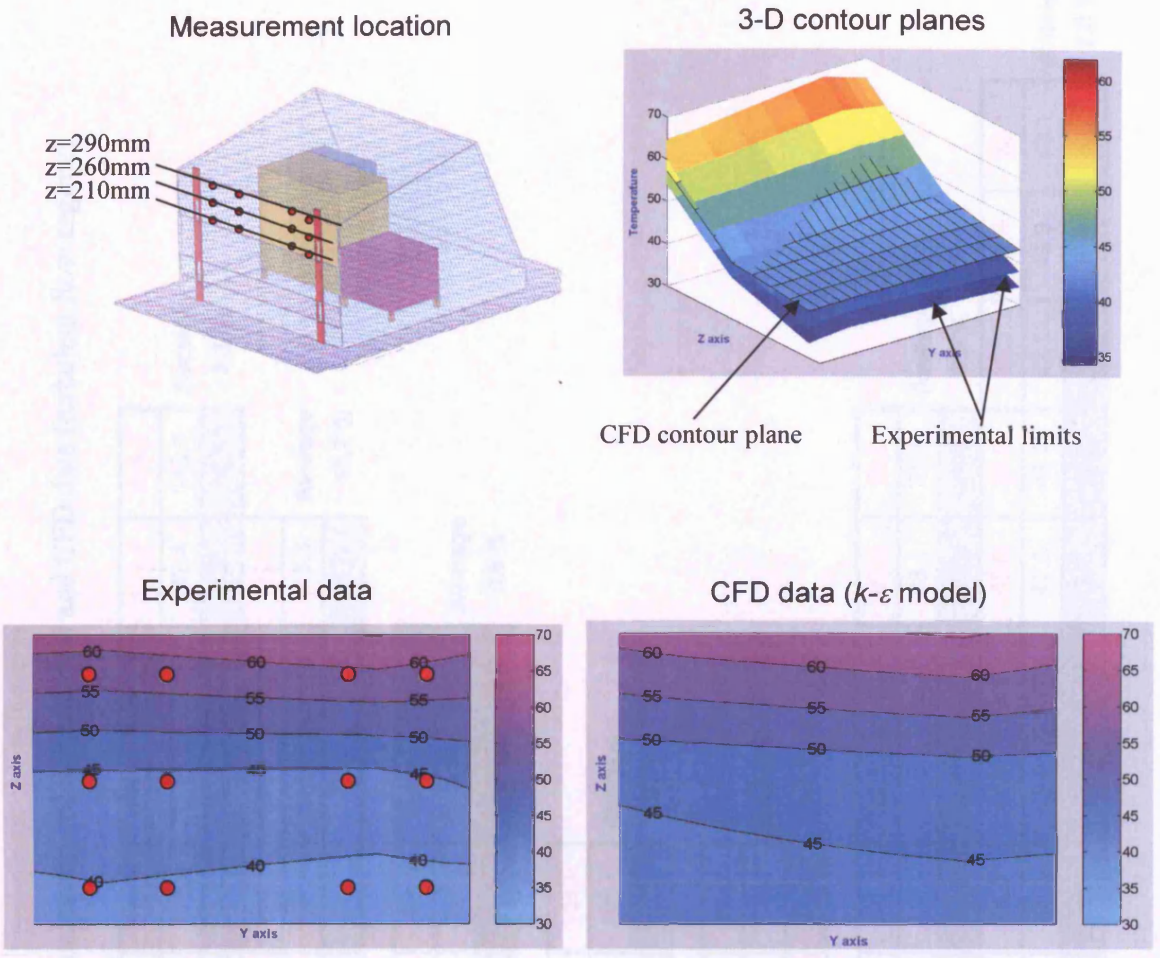

Figure 4.11 – Temperature comparison for air plane at the flow outlet slot (all data in degrees Celsius); Turbulent flow regime.

Table 4.1 – Steady-state thermal results: comparison of experimental and CFD data (turbulent flow regime).

Engine Front Surface	EXP (°C)	114.5	121.0	122.1	112.5	117.0	119.8	109.8	114.2	118.5			
	CFD (°C)	113.1	114.1	114.9	113.1	114.0	114.7	111.5	112.4	113.1	Average		
	% Elasticity	1.3	5.9	6.1	0.6	2.6	4.3	1.6	1.6	4.7	3.2 %		
Engine Top Surface	EXP (°C)	131.3	145.3	137.2	130.2	144.7	134.9	131.0	132.7				
	CFD (°C)	119.8	124.7	121.7	119.6	124.4	120.2	117.5	118.3	Average			
	% Elasticity	9.2	15.3	11.9	8.5	15.1	11.5	10.9	11.5	11.7 %			
Turbo Rear Surface	EXP (°C)	364.9	361.7	364.7	363.8	365.2	357.1	356.6					
	CFD (°C)	361.2	360.4	361.5	361.4	361.3	360.5	359.8	Average				
	% Elasticity	1.0	0.4	0.9	0.7	1.1	1.0	0.9	0.8 %				
Gearbox Front Surface	EXP (°C)	108.9	104.9	107.6	109.0	104.9							
	CFD (°C)	107.8	105.4	106.6	107.6	105.4	Average						
	% Elasticity	1.0	0.5	0.9	1.3	0.5	0.8 %						
Bonnet Top Surface	EXP (°C)	63.2	75.0	61.1	97.1	63.2							
	CFD (°C)	69.2	78.8	59.2	98.5	70.9	Average						
	% Elasticity	9.0	5.0	3.1	1.4	11.5	6.0 %						
Air Plane Behind Blocks	EXP (°C)	129.2	128.1	111.0	110.0	107.2	82.1	95.7	92.4	79.8			
	CFD (°C)	121.0	118.3	109.9	98.7	92.3	80.3	90.3	83.1	81.7	Average		
	% Elasticity	6.5	8.0	1.0	10.8	14.9	2.2	5.8	10.6	2.4	6.9 %		
Air Plane at Outlet	EXP (°C)	62.5	61.9	65.2	62.2	44.0	43.8	43.3	45.6	37.5	38.5	36.9	36.1	
	CFD (°C)	61.4	62.9	65.6	63.5	45.3	45.7	47.2	47.0	43.2	43.3	43.3	43.1	Average
	% Elasticity	1.8	1.6	0.6	2.0	2.9	4.4	8.7	3.0	14.2	11.8	15.9	17.7	7.0 %

Table 4.2 – Steady-state thermal results: comparison of experimental and CFD data (laminar flow regime).

Engine Front Surface	EXP (°C)	114.5	121.0	122.1	112.5	117.0	119.8	109.8	114.2	118.5			
	CFD (°C)	118.0	119.0	119.9	118.0	118.9	119.5	116.2	117.1	117.9	**Average**		
	% Elasticity	**3.0**	**1.7**	**1.8**	**4.8**	**1.6**	**0.2**	**5.7**	**2.5**	**0.5**	**2.4 %**		
Engine Top Surface	EXP (°C)	131.3	145.3	137.2	130.2	144.7	134.9	131.0	132.7				
	CFD (°C)	120.8	125.7	122.6	120.4	125.3	121.0	118.2	118.9	**Average**			
	% Elasticity	**8.3**	**14.5**	**11.2**	**7.8**	**14.3**	**10.8**	**10.3**	**11.0**	**11.0 %**			
Turbo Rear Surface	EXP (°C)	364.9	361.7	364.7	363.8	365.2	357.1	356.6					
	CFD (°C)	368.9	368.1	369.2	369.2	369.0	368.3	367.6	**Average**				
	% Elasticity	**1.1**	**1.8**	**1.2**	**1.5**	**1.0**	**3.1**	**3.0**	**1.8 %**				
Gearbox Front Surface	EXP (°C)	108.9	104.9	107.6	109.0	104.9							
	CFD (°C)	112.3	109.8	111.1	112.1	109.8	**Average**						
	% Elasticity	**3.1**	**4.6**	**3.2**	**2.8**	**4.6**	**3.7 %**						
Bonnet Top Surface	EXP (°C)	63.2	75.0	61.1	97.1	63.2							
	CFD (°C)	77.4	83.4	65.5	106.4	77.2	**Average**						
	% Elasticity	**20.2**	**10.6**	**7.0**	**9.1**	**19.9**	**13.4 %**						
Air Plane Behind Blocks	EXP (°C)	129.2	128.1	111.0	110.0	107.2	82.1	95.7	92.4	79.8			
	CFD (°C)	129.4	102.1	85.5	90.2	88.9	62.3	87.7	75.7	65.8	**Average**		
	% Elasticity	**0.2**	**22.6**	**25.9**	**19.8**	**18.7**	**27.4**	**8.7**	**19.9**	**19.2**	**18.0 %**		
Air Plane at Outlet	EXP (°C)	62.5	61.9	65.2	62.2	44.0	43.8	43.3	45.6	37.5	38.5	36.9	36.1
	CFD (°C)	58.8	58.6	60.8	60.9	39.0	38.8	41.9	39.4	37.6	38.1	37.2	36.7
	% Elasticity	**6.1**	**5.5**	**7.0**	**2.2**	**12.1**	**12.0**	**3.2**	**14.6**	**0.3**	**1.0**	**0.7**	**1.7**

Average 5.5 %

4.3.2 Solution with the Radiation Module and Turbulent Flow Regime

The results of the simulation incorporating the solution of radiation heat transfer are examined. The computation was carried out with the $k-\varepsilon$ turbulence model that previously demonstrated to provide better agreement with measurement when compared to assuming a laminar flow condition in the underhood.

Overall, it was noted the blocks were predicted to be at higher temperatures when solving radiation than when the heat flux approximations were incorporated. With respect to experiments, a generally over-prediction was also observed. Possible explanations are given in Section 4.5.1. The following sub-sections briefly describe the thermal results for the some of the planes previously analysed. A summary of the discrepancies between all the correlated data is given in Table 4.3 (page 151).

Front and Top Surfaces of Engine Block – The contour plots in Figure 4.12 shows that the simulated temperature distribution did not agree well with the measurements, with an over-prediction on average of 8°C (i.e. 6.5%) A larger miss-match in the temperature distribution when compared to the solution obtained by heat flux approximation (Figure 4.4) was seen.

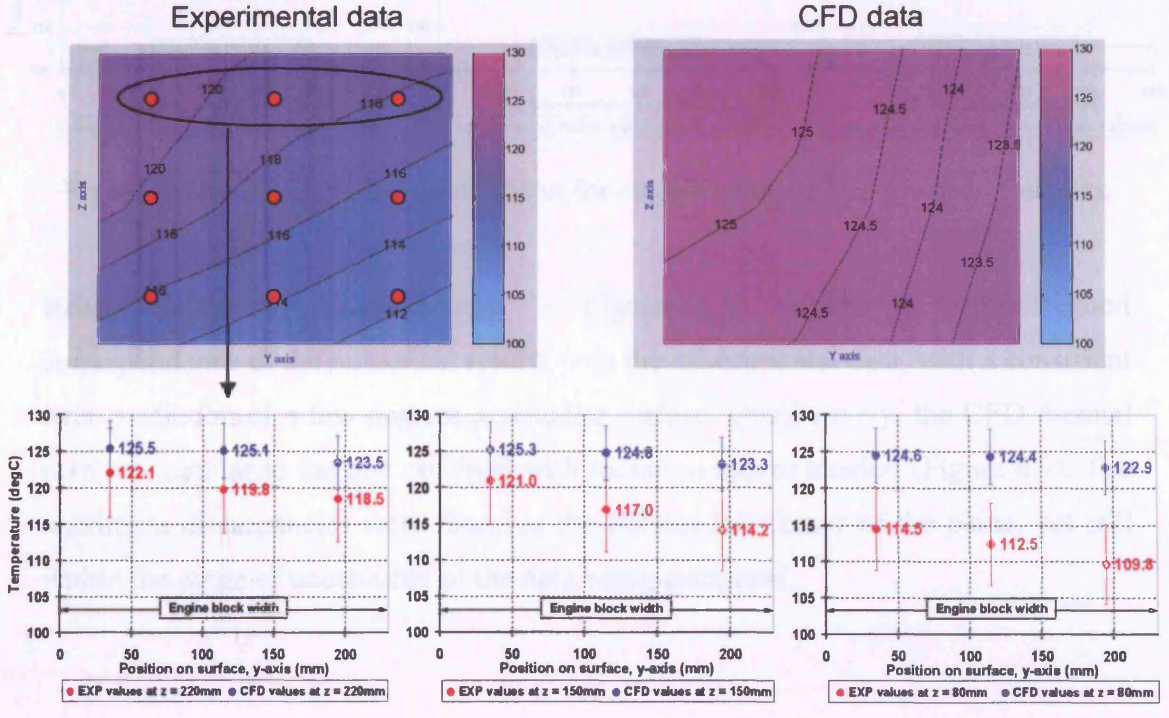

Figure 4.12 – Temperature comparison for engine's front surface (degrees Celsius).

The scatter chart of Figure 4.12 clearly shows that the predictions were outside the accuracy limits of the instrumentation at the lower region of the surface.

Similar quantitative discrepancies were observed for the top surface of the engine, Figure 4.13 and Table 4.3, albeit the qualitative agreement was superior.

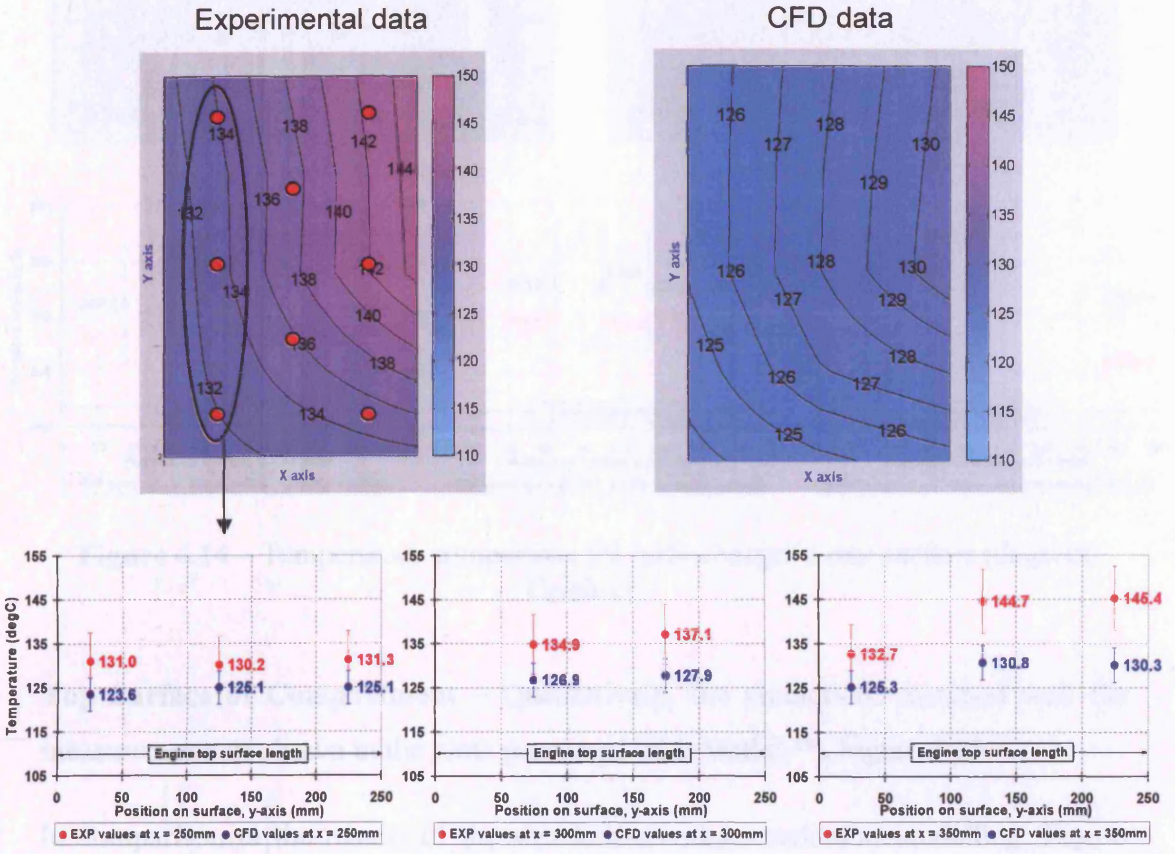

Figure 4.13 – Temperature comparison for engine's top surface (degrees Celsius).

Rear Surface of Turbocharger – Figure 4.14 depicts an overall good correspondence of the numerical results with the experimental data, with a consistent over-prediction of a few degrees across the surface. Qualitatively, the CFD thermal map was similar to the one obtained with radiation approximation (Figure 4.7). The maximum discrepancies were found at the bottom left corner of the plane, yet still within the range of uncertainty of the data being compared.

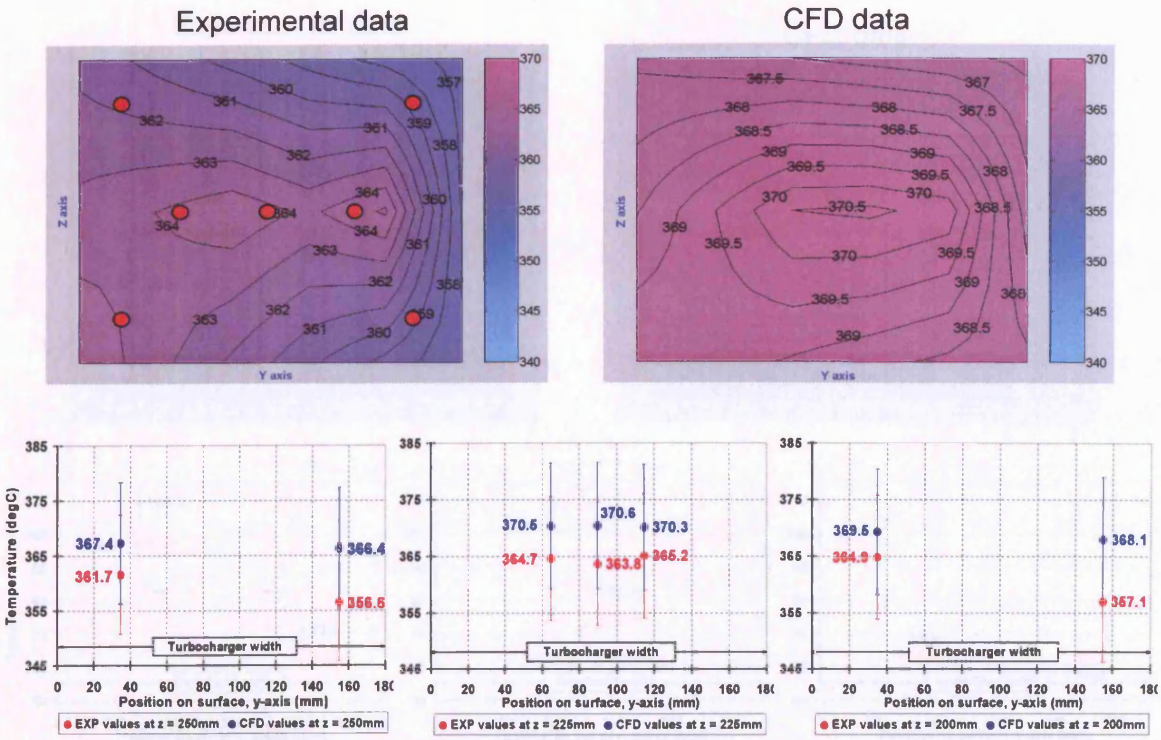

Figure 4.14 – Temperature comparison for turbocharger's rear surface (degrees Celsius).

Top Surface of Compartment – Qualitatively, the predictions matched well the measurements as shown in the plots processed with Matlab™, Figure 4.15.

In comparison to the results of the simulation without radiation modelling (Figure 4.8), the surface temperature was estimated to be higher, with the only exception at bottom left corner. The temperature was over-predicted by an average of almost 8% when compared to the measured value, as it can be inferred by comparing Tables 4.1 with Table 4.3.

The discrepancy was reasonably expected since the heat flux approximation method could not model the heat radiated by the blocks and absorbed by the glass, which as shown in Figure 4.16, was fully estimated with the radiation module.

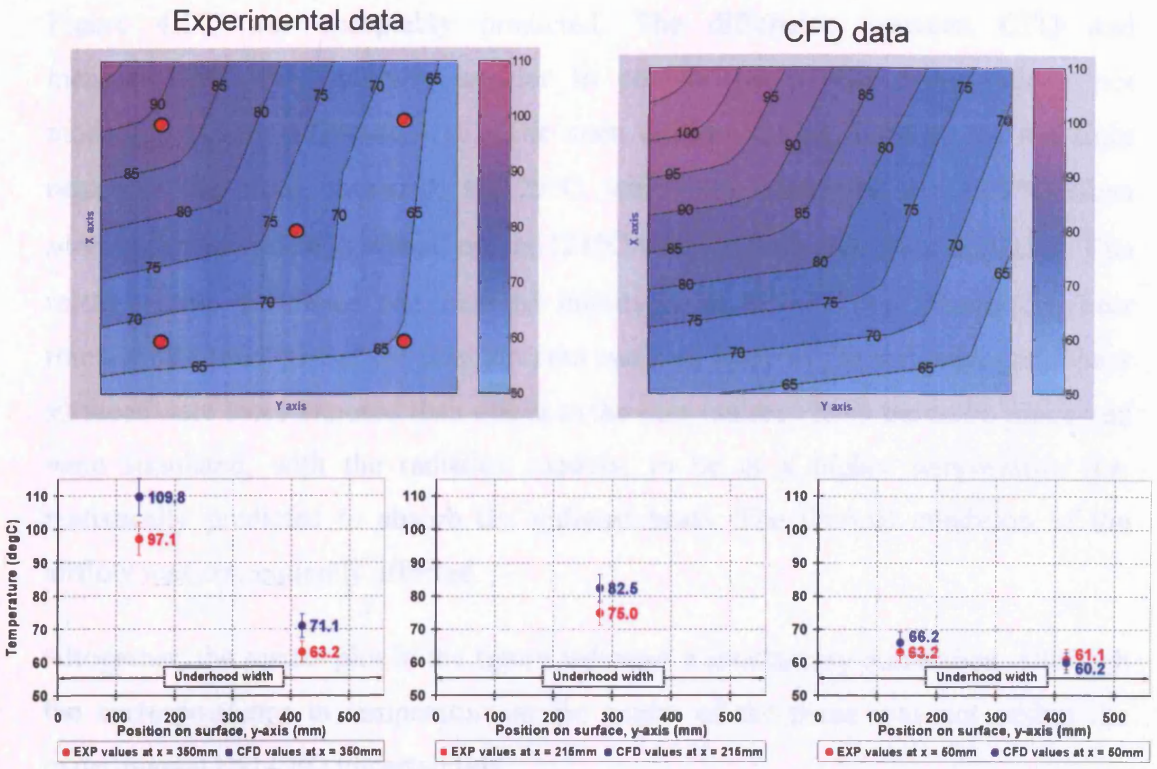

Figure 4.15 – Temperature comparison for outer bonnet's surface (degrees Celsius).

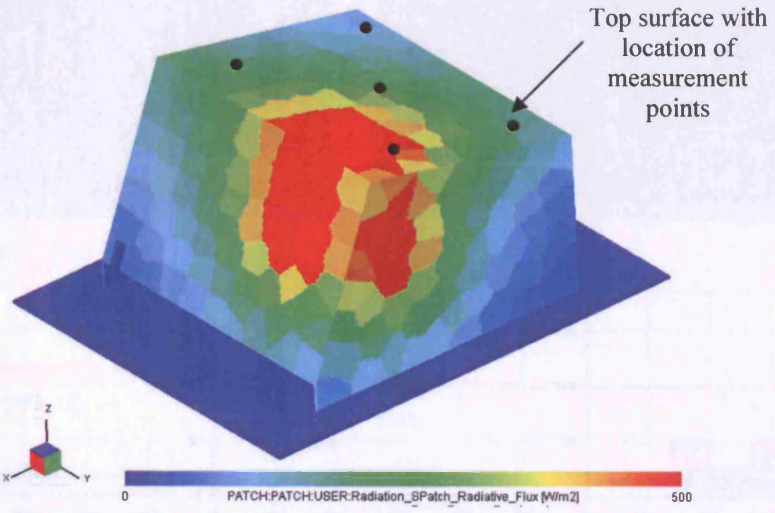

Figure 4.16 – Simulated radiation heat flux on top compartment boundaries (rear view of the underhood model).

Air Planes behind Blocks – Qualitatively, the overall temperature distribution, Figure 4.17, was acceptably predicted. The difference between CFD and measurements was generally smaller in comparison to the computations not modelling radiation (Figure 4.10). The main difference was found at the top right region of the plane, measured at 129°C, which was simulated at 131.7°C when solving for the radiation effects and at 121°C with the heat flux approximation. The relative large difference was deemed imputable to the different convective heat transfer rate predicted at the compartment walls in front of the turbocharger. These surfaces were more exposed than others to the heat radiated from the turbo block and were simulated, with the radiation module, to be at a higher temperature (i.e. realistically predicted to absorb the radiated heat). The thermal condition of the airflow was consequently affected.

Altogether, the scatter plot in the figure indicates a satisfactory correlation, although the correspondence in temperature at the centre of the plane was not within the experimental and CFD uncertainties.

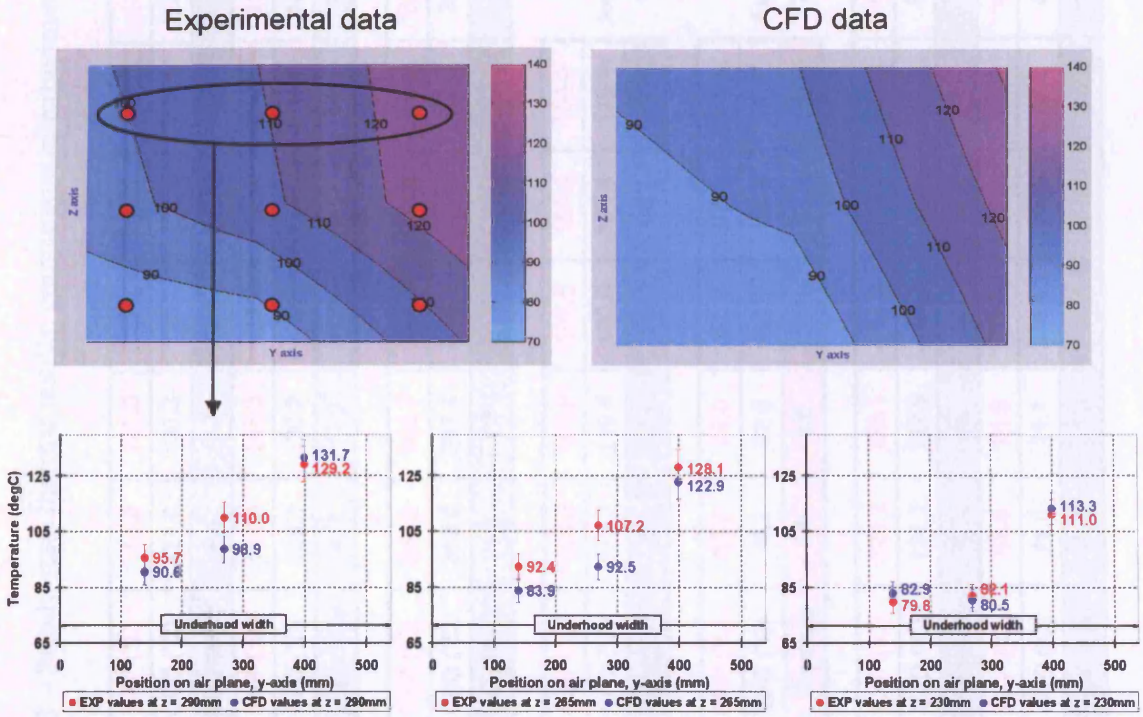

Figure 4.17 – Data comparison for the air plane behind blocks (degrees Celsius).

Table 4.3 – Steady-state thermal results: comparison of experimental and CFD data (radiation fully modelled and turbulent flow).

Engine Front Surface	EXP (°C)	114.5	121.0	122.1	112.5	117.0	119.8	109.8	114.2	118.5			
	CFD (°C)	124.6	125.3	125.1	124.4	124.8	125.1	122.9	123.3	123.5	Average		
	% Elasticity	8.4	3.5	2.4	10.1	6.5	4.4	11.3	7.6	4.1	6.5 %		
Engine Top Surface	EXP (°C)	131.3	145.3	137.2	130.2	144.7	134.9	131.0	132.7				
	CFD (°C)	125.1	130.3	127.9	125.1	130.8	126.9	123.6	125.3	Average			
	% Elasticity	4.8	10.9	7.0	4.0	10.1	6.1	5.8	5.8	6.8 %			
Turbo Rear Surface	EXP (°C)	364.9	361.7	364.7	363.8	365.2	357.1	356.6					
	CFD (°C)	369.5	367.4	370.5	370.6	370.3	368.1	366.4	Average				
	% Elasticity	1.2	1.6	1.6	1.9	1.4	3.0	2.7	1.9 %				
Gearbox Front Surface	EXP (°C)	108.9	104.9	107.6	109.0	104.9							
	CFD (°C)	121.7	119.5	120.0	121.8	119.4	Average						
	% Elasticity	11.1	13.0	10.9	11.1	13.0	11.8 %						
Bonnet Top Surface	EXP (°C)	63.2	75.0	61.1	97.1	63.2							
	CFD (°C)	66.2	82.5	60.2	109.8	71.1	Average						
	% Elasticity	4.6	9.6	1.4	12.3	11.7	7.9 %						
Air Plane Behind Blocks	EXP (°C)	129.2	128.1	111.0	110.0	107.2	82.1	95.7	92.4	79.8			
	CFD (°C)	131.7	122.9	113.3	98.9	92.5	80.5	90.6	83.9	82.9	Average		
	% Elasticity	1.9	4.2	2.1	10.6	14.7	2.0	5.5	9.7	3.8	6.1 %		
Air Plane at Outlet	EXP (°C)	62.5	61.9	65.2	62.2	44.0	43.8	43.3	45.6	37.5	38.5	36.9	36.1
	CFD (°C)	71.0	71.1	74.4	77.6	49.1	49.6	55.7	55.9	46.5	46.7	46.7	46.4
	% Elasticity	12.7	13.8	13.2	22.0	10.9	12.5	25.1	20.3	21.5	19.3	23.4	25.0

Average 18.3 %

4.4 PIV MEASUREMENTS VS. VECTIS PREDICTIONS

VECTIS's ability in predicting the airflow patterns was assessed by comparing graphically and quantitatively the computed and measured flow vectors and mean velocities in representative 2-D regions (x-z and y-z planes) within the underhood volume. The areas were chosen near the heated blocks, at the top of the compartment and at the outlet slot (locations shown in Figure D7 in Appendix D). The investigated flow fields were particularly challenging for the computational predictions because characterised, respectively, by relatively strong convective forces, separation and re-circulation, and interaction with the still ambient air.

The quantitative information on the minimum, maximum and average air velocities was extracted from the simulation. The discrepancy between the two sets of data was evaluated by calculating both the percentage *Arc Elasticity* (Equation 4.1) and the percentage *CFD-relative discrepancy* (Equation 4.2). The CFD-relative discrepancy gave a measure of the percentage "change" between the experimental and simulated vectors with reference to the CFD results.

$$CFD_{Relative\ Discrepancy} = \left(\frac{q_{CFD} - q_{EXP}}{q_{EXP}} \right) \times 100 \qquad (4.2)$$

where q is the discrete value being compared.

As discussed in Chapter 2, for a meaningful comparison with the CFD data, the PIV observations were repeated numerous times in order to obtain a mean flow representation less susceptible to measurement errors and to the shot-to-shot flow variations. An example of the flow pattern variations that affected the measurements is given in Figure 4.18, which displays velocimetry images taken in successive 1-second intervals near the top corner of the turbocharger.

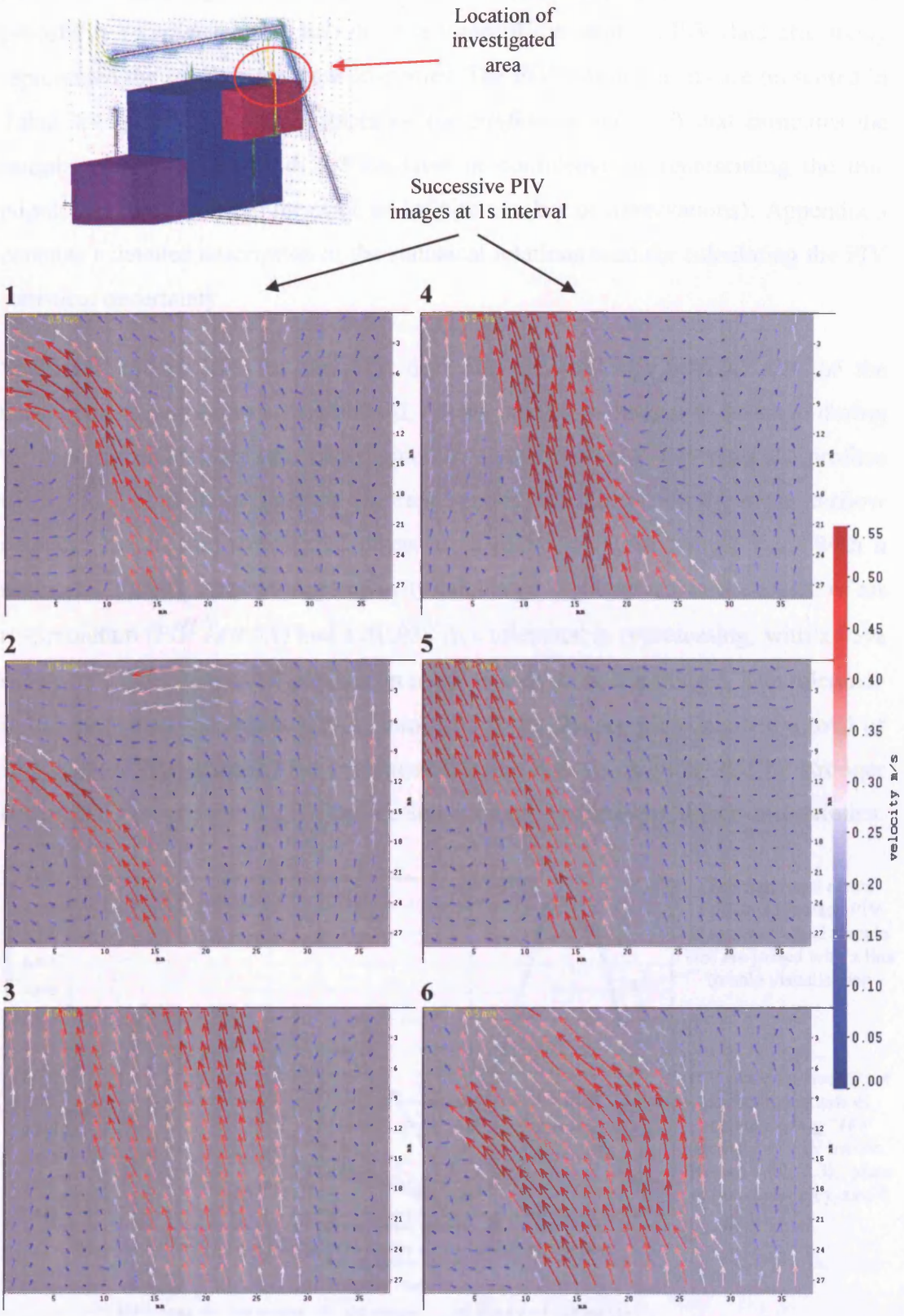

Figure 4.18 – PIV images recorded in succession over turbocharger's side surface (shot-to-shot flow variation).

Statistical sampling theory [Sampath 2001] was employed to determine the probability (*confidence interval*) that the mean of the sampled PIV data effectively represented the steady-state flow properties. The PIV measurements are presented in Table 4.4 (page 167) with a tolerance (or *confidence interval*) that estimates the sample mean precision with a 95% level of confidence of representing the true population mean (i.e. the mean of an infinite number of observations). Appendix J contains a detailed description of the statistical relations used for calculating the PIV statistical uncertainty.

Statistical manipulation of the PIV data also allowed the optimal size of the measurement samples to be established, i.e. the number of images to be taken during the experimental analysis per investigated flow region. Figure 4.19 plots the profiles of the PIV confidence interval (in representing the actual steady mean airflow velocity) for all the investigated planes as a function of the sample size. With a sample of 20 images the average velocity calculated, for instance, in the region of air re-circulation (*PIV Test 5X*) had a ±0.032 m/s tolerance in representing, with a 95% confidence level, the actual population mean (steady flow conditions). The tolerance in the measurements reduced by a factor of 3 when the sample contained a total of 120 images. The analysis also evidenced that the regions characterised by stronger convective flow motion (higher fluid velocity) were subjected to higher uncertainties.

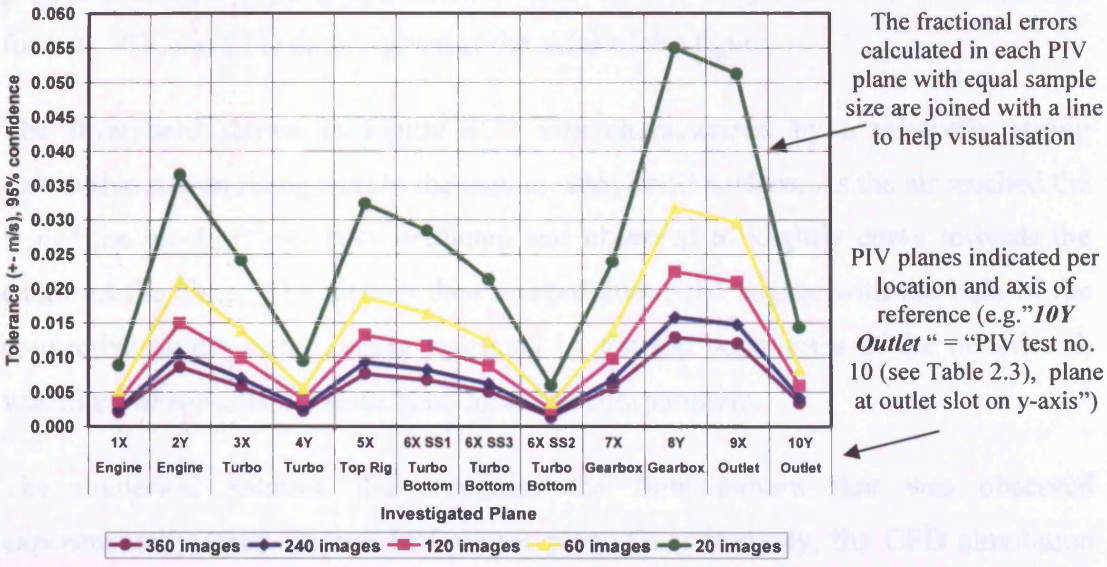

Figure 4.19 – Tolerance in estimating the steady-state mean flow velocity magnitude (population mean) for different PIV sample sizes.

From the application of the statistical sampling theory, it was established that samples of 240 images represented the best compromise when weighting the level of confidence established against the experimental effort required. The PIV recordings were therefore repeated 240 times when investigating each flow region for an effective comparison with CFD.

In the following sub-sections, the simulations carried out with reduced heat fluxes and by fully solving radiation heat transfer are examined separately (Sections 4.4.1 and 4.4.2). The flow regions that were found to be more difficult to correlate qualitatively due to a low CFD vector resolution were compared based on a simulation with a denser air domain mesh (1.2 million cells). The vector plots obtained from the computation with the denser grid were only used to aid the visualisation of the differences between measured and predicted results; no quantitative information was extracted and compared.

4.4.1 Solution with the Heat Flux Approximation and Turbulent Flow Regime

Airflow above Engine – The airflow above the engine block is displayed in Figures 4.20 and 4.21, for two perpendicular planes respectively parallel to the x- and y-axis. Both figures depict the vectors processed with PIV (grey framed) inset beside the corresponding flow area simulated with VECTIS (boxed area). The vectors were plotted with their length proportional to their velocity magnitude. The velocity scale for both PIV and CFD data is given at the sides of the figure.

The flow field shown in Figure 4.20 was characterised by a relatively strong convective stream rising next to the engine side (front) surface. As the air reached the top of the block, it was both predicted and observed to slightly curve towards the centre of the block. The airflow then merged above the engine with the bulk of the convective plume which, being restricted by the top boundaries of the underhood, was directed towards the front opening of the compartment.

The numerical solution did recognise the flow pattern that was observed experimentally (grey framed PIV vector plot). Quantitatively, the CFD simulation slightly under-predicted the average velocity by 0.0067 m/s; the corresponding percentage discrepancy (arc elasticity) was 5.3%, as given in Table 4.5.

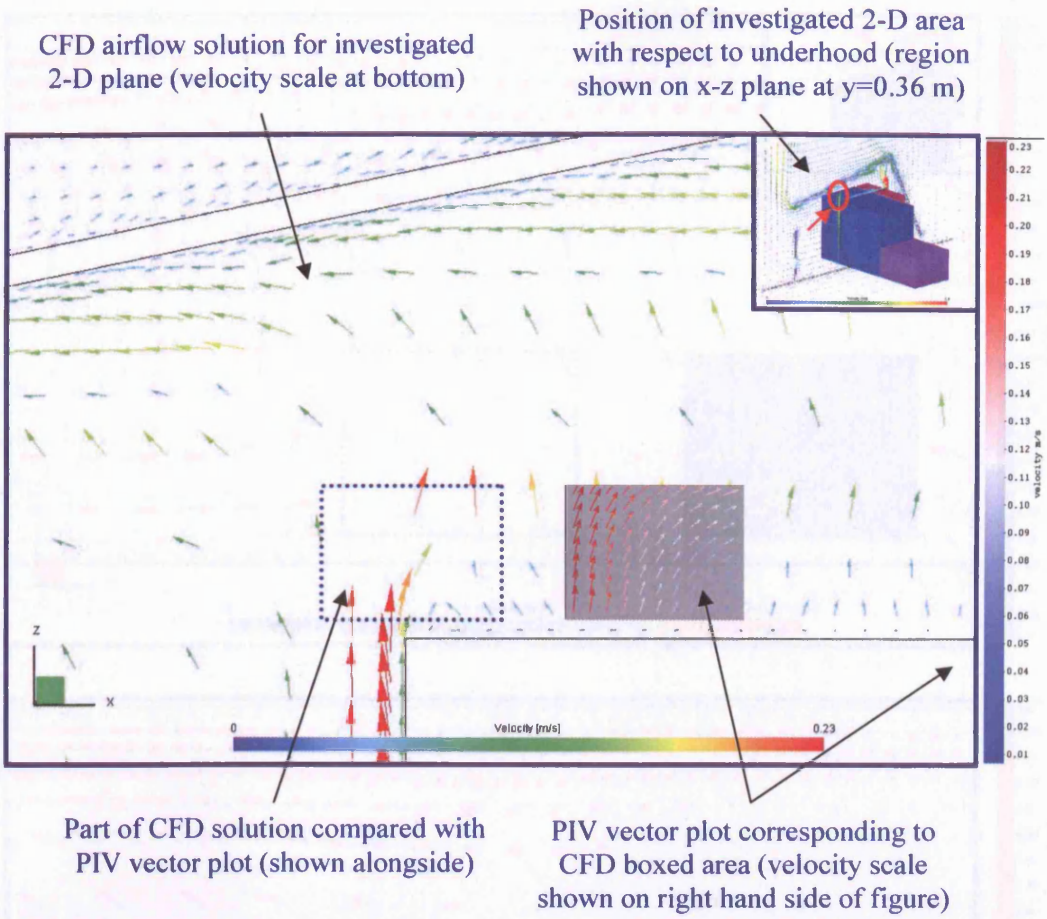

Figure 4.20 – CFD airflow predictions compared to PIV measurements above engine block (low CFD grid resolution); Flow region *1X* (y = 0.36 m).

Figure 4.21 compares the flow patterns in the middle region above the top surface of the engine (x = 0.28 m plane). The CFD simulation showed that the flow near the surface converged inward from the sides of the block before merging in the middle and rising to the compartment's upper boundary; the PIV image confirmed the simulated flow pattern. The qualitative correlation is better visualised when comparing the PIV data with the CFD solution based on the denser grid, as shown at the bottom of the figure.

The CFD discrepancy in predicting the average magnitude of the flow velocity in the region was approximately +25%. This arguably represents an acceptable discrepancy considering the very low velocity of the flow. The average difference between the two data sets was only 0.015 m/s in absolute terms.

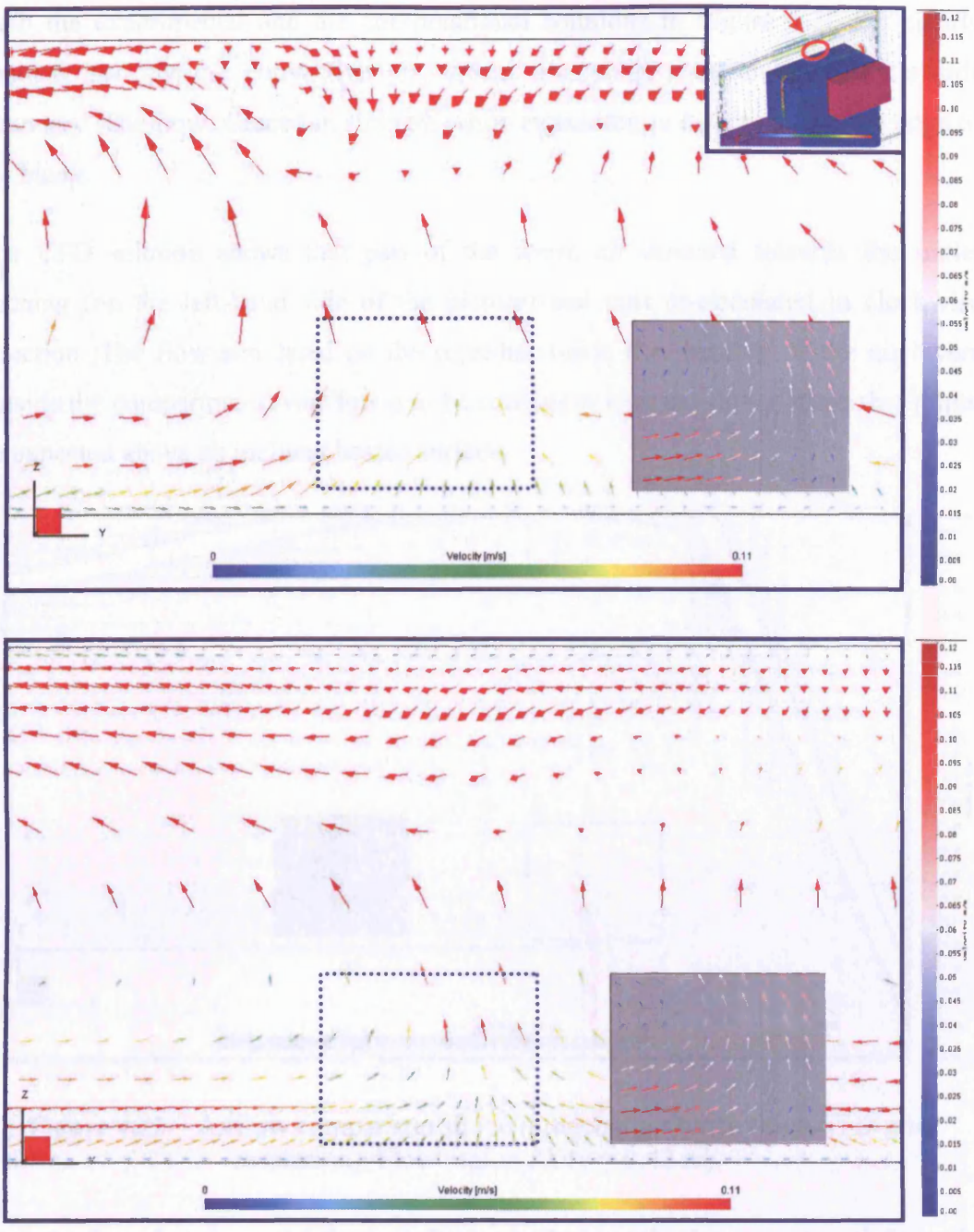

Figure 4.21 – Airflow comparison above engine block with lower (top) and higher (bottom) CFD air domain grid resolution; Flow region *2Y* (x = 0.28 m).

Airflow above Turbocharger – The flow structure in the near-region of the turbocharger was investigated in an x-z plane next to the upper edge of the block (Figure 4.22 displays the CFD simulations with a high grid density) and in a y-z plane above the block and along its length (Figure 4.23).

Both the experimental and the computational solutions in Figure 4.22 are clearly characterised by the convective air stream ascending next to the block's side boundary. The flow reduced in strength while expanding in direction past the edge of the block.

The CFD solution shows that part of the warm air directed towards the outlet opening (on the left-hand side of the picture) and part re-circulated in clockwise direction. The flow simulated on the right-hand-side (i.e. heating of the air layers outside the compartment) was found to be consistent with the flow pattern that might be expected above an inclined heated surface.

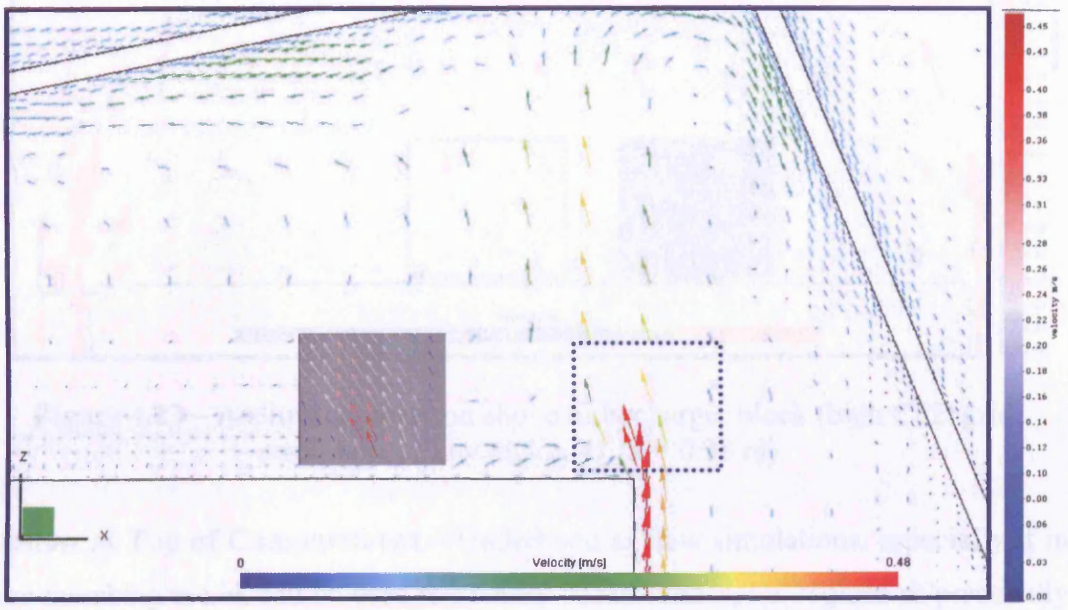

Figure 4.22 – Airflow comparison above turbocharger block (high CFD grid resolution); Flow region *3X* (y = 0.42 m).

Both the flow directions and the magnitudes in the examined area were satisfactorily predicted. The mean velocity was over-estimated by 0.028 m/s which was within the overall uncertainty associated with the PIV image scale setting (3.65%, as given in Chapter 2) and the 95% confidence in representing the actual steady mean velocity (i.e. ±0.011 m/s). The relatively high statistical uncertainty was owed to the strong fluctuations defining the convective flow, as shown in Figure 4.18.

In the y-z plane, Figure 4.23, similar flow discrepancies were determined (15%). Despite only a limited number of vectors were obtained when post-processing the

numerical solution (also from the solution with higher grid resolution), a satisfactory correspondence could be observed on qualitative terms between the two data sets. The CFD simulation gave however slightly larger horizontal velocity components, especially in the upper half of the investigated region.

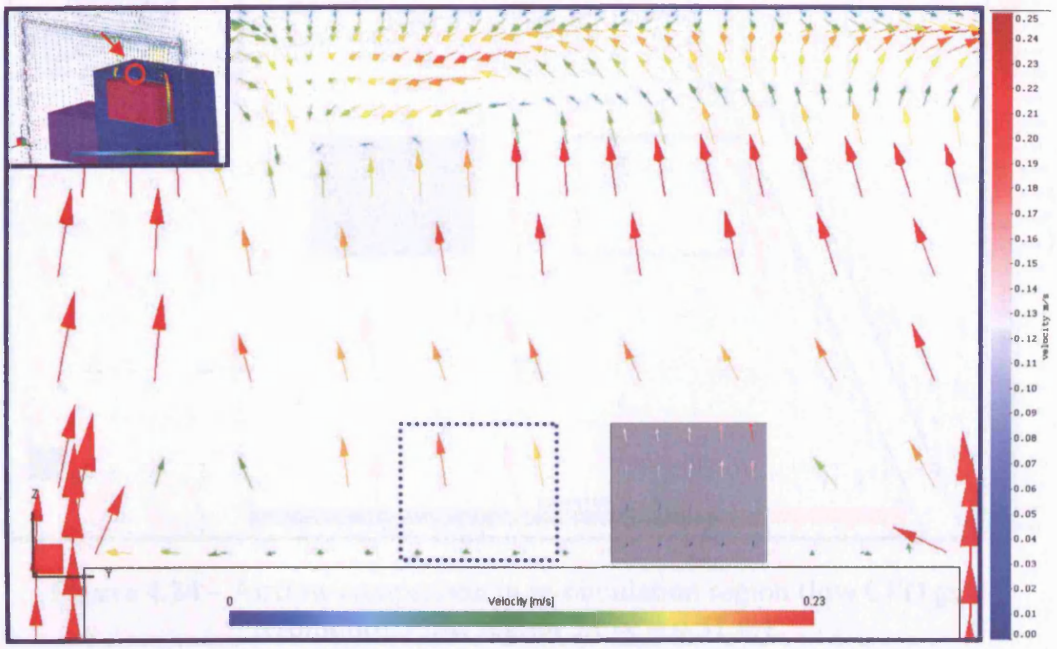

Figure 4.23 – Airflow comparison above turbocharger block (high CFD grid resolution); Flow region *4Y* (x = 0.38 m).

Airflow at Top of Compartment – Underhood airflow simulations, especially if in time-marching mode, can be used to identify "dead" zones, i.e. regions of practically quiescent flow, and zones of air re-circulation. Re-circulating airflow patterns are quite common for engine-bays under heat soak because the buoyant flow is easily affected in direction by the geometry of the compartment and by the component-packaging configuration. Re-circulating hot air is undesirable from a thermal management point of view as it tends to increases the average temperature of the underhood, potentially reducing both the convective heat transfer (heat rejection) from solid bodies and the mass flow rate discharging to ambient.

The flow regions above the engine and the turbocharger, expected to be characterised by air-circulation regimes, were studied in *Test 5X* as part of the PIV investigations (Chapter 2, Table 2.3). As demonstrated by previous studies on different applications

[Lee 1997, Leschziner 1990], it is the validity of the turbulence model that plays a fundamental role on the quality of the CFD predictions for such flow structures.

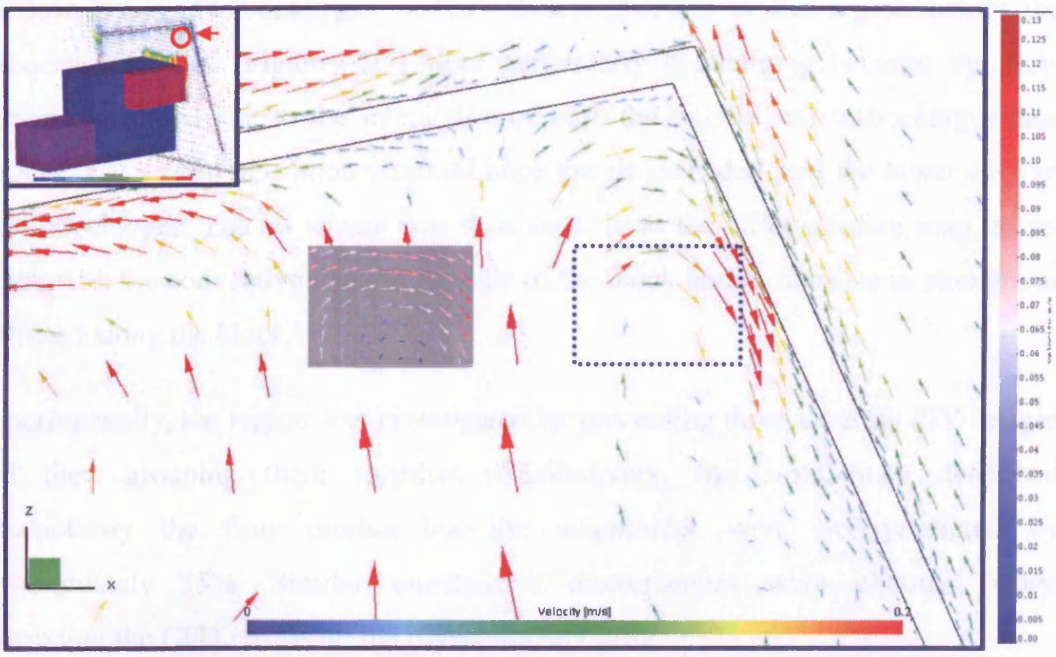

Figure 4.24 – Airflow comparison in re-circulation region (low CFD grid resolution); Flow region *5X* (y = 0.51 m).

The plot shown in Figure 4.24 indicates that the characteristics of the re-circulating buoyant airflow near the compartment's ceiling were satisfactorily predicted. However, a closer examination of the quantitative data revealed a discrepancy between the CFD and PIV mean velocities of approximately 41% (percentage arc elasticity). The difference could be caused by an over-estimation of the dissipation of the turbulent kinetic energy, ε, in the re-circulating vortex. The standard $k-\varepsilon$ turbulence model could in fact produce relatively low values of turbulent kinetic energy, leading to a reduced eddy viscosity and smaller mixing effect (i.e. higher flow velocities) within the re-circulating flow. A similar numerical behaviour was observed by Murakami *et al.* [1992] when comparing a re-circulating flow simulated with the $k-\varepsilon$ model within a building environment with wind-tunnel test data.

Apart from the effectiveness of the numerical treatment of turbulence, the calculated discrepancy could also be in part related to the general temperature over-prediction of the glass boundaries, as determined during the thermal analysis. Since the walls of

the enclosure were simulated at a higher temperature than measured, the coupled flow field would be quite expectably over-predicted in temperature and velocity.

Airflow below Turbocharger – The flow predictions in the region below the turbocharger block (Figure 4.25) were particularly challenging because the flow pattern developed due to the interaction of both the engine and turbocharger heat sources, and a flow separation occurred once the air ascended past the lower edge of the turbocharger. The air stream was then seen, from the CFD solution map, to re-attach with the convective layer at the side of the block and to increase in strength as it flowed along the block.

Experimentally, the region was investigated by processing three separate PIV images and then grouping them together. Qualitatively, the simulations described satisfactorily the flow motion but the magnitudes were over-predicted by approximately 35%. Similar quantitative discrepancies were obtained when processing the CFD results on the higher density grid.

The discrepancy was unquestionably owed to the well-acknowledged weakness of the Law of the Wall turbulence treatment in accurately resolve boundary layer flows in unstable regimes [Gatski *et al.* 1996] and in solving flows associated with separation [Loomans 1998]. The restricted validity of the wall functions originates from the assumptions made in their derivation, as further discussed in Section 4.5.2.

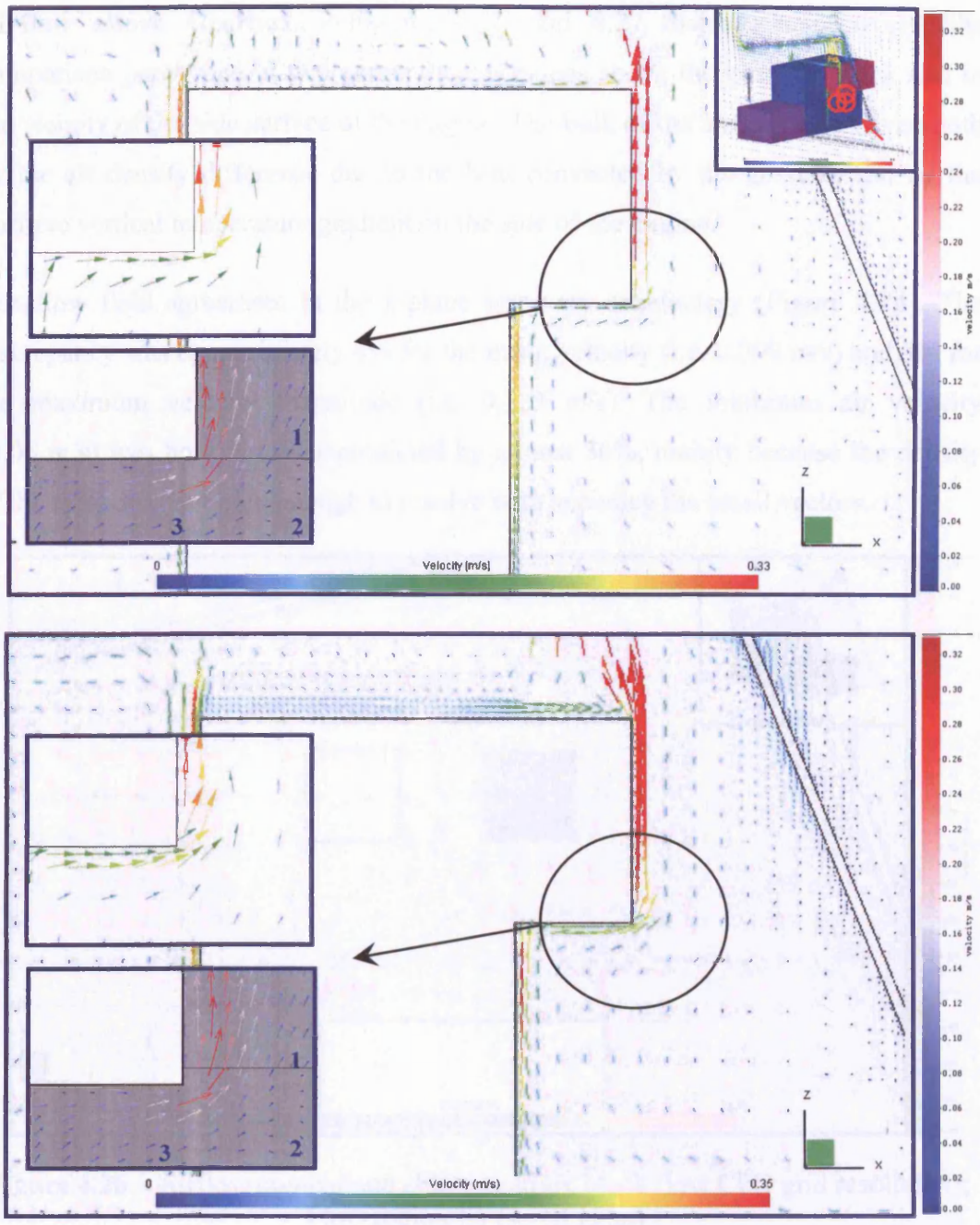

Figure 4.25 – Airflow comparison below turbocharger block with lower (top) and higher (bottom) CFD air domain grid resolutions; Flow region *6X* (y = 0.18m).

Alternative methods for the numerical solution of the near-wall flow field could not unfortunately be tested in this work, since VECTIS did not provide with any choice of alternative formulations. The simulation would however be expected to improve with a more accurate numerical representation of the viscous sub-layer, for instance using Reynolds stress turbulence models, which explicitly solve the transport equations at the wall.

Airflow above Gearbox – Figures 4.26 and 4.27 display, respectively, the comparison performed in two perpendicular planes above the gearbox block and in the vicinity of the side surface of the engine. The bulk of the airflow was driven both by the air density difference due to the heat convected by the gearbox and by the positive vertical temperature gradient on the side of the engine.

The flow field agreement in the x-plane was very satisfactory (Figure 4.26). The discrepancy was approximately 4% for the mean velocity (i.e. 0.099 m/s) and 3% for the maximum velocity magnitude (i.e. 0.122 m/s). The minimum air velocity (0.06 m/s) was however over-predicted by almost 36%, mainly because the density of the mesh was not high enough to resolve with accuracy the small vectors.

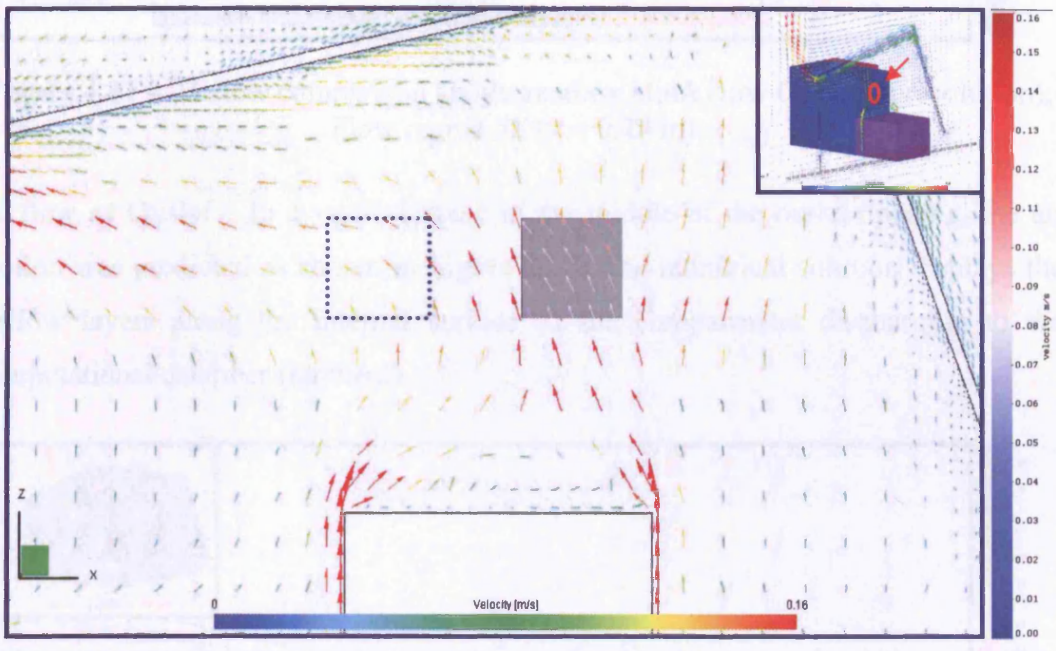

Figure 4.26 – Airflow comparison above gearbox block (low CFD grid resolution); Flow region *7X* (y = 0.18 m).

The flow patterns shown in Figure 4.27 had a disagreement in velocity of 28%. Both the flow direction, parallel to the surface of the engine, and the gradual velocity reduction away from the surface are however very similarly depicted in the two vector plots.

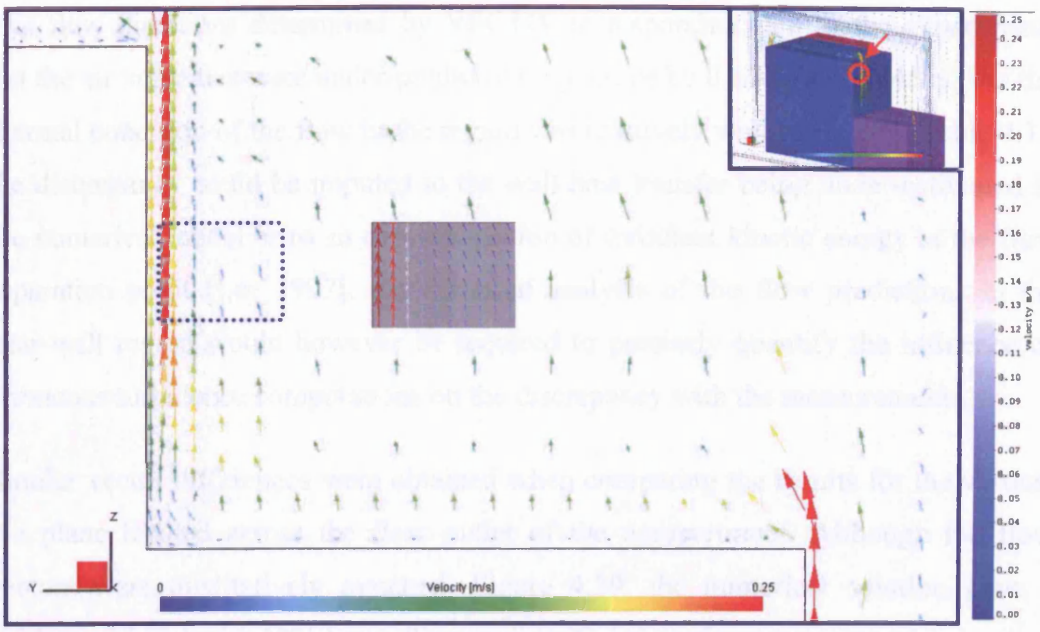

Figure 4.27 – Airflow comparison above gearbox block (low CFD grid resolution); Flow region *8Y* (x = 0.24 m).

Airflow at Outlet – In a vertical plane in the middle of the outlet opening, the air motion was predicted as shown in Figure 4.28. The numerical solution displays the airflow layers along the internal surface of the compartment discharging to the computational chamber (ambient).

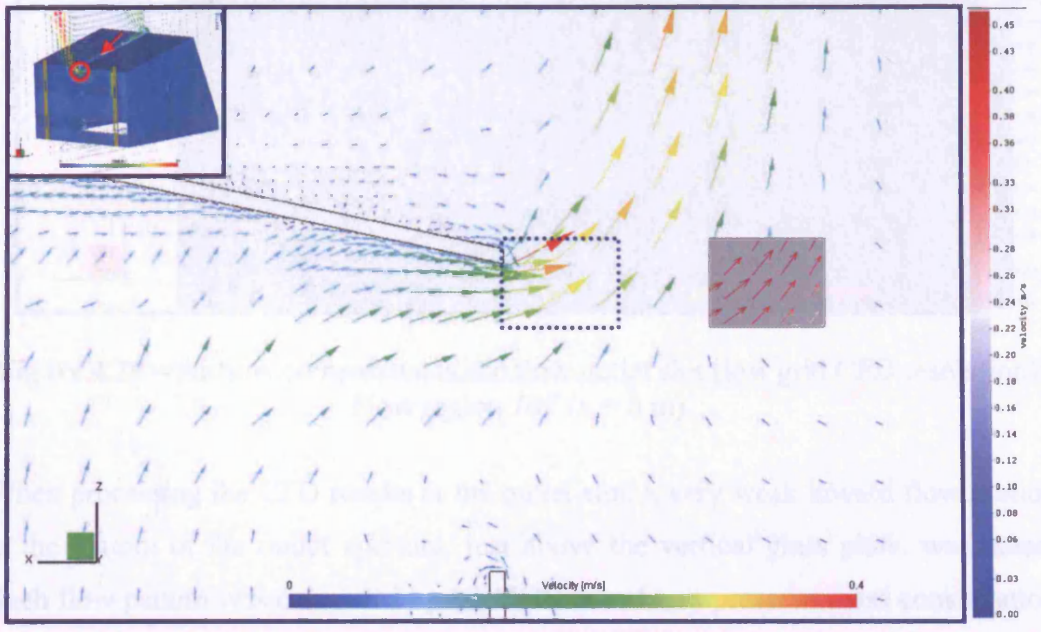

Figure 4.28 – Airflow comparison at the flow outlet slot (low CFD grid resolution); Flow region *9X* (y = 0.28 m).

The flow directions determined by VECTIS corresponded well to the experiments but the air velocities were under-predicted on average by 0.17 m/s (i.e. -45%). As the thermal condition of the flow in the region was relatively well simulated (Table 4.1), the discrepancy could be imputed to the wall heat transfer being under-estimated in the numerical model or to an over-estimation of turbulent kinetic energy at the flow separation point [Lee 1997]. An extended analysis of the flow predictions in the near-wall region would however be required to precisely quantify the influence of erroneous turbulence computations on the discrepancy with the measurements.

Similar vector differences were obtained when comparing the results for the vertical y-z plane located across the flow outlet of the compartment. Although the flow vectors were qualitatively matched, Figure 4.29, the numerical solution gave a discharge air velocity 32% lower than measured.

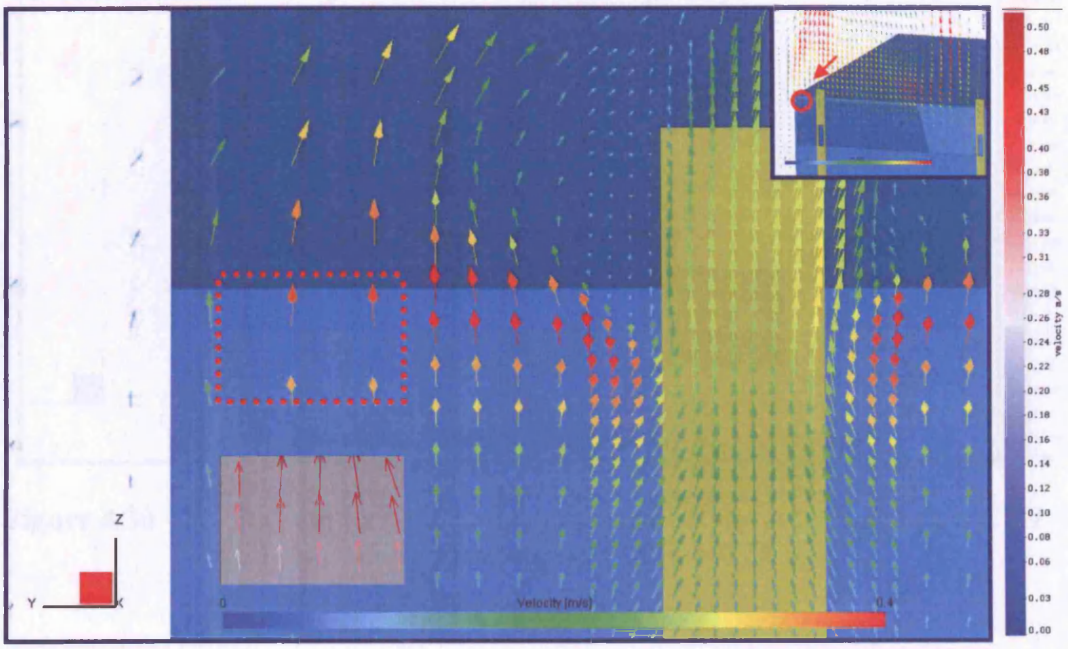

Figure 4.29 – Airflow comparison at the flow outlet slot (low grid CFD resolution); Flow region *10Y* (x = 0 m).

When processing the CFD results at the outlet slot, a very weak inward flow motion at the bottom of the outlet aperture, just above the vertical glass plate, was noted. Such flow pattern was computed by VECTIS in order to preserve mass conservation within the underhood volume. The same location was investigated with PIV to assess the correctness of the computational flow field predictions.

Figure 4.30 shows the PIV results alongside the CFD simulations. The measurements did confirm the inward motion of the flow. Slightly different vector directions were however observed and the mean air velocity was largely under-predicted. The air velocities in the area were very low (the maximum recorded value was of 0.068 m/s) and the PIV measurements would be particularly affected by the limitations of the experimental apparatus. It should indeed be recognised that at such low air speeds, the oil droplets transported by the flow would be at a velocity close to their terminal value, and therefore the expected incidence of systematic errors in the measurements was higher.

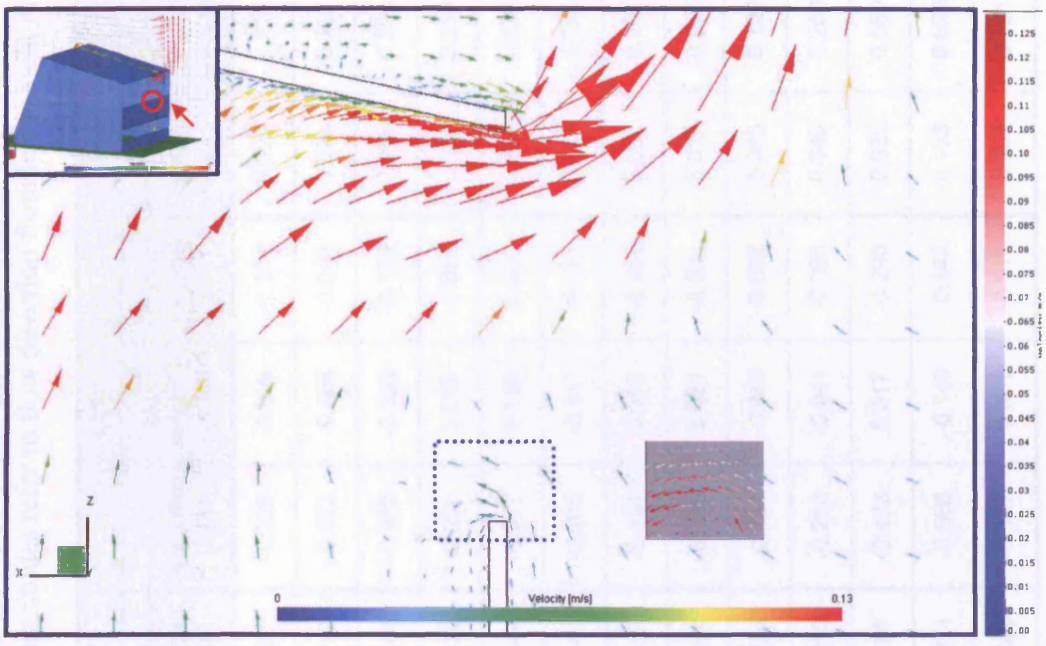

Figure 4.30 – Airflow comparison at the bottom of the flow outlet slot (low CFD grid resolution); Flow region *11X* (y = 0.28 m).

Table 4.4 – PIV vector data and statistical uncertainty.
(Positive velocity magnitudes refer to flow direction from left to right in vector plots)

INVESTIGATED PLANE		Vx			Vy			IVI					
		Min velocity (m/s)	Max velocity (m/s)	Average velocity (m/s)	Min velocity (m/s)	Max velocity (m/s)	Average velocity (m/s)	Min velocity (m/s)	Max velocity (m/s)	Average velocity (m/s)	Std Dev. (±)	Sample size, *n*	95% conf. interval (± m/s)
Above Engine	1X	0.020	0.129	0.067	-0.209	-0.029	-0.104	0.029	0.218	0.130	0.040	240	0.005
Above Engine	2Y	-0.045	0.106	0.017	-0.072	-0.008	-0.040	0.023	0.107	0.060	0.020	240	0.003
Above Turbo	3X	-0.189	0.026	-0.108	-0.360	-0.023	-0.178	0.055	0.395	0.210	0.084	240	0.011
Above Turbo	4Y	-0.035	0.041	0.009	-0.208	0.015	-0.092	0.052	0.219	0.097	0.055	240	0.007
Top of Compartment	5X	-0.018	0.089	0.044	-0.077	0.110	0.004	0.038	0.121	0.067	0.022	240	0.003
Below Turbo	6X SS1	-0.017	0.192	0.042	-0.295	-0.017	-0.141	0.044	0.304	0.152	0.074	240	0.009
Below Turbo	6X SS2	0.000	0.268	0.080	-0.131	0.010	-0.031	0.052	0.287	0.088	0.049	240	0.006
Below Turbo	6X SS3	-0.001	0.255	0.045	-0.295	0.031	-0.023	0.017	0.216	0.063	0.065	240	0.008
Above Gearbox	7X	-0.088	-0.022	-0.054	-0.102	-0.056	-0.082	0.060	0.122	0.099	0.014	360	0.001
Above Gearbox	8Y	-0.024	0.011	-0.013	-0.260	-0.041	-0.098	0.046	0.260	0.099	0.055	240	0.007
Outlet Window	9X	0.038	0.452	0.224	-0.473	0.017	-0.290	0.039	0.559	0.368	0.126	240	0.016
Outlet Window	10Y	-0.158	0.066	-0.031	-0.668	-0.148	-0.442	0.153	0.629	0.446	0.117	240	0.015
Bottom Outlet Window	11X	-0.134	0.015	-0.065	-0.127	0.071	-0.011	0.004	0.121	0.074	0.033	240	0.004

Table 4.5 – CFD predictions for simulation with heat flux approximation and quantitative data comparison.

INVESTIGATED PLANE		CFD PREDICTION (m/s)				ABS. DIFFERENCE (m/s)			CFD DISCREPANCY (%)			ARC ELASTICITY (%)		
		Min velocity	Max velocity	Avg velocity	Std Dev. (±)	IVI min	IVI max	IVI avg	IVI min	IVI max	IVI avg	IVI min	IVI max	IVI avg
Above Engine	1X	0.032	0.215	0.123	0.029	3.1E-03	-2.8E-03	-6.7E-03	10.54	-1.29	-5.14	10.01	1.29	5.27
Above Engine	2Y	0.029	0.133	0.075	0.022	6.1E-03	2.6E-02	1.5E-02	26.64	24.05	24.84	23.51	21.46	22.10
Above Turbo	3X	0.080	0.396	0.238	0.053	2.5E-02	1.4E-03	2.8E-02	45.22	0.35	13.17	36.88	0.35	12.36
Above Turbo	4Y	0.038	0.208	0.113	0.028	-1.4E-02	-1.1E-02	1.6E-02	-26.29	-4.92	16.10	30.26	5.05	14.90
Top of Compartment	5X	0.052	0.167	0.102	0.024	1.4E-02	4.6E-02	3.5E-02	38.04	37.54	51.89	31.96	31.60	41.20
Below Turbo	6X SS1	0.056	0.242	0.108	0.054	1.2E-02	-6.2E-02	-4.4E-02	26.56	-20.29	-28.85	23.45	22.58	33.72
Below Turbo	6X SS2	0.069	0.208	0.124	0.048	1.7E-02	-7.9E-02	3.6E-02	33.05	-27.53	40.94	28.36	31.92	33.99
Below Turbo	6X SS3	0.013	0.185	0.098	0.049	-4.0E-03	-3.1E-02	3.5E-02	-23.48	-14.47	54.36	26.61	15.60	42.74
Above Gearbox	7X	0.082	0.126	0.103	0.025	2.2E-02	3.5E-03	3.9E-03	35.88	2.88	3.96	30.42	2.84	3.89
Above Gearbox	8Y	0.062	0.277	0.132	0.033	1.6E-02	1.7E-02	3.3E-02	33.61	6.58	32.90	28.78	6.37	28.26
Outlet Window	9X	0.024	0.378	0.201	0.094	-1.5E-02	-1.8E-01	-1.7E-01	-38.57	-32.38	-45.41	47.78	38.63	58.75
Outlet Window	10Y	0.127	0.376	0.301	0.095	-2.6E-02	-2.5E-01	-1.5E-01	-17.07	-40.27	-32.53	18.66	50.42	38.85
Bottom Outlet Window	11X	0.006	0.068	0.042	0.018	1.8E-03	-5.3E-02	-3.2E-02	44.30	-43.95	-43.25	36.27	56.33	55.19

4.4.2 Solution with the Radiation Module and Turbulent Flow Regime

The corresponding airflow simulations determined with the radiation heat transfer model were found to be very similar to the ones previously described. The predicted flow patterns were almost identical although some quantitative differences were noted between the results. Table 4.6 lists the results of the data comparison for all the investigated flow regions, allowing for a direct comparison with the previously examined data. Figure 4.31 depicts selected flow representations, for which the quantitative discrepancies with the measurements were found to differ the most with the computation not modelling the radiation effects.

The correlation of the predicted velocity magnitudes in Table 4.6 highlights a larger disagreement with PIV data for the flow regions close to the heated blocks, i.e. in the areas *1X* and *2Y* (Figure 4.31a) close to the engine block, *3X* and *4Y* close to the turbocharger and *7X* and *8Y* above the gearbox. The CFD simulation gave in these areas a relatively larger mean flow velocity. The discrepancy is partly attributable to the higher temperature predicted for the block surfaces, most probably caused by an over-specification of the heat sources in the model, as discussed in Section 4.5.1. The flow predictions would be expected to correlate very closely to the experimental data if the block surface temperatures had been specified in the CFD model exactly as measured.

A closer data agreement was observed, on the other hand, in the region of air re-circulation (Figure 4.31b) and in the planes at the outlet of the underhood (Figures 4.31c and 4.31d). As given in Table 4.6, the CFD-relative discrepancy reduced by 28% for the x-plane at the top of the underhood, by respectively 9% and 8% for the x- and y-planes across the outlet, and by 15% in the small area at the bottom of the front slot. The improvement in accuracy lied with the more precise simulation of the thermal state of the compartment boundaries; these were not previously modelled to absorb the heat radiated from the blocks. Consequently, the airflow velocity in the vicinity of the glass was estimated to be lower in magnitude.

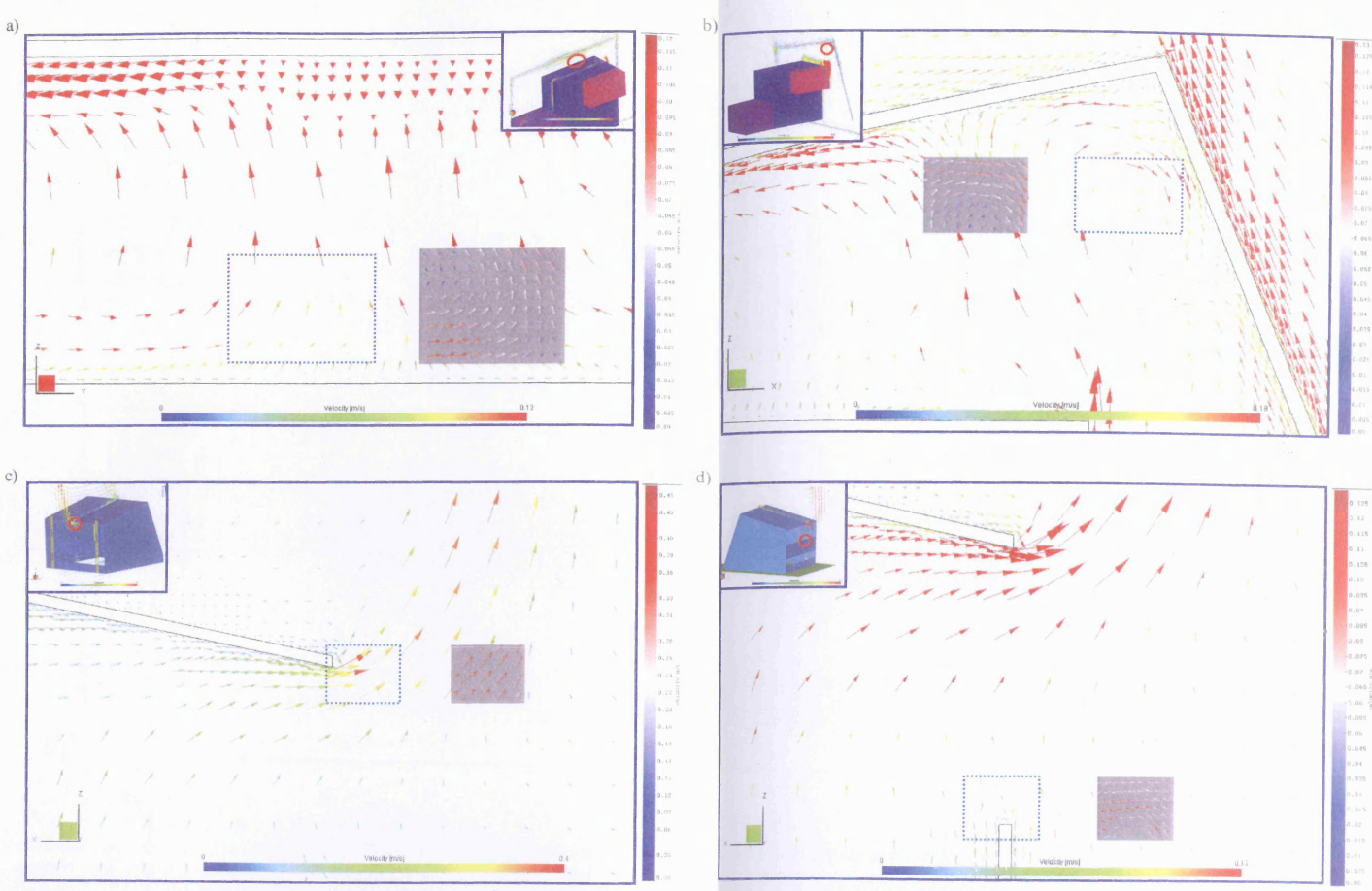

Figure 4.31 – Airflow predictions compared to measurements for simulation fully solving radiation (flow regions *2Y*, *5X*, *9X* and *11X*).

Table 4.6 – CFD predictions for simulation fully solving radiation and quantitative data comparison.

INVESTIGATED PLANE		CFD PREDICTION (m/s)				ABS. DIFFERENCE (m/s)			CFD DISCREPANCY (%)			ARC ELASTICITY (%)		
		Min velocity	Max velocity	Avg velocity	Std Dev. (±)	IVI min	IVI max	IVI avg	IVI min	IVI max	IVI avg	IVI min	IVI max	IVI avg
Above Engine	1X	0.036	0.254	0.145	0.031	7.1E-03	3.6E-02	1.5E-02	24.35	16.62	11.83	21.71	15.35	11.17
Above Engine	2Y	0.018	0.151	0.079	0.023	-4.9E-03	4.4E-02	1.9E-02	-21.40	40.83	31.50	23.96	33.91	27.22
Above Turbo	3X	0.090	0.366	0.241	0.051	3.5E-02	-2.9E-02	3.1E-02	63.37	-7.25	14.60	48.12	7.52	13.61
Above Turbo	4Y	0.078	0.269	0.128	0.026	2.6E-02	5.0E-02	3.1E-02	51.31	22.96	31.51	40.83	20.60	27.22
Top of Compartment	5X	0.028	0.126	0.077	0.021	-9.7E-03	4.6E-03	9.8E-03	-25.67	3.77	14.67	29.45	3.70	13.66
Below Turbo	6X SS1	0.041	0.355	0.134	0.054	-3.2E-03	5.1E-02	-1.8E-02	-7.34	16.93	-11.72	7.62	15.61	12.45
Below Turbo	6X SS2	0.043	0.255	0.067	0.031	-8.9E-03	-3.2E-02	-2.1E-02	-17.08	-11.15	-23.85	18.68	11.81	27.07
Below Turbo	6X SS3	0.015	0.190	0.086	0.044	-2.0E-03	-2.6E-02	2.3E-02	-11.71	-12.16	35.46	12.44	12.94	30.12
Above Gearbox	7X	0.093	0.142	0.111	0.025	3.3E-02	2.0E-02	1.2E-02	54.10	15.94	12.04	42.58	14.77	11.36
Above Gearbox	8Y	0.056	0.290	0.125	0.035	9.6E-03	3.0E-02	2.6E-02	20.68	11.59	25.86	18.75	10.95	22.90
Outlet Window	9X	0.029	0.431	0.235	0.079	-1.0E-02	-1.3E-01	-1.3E-01	-25.77	-22.89	-36.18	29.58	25.85	44.17
Outlet Window	10Y	0.133	0.456	0.336	0.087	-2.0E-02	-1.7E-01	-1.1E-01	-13.15	-27.56	-24.68	14.08	31.96	28.16
Bottom Outlet Window	11X	0.008	0.089	0.053	0.013	3.8E-03	-3.2E-02	-2.1E-02	92.40	-26.64	-28.39	63.20	30.74	33.09

4.5 DISCUSSION AND VALIDATION

From the examination of the numerical predictions and corresponding laboratory measurements the following was determined:

Heat Flux Approximation – The correlation obtained with reduced heat fluxes provided a generally good level of accuracy for both thermal and airflow predictions. The discrepancy between measured and calculated temperatures was on average about 5% when solving for turbulence, and 8% when assuming the flow to be in fully laminar regime[11]. The CFD thermal solution with a prescribed laminar flow gave higher surface temperatures and a lower air temperature within the compartment; the solution under-estimated therefore the convective heat transfer at the surfaces but did not markedly influence the temperature distribution agreement with measurements.

Figure 4.32 plots the mean vector magnitude as measured and predicted within all of the investigated PIV interrogation areas. Taking into account the data uncertainty, satisfactory mean flow predictions were obtained using the reduced heat fluxes approach. The largest discrepancies were associated with the regions characterised by air re-circulation (*PIV test 5X*) and flow separation (*PIV tests 6X, 9X* and *10Y*). The overall CFD discrepancy was approximately equal to 31%. Importantly, it must be recognised that the percentage differences were based on very low vector magnitudes; in absolute terms, the discrepancies were only in the order of 10^{-2} m/s, arguably within the accuracy requirements for underhood thermal engineering design.

Radiation Modelling – The average thermal discrepancy between the experimental and computational sets of data when fully solving for radiation heat transfer (and flow turbulence) was found to increase by 3.5% from the original 5%. On the other hand, a closer agreement was obtained when comparing the flow field data (Figure 4.32, overall discrepancy of 23%).

[11] Although the overall percentage discrepancy figures do not represent all the surfaces and air planes in the compartment, they can be generalised with confidence as the investigated areas were chosen to represent the thermal condition of all the modelled blocks (at least one surface per block examined) and of both x- and y-planes in their proximity.

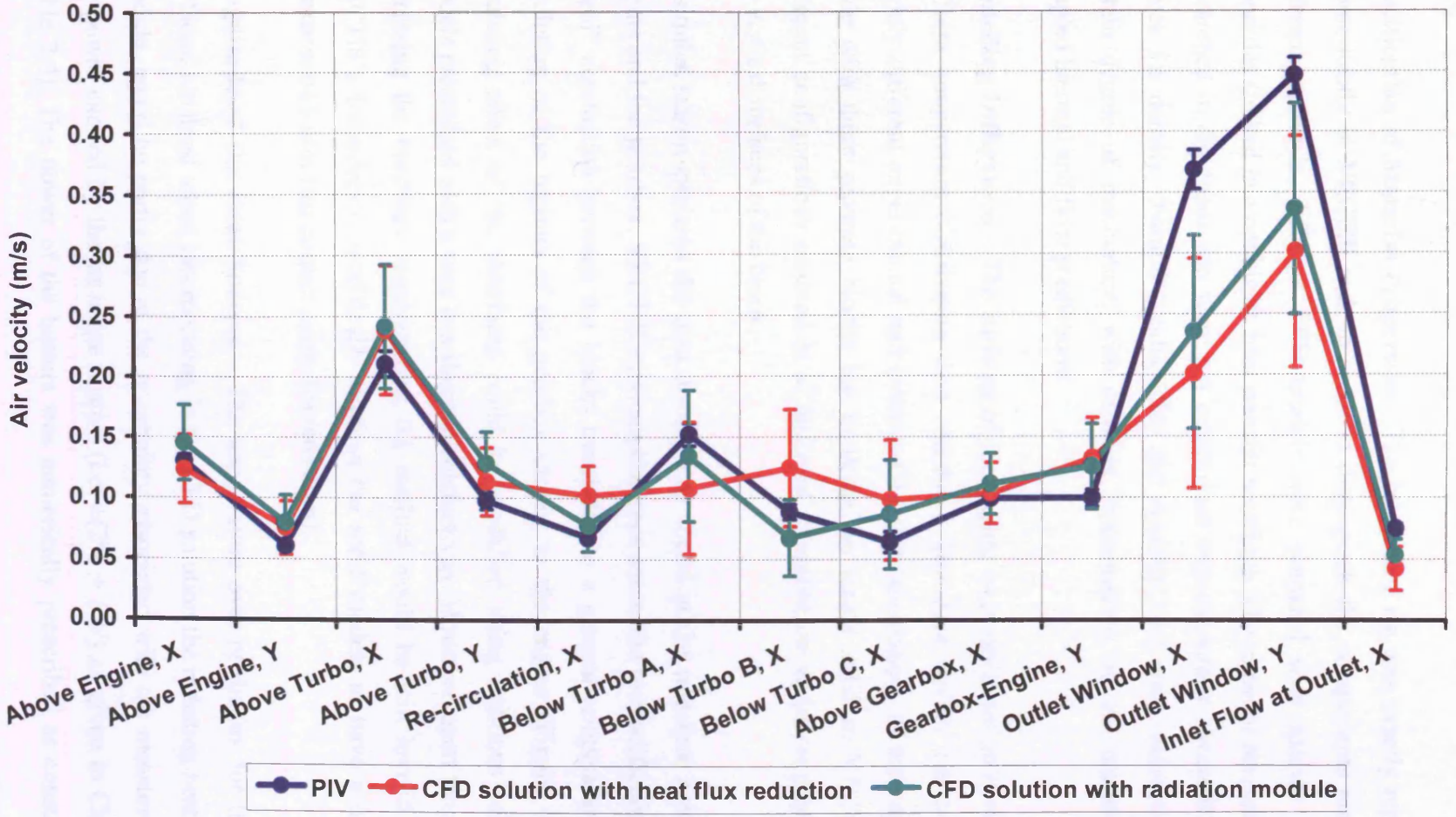

Figure 4.32 – Comparison between mean velocity vector measurements and predictions (with both heat flux approximation and radiation heat transfer solution) for all the examined flow field regions.

The main parameters expected to have influenced the CFD results and their accuracy were:

Specification of Material Properties – The laboratory rig was exactly reproduced geometrically in VECTIS and, in order to distinguish the components made from different materials, different CFD models were prepared with specific material properties (linked in a conjugate heat transfer solution). The material properties were researched in databases and were not determined experimentally. Accordingly, the values for density, thermal conductivity and specific heat were susceptible to a certain degree of inaccuracy, with obvious repercussions on the quality of the coupled thermal and flow predictions.

Modelling Differences – The surfaces of the engine were predicted to have a more uniform temperature distribution than observed. This was mainly caused by the slightly different experimental and computational representations of the engine, i.e. made with three separate blocks but modelled as single solid in VECTIS. The different configurations resulted in a 'distorted' temperature variation predicted on the vertical surfaces of the block.

A similar reason explains the data discrepancy found at the interface between the engine and the gearbox. VECTIS's assumption (not amenable to modification) of an "ideal" conduction between the blocks translated to a general temperature under-prediction of the regions of the gearbox closest to the engine (Figure 4.8). The insulating effect of the interfaces could be modelled using fictitious solid CHT models prescribed with a very low thermal conductivity. However, apart from largely increasing the hardware requirements, the method would be still invalid because VECTIS's formulation specifically requires the solid models to have a minimum thickness of 5 mm (for correct mesh discretisation).

Magnitude of the Heat Sources – The temperature over-prediction for the block surfaces, obtained when incorporating in the CFD solution the radiation heat transfer module, could be partly due to the uncertainty associated with the measurement of the power exerted by the cartridge heaters (i.e. ±(2% + 5W) as given in Chapter 2, Table 2.4). The power of the heaters was numerically prescribed as constant heat

fluxes within the blocks; any over-specification obviously translated to an over-prediction of the block temperatures.

Validity of Turbulence Model and Wall Functions – The disagreement between predictions and measurements calculated in regions of unstable regime (e.g. flow re-circulation) or characterised by flow separation were owed to the assumptions made in deriving the $k-\varepsilon$ turbulence model and the wall functions.

A significant weakness of the $k-\varepsilon$ model, when employed for simulating airflow as found in compartments, is that it assumes in its formulation a fully-developed turbulent flow existing everywhere in the model. Such assumption has been found to translate in an over-prediction of the turbulent diffusivity for wall-bounded low-Reynolds number flows [Posner *et al.* 2003] and in an excessive-production of turbulence kinetic energy in the vicinity of stagnation and separation points, the latter leading to overly mixed solutions [Lee 1997]. An attempt was made in solving the underhood with the assumption of a fully-laminar flow field but the predictions showed an overall worse agreement with PIV than the simulation with the $k-\varepsilon$ model.

An alternative would be the implementation of the *RNG* $k-\varepsilon$ model, which is available in VECTIS. This has been found in the past [Chen 1995, Speziale *et al.* 1991] to perform slightly better than the standard model when simulating simple indoor air flows. However, the validity of the *RNG* model is not yet assured due to its entirely theoretical development and lack of widespread application [Gatski *et al.* 1996, Lam 1992]. Furthermore, the results of the sensitivity analysis presented in Chapter 3 (Table 3.6) showed that the *RNG* model failed to predict correctly the average air temperature in the underhood.

A valid method for improving the simulation of natural convective flows would be the implementation in VECTIS of low-Reynolds number turbulence models, which have the advantage of integrating the flow governing equations through the turbulent boundary layer and into the viscous sub-layer adjacent to the wall. The wall-functions used in the $k-\varepsilon$ model would not be necessary [Yakhot *et al.* 1986]. This is a desiderable attribute since wall-functions are derived from simplistic flows (i.e. two-dimensional flows parallel to the wall [Tennekes and Lumley 1972]) and have

been found to be strictly valid only for fully developed, equilibrium boundary layers [Gatski *et al.* 1996]. Their application to model boundary layer flows that arise within enclosures and ventilated compartments and when pressure gradients are present (separation and impinging flows) is not fully justified as discussed, among other researchers, by Tennekes *et al.* [1972] and Abe *et al.* [1994]. Alternatively, the wall functions in the standard $k-\varepsilon$ model could be replaced by a hybrid two-layer function as successfully tested by Wofahrt *et al.* [2005]. The hybrid wall treatment would provide improved flow predictions by employing a "fitting" function to link the laminar and turbulent regions of the boundary layer.

Setup of PIV Image Length Scale – Any imprecision in manually setting the length scale of the PIV fields of view, before vector post-processing, would cause systematic errors in the calculation of the mean flow magnitudes. With the instrumentation setup of this study, it was established that an error of 1 mm in sizing the recorded images would affect the velocities by 3.65%, on average (Chapter 2, Table 2.4).

Spatial discretisation – Relatively large discrepancies (approximately 30%) were obtained when comparing experimental and numerical vectors with very low magnitudes. The different resolution of the CFD and PIV vector plots was believed to have partly caused the differences.

Overall, VECTIS demonstrated, qualitatively, to predict with sufficient accuracy the general temperature trends and the flow patterns and, quantitatively, to satisfactorily predict critical temperature parameters and flow velocities. Its implementation for simulation-based designs of thermal problems characterised by natural convection is therefore endorsed. The prerequisite for the good accuracy found was a model representation that conformed geometrically to the real system, a well-posed conjugate heat transfer simulation with consistent boundary conditions and the employment of a reliable turbulence model for simulating the airflow. Research in the CFD field is very active and it is envisaged that improvements of numerical models will inevitably improve the accuracy of the CFD simulations.

The validity of the turbulence model was found to be very important for the accuracy of the predictions. Although the flow was anticipated to be not fully-turbulent, the choice of using a turbulence model demonstrated to be favourable in comparison of forcing a laminar regime in the underhood volume. Radiation modelling was not found, on the other hand, to be critical: this is because an appropriate method to approximate the heat lost by radiation from the underhood blocks was found in this study. The radiation module implemented in VECTIS did not anyway substantially increase the CPU runtime and its use would be recommended for all future analyses.

4.6 CLOSURE

The numerical and experimental data comparison presented in the chapter demonstrated that, overall, VECTIS was able to predict to within 10% the thermal condition and within 25% the airflow magnitudes under buoyancy-driven convective environment in a simplified underhood model.

The highest discrepancies were observed for the flow simulations characterising the regions with air re-circulation and separation. The implementation in VECTIS of a more advanced and more suited turbulence model was suggested for the improvement of the predictions. The absolute quantitative differences in velocity magnitudes were however very small and arguably within typical requirements for engineering design. Overall, the analysis justified and gave confidence in the use of VECTIS for steady-state simulations of natural convection.

Chapter 5

FAST PSEUDO-TRANSIENT METHODOLOGY

5.1 PRELIMINARY REMARKS

Despite extensive research in the CFD field over the last decade, only few recent studies have explored alternative computational approaches for reducing the CPU runtime of transient simulations. In order to tackle complex time-dependent thermal flow simulations, industry has mainly relied on the continuous progresses of technology (e.g. the continuous increase in computing capacity of modern PCs) and on the evolvement of the numerical techniques for code parallelisation. The demands for accurate and detailed simulations have however also been progressively increasing and sufficient computational power may never be available to effectively counterbalance the requirements of a typical engineering analysis group [Hucho 1998].

A novel computational procedure/methodology enabling time-accurate simulations to be performed with a significantly reduced CPU turnaround time compared to a standard, fully-transient, CFD computation is investigated in this chapter.

The parameters affecting the performance of the methodology (accuracy and efficiency) were examined systematically by comparing the flow and the thermal predictions of a simple test case, henceforth referred to as *Model A*, with the corresponding results of a fully-transient computation. The investigation was then repeated on a more complex test case, *Model B*, which was solved also including the effects of radiation heat transfer.

5.2 FAST PSEUDO-TRANSIENT COMPUTATIONAL PROCEDURE

The literature review presented in Chapter 1 indicated that previous attempts to reduce the processing time for transient CFD simulations have mainly focused upon:

1. Improvement of hardware capacity and software parallelisation
2. Reduction in complexity of the computations, which was obtained for example by simplifying the modelled geometries (and thus the CFD meshes), by implementing empirical expressions as boundary condition or by adopting highly approximated numerical models (e.g. zero-equation turbulence model)
3. Development of more efficient numerical algorithms

All previous attempts have however demonstrated only relatively small savings in computing time (less than 50%) and often at the expense of marked losses in prediction accuracy.

An alternative method for transient underhood analyses would consist of using a 1-D system thermal model (STM), which provides a detailed thermal network description of the engine bay [Chang 2003]. However, a STM code would not be able to predict the state of the flow field within the underhood; any time-dependent internal and external flow condition (and any specific component or system characteristic) would need to be either assumed or entered as obtained from experimental investigation, affecting both the accuracy of the predictions and the preparation time for the analysis. The current practice is to use a combination of both CFD and STM, in order to compensate for their deficiencies as individual tools: the complex flow patterns are simulated with a 3-D CFD computation and the thermal state of solid elements is resolved with a coupled 1-D STM code. Only steady-state analyses have been attempted to date; strong doubts exist on the time-accuracy and on the actual CPU time saving that could be achieved with such method when applied to transient cases.

The current industrial requirement is for detailed time-dependent flow/thermal predictions to be computed within a feasible timeframe and preferentially within a single software tool [Somarathne *et al.* 2005]. In response, a computational methodology for fast transient simulations with a single CFD software is proposed in

this study. The methodology was developed based on a coupled heat transfer solution procedure between fluid and solid domains.

Description of Proposed Methodology – The fundamental limitation of CFD in performing a detailed and fully-conservative transient simulation is the requirement of overcoming the computationally demanding task of solving the equations expressing conservation of fluid momentum. Timesteps of the order of $1/1000^{th}$ of a second would be required to satisfy the numerical accuracy and stability constraints of the momentum solution for a model of average complexity. Consequently, many thermal processes examined for relatively long periods of time (>1 minute) and characterised by a continually changing flow field cannot currently be investigated numerically.

The method that is proposed to circumvent this limitation consists of "freezing" the flow field for periods of time during the transient simulation, i.e. pausing the solution of all governing flow equations except for the temperature. By freezing the flow, the analysis is freed from having to run for very small timesteps and the thermal solution can be advanced in time more quickly (timestep > 1s could be used). A time-accurate flow field, based on the temperatures of the modelled solid component at the end of the frozen-flow periods, can then be re-established/updated by "un-freezing" the flow field and solving again in a fully-conservative fashion.

Conceptually, the proposed computational procedure is based on the solution scheme shown in Figure 5.1. It consists of a specific number of long periods of time allocated for "frozen flow" solution processes, alternating with short periods of time allocated for "unfrozen flow" solution processes. The number of alternations between frozen and unfrozen computations, henceforth referred to as number of *methodology cycles*, would depend on the overall size of the time period of interest (i.e. the physical length of the investigated timeframe) and on the temporal advancement of the simulation within each methodology cycle.

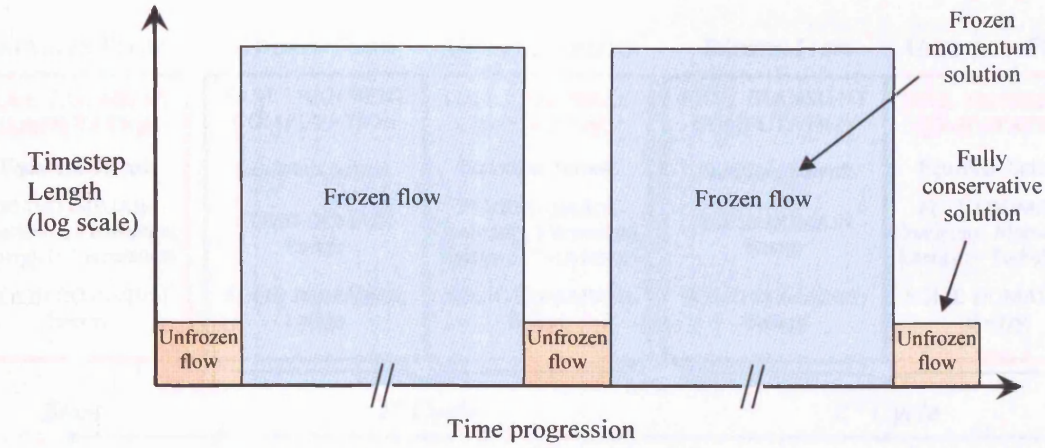

Figure 5.1 – Pseudo time-dependent solution scheme. The length of the frozen flow periods and the size of the relative timesteps are several orders of magnitude larger than for the unfrozen flow periods.

Two variants of the proposed procedure were tested. They differed in the type of CFD solver employed to update the flow field momentum transport, i.e. transient solver (methodology variant henceforth referred to as the "*UPDATE*") or steady-state solver (the "*SWITCH*" variant).

***UPDATE* Strategy** – The variant is based on a conjugate-heat-transfer transient computation solving only for thermal energy, denoted in the schematic representation of Figure 5.2 as "Fast Transient Computation". Large timesteps (optimal size to be investigated) promote the fast advancement in time of the solution. The transport of flow momentum is computed by restarting the transient simulations, after a specific time period, with both momentum and continuity equations included in the solution (referred to as "Full Transient Computation"). The fast and full transient computations are set to alternate until the physical timeframe of the investigated process is fully simulated. As shown in Figure 5.2, the *UPDATE* methodology is always set to initiate with a full transient run that provides a first approximation to the flow patterns in the modelled domain.

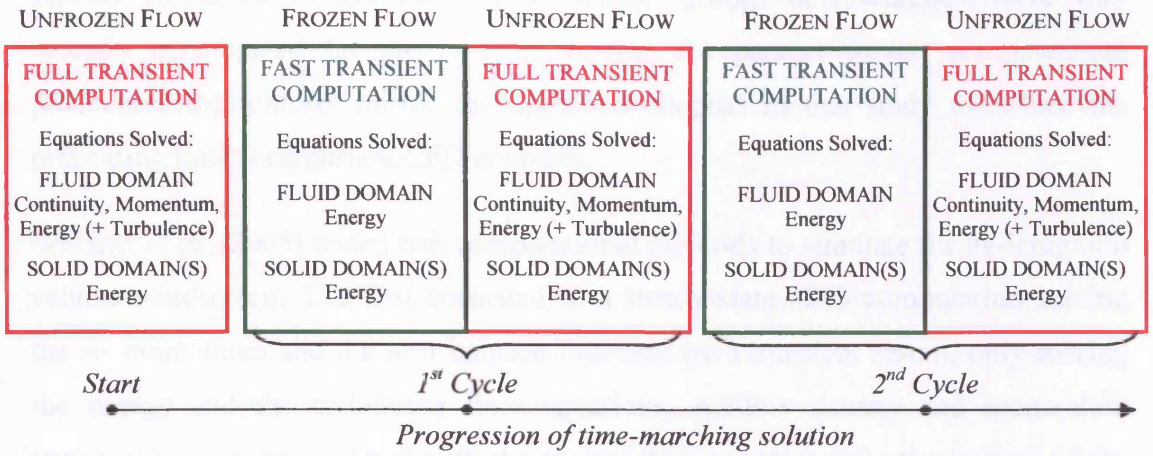

Figure 5.2 – Proposed solution scheme for *UPDATE* transient strategy.

***SWITCH* Strategy** – The solution procedure for the *SWITCH* methodology is schematically shown in Figure 5.3 and can be best described as being "pseudo-transient". A series of alternating transient and steady-state computations are set to solve, respectively, the thermal state of the solid CHT models and the complete set of governing equations of the fluid model. The main difference to the *UPDATE* strategy is in the employment of the steady-state CFD solver to update the flow momentum in place of a non-conservative transient computation. Importantly, the steady-state runs are not required to progress in time the thermal solution of the domain(s) in order to avoid affecting the overall time-dependent accuracy of the analysis.

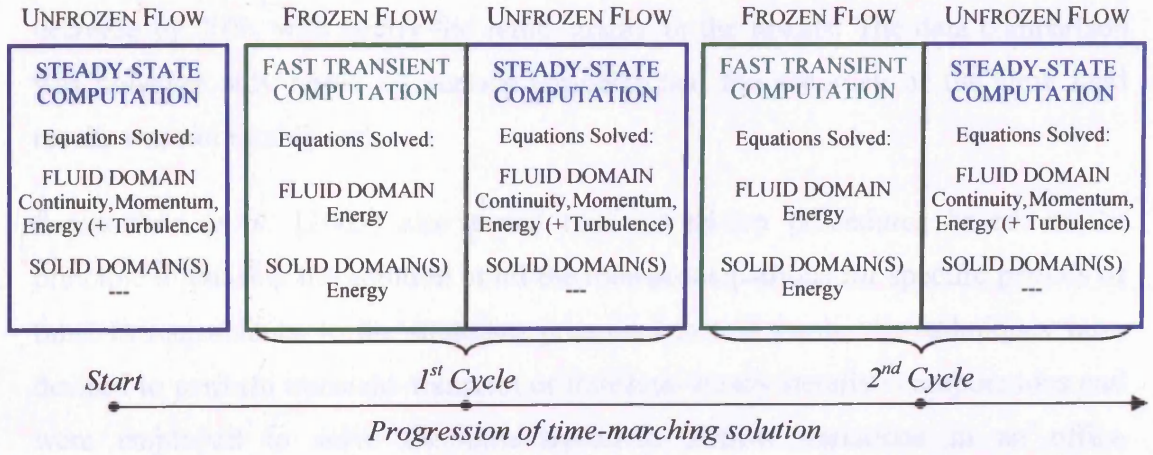

Figure 5.3 – Proposed solution scheme for *SWITCH* transient strategy.

Recent Research Progresses – Two distinct groups of researchers have very recently investigated (at the time of writing the present thesis) computational procedures that closely mirror the approach adopted in this study to reduce the processing time for transient CFD analyses.

Wofahrt *et al.* [2005] tested two computational methods to simulate the de-icing of a vehicle windscreen. The first consisted of a steady-state CFD computation solving the air momentum and the heat balance followed by a transient restart, only solving the energy and the turbulence flow equations. Airflow density and momentum transport were never updated with the temperature variation near the surface of the windscreen. Despite the analysis demonstrated to be very fast compared to a typical fully conservative transient computation, the predicted temperature distribution on the investigated surface was found to be poorly resolved due to the flow motion not being precisely captured close to the windshield.

The second method consisted of a transient computation solving for energy and turbulence that was frequently updated by a transient simulations additionally solving for momentum and continuity. The methodology, which was in principle analogous to the *UPDATE* strategy proposed and examined in this study, demonstrated the best compromise between prediction accuracy and saving of computational resources. When compared to a reference transient run (with permanent solution of all the equations), the CPU turnaround time was found to decrease by 70%, with nearly the same quality in the results. The data comparison was however only based on surface temperatures; the accuracy of the flow field results was not established.

Somarathne *et al.* [2005] also tested two calculation procedures based on the principle of pausing the solution of all the transport equations for specific periods of time. In resemblance to the strategies presented in this thesis, the techniques were devised to perform transient–transient or transient–steady iterative computations and were employed to solve the time-dependent airflow variations in an office environment. The authors determined that the strategy adopting steady-state computations to solve the flow transport was the most computationally efficient (90% runtime saving compared to the 36% saving of the transient–transient

methodology). However, a flaw in the procedure was observed by Somarathne *et al.* when modelling high rates of change in the thermal conditions; fictitious "jumps" in temperatures were predicted at the end of each steady-state process. No quantitative flow comparison with the full transient data was presented in the papers.

Both studies demonstrated that the combination of frozen and unfrozen flow computations is an effective procedure for fast transient thermal modelling. The conclusions drawn by the researches indicate, however, that specific parameters, such as the overall length of the frozen flow periods and the number and size of the timesteps/iterations discretising the unfrozen flow computations, are critical for the accuracy of the predictions and the efficiency of the computation. A detailed and systematic parametric analysis was therefore deemed necessary in order to determine the optimal set of solver parameters to be implemented in the proposed fast transient methodologies.

Computational Procedure – To reduce the effort and time required to setup and execute the separate solver runs within the solution scheme of the devised methodologies, a specific program was written with the MS-DOS Batch programming language (source code in Appendix I). The "Batch file" generated the necessary VECTIS input files and fully automated the iterative solution procedures. In particular, after the user had entered all the required computational parameters for the simulation (e.g. number of steady-state iterations, number and size of the transient steps and total number of methodology cycles), the program was able to start the analysis and automatically control the alternation between the planned CFD runs.

A specific limitation of the Batch programming language was recognised during the writing of the code: the program could not be instructed to automatically modify specific lines of the generic VECTIS's input file used to start the different CFD runs. As a consequence, at the onset of a new analysis the user was required to manually enter into the source code of the Batch program all the command lines to be then written in the input files. Such requirement did not affect the parametric analysis but would translate in relatively long setup times if the program were to be used on a routine basis. The issue was circumvented at a later stage during the research work

by using a different program written in the JAVA™ programming language [Bancroft 2005]. The program (source code and description given in Appendix I) was able to fully automate the iterative procedure of the methodology with the only requirement for a sample input file for each of the modelled CHT domain and for each type of computation (transient or steady-state).

Furthermore, to enable a fast post-processing of the complete set of transient results, an additional program was written in JAVA™ to join all the data of the separate VECTIS's output files on a common and sequential time base. The code obviated the need to manually join the numerical solutions of the frozen- and unfrozen-flow processes, otherwise fragmented in different files. Further description and the source code of the program are contained in Appendix I.

5.3 Analysis of Model A

5.3.1 Geometry and Boundary Conditions

A CFD model of a relatively simple geometry was designed with CAD software and used to investigate the effects of different solver parameters on the efficiency and accuracy of the devised strategies, in order to refine the calculation procedures. The model, shown in Figure 5.4, consisted of a hollow block (100×100×100 mm^3, wall thickness 10 mm) positioned at the centre of a computational chamber (500×500×100 mm^3).

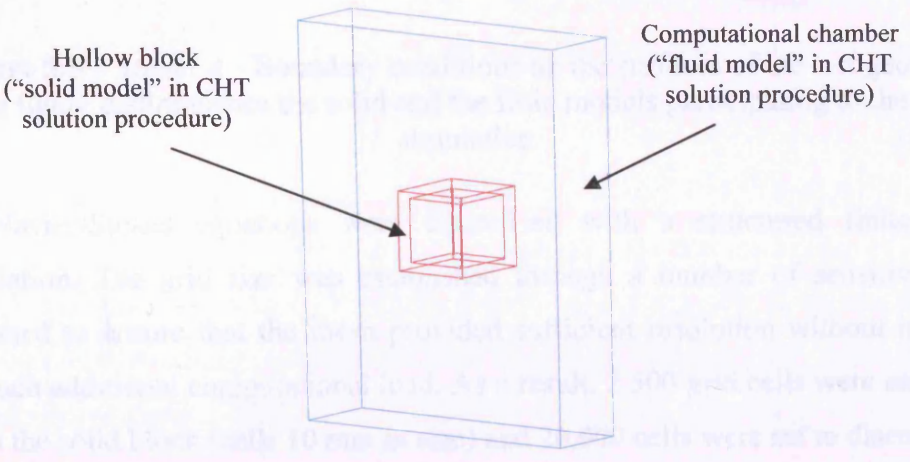

Figure 5.4 – *Model A* - CFD model for testing the solver parameters of the proposed transient strategies.

The small and identical width of block and chamber (100 mm) created a less computational-demanding configuration that enabled a reference full transient simulation to be performed within a reasonable timeframe for data comparison.

The hollow block was set to participate to the CHT simulation as a solid model with the following properties: density = 1000 kg/m^3, specific heat = 50 J/kgK, thermal conductivity = 50 W/mK. As indicated in Figure 5.5, only four of the block's six surfaces were thermally conjugated with the air domain (i.e. set to exchange local heat transfer coefficients and temperature values), with the remaining two (vertical surfaces on z-x planes) specified as "zero gradient" surfaces (slip + adiabatic walls). The temperature of the chamber's side boundaries was fixed at 473K (shown as the "isothermal boundaries" in the figure). All other boundaries were solved from an initial ambient temperature of 273K.

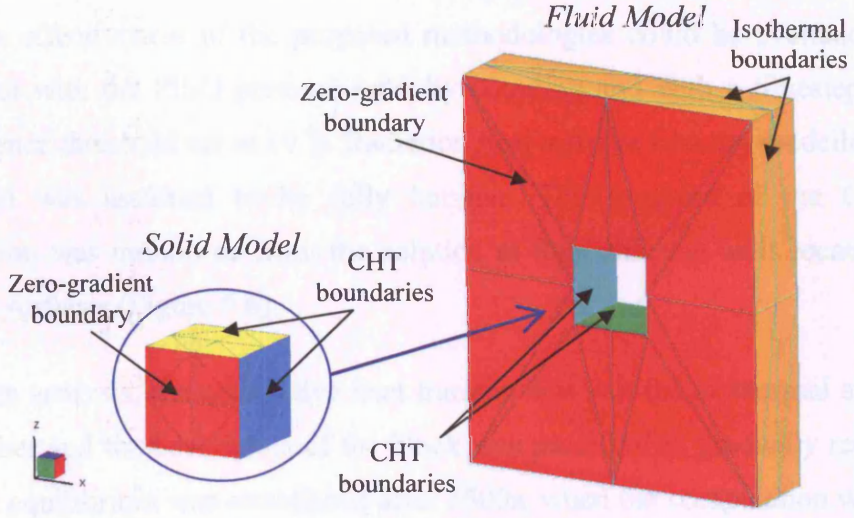

Figure 5.5 – *Model A* - Boundary conditions on the surfaces of the test geometry. The figure distinguishes the solid and the fluid models participating to the CHT simulation.

The Navier-Stokes equations were discretised with a structured finite-volume formulation. The grid size was established through a number of sensitivity tests conducted to ensure that the mesh provided sufficient resolution without imposing too much additional computational load. As a result, 2,500 grid cells were embedded within the solid block (cells 10 mm in size) and 20,000 cells were set to discretise the fluid domain, with a slight mesh refinement next to the thermally conjugated walls as shown in Figure 5.6a (cells 7.5 mm to 30 mm in size).

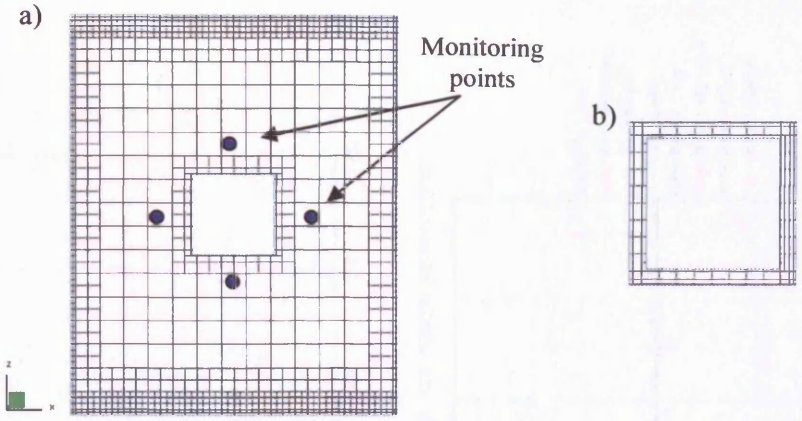

Figure 5.6 – *Model A* - Slice view of mesh grid for: (a) flow field (location of monitoring points shown); (b) hollow block (not to scale).

5.3.2 Reference Full Transient Simulation

A full transient simulation was performed to provide a comparison baseline against which the effectiveness of the proposed methodologies could be evaluated. It was carried out with the PISO pressure-velocity coupling and with a timestep of 0.01s (convergence threshold set at 10^{-6}). Radiation heat transfer was not modelled and the flow field was assumed to be fully laminar. The progress of the CFD flow computation was monitored from the solution at four different cells located nearby the block surfaces (Figure 5.6).

During the analysis, the convective heat transfer between the isothermal surfaces of the chamber and the boundaries of the block was predicted to gradually reduce until a thermal equilibrium was established after 1500s, when the computation was halted. Relatively large velocity oscillations were observed, especially in the first half of the simulated timeframe as shown in Figure 5.7.

By re-running the first 20s of the analysis with a smaller step (0.001s) and with a tighter convergence limit (10^{-7}), it was recognised that the instability of the flow solution was solely induced by the CFD solver. Indeed, the new computation shown in Figure 5.8 provided a solution (red line) that filtered the high frequency fluctuations observed when solving the flow field with a timestep of 0.01s (blue line).

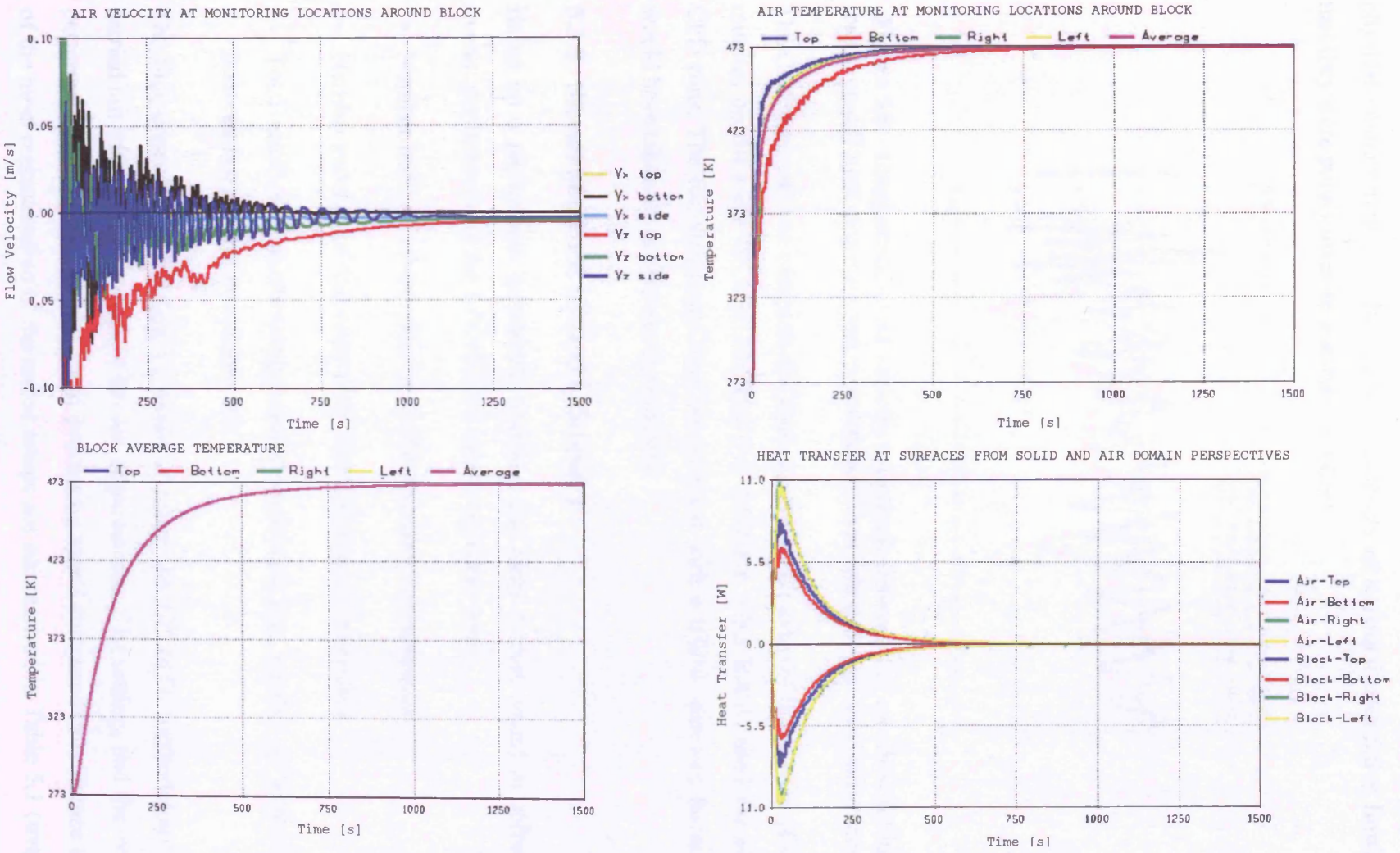

Figure 5.7 – Full transient solution of *Model A*. Plots showing the predicted air velocity, air and block temperatures and wall heat transfer.

The differences in frequencies suggested that the oscillations were not representing a physical phenomenon (e.g. the inherent instability of a natural convective flow) but that they were purely owed to a numerical effect.

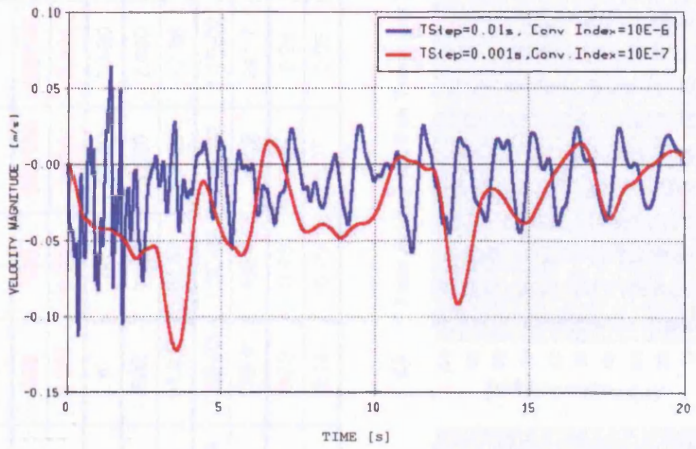

Figure 5.8 – Comparison of air velocity magnitude between full transient solutions based on different step sizes and convergence limits (first 20s of simulation shown).

The CPU time taken to complete the analysis (with a timestep of 0.01s) was of 8,918 minutes on the same PC unit (Pentium IV, 2.40GHz, 1GB RAM) used for all the CFD runs. The full simulation was not repeated with a 0.001s timestep because it would have taken several weeks to complete.

5.3.3 Simulation with *UPDATE* Strategy

Based on a preliminary parametric analysis, the main factors found to affect the overall performance of the *UPDATE* transient procedure were:

- Number and size of timesteps in the full transient computations
- Number and size of timesteps in the fast transient computations
- Total number of methodology cycles performed (i.e. number of alternations between fast and full computations).

The time-dependent simulation of *Model A* using the *UPDATE* methodology was carried out with different setups of the solver parameters. The settings and the overall performance (prediction accuracy and processing speed compared to reference data) of the most representative of the tested setups are summarised in Table 5.1 (overall, more than 50 different setups were tested).

Table 5.1 – Main features of the investigated *UPDATE* methodology setups and average discrepancy with reference full transient simulation.

Tested Variant		FULL	UP 1	UP 2	UP 3	UP 4	UP 5	UP 6	UP 7	UP 8	UP 9	UP 10	UP 11	UP 12	UP 13	UP 14
FAST TR steps	No.	–	100	99	98	(80) 100	(89) 99	100	500	500	250	30	10/20	10/50	5-50	5-50
Timestep size	sec	–	5	5	5	5	5	5	1	1	1	1	1	1	1	1
FULL TR steps	No.	150k	100	500	1000	(10k) 100	(5k) 500	500	100	500	500	100	200/100	200/100	50	100
Timestep size	sec	0.01	0.01	0.01	0.01	0.01	0.01	0.001	0.01	0.001	0.001	0.001	0.001	0.001	0.01	0.01
Methodology Cycles		0	3	3	3	3	3	3	3	3	6	50	50-50	50-20	100-20	100-20
Runtime	min	8,918	33	147	315	963	612	480	60	483	802	1,100	3,000	2,420	1,340	2,530
Time saving	%	0	99.63	98.35	96.47	89.20	93.14	94.62	99.33	94.58	91.01	87.67	66.36	72.86	84.97	71.64
Avg Vel. error	m/s	0	3.6E-02	8.2E-03	9.3E-03	7.9E-03	1.3E-02	7.2E-03	3.1E-02	5.8E-03	7.3E-03	1.6E-02	1.5E-02	1.1E-02	2.5E-03	1.3E-03
Avg Vel. error	%	0	611.1	215.7	190.9	179.7	303.9	163.1	479.4	86.0	178.4	336.4	338.2	241.7	51.0	25.5
Avg Temp error	K	0	5.82	2.09	2.75	4.78	4.82	4.92	0.69	1.20	0.60	0.43	0.34	0.29	0.31	0.44
Avg Temp error	%	0	1.24	0.44	0.58	1.02	1.03	1.06	0.15	0.26	0.13	0.09	0.07	0.06	0.07	0.09

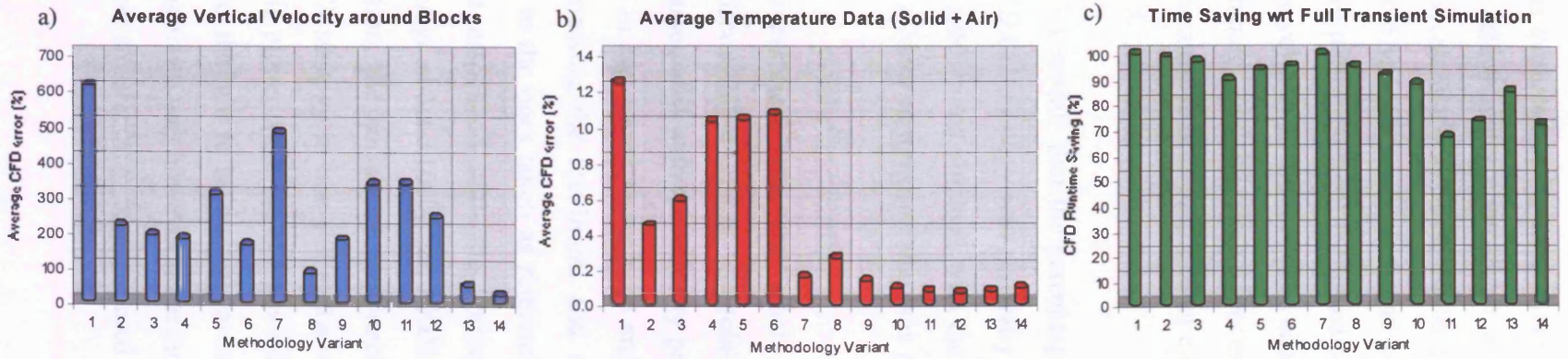

Figure 5.9 – Performance of tested *UPDATE* methodology setups compared to the full transient simulation.

The data comparison was performed between the velocity and the temperature results of the *UPDATE* and full transient simulations extracted at the same times and from (spatially) corresponding mesh cells (i.e. "cell to cell" comparison at identical timesteps of the solution). The discrepancies calculated at 500s, 1000s and 1500s were then averaged and are shown in Table 5.1, both in absolute and percentage terms. Table 5.1 presents therefore the relative performance of the tested setups, i.e. the relative accuracy in computing the airflow velocity in the modelled chamber and the mean temperature of the fluid and solid domains, and the relative processing time saving compared to the reference full transient computation. A graphical comparison between the tested setups is given in Figure 5.9.

A close examination of the results in Table 5.1 reveals that the percentage error in computing the airflow velocities with the *UPDATE* strategy was generally high (the same was also observed when analysing the predictions obtained with the *SWITCH* methodology). The reason lies with the type of data comparison that was performed and is two-fold:

1) The flow velocities in the modelled compartment were very small and thus particularly susceptible to numerical/discretisation errors, especially when compared "cell to cell". The uncertainty associated with the velocity predictions as extracted from single grid points was in fact found to be large and varying with time. This was established by extracting the maximum and minimum velocities from the grid cells contiguous to the ones taken as reference for the data comparison. The uncertainty range associated with the horizontal and vertical velocity components were on average about ±100% and ±200% of their mean value, respectively. As an illustration, the horizontal component of the flow velocity computed with the *UPDATE* strategy in one cell at the top of the block of *Model A* (shown in Figure 5.6) is plotted with the corresponding error bands in Figure 5.10. The uncertainty was thought to be mainly caused by the low density of the CFD grid employed; the mesh was however necessarily set to be relatively coarse to enable a full transient simulation to be performed and then used for the data comparison.

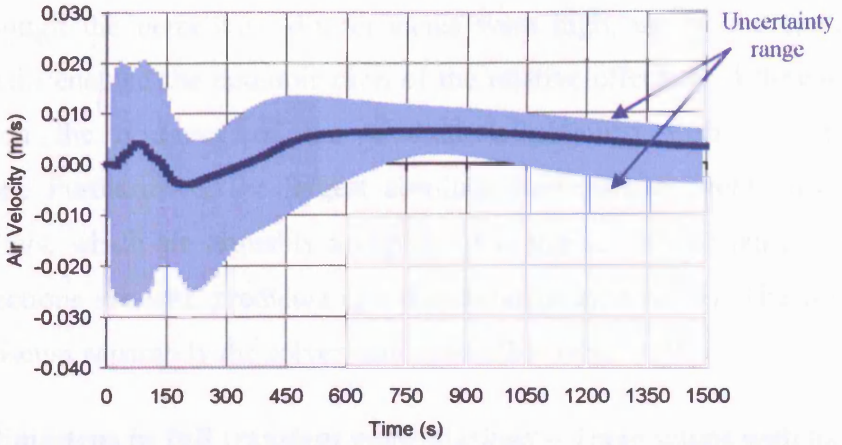

Figure 5.10 – Horizontal velocity component extracted from one grid cell with maximum and minimum limits (determined from the solution in contiguous cells).

2) The numerical instability of the transient solution affected the comparison between the CFD values extracted at specific "physical" times of the solution. Figure 5.11 displays the flow velocity computed next the block surfaces (full transient solution, 300s-700s range). The vertical velocity component at the side of the block was particularly affected by the instability (blue line in Figure 5.11a). To reduce the oscillations in velocity magnitude, the solution was filtered with a moving average of 5000 steps (Figure 5.11b). The oscillations were not however completely eliminated.

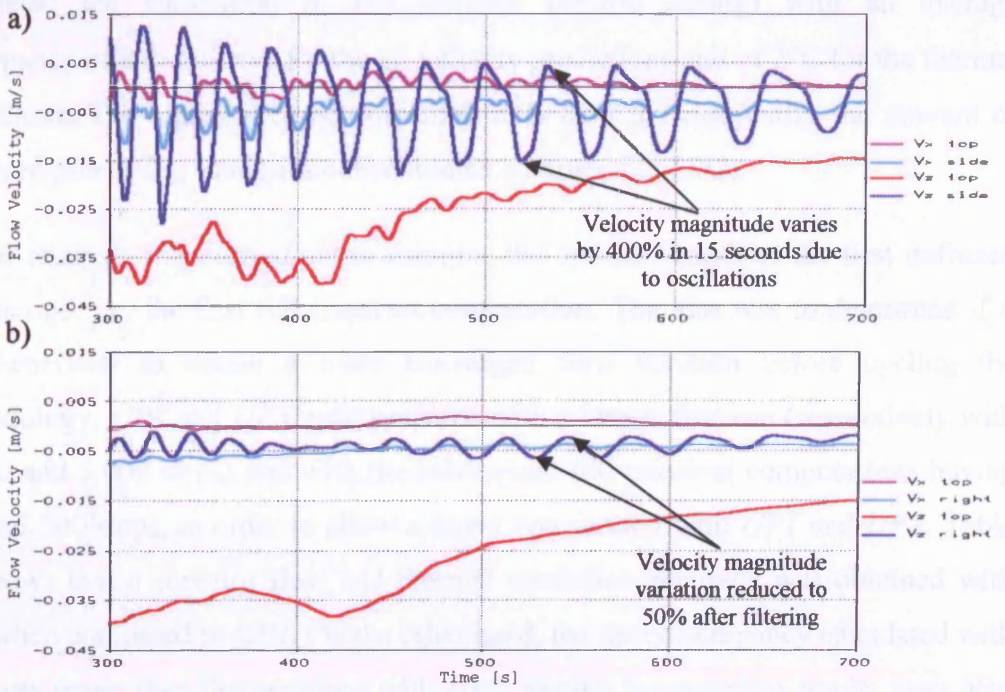

Figure 5.11 – Original (a) and filtered (b) airflow velocity solution from reference full transient simulation (300s-700s timeframe only).

Overall, although the percentage discrepancies were high, up to 600%, the data comparison still enabled the determination of the relative effects of different solver parameters on the accuracy of the predictions obtained with the proposed methodologies. Furthermore, the largest absolute discrepancies were only of the order of 10^{-3}m/s, which are arguably acceptable for engineering design purposes if the flow directions are well predicted (good qualitative agreement). The following paragraphs discuss separately the solver parameters that were used.

Number of timesteps in full transient computations – Three setups with timesteps of different size in the full transient computations but all based on identical frozen periods were investigated (*UP1* to *UP3* in Table 5.1. with respectively 100, 500 and 1000 timesteps of 0.01s). Overall, the solution scheme consisted of a total of 7 separate computations, i.e. a first full transient run followed by three methodology cycles.

The results showed that the higher the number of timesteps in the fully conservative computations, the better was the data agreement with the reference simulation, although at the expense of extended runtime (Table 5.1 and Figure 5.9). The best compromise between accuracy and processing speed was given by *UP2*, which completed the simulation in 147 minutes (98.4% saving) with an average discrepancy of 8.2×10^{-3} m/s for the air velocity predictions and of 2°C for the thermal predictions. The higher accuracy obtained with *UP3* did not justify the amount of increased processing time (more than double compared to *UP2*).

Further analysis was carried out to examine the optimal length of the first unfrozen flow period, i.e. the first full transient computation. The aim was to determine if it was beneficial to obtain a more converged flow solution before cycling the methodology. *UP4* and *UP5* were prepared with a longer first run (respectively with 10,000 and 5,000 steps) and with the subsequent full transient computations having 100 and 500 steps, in order to allow a direct comparison with *UP1* and *UP2*. Table 5.1 shows that a superior flow and thermal prediction accuracy was obtained with *UP4* when compared to *UP1*. On the other hand, the data discrepancy calculated with *UP5* was larger than that obtained with *UP2*. Similar inconclusive results were also reached when testing other setups, which are not included in the table. It was

concluded that a long full transient computation at the start of the calculation procedure did not demonstrate a consistent beneficial effect on the performance of the *UPDATE* strategy. Considering also the longer CPU runtime that was needed, its implementation was discarded from any setup successively tested.

Size of timesteps in full transient computations – The size of the timestep in a fully conservative time-marching computations depends both on the complexity of the flow and thermal configuration, and on the convergence index that is set on the Navier-Stokes equations. For a transient solution to converge successfully at every timestep and for a chosen convergence threshold, a maximum step size exists that can be selected for the calculations. The simulations of *Model A* were based on the VECTIS's default convergence index (10^{-6}) and the optimal timestep was determined to be of 0.01s. The effect of reducing the timestep on the performance of the methodology was examined by specifying 0.001s steps in *UP6* with the convergence limit also reduced to 10^{-8}. A distinctive improvement in the predictions compared to *UP2* was observed, especially for the air velocity magnitudes (Table 5.1). At the same time, the processing time also increased, despite the number of steps was identical between the two setups. The higher CPU effort was owed to the higher number of iterations performed by the CFD solver at each step of the solution, which was a consequence of the stricter convergence limit.

Number and size of timesteps in fast transient computations – The characteristics of the computations solving the frozen flow periods defined the progression in time of the simulation. The number and the length of the steps specified in the fast transient runs were inter-related and their setup depended on the selected duration of the frozen flow periods. Any change in timestep size necessitated in fact that the actual number of steps in each run be adjusted in order to resolve the same "physical" time. The effect of changing these parameters was investigated with the setup *UP7*, which was specified as *UP1* but with more (500) and smaller (1s) steps. A slightly more accurate solution, although compromised by a small increase in computing time, was obtained. In particular, the correlation of the fluid and solid domain temperature predictions with the measurements was seen to improve, with average discrepancies of only 1 degree on average.

Number of methodology cycles – All the parameters that previously demonstrated to improve the performance of the *UPDATE* methodology were specified in *UP8*. The computed thermal flow field was then taken as the baseline to assess the effects of varying the number of methodology cycles on the accuracy of the predictions. The setup of *UP8* was based on a total of 3 cycles whilst *UP9* and *UP10* were set respectively with 6 and 50 cycles, with the number of timesteps in the fast transient run reduced respectively to 250 and 30 per run (500 steps in *UP8*, Table 5.1).

The results indicated that a higher number of solver restarts (number of cycles) affected positively the accuracy of the predicted temperatures but it seemed to provide a less accurate flow field solution. The average discrepancy of the velocity predictions with reference data increased in fact to 1.6×10^{-2} m/s with *UP10* compared to 7.3×10^{-3} m/s with *UP8*. As previously indicated, the CFD errors listed in Table 5.1 were based on the average of the discrepancies calculated at different times. In order to assess the accuracy of the solution throughout the simulated timeframe, the CFD solutions were also plotted and compared on a time scale. The flow field (horizontal or vertical velocity components above and near the side of the block) and the air temperatures obtained with *UP8*, *UP9*, *UP10* and with the full transient run are shown in Figure 5.12. It can be seen that the computation based a higher number of methodology cycles (*UP10*) demonstrates to be actually superior in representing the time-dependent evolution of the reference computation. The flow field solution from *UP10* (pink line) is in fact shown to be very similar to the one of the full transient run (black line), although about 0.01 m/s lower in magnitude.

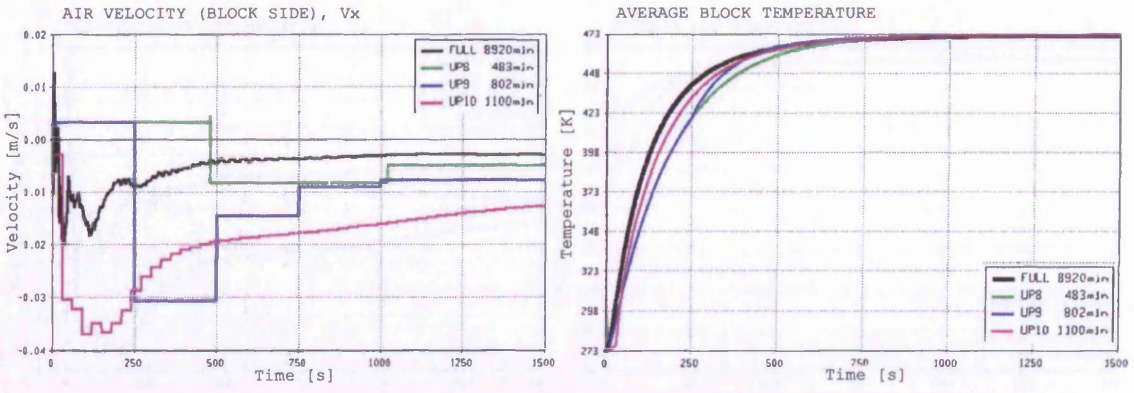

Figure 5.12 – Comparison of flow and thermal predictions as obtained with the setups *UP8*, *UP9* and *UP10* and with the reference full transient simulation.

The drawback of specifying a higher number of cycles was an increase in the CPU runtime and in the disk space requirements, due to the higher number of CFD runs performed and, consequently, of output files written by the software.

With the aim of further improving the agreement with reference results, the *UPDATE* strategy was tested with an even higher number of cycles set in *UP11* and *UP12*. The rest of the solver parameters were selected compromising between prediction accuracy and CPU time saving. In particular, a higher number of timesteps (200) was set to discretise the unfrozen flow periods during the first part of the simulation (i.e. for the first 500s, when the numerical solution was less stable) and a lower number (100) to solve the remaining timeframe of interest. Similarly, the number of steps in the frozen flow processes was increased from 10 per run, as set in the first 500s, to 20 or 50 per run (respectively in *UP11* and *UP12*) for the rest of the solution range.

UP11 performed 100 cycles in total, which were completed in approximately 3000 minutes (i.e. 66.4% saving compared to reference). *UP12* iterated the computational procedure for 70 times in 2420 minutes (72.6% saving). The predicted flow velocities and temperatures are compared in Figure 5.13. Both setups exhibited higher accuracy than observed in previous tests, especially in the first part of the simulation. Furthermore, it was attested that the number of steps for the frozen flow periods did not represent a critical parameter when the numerical solution was relatively stable; the 500s-1500s solution range was in fact computed with a similar accuracy both with 20s and 50s steps (the solutions are marked in Figure 5.13 respectively with a yellow and blue line).

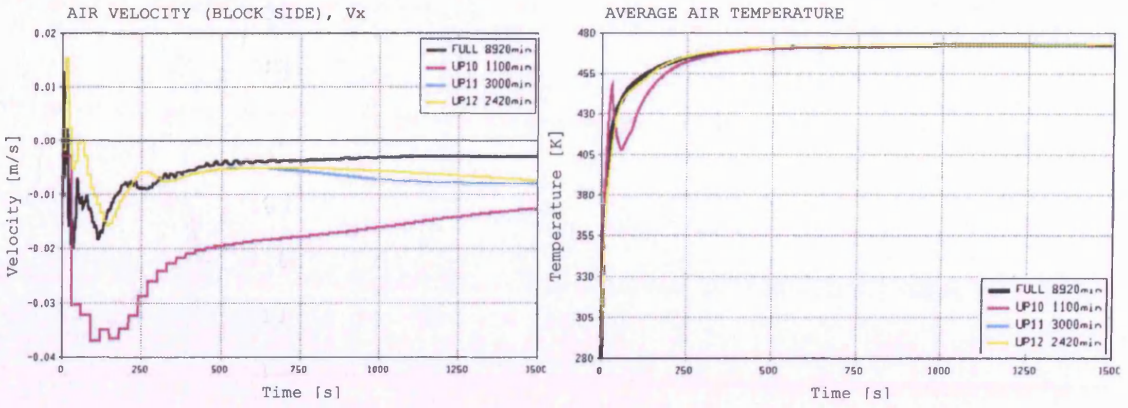

Figure 5.13 – Comparison of flow and thermal predictions as obtained with the setups *UP10*, *UP11*, *UP12* and with the reference full transient simulation.

The setups *UP13* and *UP14* were next examined. These were set with a higher cycle frequency (shorter unfrozen flow periods) than for the previously tested setups and were also set to differentiate in the number of steps discretising the full transient processes (i.e. 50 and 100, respectively). As shown in Figure 5.14, the quality of the predictions improved in comparison to the results of *UP12* (yellow line). The numerical results confirmed that the number of flow updates was decisive for the time-accuracy of the simulation. Between the two setups, the solution obtained with *UP14* was found to be slightly more accurate and stable in the first part of the investigated time period in comparison to that of *UP13*. On the other hand, *UP14* required a significantly longer runtime to complete the computations and the 71.6% saving calculated with respect to the baseline processing time was considered below the desired target.

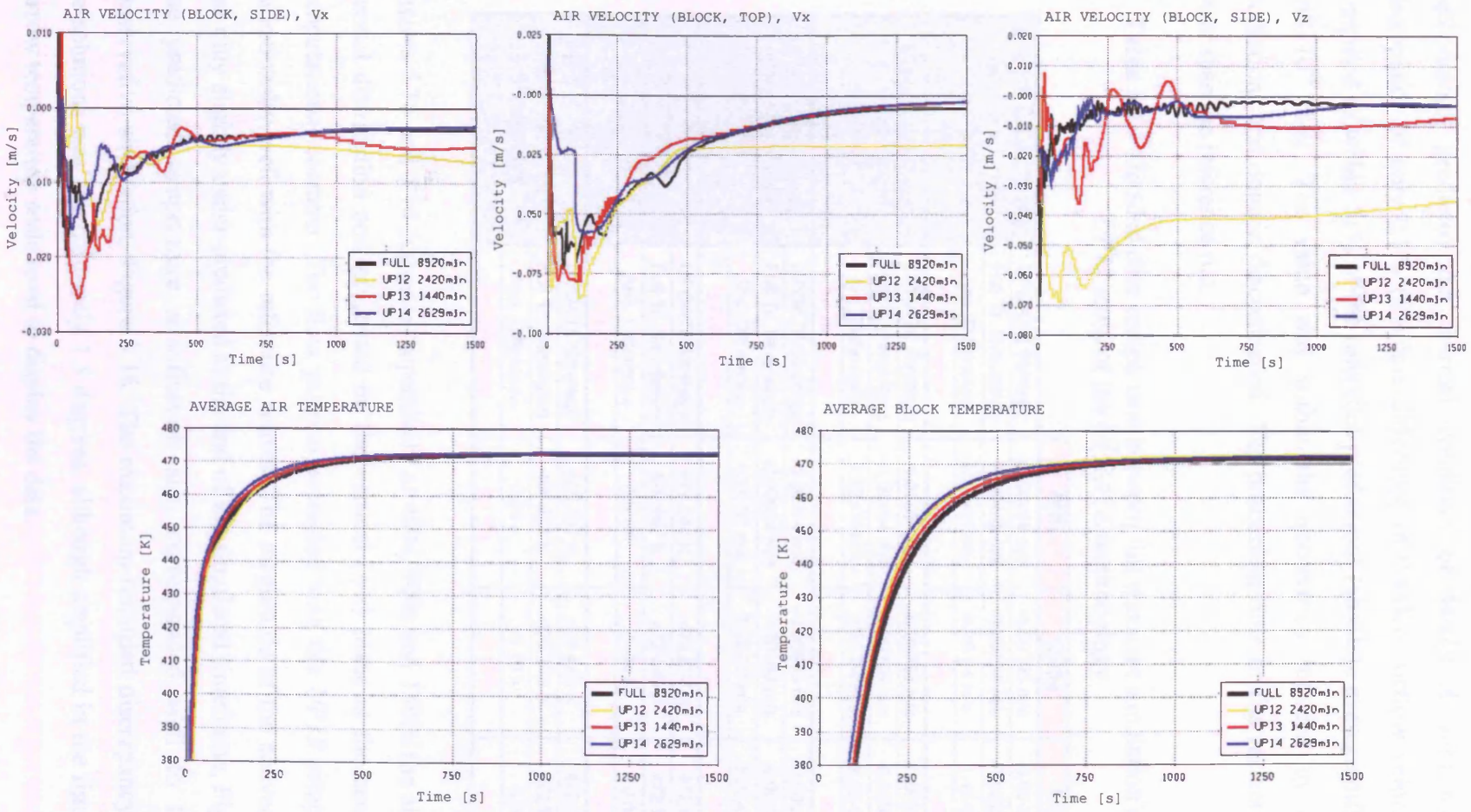

Figure 5.14 – Comparison of flow field predictions as obtained with the setups *UP12*, *UP13* and *UP14* and with the reference full transient simulation.

Table 5.2 presents a detailed comparison at different times between the results from the fully transient computation and the *UP13* setup. Overall, the *UPDATE* methodology predicted the thermal condition of *Model A* with an average discrepancy of only 0.1% (absolute difference of 0.44K). Airflow velocities were computed to within 51% of the reference predictions (absolute average difference of 2.48×10^{-3} m/s). The value was within the uncertainty induced by numerical oscillations and domain discretisation. The processing time of the variant was 85% lower than the reference run.

Table 5.2 – Detailed data comparison between full transient simulation and the *UP13* setup of the *UPDATE* methodology.

		500s	1000s	1500s
Horizontal air velocity (near block side surface), V_X	*UPDATE* Strategy	-0.00418 m/s	-0.00395 m/s	-0.00427 m/s
	Full Tr. Simulation	-0.00445 m/s	-0.00307 m/s	-0.00289 m/s
	Abs. Difference	2.7E-04 m/s	8.8E-04 m/s	1.4E-03 m/s
	% Difference	6%	-29%	-48%
Vertical air velocity (near block top surface), V_Z	*UPDATE* Strategy	-0.01857 m/s	-0.00758 m/s	-0.00289 m/s
	Full Tr. Simulation	-0.02434 m/s	-0.00798 m/s	-0.00553 m/s
	Abs. Difference	5.8E-03 m/s	3.9E-04 m/s	2.6E-03 m/s
	% Difference	24%	5%	48%
Vertical air velocity (near block side surface), V_X	*UPDATE* Strategy	-0.00214 m/s	-0.00633 m/s	-0.00644 m/s
	Full Tr. Simulation	-0.00624 m/s	-0.00268 m/s	-0.00325 m/s
	Abs. Difference	4.1E-03 m/s	3.6E-03 m/s	3.2E-03 m/s
	% Difference	-66%	-136%	-98%
Average air temperature in chamber	*UPDATE* Strategy	471.244 K	472.678 K	472.870 K
	Full Tr. Simulation	470.947 K	472.643 K	472.794 K
	Abs. Difference	0.30 K	0.04 K	0.08 K
	% Difference	0.06%	0.01%	0.02%
Average block temperature	*UPDATE* Strategy	465.757 K	471.469 K	472.398 K
	Full Tr. Simulation	466.292 K	472.173 K	472.599 K
	Abs. Difference	0.53 K	0.70 K	0.20 K
	% Difference	-0.11%	-0.15%	-0.04%

Figures 5.15 and 5.16 compare respectively at 480s, 900s and 1500s the airflow and thermal distribution post-processed on the vertical (z-x) plane at the centre of the computational chamber. The flow patterns predicted with the *UP13* setup matched exceptionally well with the reference results. The magnitude of the convective flow was only slightly under-predicted at the end of the simulated timeframe, Figure 5.15. The predicted temperature stratification also corresponded well to the fully-conservative simulation, Figure 5.16. The maximum-recorded discrepancy between the solutions was approximately 1.5 degrees, although amplified in the figure by the narrow temperature scale used to display the data.

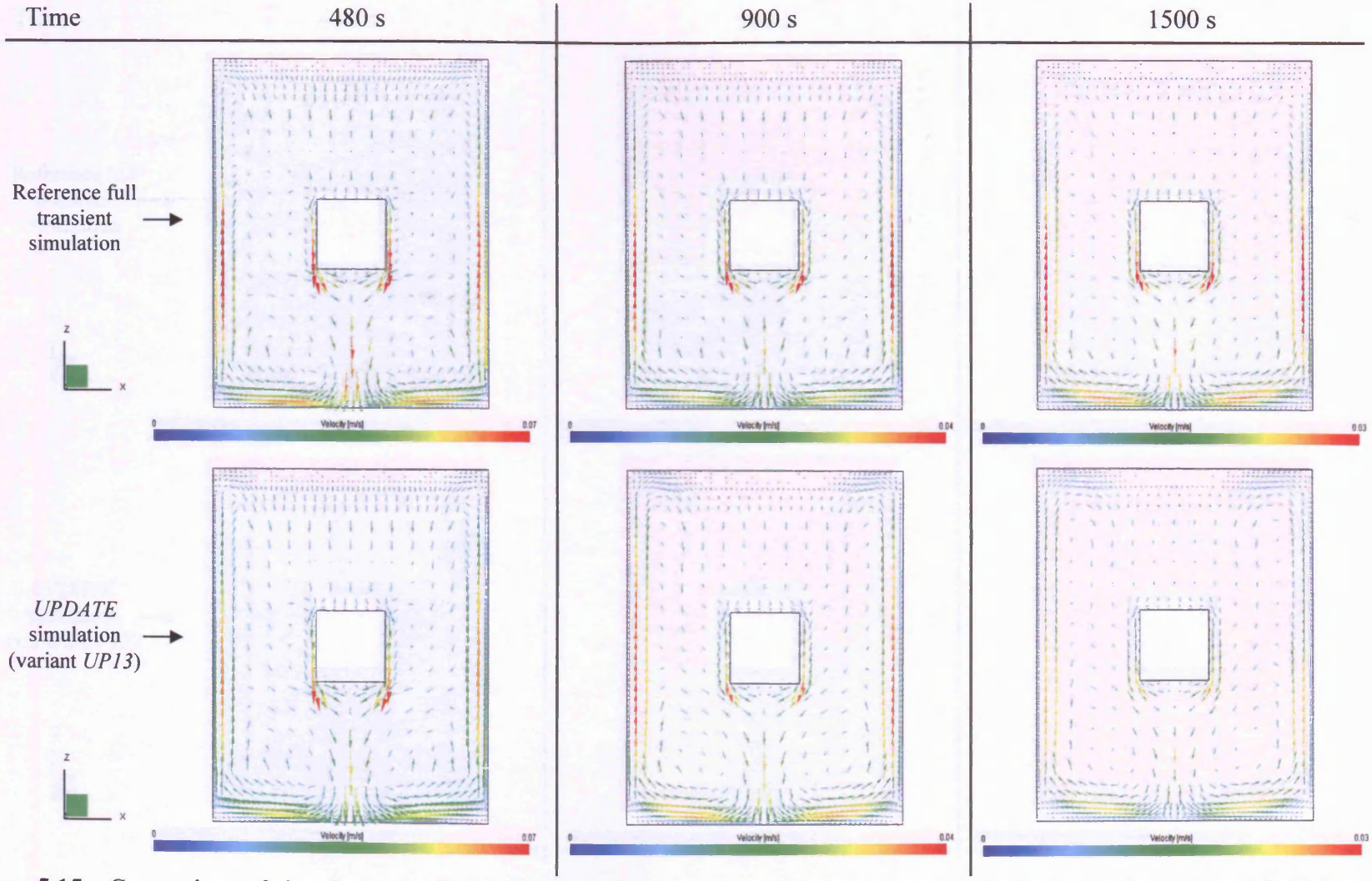

Figure 5.15 – Comparison of air velocity predictions between full and *UPDATE* simulations (vertical plane at the centre of fluid domain).

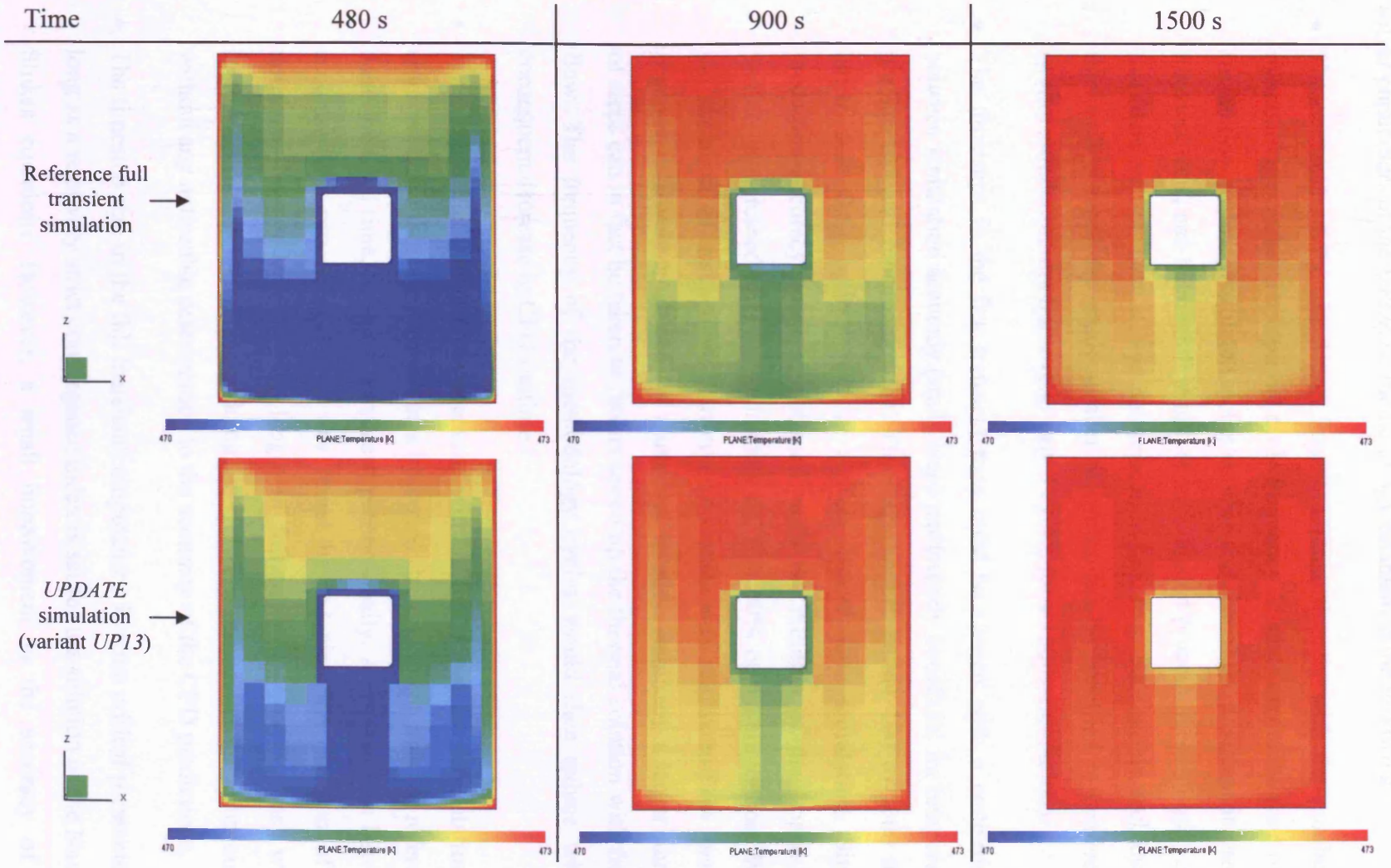

Figure 5.16 – Comparison of air temperature predictions between full and *UPDATE* simulations (vertical plane at centre of fluid domain).

Conclusions drawn from the analysis – The preliminary analysis performed on the solver parameters of the *UPDATE* methodology established the following:

- The accuracy of the simulation improves proportionally with the number of methodology cycles. The optimal cycle frequency depends on the duration of the frozen flow periods (regulated by the number and size of the timesteps in the fast transient runs) and the overall length of investigated process. Accordingly, if the fast transient runs have a large progression in time (e.g. 500s within each cycle), then only a relatively small number of cycles can be specified to resolve the overall simulation timeframe (e.g. only 3 cycles for a 1500s-simulation).

- The timesteps in the fast transient runs must be chosen with a compromise between simulation accuracy (small steps particularly beneficial for temperature predictions) and processing time. The steps should be set 100 to 1000 times larger than their optimal size in a fully conservative simulation. Similar prediction accuracy could be obtained when the duration of the frozen-flow periods is increased after approximately the first 30% of the simulation. When the variation of momentum between two successive unfrozen-flow periods becomes relatively small and the numerical solution stabilises, a larger number of steps can in fact be taken to further speed up the thermal solution with frozen flow. The frequency of the methodology cycles would then reduce with a consequent decrease in CPU runtime.

- When updating the flow momentum with a full transient computation, it emerged that a large number of steps improved the agreement with the reference data; the CPU time, however, increased proportionally. A compromise between accuracy and processing speed was found by reducing the duration of the unfrozen flow periods (i.e. the length of full transient computations) whilst increasing the number of methodology cycles. The processing time diminished without any noticeable deterioration to the accuracy of the CFD predictions.

- The timestep size in the full transient computations is not a critical parameter as long as a relatively strict convergence index is set for the solution of the Navier-Stokes equations. However, a small improvement in the accuracy of the

predictions was obtained by reducing both the convergence limit and the step size. The CPU requirements also noticeably increased.

- The number of output files written by the software increased proportionally to the number of methodology cycles performed by the *UPDATE* strategy. To reduce the disk storage space requirements, the files mapping the transient solution in the time intervals not of interest to the user should be deleted.

5.3.4 Simulation with *SWITCH* Strategy

The *SWITCH* strategy was based on the CFD solver switching between transient and steady-state mode within each methodology cycle. Various setups of the strategy and the corresponding computational performance are summarised in Table 5.3 and plotted Figure 5.17. The following parameters were studied:

- Number of iterations in steady-state computations
- Number and size of timesteps in transient computations
- Number of methodology cycles

Number of iterations in steady-state computations – The optimal number of steady-state iterations was investigated by testing the performance of four different setups, listed in Table 5.3 as *SW1*, *SW2*, *SW3* and *SW4*. The fast transient runs were set to solve only the energy equation with 100 steps of 5s each. The steady-state runs solved the complete set of the N-S equations and the thermal state of the solid model with respectively 100, 500, 1000 and 5000 iterations. The steady-state solution convergence (and computational speed) was enhanced by using an under-relaxation factor of 0.99, except for the momentum equations ($urf = 0.7$). A multigrid iterative solution with a 10^{-10} convergence limit was used to increase the numerical stability. The methodology included a first steady-state run followed by 3 cycles (i.e. 6 separate computations), all automated by the JAVA™ code. It was found that the accuracy of the solution improved proportionally with the length of the steady runs (Table 5.3). The runtime was however similarly affected.

Table 5.3 – Main features of investigated *SWITCH* methodology setups and average data discrepancy with reference full transient simulation.

UPDATE Variant		FULL	SW1	SW2	SW3	SW4	SW5	SW6	SW7	SW8	SW9	SW10	SW11	SW12*	SW13*	SW14*
STEADY iterat.	No.	--	100	500	1000	5000	500	500	500	500	500	500	1000	50	50	100
FULL TR steps	No.	150k	100	100	100	100	50	500	300	50	250	250	1000	30	30	15
Timestep size	sec	0.01	5	5	5	5	10	1	5	5	1	1	0.1	1	1	1
Methodology Cycles		0	3	3	3	3	3	3	1	6	6	6, no 1st	15	50	50	150
Runtime	min	8,918	17	76	150	750	66	96	47	120	143	126	1,428	136	60	545
Time saving	%	0	99.81	99.15	98.32	91.59	99.26	98.92	99.47	98.65	98.40	98.59	83.99	98.47	99.30	93.89
Avg Vel. error	m/s	0	3.4E-02	1.8E-02	1.4E-02	1.3E-02	2.1E-02	1.5E-02	2.3E-02	1.4E-02	1.2E-02	1.7E-02	6.1E-03	1.4E-02	1.4E-02	4.5E-03
Avg Vel. error	%	0	618.3	305.2	244.9	205.6	340.7	243.3	659.8	232.9	244.8	291.5	68.4	202.3	237.3	69.9
Avg Temp error	K	0	4.06	2.86	3.03	2.35	7.06	1.34	0.70	4.32	0.51	2.14	1.28	0.74	0.52	0.53
Avg Temp error	%	0	0.86	0.61	0.64	0.50	1.51	0.29	0.15	0.92	0.11	0.46	0.27	0.16	0.11	0.11

* No solution of temperature equation for fluid domain in steady-state computations

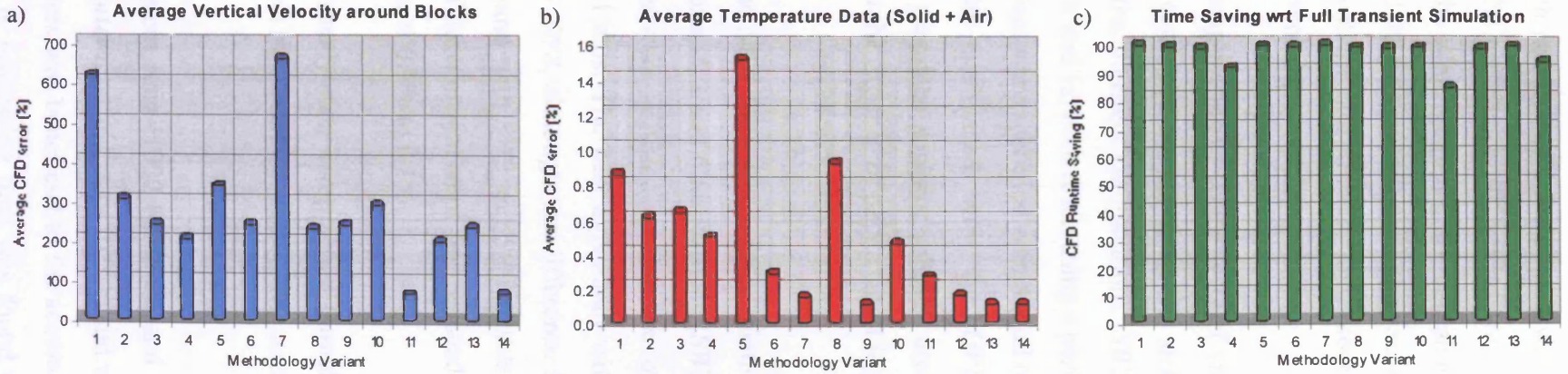

Figure 5.17 – Performance of tested *SWITCH* methodology setups compared to the full transient simulation.

The best data agreement was obtained with the solver parameters specified in *SW4*: the average vertical velocity was predicted with an error of 1.3×10^{-3} m/s while the average temperature discrepancy was 2.3°C. The percentage differences are plotted in Figures 5.17a and 5.17b. Considering the time required to complete the computations (Figure 5.17c), *SW2* demonstrated the best overall performance, with a prediction error slightly higher than *SW4* but with an exceptionally high processing speed (99.15% runtime saving compared to reference).

Number and size of timesteps in transient computations – The effects of varying the duration of the frozen flow periods was examined by changing the size and consequently the number of the timesteps in the transient computations. *SW5* and *SW6* were based respectively on timesteps of 10s and 1s, both discretising a period of 500s. The steady-state computations of both setups were specified with a total of 500 iterations. The results confirmed what was established with the *UPDATE* methodology, i.e. that relatively shorter steps guarantee superior solution accuracy especially for the temperature predictions and at the expense of only a small increase in hardware requirements.

Number of methodology iterations – *SW7* and *SW8* were set to differentiate from *SW2* in the number of methodology cycles performed, 1 and 6 respectively (*SW2* was based on 3 cycles). The frozen flow periods were adjusted so that the overall simulated timeframe corresponded exactly to 1500s. The best agreement with the reference velocity predictions was achieved by *SW8*, although the difference in the temperature results was slightly higher than found with *SW2* and *SW7* (Table 5.3). The thermal solution improved when the size of the transient steps was reduced to 1s (*SW9*): the discrepancy reduced from an average of 0.9% to 0.1%.

SW10 was set as *SW9* but without the initial steady-state computation (simulation starting directly with the transient run of the first methodology cycle). The accuracy and speed of the computation did not meliorate.

SW11 was tested with longer steady and transient runs (1000 iterations and 1000 timesteps respectively in each computation), shorter transient steps (0.01s) and with a total of 15 cycles. The combination of parameters was beneficial to the accuracy of the flow and thermal solution, but the saving in processing time was found to be

largely compromised, Figure 5.17c. In order to speed-up the computation, the solution schemes of *SW12* and *SW13* were discretised with a higher number of cycles (i.e. 50 rather than 15) and the steady-state runs were shortened (50 iterations). *SW13* was run without solving, during the steady computations, the energy equation of the air domain; i.e. only the momentum and pressure equations were computed. The results showed that, although the unfrozen flow periods were shorter, the flow and thermal predictions of *SW12* and *SW13* were only marginally worse than those of *SW11*. The temperature predictions obtained with *SW13* were on the other hand superior, suggesting that the heat transfer calculations performed during the steady runs were actually detrimental to the time-accuracy of the solution.

By further increasing the cycle frequency (150 cycles) and by adjusting the number of steady iterations to 100 per run (instead of 50) in *SW14*, the CFD correlation was seen to further improve without any significant increase in processing time. Table 5.3 indicates that the velocity predictions obtained with the *SW14* setup were similar to the ones of *SW11*, but the runtime reduced by a factor of 2.6 (i.e. a 94% computing saving was obtained with *SW14* compared to reference). The average velocity discrepancy was 4.5×10^{-3} m/s, while the average temperature difference was only about 0.5 degrees.

The numerical solutions of a selected number of tested *SWITCH* setups are plotted together in Figure 5.18 against the baseline full transient solution (black line). The solver parameters implemented in *SW14* (red line) clearly provided the best compromise between accuracy and computing speed.

Flow maps of the central z-x plane of *Model A* are compared in Figure 5.19. The *SWITCH* methodology (*SW14*) correctly modelled the flow field in the chamber, although small discrepancies in magnitudes can be observed. A very good agreement is shown in Figure 5.20, which compares the air temperature stratifications predicted on the same 2-D plane at 480s, 900s and 1500s. The average temperature of the buoyant flow was over-estimated by less than 1°C.

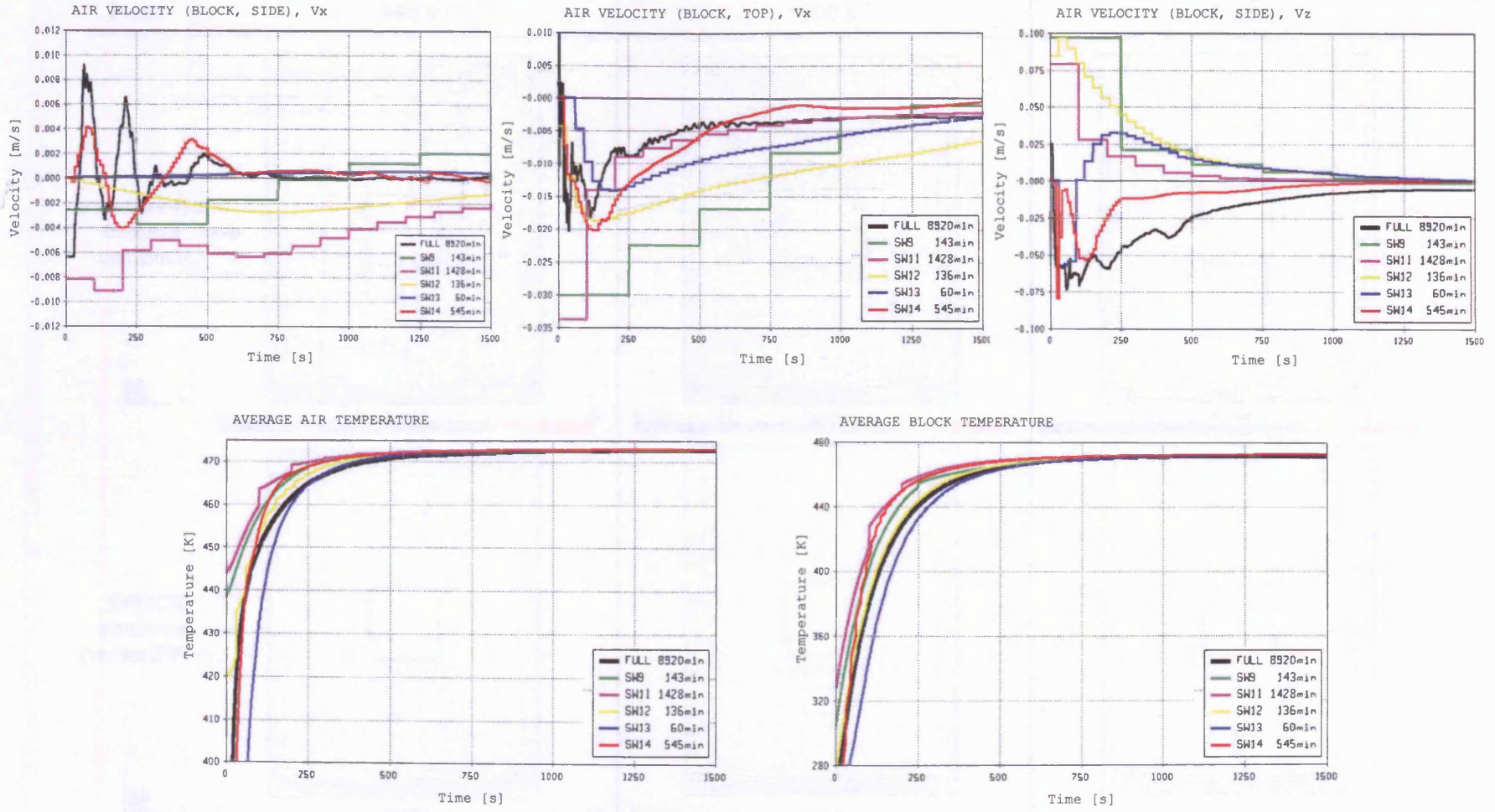

Figure 5.18 – Comparison of flow field prediction as obtained with the setups *SW12*, *SW13* and *SW14* and with the reference full transient simulation.

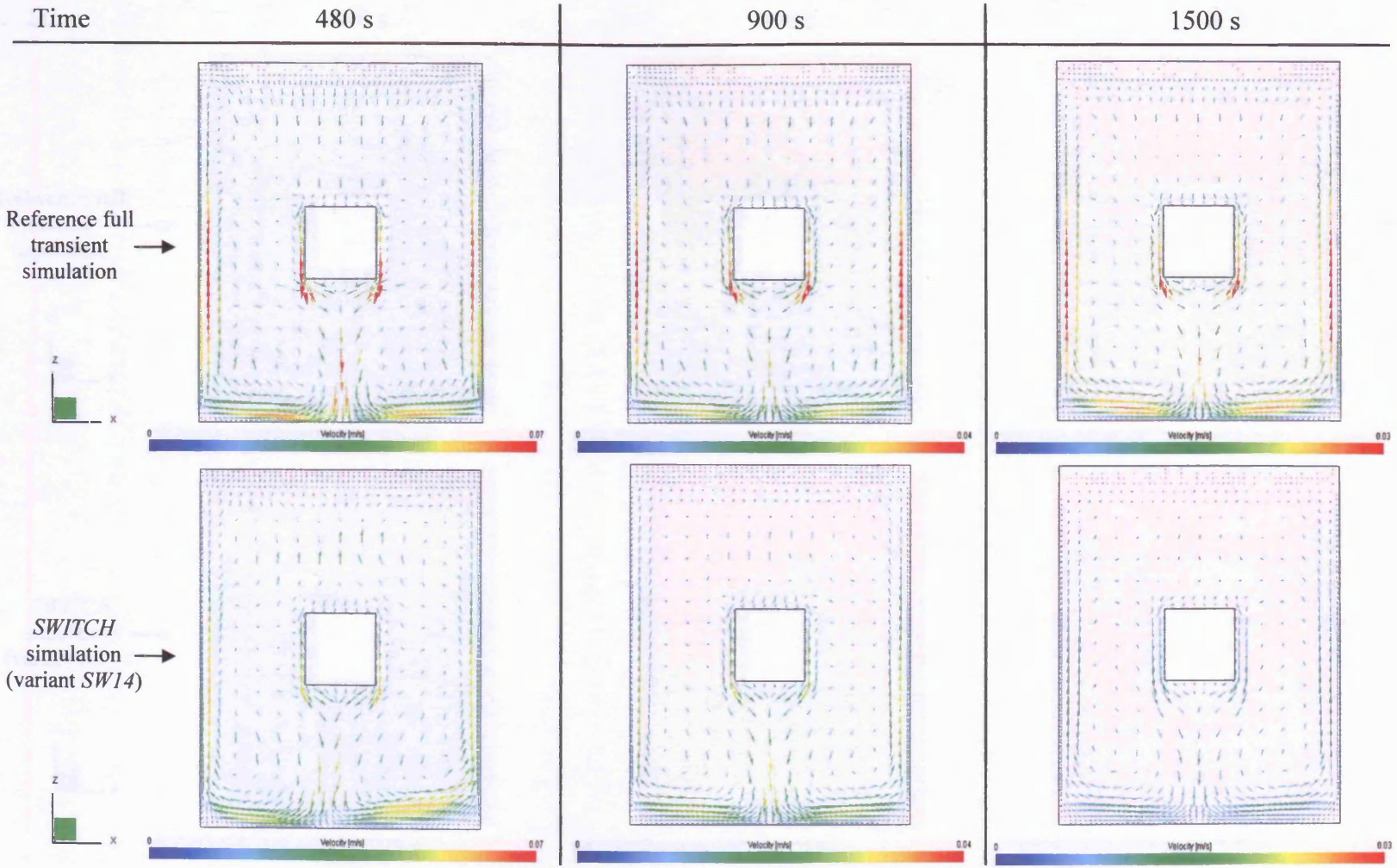

Figure 5.19 – Comparison of air velocity predictions between full and *SWITCH* simulations (vertical plane at the centre of fluid domain).

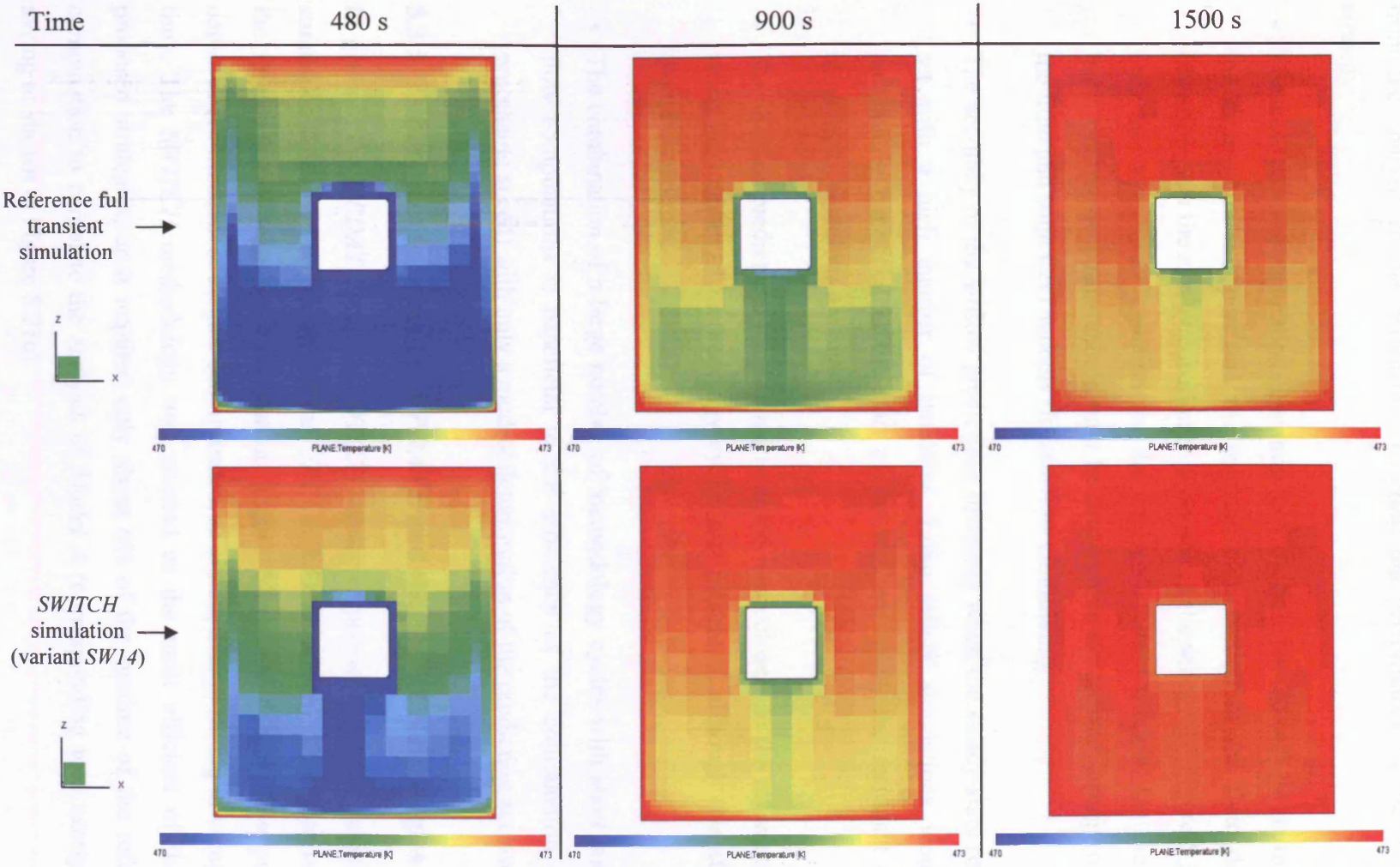

Figure 5.20 – Comparison of air temperature predictions between full and *SWITCH* simulations (vertical plane at the centre of fluid domain).

Conclusions drawn from the analysis – The following conclusions were drawn from the analysis of the parameters affecting the performance of the *SWITCH* strategy:

- The steady-state computations updating the flow field should only be set to solve the momentum transport and the pressure conservation of the fluid domain (therefore, not the energy equation as proposed in the scheme of Figure 5.3) and only the temperature equation for the conjugated solid models. On the other hand, the transient runs should only be set to solve the thermal energy of both the fluid and solid CHT models (frozen-flow conditions).

- The accuracy of the airflow predictions increases when the steady-state runs are set with a high number of iterations. Long steady simulations would be particularly beneficial at the start of the analysis when the residuals of the momentum equations are high.

- The thermal predictions were found to agree more closely to the reference data when the number of methodology cycles was increased, although this affected the CPU runtime.

- The combination of a large number of methodology cycles with short unfrozen flow computations is beneficial to the efficiency of the computation (faster processing speed) with only a modest deterioration of the prediction accuracy.

5.3.5 Differences between the *UPDATE* and the *SWITCH* Strategies

In general, the *UPDATE* and the *SWITCH* strategies provided equally satisfactory simulation (based on the results of the *UP13* and *SW14* setups) when compared to the reference full transient computation (Figure 5.21a and 5.21b). The pseudo-conservative transient strategies demonstrated, as aimed, a large saving in computing time. The *SWITCH* methodology was attested as the most efficient of the two proposed strategies, as it required only about 6% of the runtime of the reference computation to complete the analysis of *Model A* (corresponding to a nearly 94% saving as shown in Figure 5.21c).

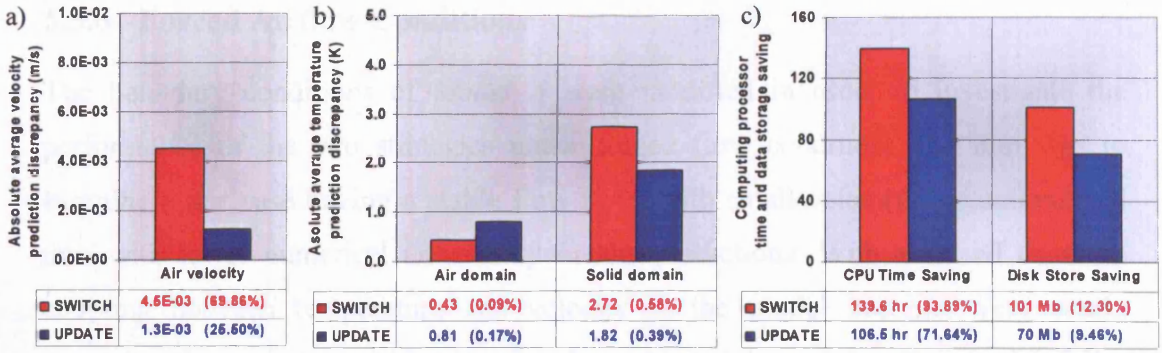

Figure 5.21 – Absolute average data discrepancy (a, b) and CPU processing saving (c) for *SWITCH* and *UPDATE* strategies relative to reference full transient simulation (corresponding percentage difference given in brackets).

The average convective heat transfer and the heat transfer coefficient computed at the top and side surfaces of the block with the fully-conservative computation and by employing the two proposed methodologies are plotted in Figure 5.22. The graphical comparison provides a direct measure of the quality of the tested strategies in predicting the strength of the buoyant flow in the chamber. The figure shows that the agreement of the two methodologies with reference was remarkable and very similar in comparison.

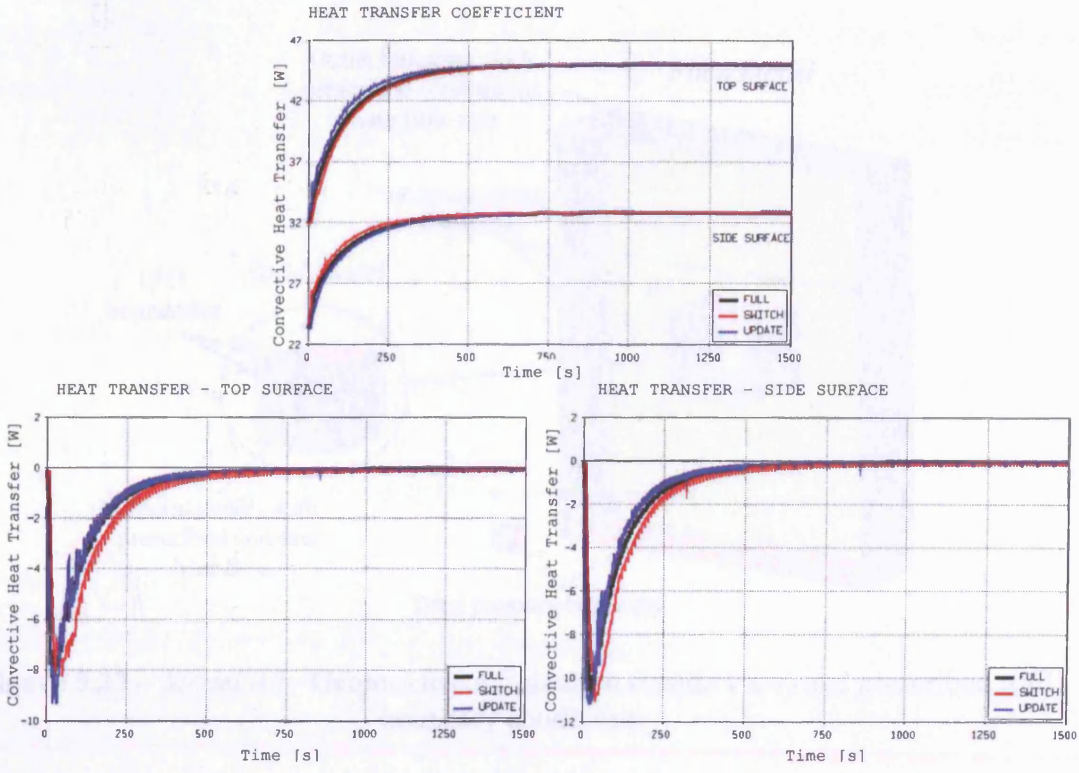

Figure 5.22 – Comparison of convective heat transfer [W] and cHTC [W/m^2] for the block surfaces as predicted by full transient, *UPDATE* and *SWITCH* simulations.

5.3.6 Forced Airflow Conditions

The boundary conditions of *Model A* were modified in order to investigate the performance of the two strategies under forced flow condition. The aim was to examine a test case having a stable flow field, with small velocity fluctuations and thus with lower numerical uncertainty on the predictions. With a forced flow the coupling between temperature and velocity in the model becomes very weak; consequently, a fast analysis can also be achieved by solving the model fully-transiently until a fully developed flow is established in the chamber and then freezing the momentum transport (i.e. only solving for the enthalpy transport). In other words, from a practical point of view the implementation of the proposed pseudo-transient methodologies would not be strictly needed to speed-up the simulation of a forced flow. Nevertheless, the test case was deemed still representative to further the investigation on the performance of the two calculation strategies.

The side, top and bottom surfaces of the model, henceforth referred as *Model A2*, were set respectively with zero-gradient, inlet and outlet boundaries (Figure 5.23).

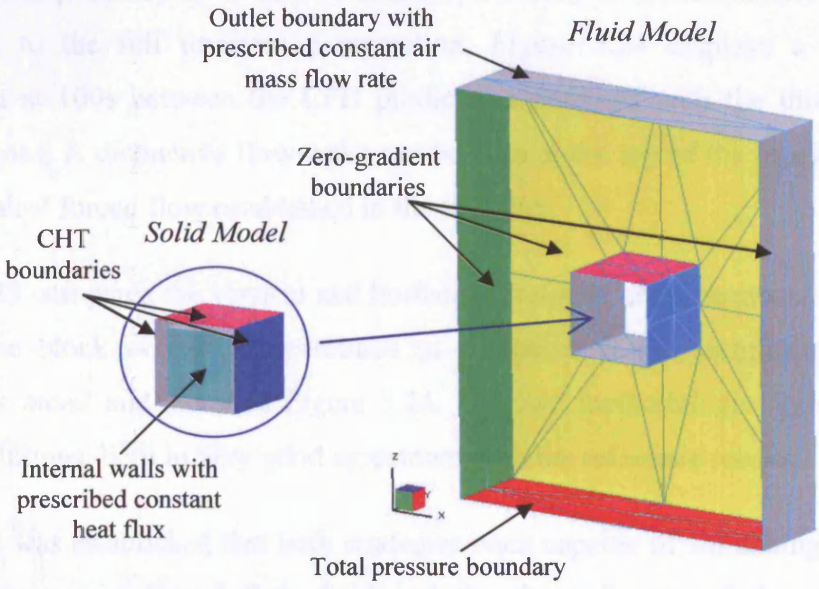

Figure 5.23 – *Model A2* - Geometric configuration (inside view) and prescribed wall boundary conditions.

The air was specified to exit the chamber with a uniform mass flow rate of 0.1 kg/s while the inlet boundary was prescribed with a total pressure condition (static + dynamic pressure). A constant heat flux of 400W was specified on the internal walls of the hollow block, therefore representing the transient heating of the air instead of the cooling. The model was solved from an initial temperature of 273K. The computational chamber was discretised with the same global mesh used for *Model A*. The monitoring points were located as shown in Figure 5.24.

The full transient simulation was carried out with a timestep of 0.01s and was halted after 500s. The methodologies were set-up with a combination of parameters established from the previous analysis to give an overall better performance. In particular, the *UPDATE* strategy was set to perform 50 cycles, with the fast transient runs comprising 10 steps of 1s and the full transient runs comprising 50 steps of 0.01s. The *SWITCH* strategy was also based on 50 methodology cycles and frozen flow periods of 10s, and was set with the steady-state flow updates based on 100 iterations per run.

The simulations carried out with the *UPDATE* and *SWITCH* strategies were completed respectively in 83 and 78 minutes, a saving of approximately 97% when compared to the full transient computation. Figure 5.24 displays a remarkable agreement at 100s between the CFD predictions obtained with the three different computations. A distinctive flow wake can be seen at the top of the block as a result of the vertical forced flow established in the chamber.

Figure 5.25 compares the vertical and horizontal velocity components as well as the air and the block average temperatures as computed at the monitoring locations denotes as *mon2* and *mon4* in Figure 5.24. The two methodologies provided very similar solutions, both in very good agreement with the reference results.

Overall, it was established that both strategies were capable of simulating accurately the time-dependent forced flow field and the thermal state of the model with significant saving in the CPU time compared to a typical fully conservative transient computation (less than $1/20^{th}$ of the run time).

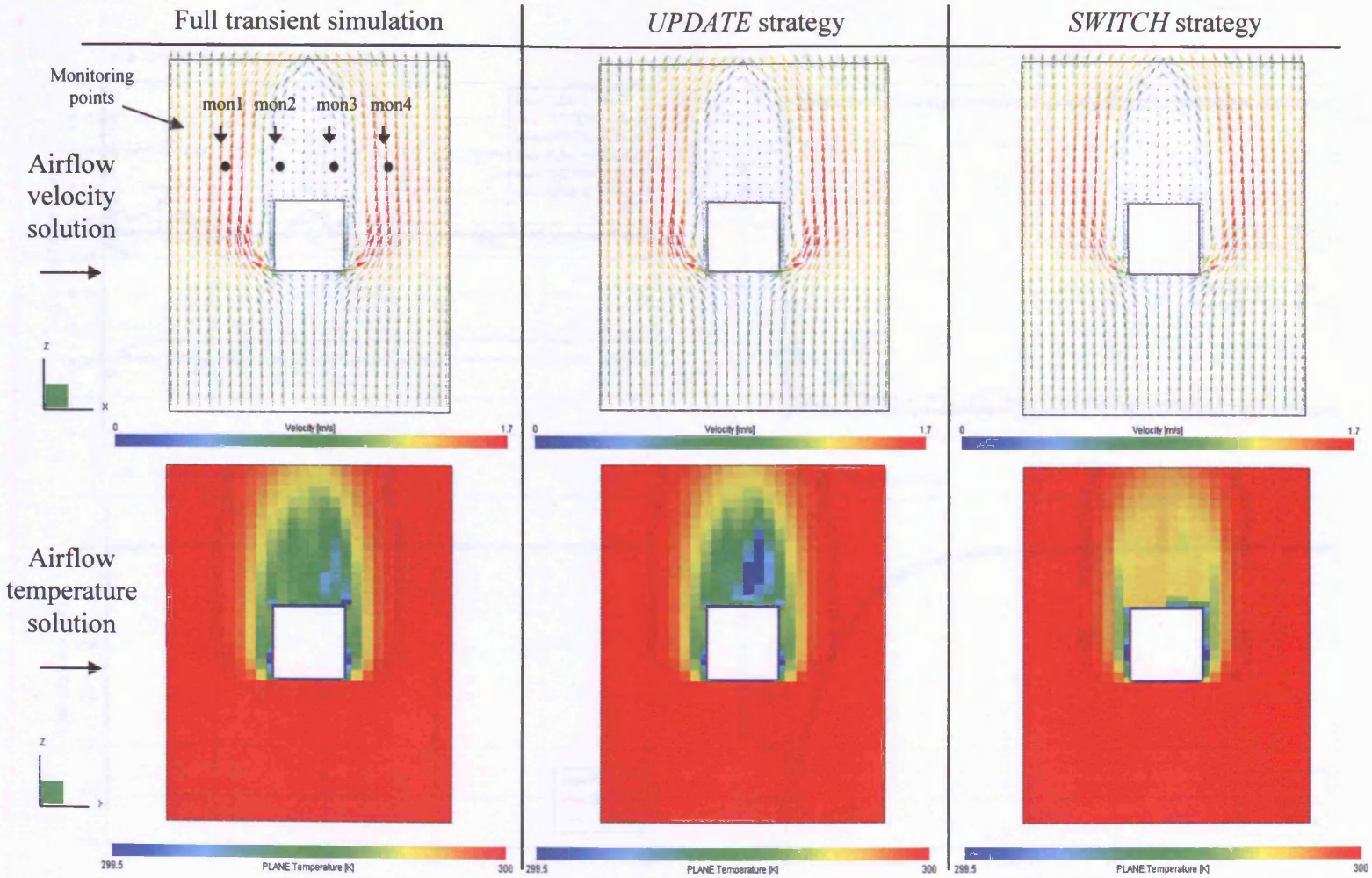

Figure 5.24 – Comparison of airflow velocity and temperature predictions after 100s from start of numerical analysis. The location of monitoring points is superimposed on the airflow map at the top left corner.

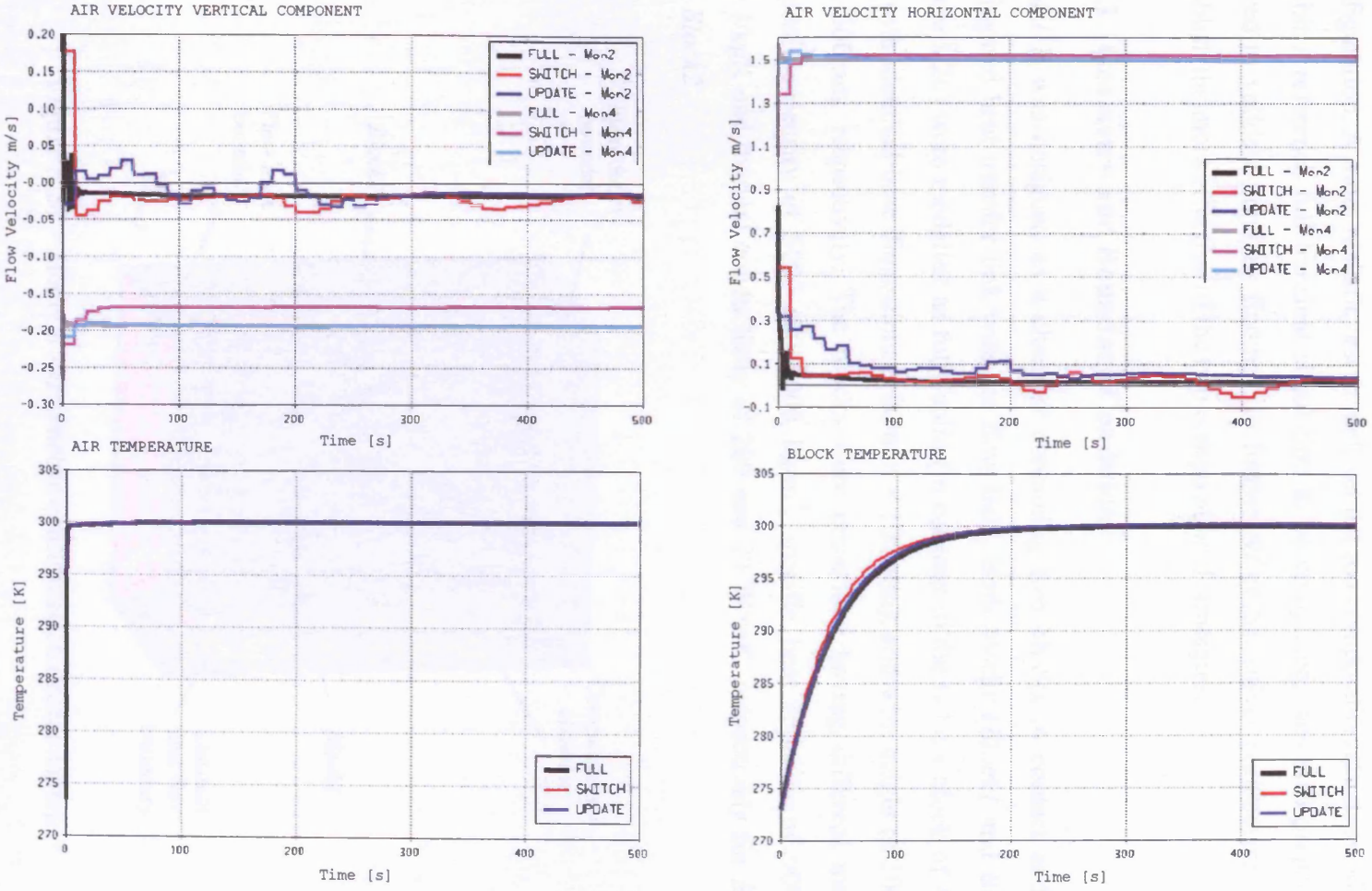

Figure 5.25 – Comparison of CFD solutions as obtained with the reference full transient simulation and with the proposed strategies.

5.4 ANALYSIS OF *MODEL B*

The previous parametric investigations were carried out on a simple 2-D geometric configuration. A more realistic test model, yet not too computationally demanding to inhibit a reference full transient simulation to be completed, was also prepared. It served to validate previous findings, to further refine the solver parameters and to establish the more effective of the two computational strategies.

5.4.1 Geometry and Boundary Conditions

Model B was designed as a chamber containing two blocks in contact and in a conjugated heat transfer link with the flow field. Both blocks (*Block1* and *Block2*, Figure 5.26) were modelled as fully solid (in contrast to the hollow block of *Model A*), with identical base dimensions (100 mm × 100 mm), and with height of 100 mm and 300mm, respectively. The blocks were prescribed having different material properties: density of 3000 and 8000 kg/m^3, specific heat capacity of 900 and 450 J/kgK and thermal conductivity of 200 and 70 W/mK, respectively for *Block1* and *Block2*

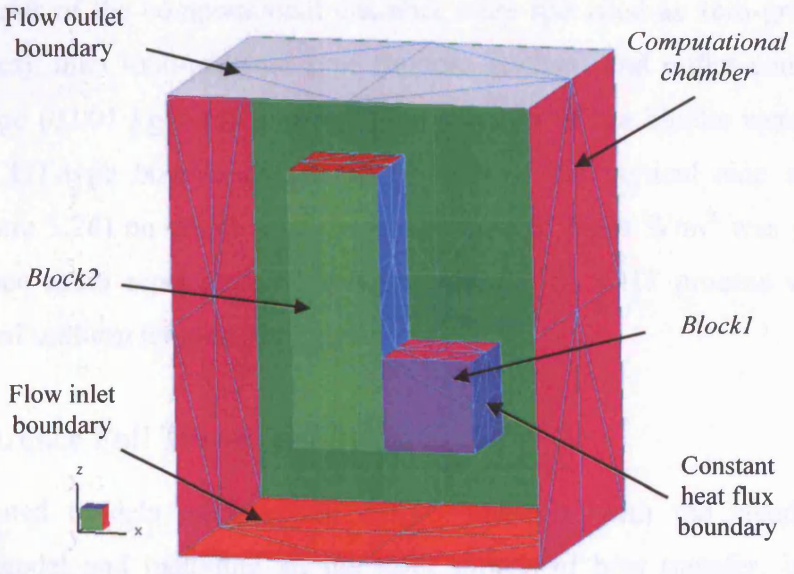

Figure 5.26 – *Model B* - Geometric configuration (inside view).

The computational chamber, representing the boundaries of the fluid domain, had a volume of (300×400×500) mm^3. The mesh consisted of a total of 19,300 cells for the airflow, 1,330 cells for *Block1* and 3,400 cells for *Block2* (average cell size of

20 mm); a smaller cell size (5 mm) was imposed at the boundaries. Quantitative information on the convective plume rising on the side of *Block2* was extracted, for data comparison, from ten monitoring points assigned to cells on a horizontal line within the fluid domain, Figure 5.27.

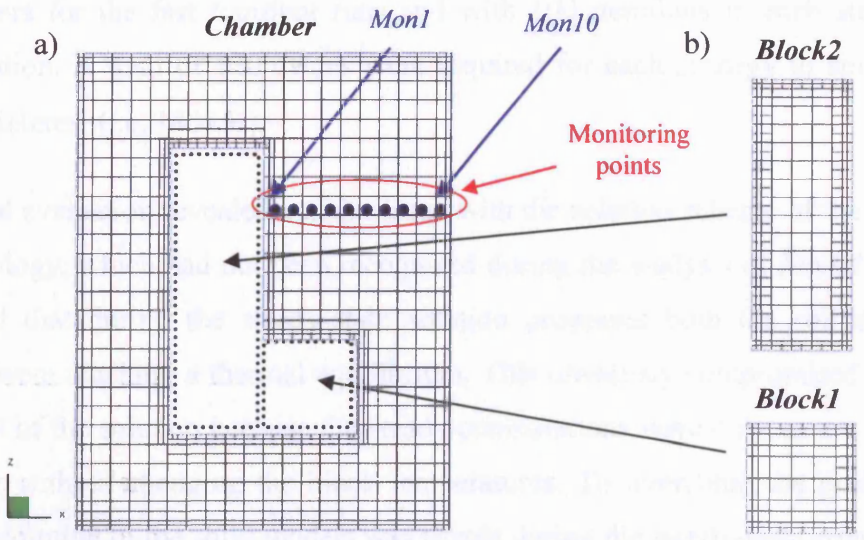

Figure 5.27 – *Model B* - Slice view of Cartesian meshes: (a) air domain mesh with location of monitoring points; (b) solid domain meshes.

The boundaries of the computational chamber were specified as zero-gradient type (side surfaces), inlet total-pressure type (bottom surface) and outlet constant mass flow rate type (0.001 kg/s, top surface). The surfaces of the blocks were all set as "external" CHT-type boundaries except for one of the vertical side surfaces of *Block1* (Figure 5.26) on which a constant heat flux of 5000 W/m^2 was prescribed, therefore once again representing transient heating. The CHT process was solved from an initial uniform temperature condition of 273K.

5.4.2 Reference Full Transient Simulation

The conjugated models were solved fully transiently with the standard $k-\varepsilon$ turbulence model and including all the three modes of heat transfer, in order to "challenge" the accuracy of the transient strategies on thermal conditions similar to the ones characterising the underhood compartment studied in this thesis. The full transient simulation was run for 90,000 timesteps, each of 0.01s (i.e. physical timeframe of 900s). The CPU runtime was of 15,810 minutes.

5.4.3 Simulation with Transient Strategies and Data Comparison

The setup of the *UPDATE* methodology consisted of fast transient computations progressing in physical time by 5s (1s-timestep) and full transient computations with 100 timesteps of 0.01s. The *SWITCH* methodology was set up with the same parameters for the fast transient runs and with 100 iterations in each steady-state computation. A total of 180 cycles were required for each strategy to simulate the 900s of interest (i.e. 180×5s).

A careful evaluation revealed a major issue with the solution scheme of the *SWITCH* methodology, which had not been recognised during the analysis of *Model A*. It was observed that during the steady-state solution processes both the solids and the airflow were reaching a thermal equilibrium. This obviously compromised the time-accuracy of the solution because the steady computations were only meant to update the flow without changing the block temperatures. To overcome the problem, the thermal solution of the solid models was frozen during the steady-state computations by de-selecting the material specifications of the solids but leaving unaltered the thermal links with the fluid domain. Figure 5.28 presents the equations solved by the strategies during each methodology cycle, which refine the proposed schemes previously given in Figures 5.2 and 5.3.

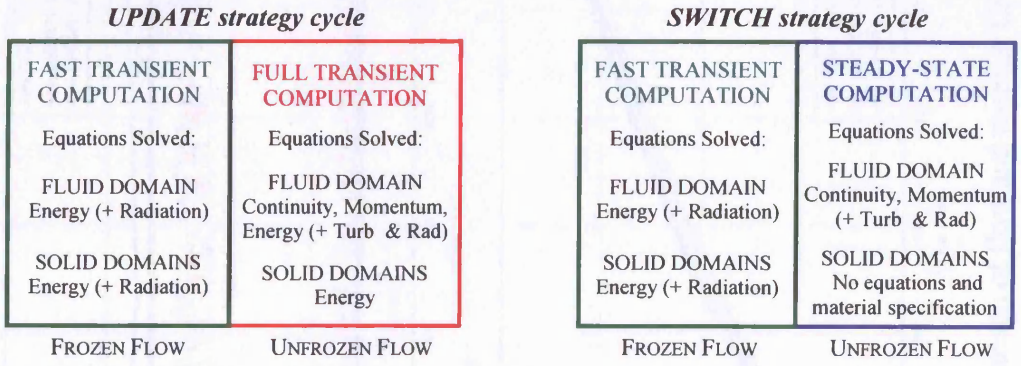

Figure 5.28 – Refined solution schemes for fast transient simulation strategies (equations solved per methodology cycle).

The flow and thermal solutions obtained by applying the proposed calculation procedures (red and blue lines in Figure 5.29) showed a remarkably good agreement with reference data (black line). The vertical velocities extracted at two monitoring points (*Mon3* and *Mon5*) were predicted with a discrepancy of only 0.1 m/s.

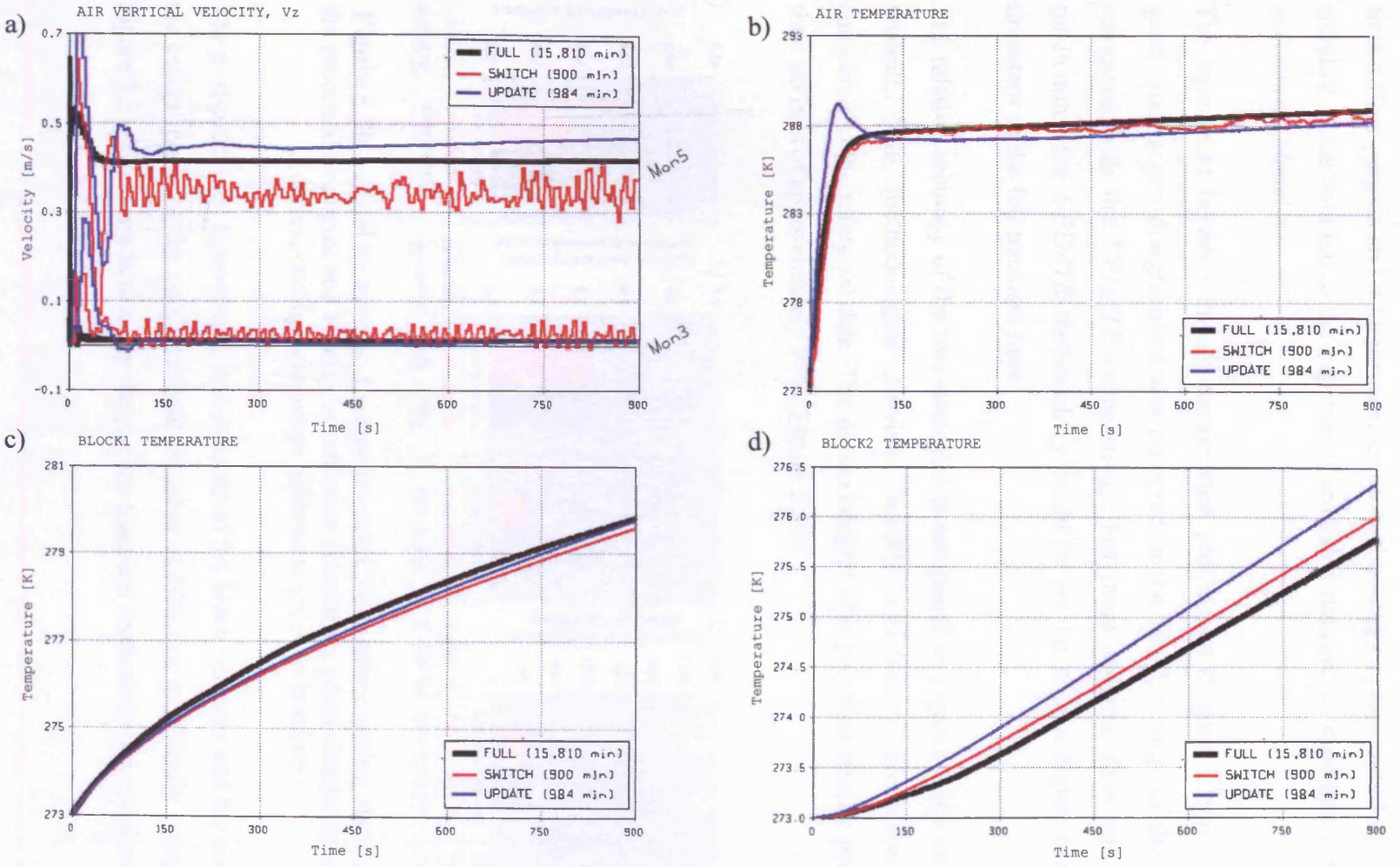

Figure 5.29 – Comparison of flow and thermal CFD solutions obtained with full transient, *UPDATE* and *SWITCH* simulations.

The solutions were however observed to be affected by numerical oscillations, especially in the early part of the investigated timeframe (Figure 5.29a). Shorter frozen flow periods and a larger number of methodology cycles would improve the stability of the solution at the expense of extended runtime, as established from the analysis on *Model A*.

The agreement between the air temperature predictions (Figure 5.29b) was very good. The largest disagreement was observed in the 30s-75s range of the solution computed with the *UPDATE* methodology. For more accurate flow and thermal predictions, the *UPDATE* methodology could be set up with a higher number of timesteps in the full transient runs.

The relative accuracy of the two strategies is compared in Figures 5.30a and 5.30b. Overall, both methodologies provided equally satisfactory predictions when compared to the reference data. The methodologies also provided similar processing time savings of approximately 94%, Figure 5.30c.

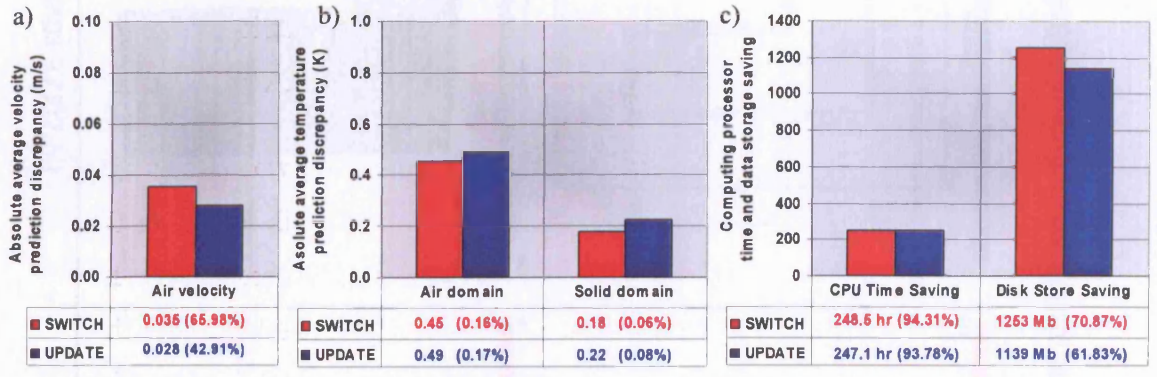

Figure 5.30 – Absolute average discrepancy and CPU runtime saving obtained with the proposed strategies and relative to reference simulation when simulating *Model B* (corresponding percentage difference given in brackets).

The post-processed temperature distributions of the block surfaces and the airflow on the central plane of the computational chamber at 600s are graphically compared in Figure 5.31. Good predictions by the pseudo-transient methodologies are shown.

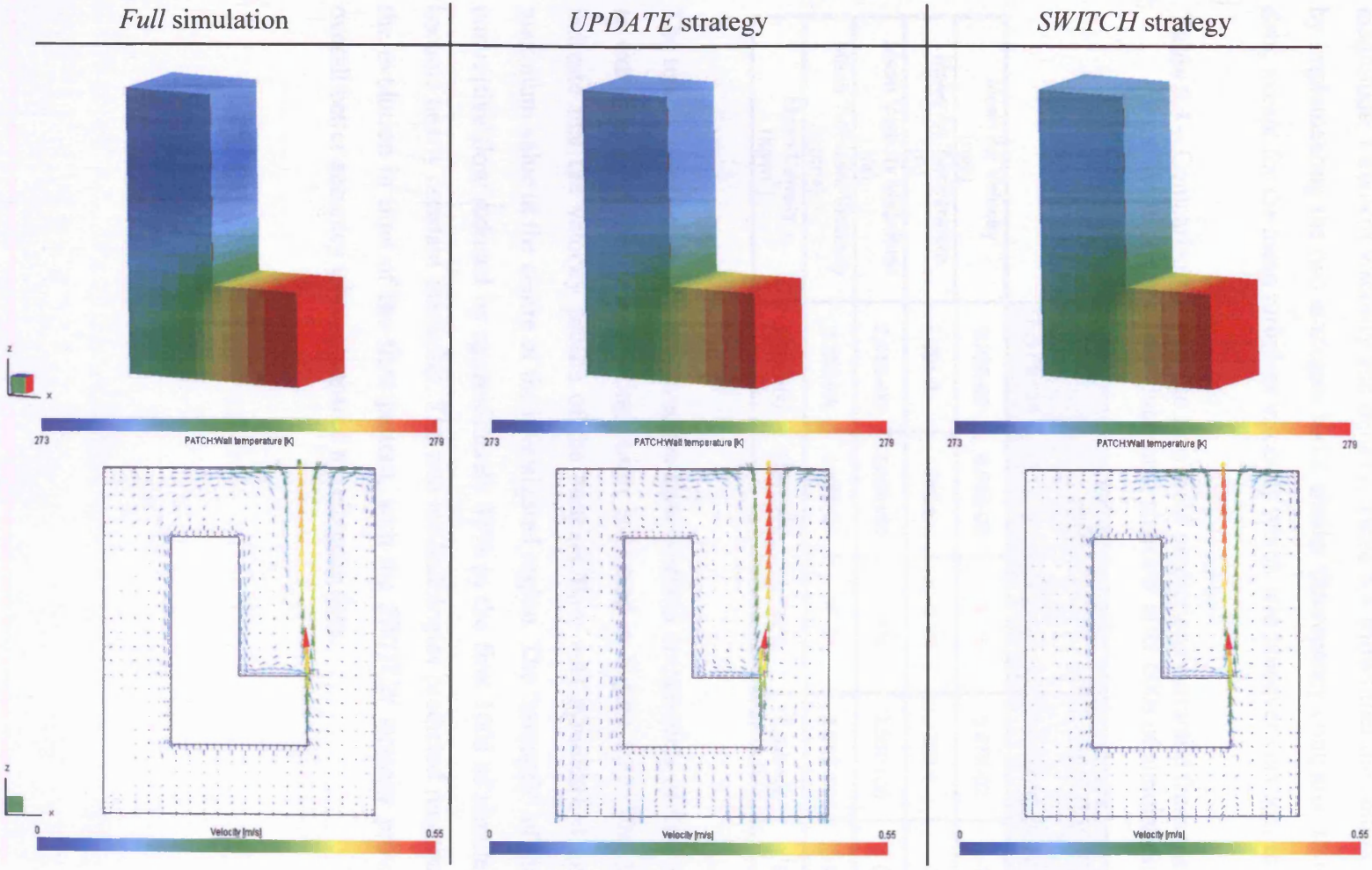

Figure 5.31 – Comparison of thermal and airflow predictions obtained with full transient, *UPDATE* and *SWITCH* simulations at 600s.

The z-x plane at the centre of the compartment was further examined by extracting from the three flow solutions the mean values for the velocity, temperature, vorticity magnitude, turbulent viscosity and density. Table 5.4 shows that the results obtained by implementing the two strategies had a similar discrepancy compared to reference data, except for the mean turbulent viscosity which was however very low in value.

Table 5.4 – Comparison of average flow field predictions extracted from the vertical plane at the centre of computational chamber after 600s of simulation.

	FULL	*SWITCH*		*UPDATE*	
	Predicted	Predicted	Discrepancy	Predicted	Discrepancy
Mean Air Velocity (m/s)	6.20E-02	6.53E-02	5.3%	5.97E-02	-3.7%
Mean Air Temperature (K)	291.0	290.8	-0.1%	290.4	-0.2%
Mean Vorticity Magnitude (1/s)	2.54E+00	2.60E+00	2.1%	2.55E+00	0.2%
Mean Turbulent Viscosity (kg/ms)	2.25E-04	2.67E-04	18.7%	1.84E-04	-18.2%
Mean Density (kg/m^3)	1.20E+00	1.20E+00	0.1%	1.20E+00	0.2%

The temporal evolution of the convective flow (vertical components of flow velocity) as extracted from the 10 monitoring points is plotted in Figure 5.32. The 3-D plots indicate that the velocity profile of the buoyant flow was symmetrical and had a maximum value at the centre of the investigated region. The "strength" of the natural convective flow reduced by approximately 35% in the first 100s of simulation and became nearly constant thereafter. The two methodologies predicted reasonable well the evolution in time of the flow pattern, with the *SWITCH* strategy providing an overall better accuracy when compared to reference data.

Full Transient Simulation

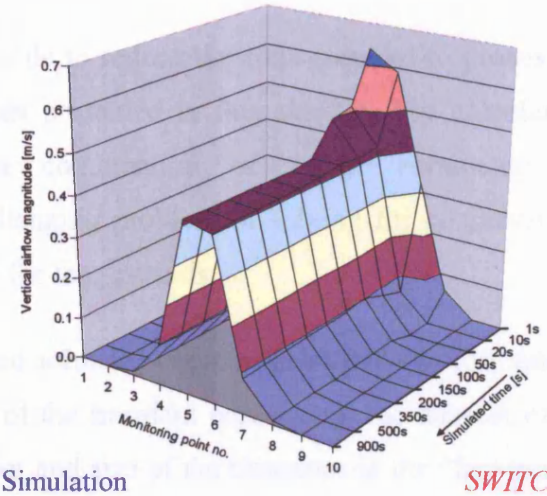

UPDATE Simulation

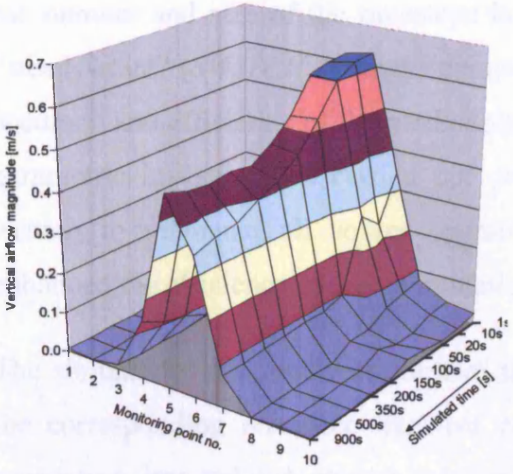

SWITCH Simulation

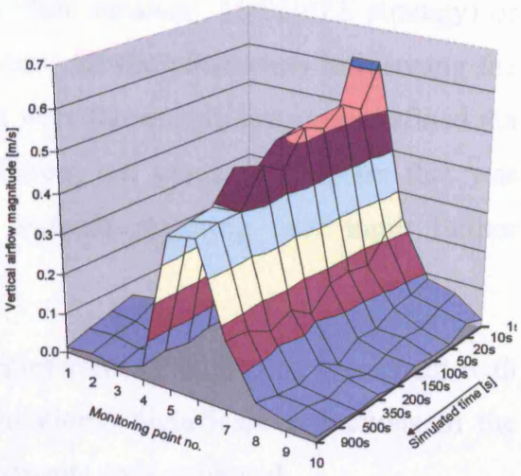

Figure 5.32 – Time-dependent development of convective plume as computed at monitoring cells (point no.1 to 10 from left to right in Figure 5.27) with fully transient, *UPDATE* and *SWITCH* simulations.

5.5 CLOSURE

Two methodologies able to reduce the time required to process fully transient CFD simulations have been presented in this chapter. The calculation procedures were developed using a combination of solver parameters to overcome the computationally challenging problem of solving for conservation of momentum in time-marching mode for long periods.

Based on the proposed solution schemes, three main factors were found to affect the overall performance of the transient procedures: the number of methodology cycles performed, the number and size of the timesteps in the "fast transient" computations, the number and size of the timesteps in the "full transient" (*UPDATE* strategy) or "steady-state" (*SWITCH* strategy) computations. All the parameters influencing the accuracy and efficiency of the methodologies were thoroughly tested and refined via parametric investigations carried out on different test cases. A program that was written to automate all solver operations without requiring user input further enhanced the efficiency of the computations.

The simulations obtained with the two strategies were in very good agreement with the corresponding reference transient computations. Significant reductions in the processing time and disk storage space requirements were achieved.

Chapter 6

DATA COMPARISON – TRANSIENT

6.1 PRELIMINARY REMARKS

The parametric investigations presented in the previous chapter established that the steady-state solution process for updating the frozen flow simulations was the most effective and computationally efficient procedure to mimic a full transient CFD computation.

The *SWITCH* pseudo-transient calculation methodology was thus implemented to simulate the scaled underhood model while cooling down from a high temperature condition. The resulting time-dependent block surface and air plane temperature predictions, and the patterns of the thermally-driven airflow were examined and compared with experimental measurements. The objective of the analysis was to assess the effectiveness of the proposed calculation methodology, in particular with reference to the time-accuracy of the predictions and the overall speed of the computation. The present chapter discusses the transient CFD results and quantifies any discrepancy with measured data.

6.2 ANALYSIS PROCEDURE

6.2.1 Laboratory Measurements

Flow field and temperature measurements were taken after the cartridge heaters embedded in the blocks were turned off to replicate the heat soak operating condition. The temperature distribution of both block surfaces and air planes was recorded continuously for 30 minutes with K- and T-type thermocouples. Flow field measurements were taken with the PIV instrumentation either every 5 seconds for the first minute after the heaters were turned off (*T1* procedure, Table 2.6) or every 15 seconds at different time intervals within a 30-minute timeframe (*T2* procedure, Table 2.7). The measurements were taken in replicates and the results were ensemble averaged. The resulting PIV vector plots represented therefore quasi steady-state snapshots of the flow at regular intervals.

6.2.2 VECTIS Computations

Setup of CFD Analysis – The underhood model was simulated for 30 minutes while cooling down from the thermal condition computed by the steady-state simulation (steady-state solution modelling radiation, Chapter 4). The coupling between momentum and continuity equations was governed by the pressure-correction-solver scheme with the PISO algorithm. For the solution of the velocity field, the turbulent flow was modelled by the standard $k-\varepsilon$ isotropic eddy-viscosity model of Launder and Spalding [1974], in conjunction with the wall functions representing the turbulent wall boundary conditions [Tennekes and Lumley 1972]. For the solution of the thermal field, all three mechanisms of heat transfer, i.e. convection, conduction and radiation, were included in the analysis. The convective heat transfer was modelled with the Reynolds analogy between momentum and heat transfer and the assumption of constant turbulent Prandtl number (≈ 0.9) [Ricardo Ltd 2004b]. The heat conduction was solved in the solids by directly specifying the corresponding material properties. Thermal radiation between the different surfaces was calculated via the specific model incorporated into VECTIS, which was based on the diffuse theory formulation [Mahan 2002]. Accordingly, the distribution of radiated heat to surrounding surfaces (Figure 6.1a) was determined from the value of the view factors

computed on selected "patches" prescribed on the surfaces of the underhood blocks (Figure 6.1b). The radiation model was fully coupled with the flow field solver.

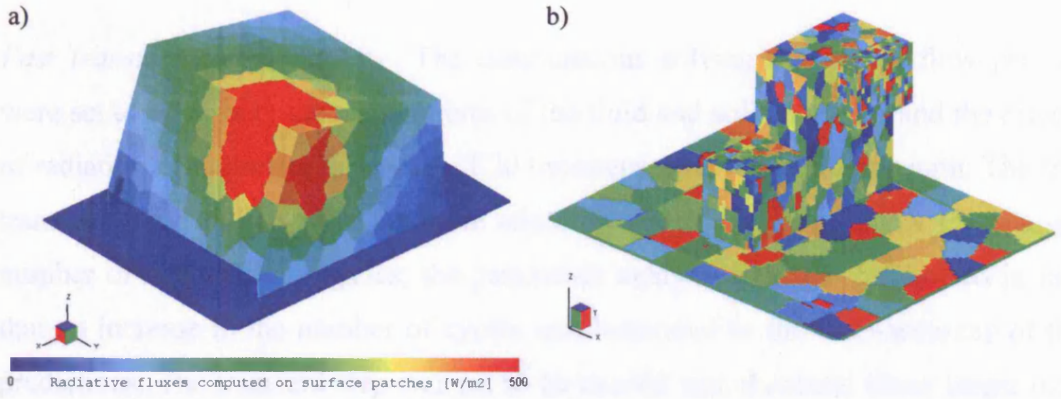

Figure 6.1 – Radiation modelling: (a) heat flux predictions on compartment surfaces, rear view (area above turbocharger shown to be particularly affected by radiated heat); (b) surface patches for view factor calculation (compartment not shown).

Between the fluid-solid interfaces of the components of thermal interest, a conjugate heat transfer was assumed to take place. The governing equations for the velocity and thermal fields were solved in a coupled approach, where the velocity field affected the thermal field via convective heat transfer and the thermal field affected the fluid velocity indirectly via the equation of state. As for the steady-state analysis, the transient CHT simulation consisted of five solid models (engine, gearbox, turbocharger, glass boundaries of the underhood and insulating pad between engine and turbocharger bocks) and one fluid model (air domain).

Mesh and Boundary Conditions – The calculations were based on the same grid employed for the steady-state simulation, i.e. approximately 330,000 cells for the mesh discretising the flow domain and a total of 67,000 cells for the solid models. Identical boundary conditions were also prescribed (see Section 3.3.2), except for the heat fluxes in the blocks that were set equal to zero. The control volume of the computational chamber was configured with a total pressure bottom boundary and a constant mass flow rate upper boundary (-0.001 kg/s). Model surfaces not exchanging thermal information were specified as being adiabatic.

Pseudo-Transient Methodology – Based on the preliminary evaluation of the various solver parameters and striking a compromise between accuracy and CPU runtime, the *SWITCH* methodology was setup as follows:

Fast transient computations – The computations solving the frozen flow periods were set to solve only the temperatures of the fluid and solid domains and the effects of radiation heat transfer for a total of 20 timesteps, each 1 second in length. The fast transient computations were set to be relatively short in order to allow for a larger number of methodology cycles; the parametric analysis (Chapter 5) showed in fact that an increase in the number of cycles was beneficial to the time-accuracy of the predictions. The transient step was set to be exactly one thousand times larger than its optimal size for a fully conservative transient computation of the same model, i.e. 1000×0.001s (based on a 10^{-6} solution convergence).

Full steady-state computations – The steady computations updating the flow field momentum were set to comprise a relatively small number of iterations (50 per cycle) in order to achieve an overall fast analysis without significantly affecting the accuracy of the simulation. The optimal number of iterations was determined after establishing that the momentum residuals of the steady-state computations reduced to approximately 10^{-4} at the end of the first 100s of simulated time (i.e. after 5 cycles). The steady-state processes solved all governing equations for the fluid domain except for the enthalpy. Flow turbulence was fully modelled, and the momentum and continuity equations were coupled via the SIMPLE algorithm. Solution stability and convergence were enhanced by the Multigrid Iterative Solver scheme of VECTIS [Ricardo Ltd 2004b]. The solver was set to perform up to 100 iterations through the mesh of the fluid domain to increase the convergence of the pressure equation. The solid CHT domains were fully coupled with the airflow; however, as found to be necessary from the results of the analysis on *Model B* (Chapter 5), the material properties were not specified. The thermal solution was therefore frozen during the steady-state computations with the exception for surface radiation, which was computed based on the solid boundaries being at the fixed temperature determined by the fast transient runs.

Number of methodology cycles – Since the advancement in time of the simulation during each methodology cycle was exactly equal to the time simulated by the transient computations (i.e. 20s), a total of 90 iterations were prescribed in order to cover the timeframe of interest (20s × 90 = 1800s).

Time-Dependent Solution and CPU Runtime – Figure 6.2 presents the variation of the flow velocity components with time as calculated at two different monitoring points, one close to the centre of the air plane at the outlet of the underhood (Figure 6.2a, point F2) and the other on the air plane located in front of the engine and gearbox blocks (Figure 6.2b, point A6). The flow vectors remained relatively constant in magnitude throughout the investigated timeframe. The time-dependent air temperatures predicted at these locations and also at the nearby monitoring points are plotted in Figure 6.2c. As shown, the temperature of the air was predicted to initially increase before levelling off during the cooling of the blocks.

The engine and gearbox were predicted, Figure 6.3(a), to cool by approximately 8 degrees (blue and red lines in the data plot). The temperature of the turbocharger reduced from approximately 640K to 450K (green line) with a higher cooling rate at the beginning. Figures 6.3(b) to 6.3(f) display plots of the convective, conductive and radiative heat transfer for, respectively, the airflow, the engine, gearbox and turbo blocks, and the glass boundaries of the model. The predicted average temperature of the CHT models is superimposed in each sub-figure (green line).

The average time taken to simulate 1 second of the thermal process with the proposed pseudo-transient methodology was approximately 5 minutes; a typical fully conservative transient simulation took approximately 60 minutes using the same hardware unit, as it was determined when solving 1 minute of cooling with timesteps of 0.001s. The application of the devised calculation methodology resulted therefore in a saving in CPU runtime greater than 90% compared to solving the model with a conventional transient simulation. The latter would have taken more than 75 days to complete.

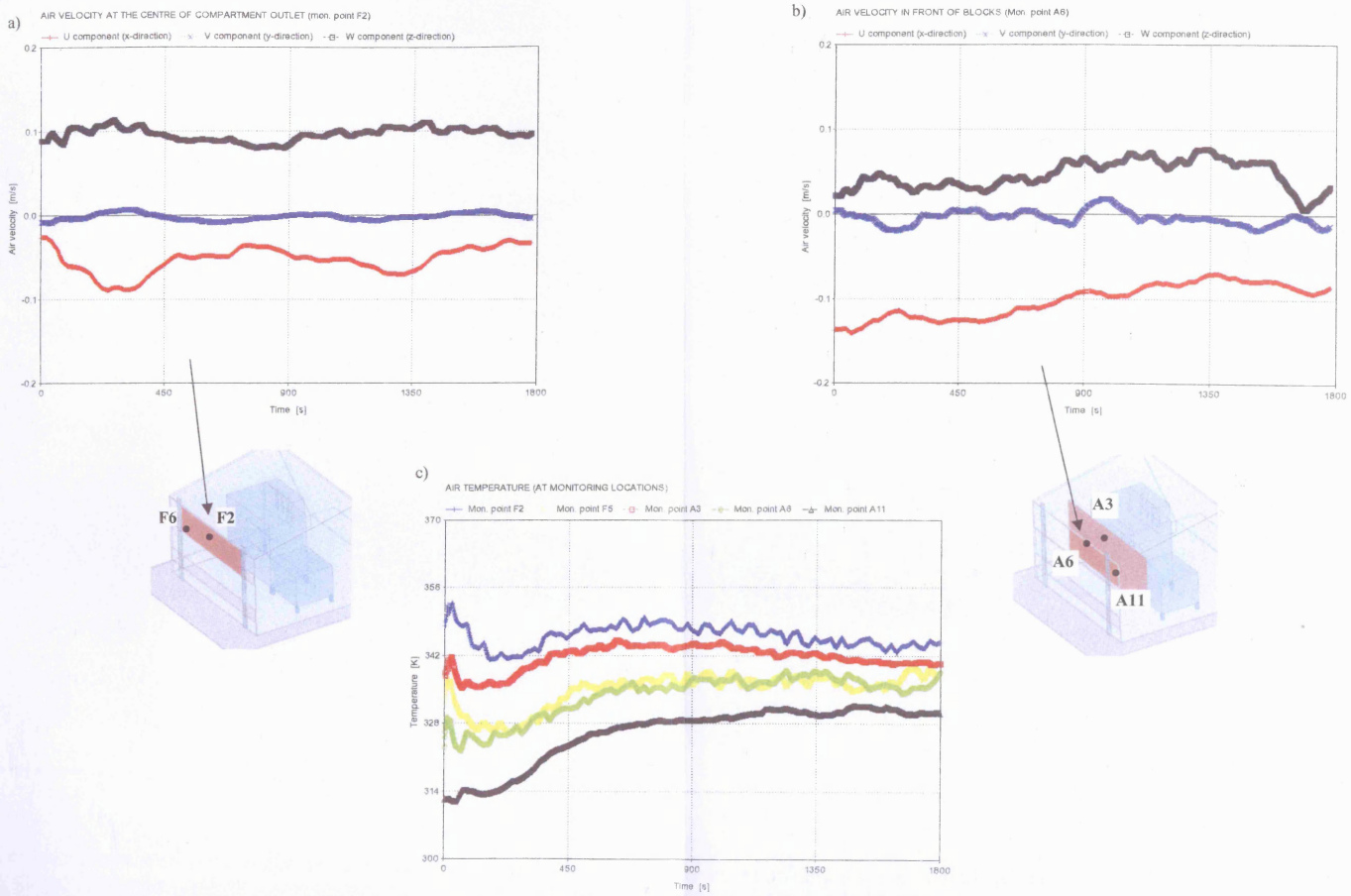

Figure 6.2 – Velocity and thermal flow solutions computed with pseudo-transient methodology at random locations within the underhood

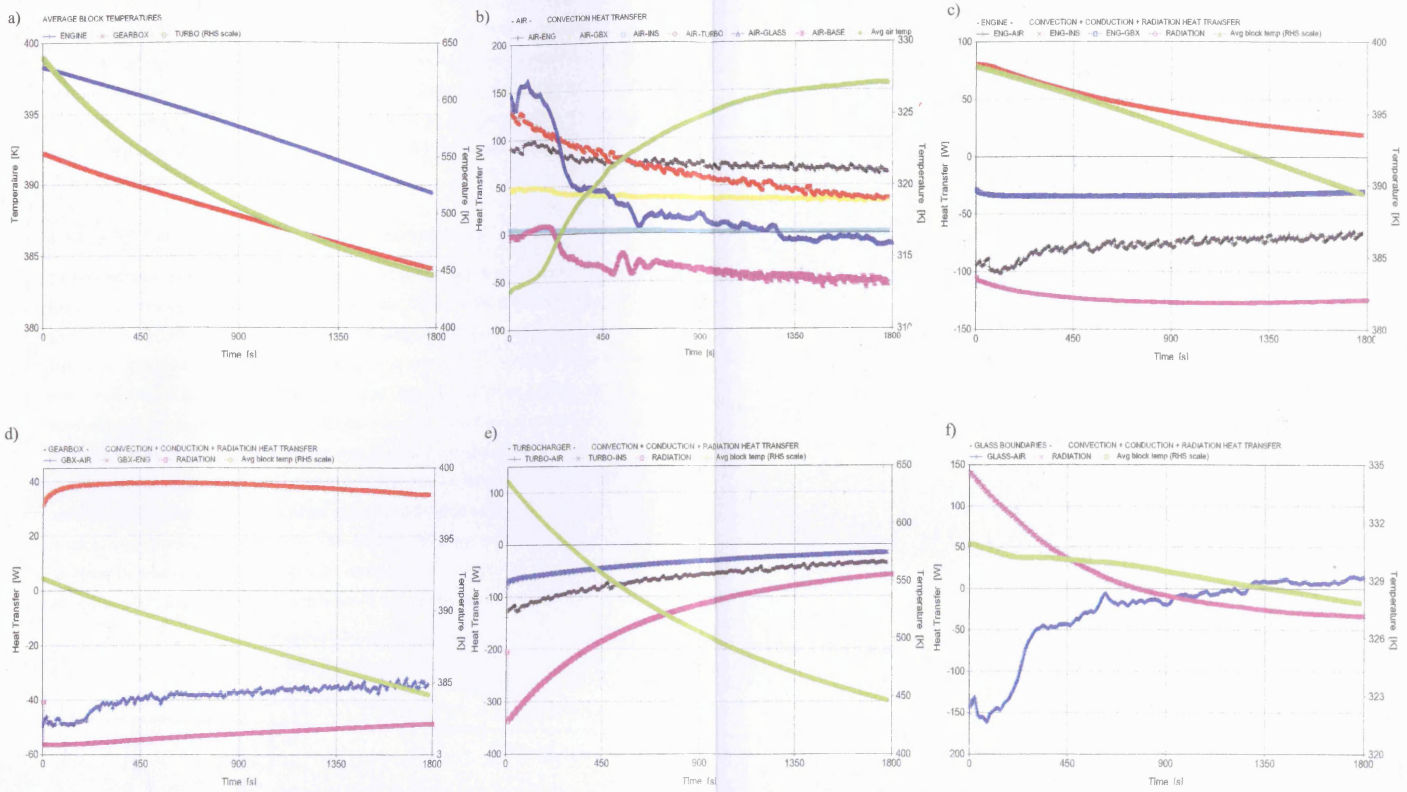

Figure 6.3 – Predicted average temperature variation and time-dependent heat transfer for each of the thermally conjugated CFD domain

6.3 DATA COMPARISON

Temperature measurements and PIV results for selected planes/regions were compared with the corresponding CFD predictions, as separately discussed in the following sub-sections. The thermally investigated planes were chosen to represent the time-dependent temperature distribution of at least one surface of each solid component. The flow field regions were selected to be characterised by unique thermal features and flow patterns, such as vertical temperature stratification and flow re-circulation.

6.3.1 CFD Comparison with Thermal Measurements

Engine Block – The experimental data is plotted in Figure 6.4, as an average surface temperature among all thermocouple measurements, while the CFD data represents the average of the temperature predictions extracted at the corresponding co-ordinate locations. The CFD thermal results were characterised by a constant temperature over-prediction of approximately 5 degrees and by a slightly lower cooling rate. The methodology employed for the computation was considered not responsible for the initial temperature discrepancy, which was expected as established by the steady-state simulation from which the transient analysis was set to restart. The steady-state error was caused by small inaccuracies in the specification of the heat sources in the blocks, as discussed in Chapter 4. The slightly different cooling rate caused an increase in temperature discrepancy of about 5% by the end of the investigated period, a difference within the uncertainties of the experimental and CFD data.

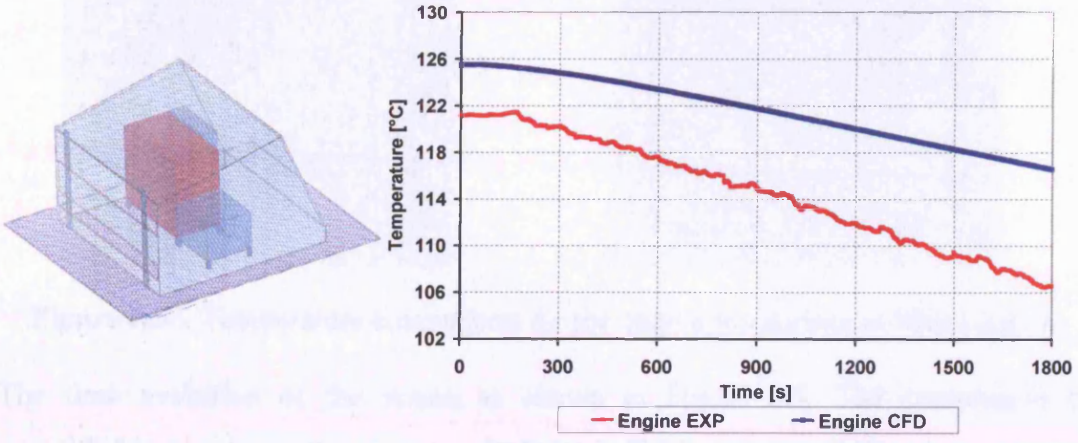

Figure 6.4 – Comparison of average temperature variation in transient (cooling) condition for the engine block.

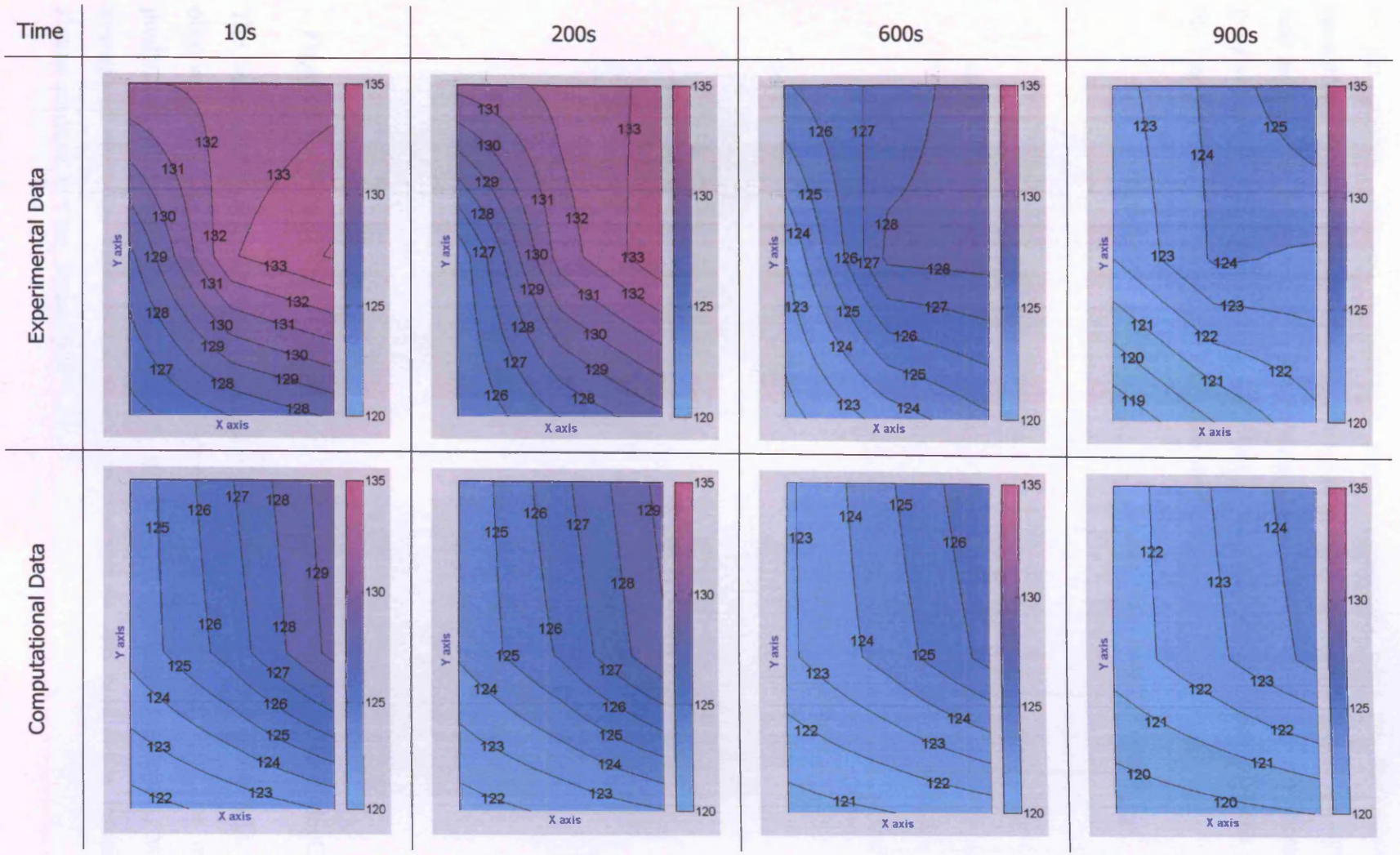

Figure 6.6 – Comparison at specific times between the measured and predicted temperature distributions on the engine top surface (degC).

The temperature predictions on the vertical surface, on the opposite side with respect to the gearbox, showed a relatively poorer agreement with the thermocouple recordings. Figure 6.7 shows for example that at 400s the bottom part of the surface was erroneously computed at a temperature above 120°C, whilst the measurements gave around 110°C. The scatter plot indicates that two measurement locations (TC No.3 and TC No.5) were excessively over-predicted.

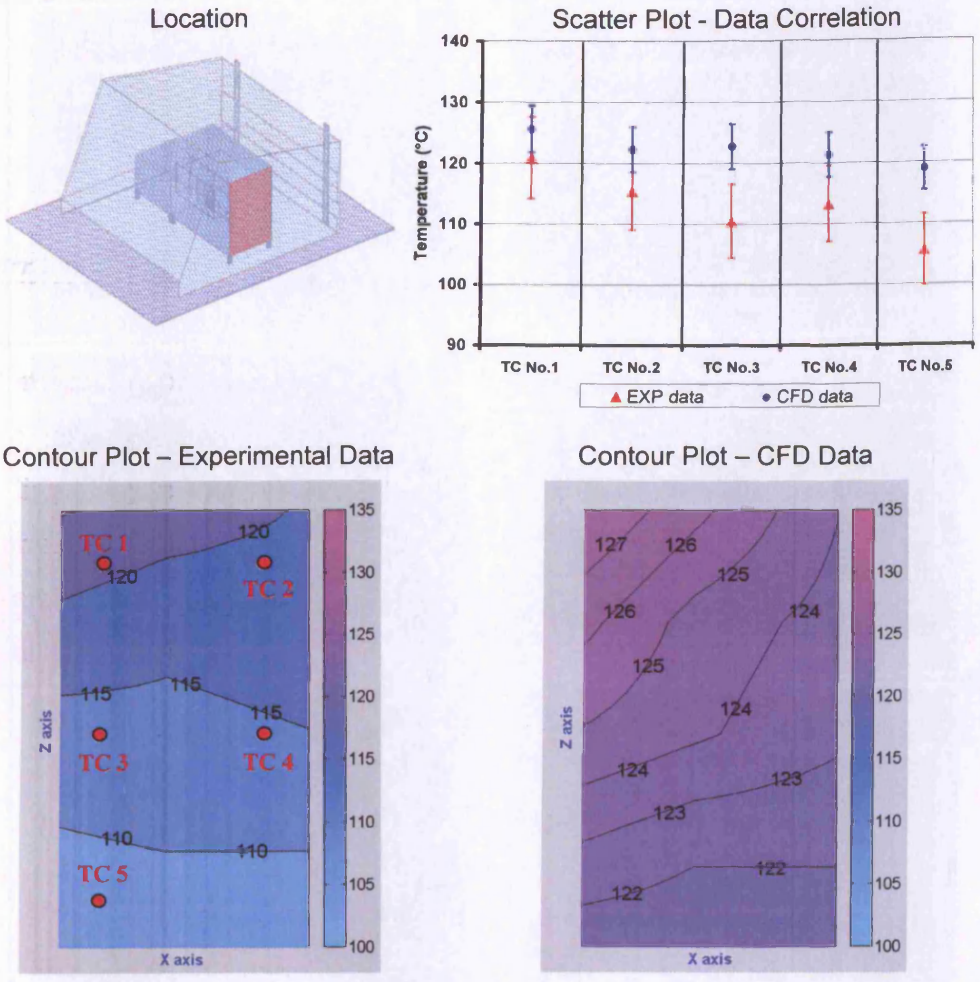

Figure 6.7 – Temperature comparison for the engine side surface at 400s (degC).

The same quantitative difference, averaging approximately to 7.5% (Table 6.1), was observed throughout the simulated timeframe (Figures 6.8 and 6.9). The over-prediction was mainly a carry over of the steady-state simulation inaccuracy, as the average discrepancy between the surface measurements and predictions remained almost constant in time, Figure 6.9.

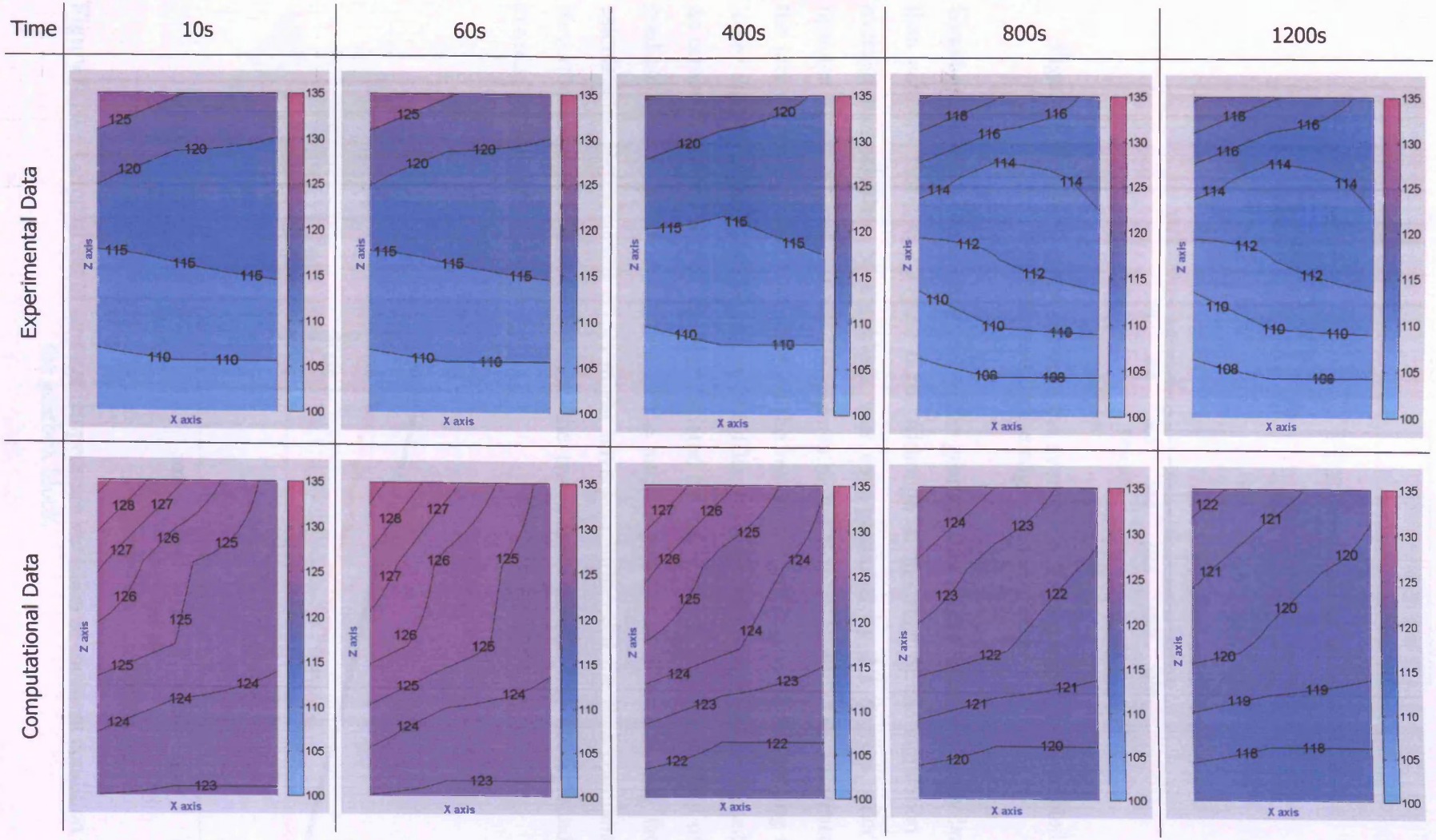

Figure 6.8 – Comparison at specific times between the measured and predicted temperature distributions on the engine side surface (degC).

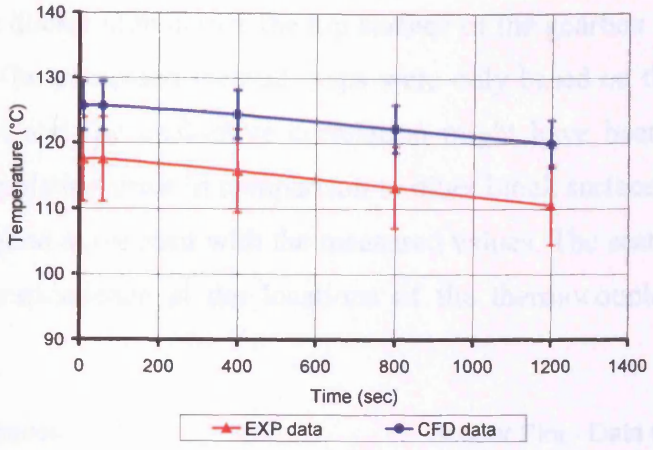

Figure 6.9 – Comparison between the averages of the measured and predicted temperatures on the engine side surface.

Gearbox Block – The cooling rate of the gearbox was predicted to be slightly larger than actually measured, Figure 6.10. Although at the start of the simulation the average thermal state of the block was over-predicted by 2.1 degrees, after 30 minutes it was estimated to be 1.4 degrees higher than measured. The difference in the rate of cooling was in contrast to the results for the engine block (cooling rate lower than measured) and therefore of difficult interpretation. It could be caused by an erroneous estimation of the heat radiated by the block, which was slightly over-predicted due to a low resolution of the surface patches used for the view factor calculations. Experimental errors might have also influenced the data comparison. Nevertheless, the difference between the two sets of results was never found to exceed 2% of their values.

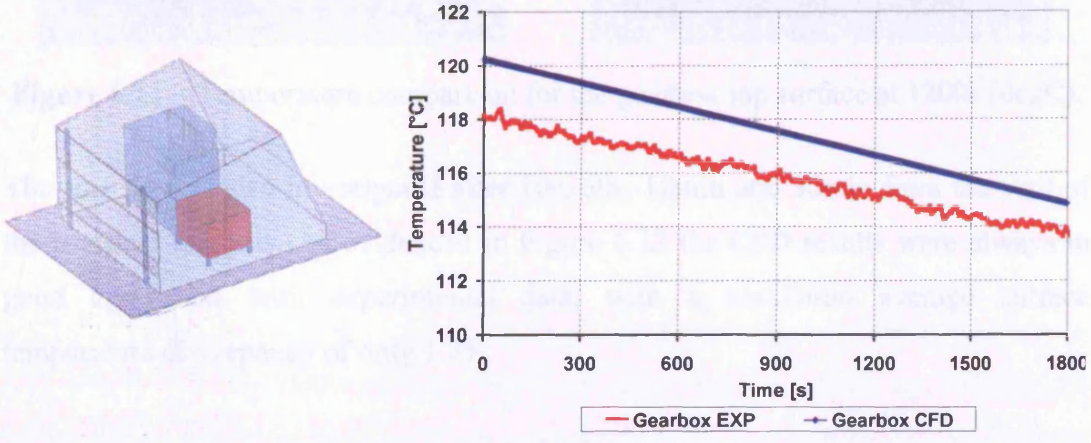

Figure 6.10 – Comparison of average temperature variation in transient condition for the gearbox block.

The temperature distribution across the top surface of the gearbox at 1200s is shown in Figure 6.11. The processed thermal maps were only based on the results of three surface locations and the qualitative correlation might have been susceptible to a higher data interpolation error in comparison to other block surfaces. The predictions were overall in good agreement with the measured values. The scatter plot reveals an exceptional correspondence at the locations of the thermocouples (0.1% average difference).

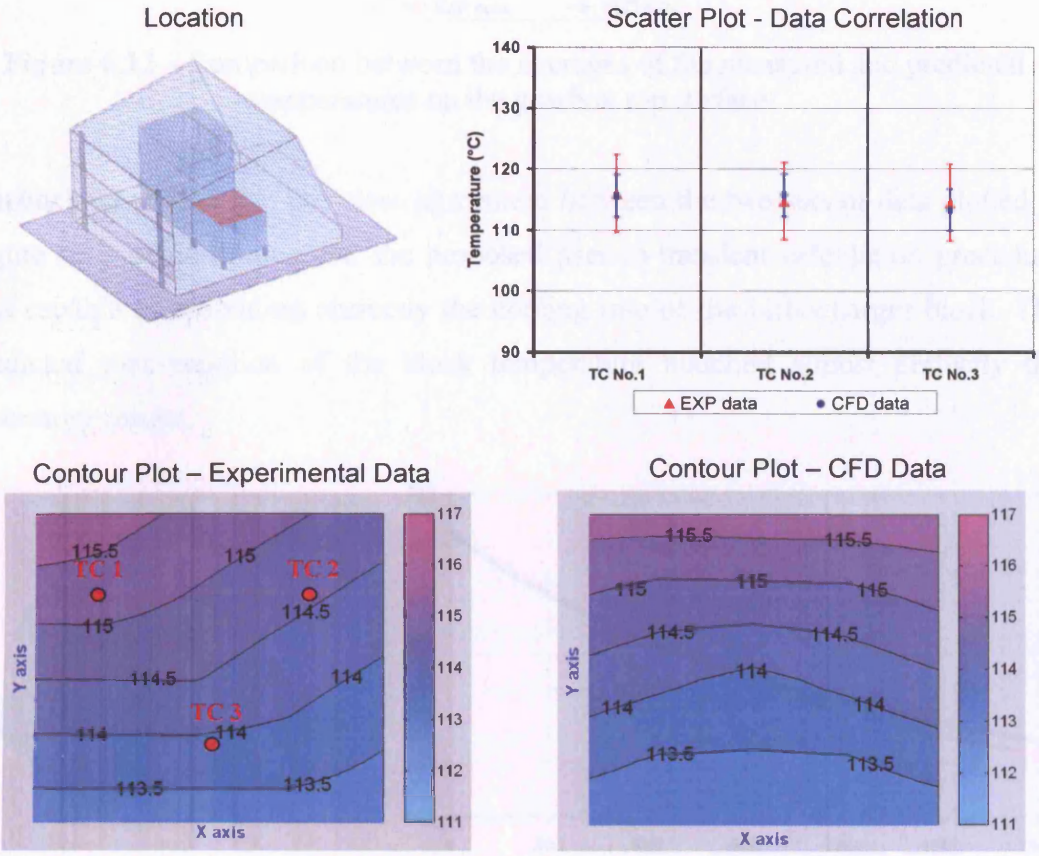

Figure 6.11 – Temperature comparison for the gearbox top surface at 1200s (degC).

The surface was also investigated after 10s, 60s, 10min and 30min from the start of the transient analysis. As evidenced in Figure 6.12 the CFD results were always in good agreement with experimental data, with a maximum average surface temperature discrepancy of only 1.7%.

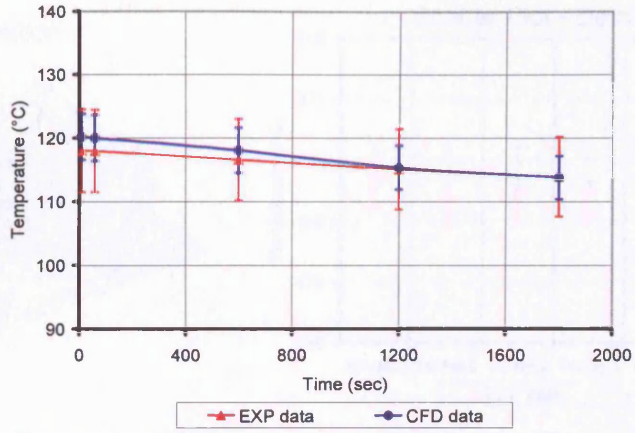

Figure 6.12 – Comparison between the averages of the measured and predicted temperatures on the gearbox top surface.

Turbocharger Block – The close agreement between the two sets of data plotted in Figure 6.13 demonstrates that the proposed pseudo-transient calculation procedure was capable of estimating correctly the cooling rate of the turbocharger block. The predicted time-variation of the block temperature matched almost perfectly the laboratory results.

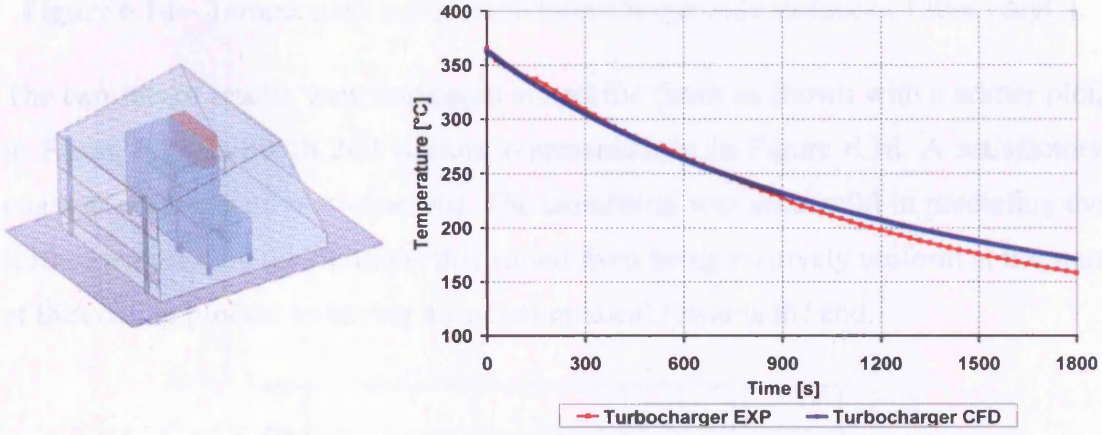

Figure 6.13 – Comparison of average transient temperature variation for the turbocharger block.

A satisfactory agreement was also obtained when comparing the measured and predicted temperatures for the side surface of the block. The scatter graph in Figure 6.14 shows that the readings were predicted with good accuracy by VECTIS at 1200s. On average, the measured temperatures were over-predicted by approximately 5%, with a maximum discrepancy of 6.2% at the lower part of the surface. The error bands in the plot did overlap.

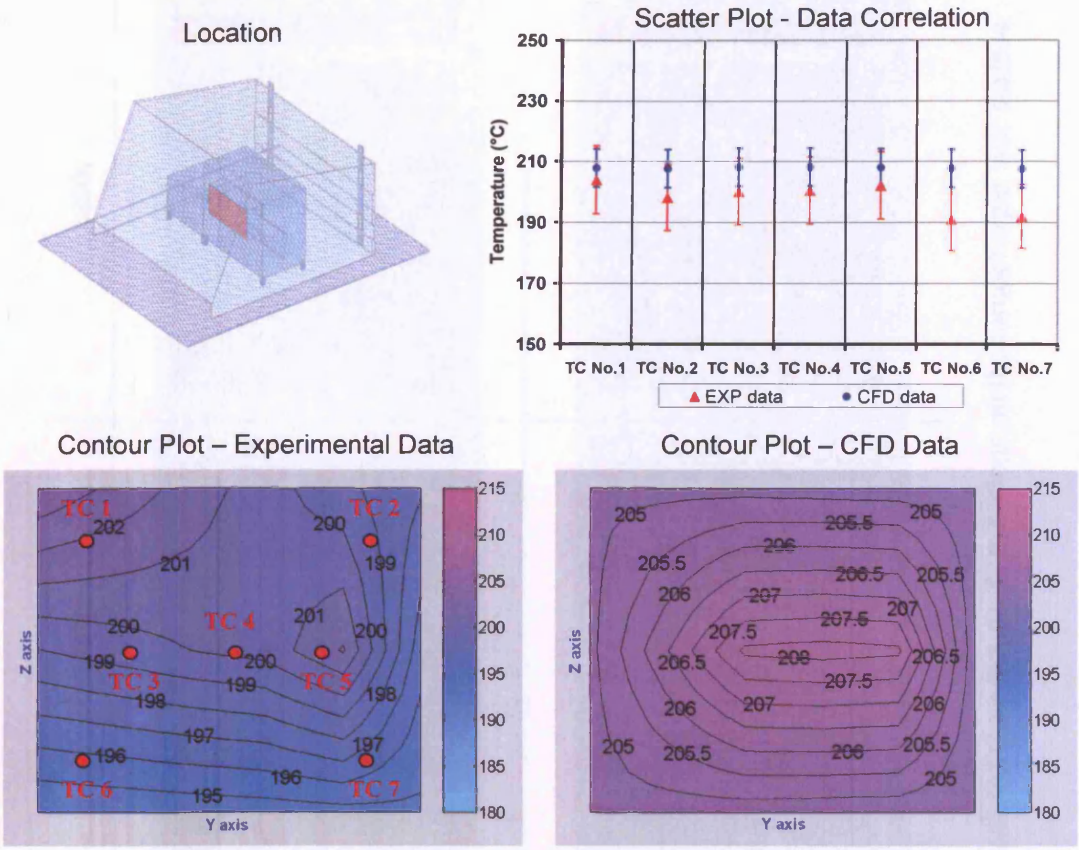

Figure 6.14 – Temperature comparison turbocharger side surface at 1200s (degC).

The two sets of results were compared at specific times as shown with a scatter plot, in Figure 6.15 and with 2-D contour representations in Figure 6.16. A satisfactory qualitative agreement was observed. The simulation was successful in predicting the surface temperature distributions that varied from being relatively uniform at the start of the cooling process to having a vertical gradient towards the end.

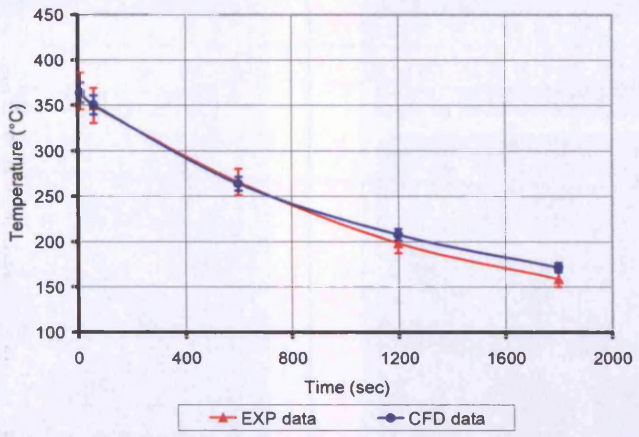

Figure 6.15 – Comparison between the averages of the measured and predicted temperatures on the turbocharger side surface.

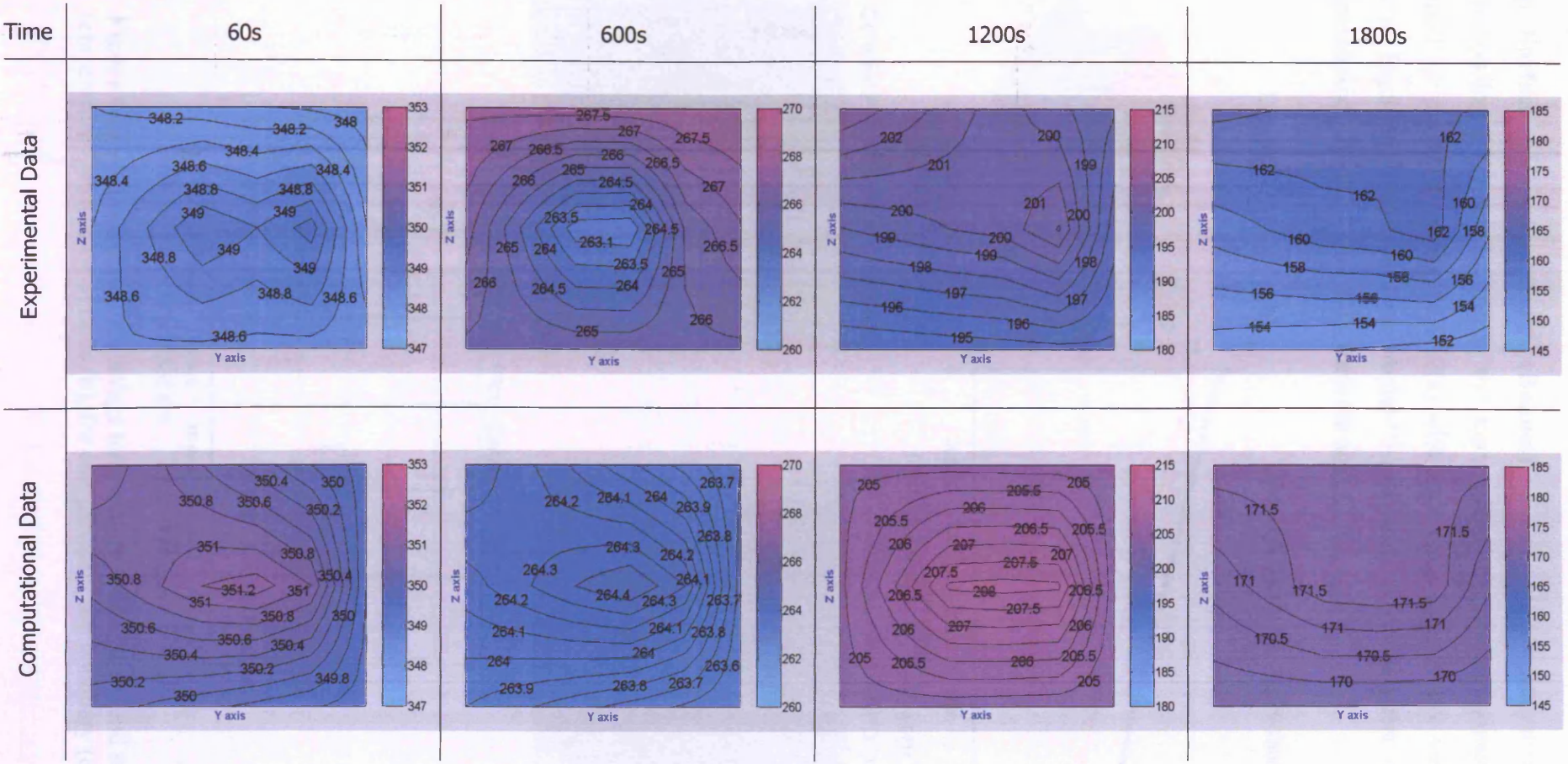

Figure 6.16 – Comparison at specific times between the measured and predicted temperature distributions on the turbocharger side surface (degC).

Top Surface of Compartment (Bonnet) – Temperature measurements and corresponding CFD predictions at the top surface of the compartment (vehicle bonnet) are presented in Figure 6.17(a) with an average temperature variation plot and in Figure 6.17(b) with two Matlab™ mappings comparing the interpolated temperature distribution after 600s from the start of the analysis.

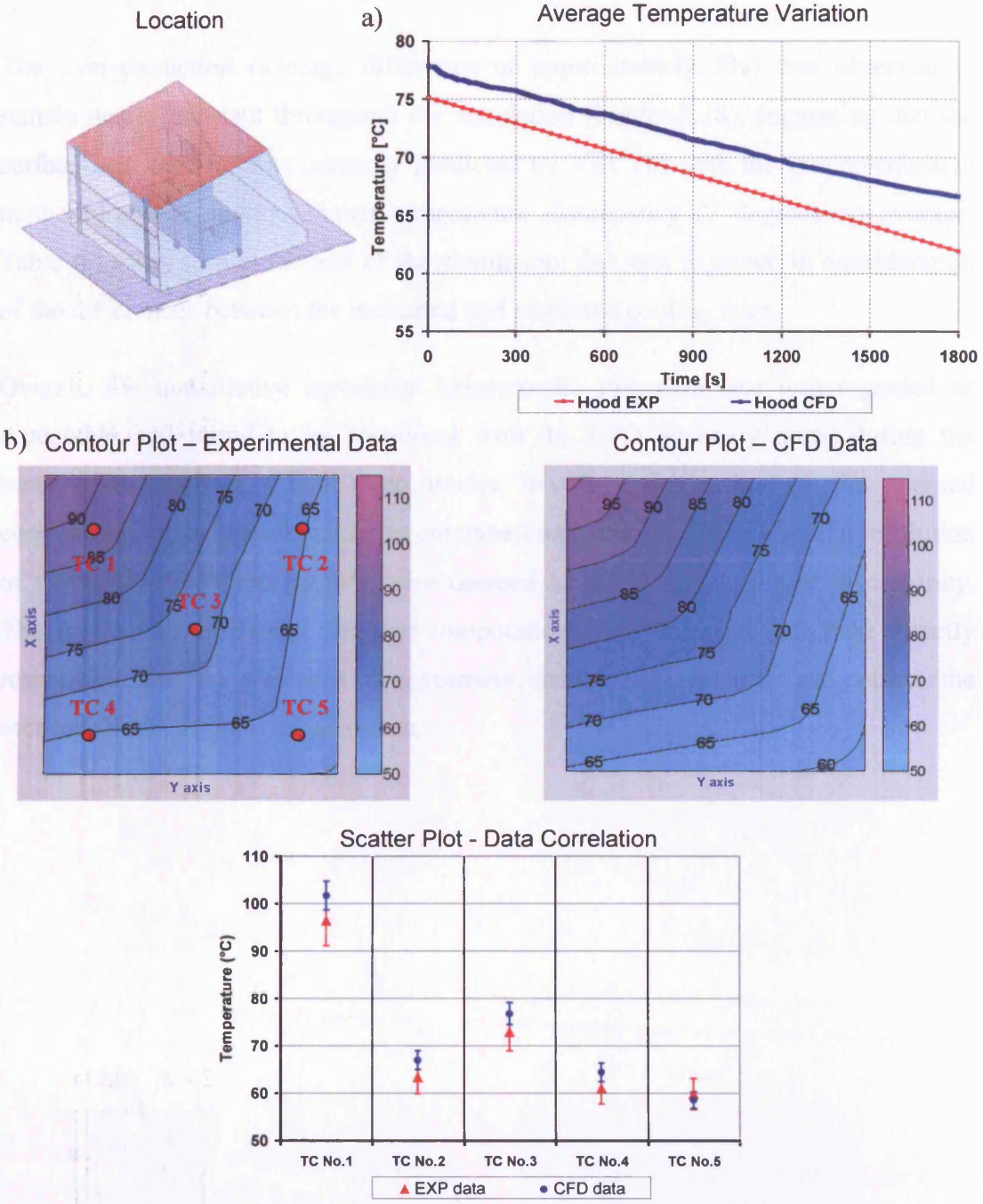

Figure 6.17 – Comparison of average temperature variation (a) and surface temperature distribution at 600s (b), for compartment top boundary (degC).

The computations were found to provide a solution with a slightly lower cooling rate than observed in the laboratory. The surface was simulated to undergo an 11.2-degree temperature drop in the 30 minutes while the measurements recorded a 12.8-degree change (Table 6.1). A close agreement between the temperatures was observed at all locations as it is also shown in the scatter plot of Figure 6.17(b), which compares the results at 600s.

The over-prediction (average difference of approximately 5%) was observed to remain nearly constant throughout the simulation (Figure 6.18), suggesting that the surface heat transfer was correctly predicted by VECTIS with the pseudo-transient methodology. A slightly higher temperature discrepancy (7 degrees on average, Table 6.1) was seen at the end of the simulation; this was expected in consideration of the differences between the measured and predicted cooling rates.

Overall, the quantitative agreement between the two data sets was regarded as acceptable and found to be consistent with the CFD accuracy noted during the steady-state analysis. Small inaccuracies in the specification of the thermal conductivity of the glass boundaries combined with a relatively low spatial resolution of the surface radiation patches were deemed as the main sources of discrepancy. The implemented strategy for fast computations was therefore not held directly responsible for the observed disagreement, which was in any case within the accuracy limits of the compared data.

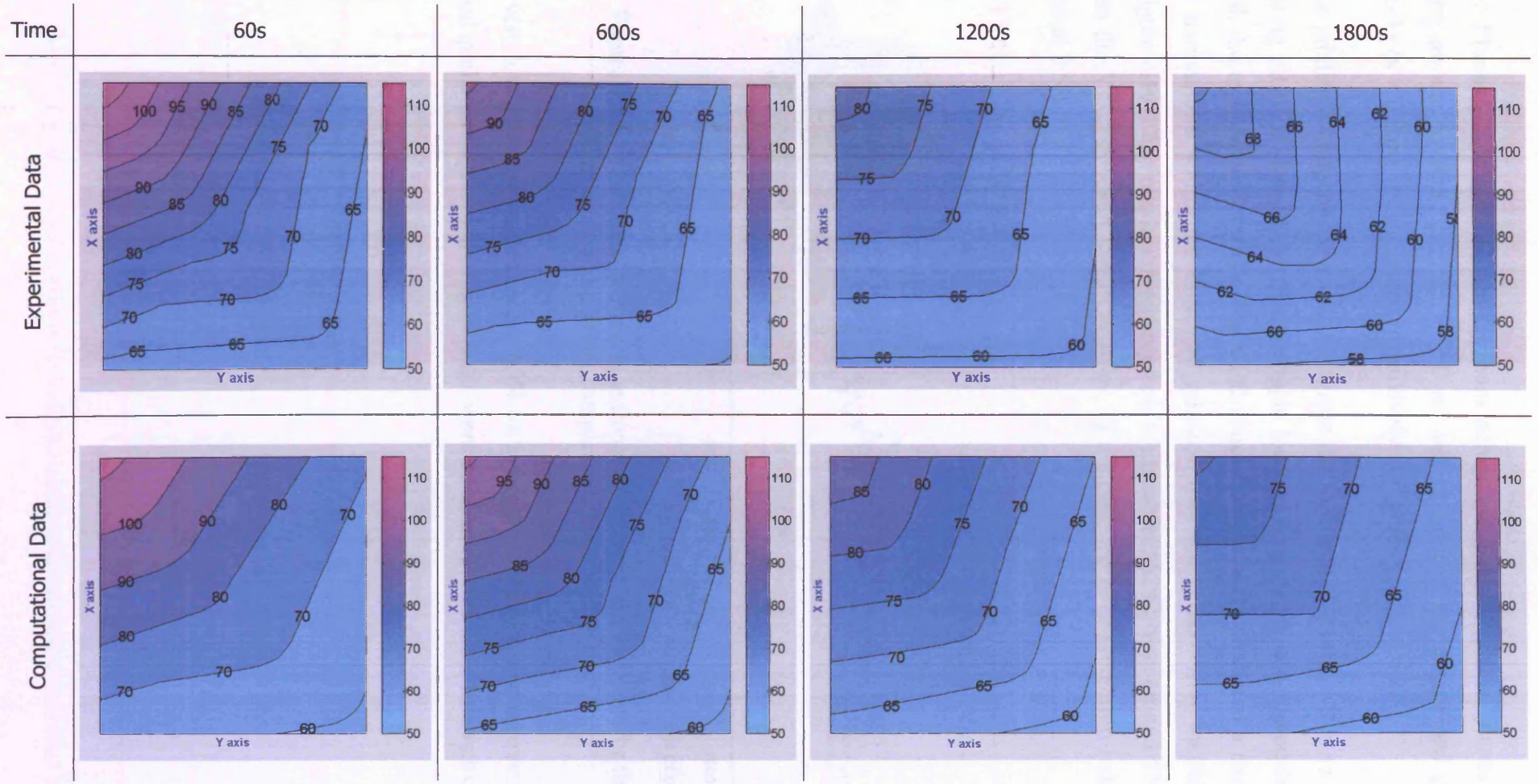

Figure 6.18 – Comparison at specific times between the measured and predicted temperature distributions on bonnet surface (degC).

Air Planes – The thermal stratifications across two parallel airflow planes, at the compartment's outlet opening (x = 0 m) and in front of the engine and gearbox blocks (x = 0.8 m), are presented respectively in Figures 6.20 and 6.22.

The predicted temperature evolution across the top front slot at x = 0 m (averaged among all CFD data at the thermocouple locations) corresponded reasonably well with the experimental results. The CFD simulation correctly predicted a rise in the air temperature within the initial 10 minutes after the heaters were switched off (Figure 6.19). The maximum-recorded air temperature (52°C) was around 5% lower than the VECTIS result (54.7°C). After 30 minutes, the over-prediction reduced to around 2.5%.

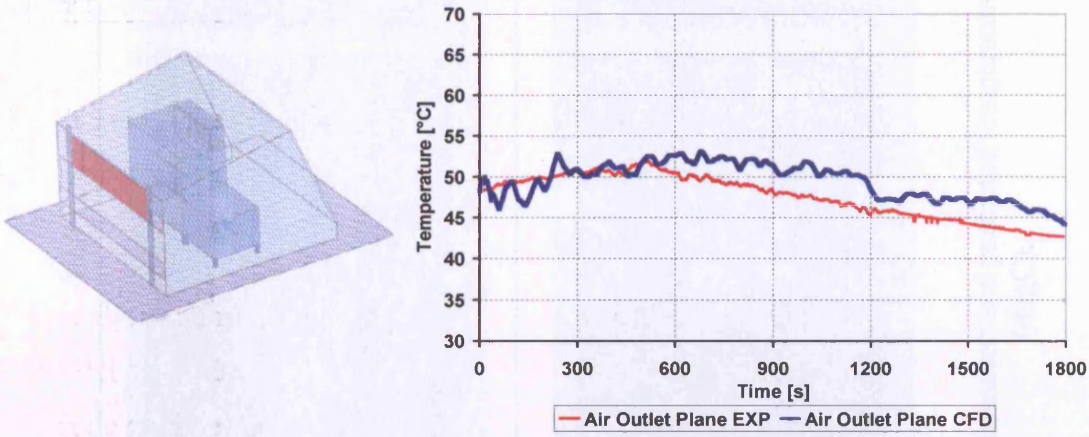

Figure 6.19 – Comparison of average transient temperature variation for the air plane located across the compartment flow outlet (degC).

A very low quantitative difference, 2.3% on average (Table 6.1), and an overall very good qualitative agreement, Figure 6.20, were obtained between the two sets of data.

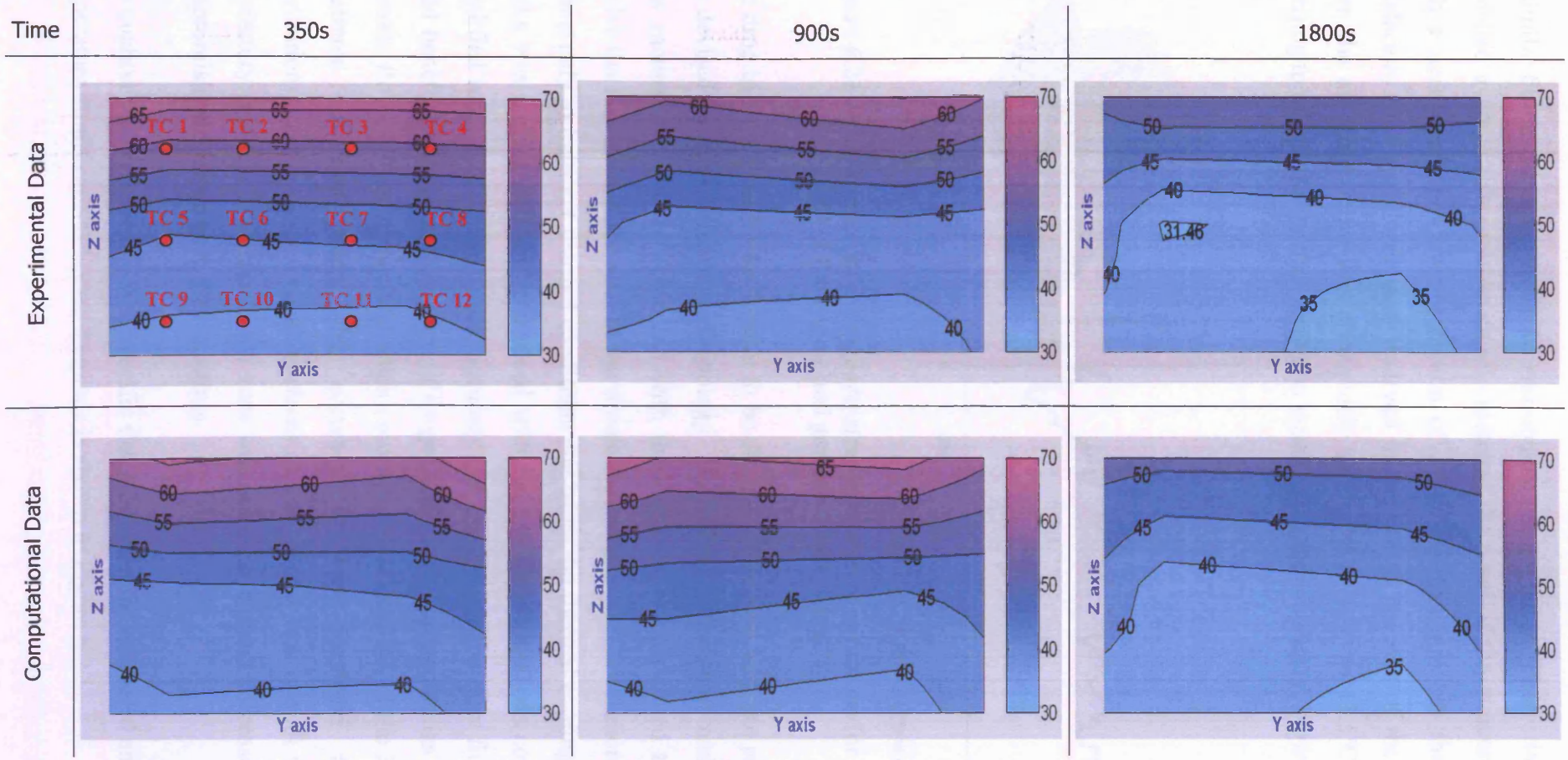

Figure 6.20 – Comparison at specific times between the measured and predicted temperature stratifications at the compartment flow outlet (degC).

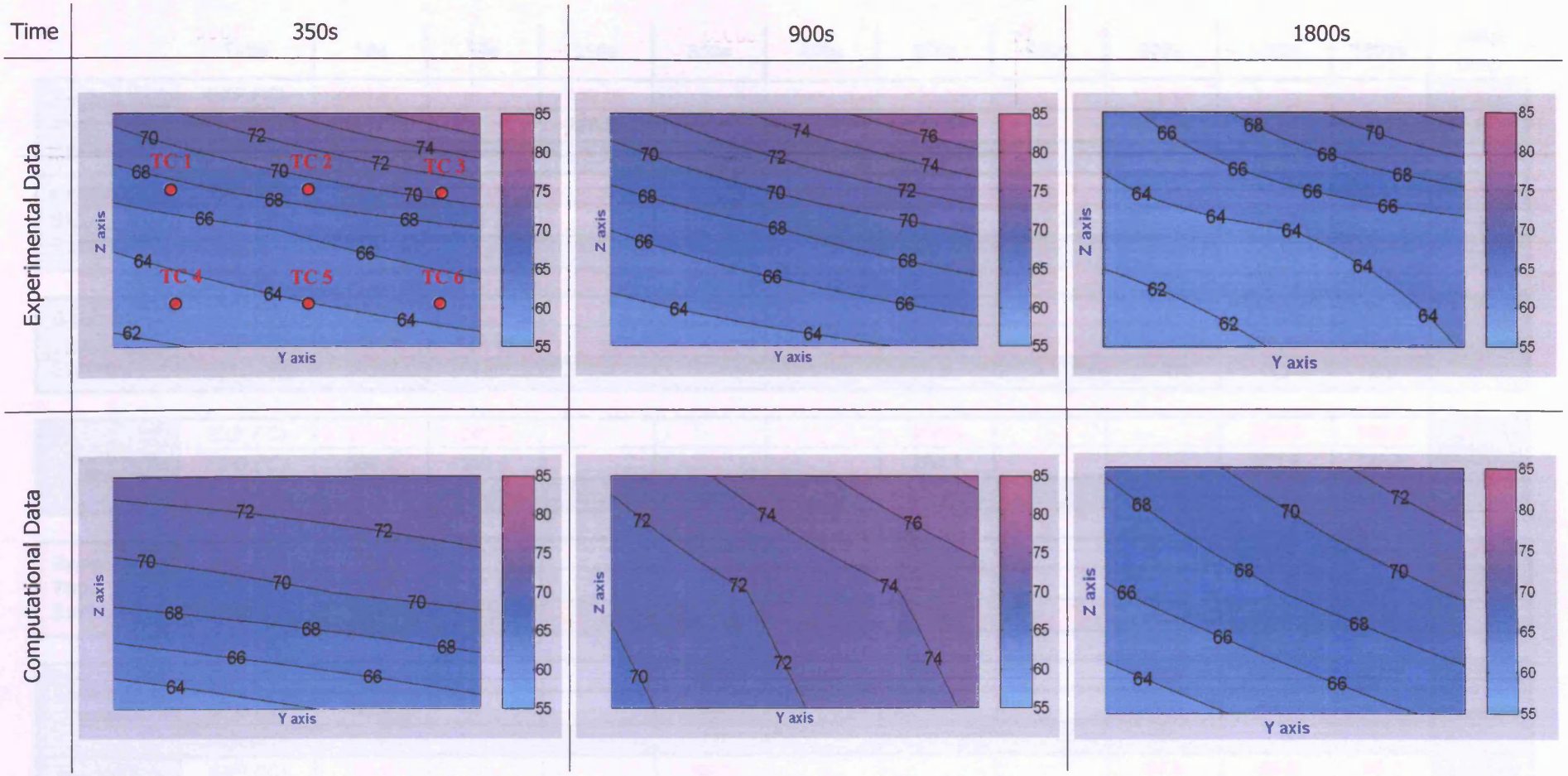

Figure 6.22 – Comparison at specific times between the measured and predicted temperature stratifications in the air plane located in front of the blocks (degC).

6.3.2 CFD Comparison with PIV Measurements

Airflow above Engine – Figure 6.23 displays the airflow vectors on two perpendicular planes just above the engine top surface (respectively parallel to the x- and y-axis of the reference co-ordinate system) after 1 minute of transient cooling of the blocks, i.e. at the start of the simulation. This is when the pseudo-transient methodology evidenced the highest difficulty in correctly predicting the time-variation of the thermal condition of the airflow (Figure 6.21).

The two investigated fields of view were in size and location identical to the flow regions examined during the steady thermal analysis (Chapter 4). In each representation of Figure 6.23, the PIV results (grey framed) are inset beside the corresponding flow areas simulated with VECTIS (boxed results with blue dashed lines). In order to enhance the qualitative comparison, the measured and predicted vector plots are also presented underneath the two flow representations with a magnified geometric scale.

Both the directions and magnitudes of the flow vectors were found to be satisfactorily predicted with the proposed computational strategy. Quantitatively, the numerical results under-predicted only slightly the mean air velocity at the point of separation from the edge of the block (Figure 6.23a) and next to the block's top surface (Figure 6.23b). Table 6.2 (page 264), presents the minimum, maximum and average magnitude of the flow velocity vector $|V|$ and of its x- and y-velocity components obtained with PIV. The CFD results and the data comparison are presented in Table 6.3 (page 265), with the latter given in terms of both CFD-relative discrepancy and percentage arc elasticity. The difference between the predicted and measured average velocity vectors was -3.2% and -7.3%, respectively in the flow regions *1X* and *2Y*. The CFD under-estimation of the mean velocity is mainly the direct consequence of the temperature under-prediction observed on the upper surface of the block (Figure 6.5). Nonetheless, the discrepancies were relatively small in magnitude and the short unfrozen flow processes (short steady-state computations) were not found to distinctly disturb the accuracy of the flow pattern predicted at the start of the simulated timeframe.

Airflow above Turbocharger – The flow structures at the top of the turbocharger (on the x-z plane next to the upper edge of the block) at 30s and 1min respectively are illustrated in Figure 6.24(a). The experimental and the computational solutions exhibited a good qualitative match, both depicting the airflow to direct at a nearly 45-degree angle towards the top of the engine bay. The maximum velocity in the region was measured to reduce from 0.390 m/s to 0.372 m/s during the time interval. VECTIS predicted a similar velocity drop, from 0.418 m/s to 0.402 m/s as given in Table 6.3. There was a slight CFD over-prediction in the average velocity magnitude. The resulting CFD percentage differences (+18.3% and +9.5%, respectively) were however similar to the discrepancies calculated between the two sets of results in steady conditions (+12.3%). Consequently, the proposed calculation procedure was not regarded to pose additional sources of CFD error.

Figure 6.24(b) displays the flow structure on the y-z plane located above and along the length of the block (y-z plane at x = 0.38 m). The graphical comparison between the results was rendered difficult by the low vector density of the numerical solution. The comparison between the average velocity vectors gave however an indication of the CFD accuracy: the simulation over-predicted the strength of the convective flow on average by 0.017 m/s, both after 30 seconds and 1 minute of cooling. The corresponding percentage differences (arc elasticity) were approximately 15%, Table 6.3. The difference between CFD and PIV results was overall acceptable, especially when considering the uncertainty in the measurements and the low spatial resolution of the simulation (the two data sets are plotted with error bands in Figure 6.32, page 267). The CFD inaccuracy obtained from the transient predictions was again found to match with the discrepancies observed during the steady-state analysis.

Airflow at Top of Compartment – The flow field at the top of the compartment was examined at 5, 20 and 30 minutes (Figure 6.25) in order to assess the time-accuracy of the calculation procedure when simulating the unstable clock-wise circular motion of the convective stream. All of the flow representations were processed based on an identical vector velocity scale in order to allow a better visual comparison.

Qualitatively, the flow motion was overall satisfactorily predicted by VECTIS as shown in the figure. The average flow velocity based on the PIV measurements increased from 0.047 m/s at 5 minutes, to 0.051 m/s after 20 minutes and 0.059 m/s after 30 minutes. The same trend was not predicted with CFD, which gave a mean flow velocity of 0.064 m/s at 5 minutes, reducing to 0.056 m/s after 20 minutes and increasing back to 0.060 m/s at the end of the timeframe.

The exact reason for the quantitative differences is difficult to pin point, especially because of the uncertainty affecting the PIV measurements at such low air velocities. Nevertheless, the numerical discrepancy was not deemed entirely owed to the procedure employed for the computations: an increase in length of the unfrozen flow periods or of the number of methodology cycles carried out by the *SWITCH* strategy could not compensate for the underlying shortcomings of the natural convection predictions. On the other hand, it is believed that the accuracy of the flow simulation would benefit from an increase in the density of the air domain mesh and by implementing a turbulence model more suited to natural convection simulations, especially if this obviates the need of using the Law of the Wall treatment at the boundaries.

Airflow at Outlet – The flow field simulation at the outlet slot of the compartment (top front aperture) exhibited a general poor accuracy when compared to the PIV measurements. Figure 6.30 displays that the vectors computed on the x-z plane across the centreline of the opening corresponded well in direction with the experimental results but they were largely under-predicted in magnitude. The discrepancy was relatively constant and on average equal to 0.013 m/s (-37%, Table 6.3) over the cooling period. One possible reason explaining the observed CFD inaccuracy could be an over-estimation of the turbulent kinetic energy of the flow in the region. As discussed in Chapter 4, the $k-\varepsilon$ turbulence model solves in fact with difficulty the flow vectors at the separation and re-attaching points of a surface. The manual setup of the geometric scale of the PIV field of view (Chapter 2), might have also added a small systematic error to the experimental data, contributing to the discrepancy.

The flow patterns and magnitudes at 15 and 30 minutes at a plane parallel to the outlet slot were also compared (Figure 6.31) and similar disagreements in the average flow velocities were found. Unfortunately, the resolution of the CFD solution was not high enough to allow a detailed qualitative comparison with the PIV measurements. However, the figure does shows that the flow pattern was acceptably estimated in its direction. Quantitatively, the simulation gave a discrepancy with the PIV data of –37.8% at 15 minutes and –39.4% at the end of the processed period.

6.4 SUMMARY OF RESULTS AND DISCUSSION

Based on the comparisons over the 30 minutes of transient cooling, it was established that the devised pseudo transient methodology was successful in replicating, with satisfactory accuracy, a fully conservative time-dependent simulation. The overall inaccuracy was calculated to be within the uncertainty associated with both the numerical and the experimental techniques. The saving in CPU processing time was over 90% in comparison to a standard transient simulation with VECTIS.

The temperature predictions were in general found to slightly over-estimate the thermal condition of the model. The average discrepancy between the two data sets was 3.4% when considering the average temperature of all the planes being compared (both solid and fluid planes) at different time intervals (i.e. all the results tabulated in Table 6.1). The largest disagreement (8.2%) was on the vertical side surface of the engine block at the end of the simulated period (i.e. after 30 minutes). The surface temperature distribution and the airflow thermal stratification corresponded well in time with the thermocouple measurements.

The accuracy of the CFD data was further confirmed when the transient flow predictions were compared with the PIV measurements. The quantitative difference, based on the average velocity vector magnitude (correlated at different times during the cooling period), was of 20%. The discrepancy at the outlet of the compartment was particularly affected by systematic errors due to the length scales of the 2-D regions being manually setup in the PIV data processing software. When the results of these regions were excluded, the average data disagreement reduced to 12%. Figure 6.32 clearly shows the CFD results matched very satisfactorily with the PIV data at any time during the simulated period.

Overall, the CFD error magnitude determined from the transient analysis was found to be very similar to the CFD discrepancy calculated under steady thermal conditions (Chapter 4). This suggests that the sources of error affecting the pseudo-transient simulation were most probably the same sources of error affecting the steady results, i.e.

- Modeling errors, from the differences between the computational and the laboratory models (boundary conditions). The specification of the material properties and the approximation in modeling the interfaces between the block would have particularity contributed to the differences observed between measurements and predictions.
- Discretisation errors, especially due to the relatively low spatial resolution of the CFD domain and of the surface patches used for radiation heat transfer computations.
- Systematic errors, introduced for example in the experimental data by small inaccuracies in the specification of the length scale of the PIV images.
- Validity of the Law of the Wall turbulence formulation and, more in general, of the standard $k-\varepsilon$ turbulence model, which were employed to solve the turbulent flow fluctuations in the underhood.

On the other hand, the similar discrepancies of the steady and transient CFD predictions compared to measurements implies that the pseudo-transient methodology and its non-conservative approximation for fluid momentum and energy convection did not distinctly deteriorated the data correlation and therefore the quality of the CFD results. It is believed that the use of a turbulence model more suited to natural convection simulation and an increase in mesh density would have greatly improved the accuracy of the flow and thermal predictions.

6.5 CLOSURE

The comparison between the experimental and numerical transient data has established that the proposed methodology was successful in providing a time-accurate thermal simulation of a simplified underhood model during transient cooling, allowing investigations into the heat soak condition.

An average discrepancy of approximately 3.4% was calculated when comparing at specific times the measured and predicted temperature distribution on selected model surfaces and air planes. The velocimetry predictions showed an average discrepancy in the mean airflow magnitude of 20% compared to measurements.

The differences with laboratory data were in general found to be within the accuracy limit of the instrumentation used and they were regarded as satisfactory. The quantitative discrepancies were in magnitude very similar to the ones determined during the steady-state analysis, and they were therefore believed to be caused by the underlying shortcomings of the natural convection simulation within VECTIS rather then being directly induced by the proposed fast computational methodology.

Most significantly, the application of the proposed pseudo-transient calculation strategy resulted in a reduction in computing time in excess of 90% when compared to a fully transient simulation performed on the same hardware unit.

Chapter 7

CONCLUSIONS AND FURTHER WORK

Experimental and numerical investigations were carried out on a scaled underhood model under transient cooling. Emphasis was placed on determining the accuracy of the CFD technique in simulating the thermally-driven convective flow in a simplified engine compartment with a conjugated heat transfer analysis and on defining a computational procedure enabling long transient simulations to be performed with significantly reduced CPU runtime. The principal findings of the research, arranged according to the investigative tools used for the analysis (measurement and simulation), are reviewed. The conclusions drawn from the development of the fast transient methodology are also given. Finally, possible future developments of the research are suggested.

7.1 SUMMARY AND CONCLUSIONS

7.1.1 Measurements

No previous work suitable for validation purposes was found in the literature for buoyancy driven flows in vehicle engine compartments. Only a restricted number of indoor airflow experiments (building ventilation) have been published. To compensate the dearth of such experimental analyses, a purpose-built half-scale underhood model was constructed in the initial stages of the research, providing data to validate the steady-state and transient CFD predictions obtained with the software VECTIS. The following concluding remarks are made from the measuring techniques employed and the data collected:

- A geometrically simplified underhood model, with a slotted glass compartment and internally heated metal blocks, is effective in reproducing the convective flow patterns prevailing in an engine bay under thermal soak and in allowing flow velocimetry investigations. The use of a scaled model for efficiently scrutinising the flow events was fully justified by the quality of the recorded measurements. Informative data was obtained during both steady thermal conditions and cooling of the blocks and would be applicable for further validation studies.

- The use of thermocouples is a well developed and the most practical technique for the measurement of surface and airflow temperatures. The accuracy of the technique depends on the type of sensors employed (metal used in their construction), the effectiveness of any measure taken to reduce the effects of radiative heat (e.g. screening of the thermocouple tips) and the sensitivity of the hardware unit used for logging the data.

- Accurate measurement of the natural convective flow velocity is difficult, as its mean value is generally very low (< 0.5 m/s). The characteristics of most of the commercially available velocity sensors and techniques restrain their usage for thermally-driven flows. From a careful evaluation, Particle Image Velocimetry (PIV) was chosen as the most suitable non-invasive technique. Issues with optical access and flow seeding distribution restrict however its applicability to full-scale measurements (i.e. measurements in real engine compartments).

- The PIV apparatus as assembled in this study provides time-averaged two-dimensional flow vectors in different planes of the investigated field with good resolution for CFD comparison. The use of neutrally buoyant oil droplets as flow tracers was supported by theoretical analysis and proved successful even if the flow velocities were particularly low. PIV errors were found to be of difficult quantification being of systematic type and often function of the algorithms used for the particle-displacement detection. Statistical sampling theory successfully enabled the measurement uncertainty in representing the actual mean flow parameters to be quantified.

7.1.2 Simulations

The simulations of the coupled flow and thermal fields were performed, for both steady state and transient cooling, on a computational model that replicated at best the geometry and boundary conditions of the laboratory setup. The following was noted:

- The applicability of CFD with RANS formulation and with a conjugate heat transfer solution procedure is confirmed for the investigation of natural convective flows in underhood environments. It is envisaged that a CHT type analysis, modelling simultaneously all the components of a real underhood compartment, would pose severe challenges to the memory of the most powerful computer available nowadays. Such simulations could only be tackled with approximations to the boundary conditions or by coupling the CFD software with a 1-D system thermal code.

- Under-relaxation factors as high as 0.95 coupled with a two-level matrix solver were found to highly increase the convergence of the steady-state CFD solution without affecting its numerical stability. The feasibility of specifying a large under-relaxation depends, however, on the complexity of the flow patterns being investigated (i.e. geometric complexity of the underhood architecture).

- Comparison of experimental and computational steady-state results evidenced that, within the accuracy of the measurement instrumentation and the resolution of the computational mesh, the structure, size and intensity of the flow patterns was satisfactorily simulated by VECTIS (23% average discrepancy between mean flow velocities) and that the temperature predictions agreed well with measurements (9% average difference).

- The accuracy of the simulations depends mainly on the accuracy with which wall heat transfer and turbulence are modelled. The application of wall functions as part of the $k-\varepsilon$ turbulence model yields grid dependent solutions for the heat transfer and temperature distribution at boundaries. The wall heat transfer characteristics are not correctly predicted with logarithmic

wall functions (Law of the Wall) unless rigorous control on the near-wall grid distribution (y^+ value) is executed. This has also implications for modelling radiation heat transfer when a heat flux is defined at the boundary of a heat source.

- Comparison of experimental and numerical results showed that the heat transfer was generally over-estimated by the numerical model in VECTIS. This affected the vertical temperature gradient, and therewith the energy balance and the plume development above the heat sources (flow velocity). The law-of-the-wall is considered invalid for developing buoyant flows and free convective boundary layers as appear in engine compartments. Recent developments in the mathematical and numerical modelling of turbulent flows allow, in theory, improved simulations although at the expense of higher computing requirements. However, the lack of validation studies for realistic underhood airflow fields have not yet allowed a proper evaluation of these improved models. The experimental and CFD results presented in this work could be usefully employed for such validations.

- The comparison between the predictions with the standard and the *RNG* version of the $k-\varepsilon$ turbulence model did not provide a clear distinction in terms of simulation accuracy. Any differences should be more convincingly determined by extending the investigation to other flow configurations. It was however determined that the "soft turbulence" regime of the studied flow was more accurately simulated when employing the $k-\varepsilon$ model rather than when prescribing the flow to be fully laminar.

- The simulation performed by accounting for the effects of radiation heat transfer with reduced heat fluxes in the blocks provided generally satisfactory predictions, not too different from the results obtained when fully modelling radiation. The heat flux approximation can be usefully employed to reduce the computing effort when simulating models with the heat source(s) directly specified at the boundaries. However, the use of a radiation model based on surface-to-surface calculation is endorsed for future underhood CFD analyses.

7.1.3 Fast Transient Methodology

A novel contribution to the development of a calculation procedure for efficient time-marching CFD simulations was made. Two methodologies were proposed, both operating on the basis of pausing the flow transport solution for periods of time during the computations. The fluid domain was updated with a fully-conservative transient or steady-state run. All the parameters influencing the performance of the strategies were examined. The following was evidenced:

- The most significant parameter affecting prediction accuracy was identified as the number of flow solution updates performed during the computation, i.e. the total number of frozen/unfrozen flow cycles carried out to resolve the transient timeframe. In general, the accuracy of the simulation was found to benefit more from a larger number of "short" momentum updates (full transient or steady-state computations) than from a smaller number of "long" ones.

- The step size for the transient runs solving the frozen flow periods should be in the range of 100 to 1000 times larger than its maximum allowed size in a corresponding standard, fully-transient computation. To reduce the cycle frequency and consequently further reduce the CPU runtime, the length of the frozen flow periods can be increased after approximately the first 30% of the simulation, when the numerical solution is generally more stable.

- The solution strategy giving the best compromise between simulation accuracy and computational efficiency operates based on steady-state flow momentum updates with a frozen heat balance solution between the thermally-conjugated solid models (i.e. between the underhood components being modelled).

- The efficiency of the pseudo-transient calculation procedure further improves when the solver operations are fully automated without the need for user input. A specific program was written for this task in this study.

- The proposed methodology was employed for simulating the simplified underhood model during 30 minutes of transient cooling. The flow and thermal predictions demonstrated a good correlation with measurements, arguably within the range of the data uncertainty. The average discrepancy between the data was 3.4% for the temperatures and 20% for the mean vector magnitudes. The runtime was over 90% shorter than for a standard fully-conservative simulation.

- In conjunction with further work, the proposed methodology extends the capabilities of CFD for underhood thermal management studies by allowing a fully-conservative transient simulation to be replicated with acceptable time accuracy and with greatly reduced CPU runtime. It is envisaged that its implementation for transient underhood simulations will enable engineers to better diagnose thermal issues, optimise system designs and generally improve the thermal efficiency of engine compartments at reduced time and costs.

7.2 RECOMMENDATION FOR FUTURE RESEARCH

This thesis has provided a greater insight into the coupling of the flow and thermal fields in a vehicle engine-bay and has confirmed the applicability of the CFD technique as adopted in VECTIS for natural convection studies. The findings and achievements of the study provides unique opportunities for further experimental and CFD research.

Measurements – For validation purposes, the number of carefully documented underhood measurement results should be increased. In this respect, whole-field velocimetry techniques such as PIV are the most promising, but the use of a double-head laser type is strongly recommended for future applications in order to maximise the size of the investigated interrogation areas. Difficulties in acquiring velocimetry data in real engine compartments are prefigured and alternative measurement techniques should therefore be researched to enable full-scale CFD validations.

The present study has concentrated on the airflow prevailing within a simplified underhood geometry. Several additional components would affect the flow pattern in the engine compartment of an actual production vehicle, e.g. the heat exchangers of the cooling pack; it would be a worthwhile undertaking to integrate such components in the laboratory model for further testing. Parametric investigations into the cooling fan position, for instance, would be of significant benefit for studying the effects on the thermal management. Extensive examination into component packaging configurations would be another area for further exploiting the scaled model used in this study.

Simulations – To promote and widen the application of the CFD technique in a vehicle development programme, numerical simulations must be further developed and improved towards a higher degree of reliability and accuracy. On one hand, the development should follow the general, mainstream research in fluid mechanics and numerical methods; on the other hand, extensive validation studies are required on realistic underhood configurations so that newly derived turbulence models and numerical techniques can be tested and refined.

Improvement of the CFD technique should certainly also address the convective heat transfer mechanism. The results of the work have indicated that the correct specification of boundary conditions and the correct prediction of the convective heat transfer at the walls represent critical issues in the simulation of buoyant airflows in a compartment. Underhood flows have, locally and globally, their own specific features, such as being characterised by low-Reynolds-number turbulence, mixing and re-circulating air motions, thermal stratification and so on. These must be well accounted, especially by the turbulence model. It is therefore proposed that further studies will delve further in investigating the benefits of alternative and new turbulence models and possibly derive new and more suited wall functions to improve the boundary layer solution.

Transient Simulation Technique – Further work should be undertaken to validate the accuracy of the devised pseudo-transient methodology for the simulation of complex full-scale engine compartments. It is envisaged that a CHT type analysis modelling all the underhood systems and components would be

computationally prohibitive due to CPU memory requirements. Further research should be aimed at investigating the effectiveness of implementing the methodology in a coupled 3D-1D simulation. The 3-D CFD software would solve transiently the flow field of the model and the 1-D system software would be employed to quickly advance in time the thermal solution.

In addition, the use of numerical "triggers" as part of the solution procedure of the proposed methodology could be investigated. The triggers would automatically detect when a flow update is necessary, in order to maximise the accuracy of the predictions while minimising CPU runtime expenditure. These could be for example calibrated on the size of the equation residuals at the end of each CFD computation or on the variation of specific flow properties between successive methodology cycles.

References

ADRIAN, R. J. [1984]: Scattering Particle Characteristics and their Effect on Pulsed Laser Measurements of Fluid Flow: Speckle Velocimetry vs. Particle Image Velocimetry, *Journal of Applied Optics,* Vol. 23, pp. 1690-1691.

AEI – AUTOMOTIVE ENGINEERING INTERNATIONAL [2000]: *Tech Brief: Radiant Heat Protection*, AEI-Online, April Issue, [Online], Available: www.sae.org/automag/techbriefs_04-00/10.htm, June 2004.

AL-TAWEEL, A. M., CARLEY, J. F. [1971]: Dynamics of Single Spheres in Pulsated Flowing Liquids, *Chemical Engineering Program Symposium Series*, p. 116.

ANDERSON, J. D. [1995]: *Computational Fluid Dynamics - The Basics with Applications*, International Editions McGraw-Hill, ISBN 0-07-113210-4.

AROUSSI, A., AGHIL. S. [2000]: Characterisation of the Flow Field in a Passenger Car Model, *Optical Diagnostics in Engineering*, Vol. 4, No. 1, pp. 1-15.

ASGHARI, T. A. [2001]: A Transient Thermal Analysis Using a Simplified Heat Transfer Coefficient Model, *Procs. Int. Symposium on Advanced Packing Materials: Processes, Properties and Interfaces*, pp. 366-371.

AWBI, H. B., HATTON, A. [1999]: Natural Convection from Heated Room Surfaces, *Energy and Buildings*, Vol. 30, pp. 233-244.

BANCROFT, T. G. [2005]: Java™ program for automation of fast transient methodology computational procedure. Program Code.

BAKER, A. J., KELSO, R. M. [1990]: On the Validation of Computational Fluid Dynamics Procedures for Room Air Motion Prediction, *ASHRAE Transactions*, Vol. 96 (1), p. 760.

BAKER, N., LINDEN, P. F. [1991]: Physical Modelling of Airflows – A New Design Tool, *Atrium Build. Archit. Eng.*, pp. 13-22. Ed. F. Mills. CICC Publications, Welwyn, UK.

BAKER, A. J., KELSO, R. M., GORDON, E. B., ROY, S., SHAUB, E. G. [1997]: Computational Fluid Dynamics: A Two Edged-Sword, *ASHRAE Journal*, August, p. 51.

BATURIN, V. V. [1972]: *Fundamental of Industrial Ventilation*, 3rd Edition, Chp. 1, Pergamon Press, ISBN 0080158285.

BEJAN, A., AL-HOMOUD, A. A., IMBERGER, J. [1981]: Experimental Study of High-Rayleigh-Number Convection in a Horizontal Cavity With Different End Temperatures, *Journal of Fluid Mechanics*, Vol. 109, pp. 283-299.

BENDELL, E. [2005]: Investigation of a Coupled CFD and Thermal Modelling Methodology for Prediction of Vehicle Underbody Temperatures, 7th *Vehicle Thermal Management Systems Conference, SAE Paper No. 2005-01-2044.*

BERLANDIER, P., RAPP, R., SERIEYS, J. C. [1989]: General Feature of a Two-Dimensional Isothermal Mean Flow Inside a Ventilated Room with a Wall Mounted Obstacle, *Procs. 10th AIVC Conference*, Dipoli, Finland, pp. 167-187.

BOLINDER, J. [1999]: *On the Accuracy of a Digital Particle Image Velocimetry System*, Technical Report, Lund Institute of Technology, Lund, Sweden, ISSN 0282-1990.

BOULARD, T., HAXAIRE, R., LAMRANI, M. A., ROY, J. C., JAFFRIN, A. [1999]: Characterization and Modelling of the Air Fluxes Induced by Natural Ventilation in a Greenhouse, *Journal Agricultural Engineering Research*, Vol. 74, pp. 135-144.

BURMEISTER, L. C. [1993]: *Convective Heat Transfer*, 2nd Edition, Wiley & Sons Inc., ISBN 0-471-57709-X.

BUTLER, D. J., STEVENS S. P. [1999]: Modelling of Vehicle Thermal System, *Procs. 4th Vehicle Thermal Management Systems Conference, SAE Paper No.* L07/C543-57.

CHAN, V. S. S. C. [1999]: *Particle Based Velocimetry Techniques for Measurements in Reciprocating Engines*, Ph.D. Thesis, School of Engineering, Manchester, UK.

CHANG, F.C. [2003]: Underhood Thermal Management of Off-Highway Machines Using 1D-Network Simulations, *SAE Int. Truck and Bus Meeting and Exposition, SAE Paper No.* 2003-01-3405.

CHANG, J. S., BROCILO, D., URASHIMA, K. [2004]: Optimization of Seed-Particle Size and Density Used in the Particle Image Velocimetry under Corona Discharges and Non-Thermal Plasmas, *Procs. 7th Int. Congress on Optical Particle Characterization*, Japan.

CHEN, Q. [1988]: *Indoor Airflow, Air Quality and Energy Consumption of Buildings*, Thesis, Delft University of Technology, Delft, The Netherlands.

CHEN, Q., JIANG, Z. [1992]: Significant Questions in Predicting Room Air Motion, *ASHRAE Transactions*, Vol. 98, Part 1, pp. 929-939.

CHEN, Q. [1995]: Comparison of Different $k-\varepsilon$ Models for Indoor Air Flow Computations, *Numerical Heat Transfer*, Vol. 28, Part B, pp. 353-369.

CHEN, Q. [1996]: Prediction of Room Air Motion by Reynolds-Stress Models, *Building and Environment*, Vol. 31, No. 3, pp. 233-244.

CHEN, Q. [1997]: Computational Fluid Dynamics for HVAC: Successes and Failures, *ASHRAE Transactions*, Vol. 103, Part 1, pp. 178-187.

CHEN, Q., XU, W. [1998]: A Zero-Equation Turbulence Model for Indoor Airflow Simulation, *Energy and Buildings*, Vol. 28, No. 2, pp. 137-144.

CHEN, Z. D., LI, Y., MAHONEY, J. [2001]: Experimental Modelling of Buoyancy-Driven Flows in Buildings Using a fine-Bubble Technique, *Building and Environment*, Vol. 36(4), pp. 447-455.

CHEN, J., KATZ, J. [2005]: Elimination of Peak Locking Error in PIV Analysis Using the Correlation Mapping Method, *Meas. Sci. Technol.*, Vol. 16, pp. 1605-1618.

CHO, N. H., KIM, M. R. [1997]: Numerical Investigation of Fluid Flow in an Automotive HVAC Module, *Procs. 3rd Vehicle Thermal Management Systems Conference, SAE Paper No. 971778,* pp. 61-67.

CHUNG, T. J. [2002]: *Computational Fluid Dynamics*, (Chp 1.4), Cambridge University Press, ISBN 0-521-9416-2.

COHEN, M. F., WALLACE, J. R. [1993]: *Radiosity and Realistic Image Synthesis*, Academic Press Professional, ISBN 0-12-178270-0, Cambridge, MA.

CONTINUUM [1995a]: *Operation and Maintenance Manual for Surelite Lasers*, Continuum.

CONTINUUM [1995b]: *Dual Pulse Option (DPO). Operation Manual*, Continuum.

CURRAN, A. R., JOHNSON, K. R., MARTTILA, E. A. [1995]: Automated Radiation Modeling for Vehicle Thermal Management, *SAE paper No. 950616.*

DALY, B. J., HARLOW, F. H. [1970]: Transport Equations in Turbulence, *Phys. Fluids*, Vol. 13(11), pp. 2634-2649.

DUTMER, G. [2003]: *Advantages in Under-the-Bonnet Applications of Performance Engineering Plastics*, Business Briefing: Global Automotive Manufacturing & Tech.

ELECTRONIC DATA SYSTEMS [2003]: *I-DEAS™, Ver.10 Software Manual*, Electronic Data Systems Corporation, Website: www.eds.com.

EMMERICH, S., MCGRATTAN, K. [1998]: Application of a Large Eddy Simulation Model to Study Room Airflow, *ASHRAE Transactions*, Vol. 104, Part 1b, pp. 1128-1140.

ENQUIST, B. J., EARSOME, S. D. [1996]: Scale/Scaling in Ecology. *Ecological Complexity Seminar*, University of New Mexico, Online, Available: http://sevilleta.unm.edu/~ehdecker/complexity/96fall/scale.html, May 2003.

FORTUNATO, F., DAMAINO, F. OLIVA, P., DI MATTEO, L. [2005]: Underhood Cooling Simulation for New Vehicles Development, 7th *Vehicle Thermal Management Systems Conference, SAE Paper No. 2005-01-2046.*

FUJI, T., IMURA, H. [1972]: Natural Convection Heat Transfer From a Plate with Arbitrary Inclination, *International Journal of Heat Mass Transfer*, Vol. 15, No. 4, pp. 755-767.

GHANI, A. G. A., FARID, M. M., CHEN, X. D. [2002]: Numerical Simulation of Transient Temperature and Velocity Profiles in a Horizontal Can During Sterilization using Computational Fluid Dynamics, *Journal of Fluid Engineering*, Vol. 51 (1), pp. 77-83.

GLADSTONE, C., WOODS, A. W. [2001]: On Buoyancy-Driven Natural Ventilation of a Room with a Heated Floor, *Journal Fluid Mech.*, Vol. 441, pp. 293-314.

GORTZ, S., MOLLER, J. [2004]: Evaluation of the Recursive Projection Method for Efficient Unsteady Turbulent CFD Simulations, *Procs. 24th Int. Congress of the Aeronautical Sciences*, ICAS 2004.

GOSMAN, A. D., NIELSEN, P. V., RESTIVO, A., WHITELAW, J. H. [1980]: The Flow Properties of Rooms with Small Ventilation Openings, *Journal of Fluids Engineering, Transactions of ASME*, Vol. 102, pp. 316-323.

GUI, L. WERELEY, S. T. [2003]: A Correlation-Based Continuous Window Shift Technique for Reducing the Peak Locking Effect in Digital PIV Image Evaluation, Experiments in Fluids, Vol. 34(4), pp. 504-514.

GUNNAR, I., HELLSTROM, J. [2005]: *Redesign of an Existing Hydropower Draft Tube*, MSc Thesis, Division of Fluid Mechanics, Lulea University of Technology, Sweden.

HAIDAR, N., DRAPER, E. [1998]: Computational Modelling of the Underbonnet Cooling Flow Characteristics of the New Daewoo Van, *Procs. 2nd MIRA International Conference on Vehicle Aerodynamics.*

HEMPH, R. [2003]: *A CFD Investigation of 2D and 1D Viscous Pulse Propagation in Engine Exhaust Systems*, MSc Thesis, Chalmers University of Technology and Gothenburg University.

HOWELL, S. A., POTTS, I. [2001]: On the Natural Displacement Ventilation Flows Through a Full Scale Enclosure, Driven by Buoyancy at Floor Level, *Procs. 7th International IBPSA Conference*, Rio de Janeiro, Brazil.

HUANG, H., DABIRI, D., GHARIB, M. [1997]: On Errors of Digital Particle Image Velocimetry, *Measurement Science & Technology*, Vol. 8, pp. 1427-40.

HUCHO, W.-H. [1998]: *Aerodynamics of Road Vehicles*, edited by W.-H. Hucho, 4th Edition, ISBN 0-7680-0029-7.

HUTCHINSON, B. R., RAITHBY, G. D. [1986]: A Multigrid Method Based on the Additive Correction Strategy, *Numerical Heat Transfer*, Vol. 9, pp. 511-537.

INCE, N. Z., LAUNDER, B. E. [1989]: On the Computation of Buoyancy-Driven Turbulent Flows in Rectangular Cavities, *Int. Journal of Heat Fluid Flow*, Vol. 10(2), pp. 110-117.

INCE, N. Z., LAUNDER, B. E. [1995]: Three-Dimensional and Heat-Loss Effects on Turbulent Flow in a Nominally Two-Dimensional Cavity, *Int. Journal of Heat Fluid Flow*, Vol. 16, Issue 3, pp. 171-177.

INCROPERA, F. P., DEWITT, D. P. [2001]: *Fundamental of Heat and Mass Transfer*, 5th Edition, Wiley & Sons, ISBN 0-471-38650-2.

ISHIHARA, Y., HARA, J., SAKAMOTO, H., KAMEMOTO, K., OKAMOTO, H. [1991]: Determination of Flow Velocity Distribution in a Vehicle Interior Using a Visualisation and Computational Techniques, *SAE Paper No. 910310, (SP-855 pp. 51-62).*

ISSA, R. I. [1986]: Solution of Implicitly Discretised Fluid Flow Equations by Operator-Splitting, *Journal of Computational Physics*, Vol. 62, pp 40-65.

JALURIA, Y. [1998]: *Design and Optimization of Thermal Systems*, Chp. 3, McGraw-Hill, ISBN 0-07-032388-7.

JAMESON, A. [1991]: Time Dependent Calculations using Multigrid, with Applications to Unsteady Flow Past Airfoils and Wings, *Procs. AIAA 10th CFD Conference.*

JAN, J. Y., SRINIVASAN, K., SUN, R. L., GLEASON, M. E. [2000]: Rapid Simulation Methodology for Under-Hood Aero/Thermal Management, *Int. Journal of Vehicle Design*, Vol. 23, No. 1/2, pp. 109-123.

JANSSEN, K., BERCKMANS, D. [1997]: Building a Model to Predict the 3-D Distribution of Temperature in a Ventilated Test Room, *IFAC Workshop*, Hannover, Germany, p. 295.

JAROŠ, M., CHARVÁT, P., ŠVORČÍK, P., GORNÝ, R. [2001]: *Possibilities of CFD-Simulation of Solar Heated Spaces*, Brno University of Technology, Institute of Power Engineering, Dept. of Thermodynamics and Environmental Eng., [Online], Available: http://dt.fme.vutbr.cz/~cfd/solar/paper3.htm, April 2003.

KEANE, R. D., ADRIAN R. J. [1990]: Optimization of Particle Image Velocimeters. Part I: Double Pulsed Systems, *Measurement Science & Technology*, Vol. 1, pp. 1202-15.

KHALIFA, A. J. N., ABDULLAH, S. E. [1999]: Buoyancy Driven Convection in Undivided and Partially Divided Enclosures, *Energy Conversion & Management*, Vol. 40, p. 717.

KIRKUP, L. [1994]: *Experimental Methods: An Introduction to the Analysis and Presentation of Data*, John Wiley & Sons, ISBN 0-471-33579-7.

KLEET, J., OTT, R., MCMILLAN, A. [2000]: Heat Exchangers for Heavy Vehicles Utilizing High Thermal Conductivity Graphite Foams, *SAE Paper No. 2000-01-2207.*

KOBAYASHI, T., SAGA, T., SEGAWA, S. [1992]: Simultaneous Measurement of Temperature and Velocity using Capsuled Thermo-Sensing Liquid Crystals and Nylon Tracer Particles, *Journal of the Visualization,* Society of Japan, Vol. 12, No.1, pp. 71-74.

KREYSZIG, E. [1999]: *Advanced Engineering Mathematics*, 8th Edition, John Wiley & Sons Inc, ISBN 0-471-33328-X.

LAMRANI, M. A., BOULARD, T., ROY, J. C., JAFFRIN, A. [2001]: Airflows and Temperature Patterns Induced in a Confined Greenhouse, *Journal of Agricultural Engineering Research*, Vol. 78, Issue 1, pp. 75-88.

LAUNDER, B. E., SHARMA, B. I. [1974]: Application of the Energy Dissipation Model of Turbulence to the Calculation of Flow Near a Spinning Disc, *Letters in Heat and Mass Transfer*, Vol. 1, pp. 131-138.

LAUNDER, B. E., SPALDING, D. B. [1974]: The Numerical Computational of Turbulent Flow, *Computer Methods in Applied Mechanics and Engineering*, Vol. 3 (2), p. 269-289.

LAUNDER, B. E. [2002]: Modelling of Buoyancy Dominated Turbulent Flows, *Instabilities, Transitions and Regimes in Turbulent Thermal Convection*, Panel Discussion, 12th IHTC, Grenoble.

LAVISION [2002a]: *DaVis Flowmaster Manual, PIV Hardware Manual for DaVis 6.2*, Client Software Manual, LaVision GmbH.

LAVISION [2002b]: *DaVis Flowmaster-Getting Started*, Software Manual, LaVision GmbH.

LEE, S. S. [1997]: Unsteady Aerodynamic Force Prediction on a Square Cylinder Using k–ε Turbulence Models, *Journal of Wind Engineering and Industrial Aerodynamics*, Vol. 67-68, pp. 79-90.

LEE, H., AWBI, H. B. [2004]: Effect of Internal Partitioning on Indoor Air Quality of Rooms with Mixing Ventilation - Basic Study, *Building and Environment*, Vol. 39, pp. 127-141.

LESCHZINER, M. A. [1990]: Modelling Engineering Flows with Reynolds Stress Turbulence Closure, *Journal of Wind Engineering and Industrial Aerodynamics*, Vol. 35, pp. 21-47.

LIENHARD, J. H. IV, LIENHARD, J. H. V. [2002]: *A Heat Transfer Textbook*, 3rd Edition, Phlogiston Press, Cambridge, Massachusetts, U.S.A.

LINDEN, P. F., LANE-SERFF, G. F., SMEED, D. A. [1990]: Emptying Filling Boxes: The Fluid Mechanics of Natural Ventilation, *Journal of Fluid Mechanics*, Vol. 212, p. 300.

LOOMANS, M. G. [1998]: *The Measurement and Simulation of Indoor Air Flow*, Ph.D. Thesis, University of Eindhoven.

MA, G., SHEN, G., PAN, X. [1995]: Bubbles Used as Flow Tracer in PIV in Water Tunnel, *Procs. International Workshop on PIV-Fukui'95*, edited by T. Kobayashi and F. Yamamoto, VSJ, pp. 205-216.

MAHAN, R. [2002]: *Radiation Heat Transfer: A Statistical Approach*, (Chp. 8), John Wiley & Sons, ISBN 0-471-21270-9.

MANN, M., HAIGIS, M. [2000]: Numerical Investigation of the Ventilation and Thermal Comfort in a Commuter Train, *Procs. 3rd MIRA International Vehicle Aerodynamics Conference*, 18/19 October, Rugby, U.K.

MASSEY, B. [1998]: *Mechanics of Fluids*, 7th Edition, Stanley Thornes (Publishers) Ltd, ISBN 0-7487-4043-0. Chp. 6.

MATHWORKS, THE [1999]: *Matlab™, The Language of Technical Computing*, Software Version 5.3.0.10183 (R11), January 21, Copyright 1984-1999.

MELLING, A. [1997]: Tracer Particles and Seeding for Particle Image Velocimetry, *Meas. Science Technology*, Vol. 8, pp 1406-1416.

MICHELSEN, J. A. [1995]: *CFD Vocabulary*, Mechanical Engineering Department, Technical University of Denmark, [Online], Available: http://www.afm.dtu.dk/Staff/jam/vocabulary/vocabulary.html, January 2006.

MISHRA, D., MURALIDHAR, K., MUNSHI, P. [1999]: Experimental Study of Rayleigh–Benard Convection at Intermediate Rayleigh Numbers Using Interferometric Tomography, *Fluid Dynamics Research*, Vol. 25, pp. 231-255.

MISTRIOTIS, A., ACIDIACONO, C., PICUNO, P., BOT, G. P. A., SCARASCIA-MUGNOZZA, G. [1997]: Computational Analysis of Ventilation in Greenhouses at Zero- and Low-Wind-Speeds, *Agricultural and Forest Meteorology*, Vol. 88, No. 2, pp. 121-135.

MOIN, P., SPALART, P. R. [1987]: Contribution of Numerical Simulation Data to the Physics, Modelling, and Measurements of Turbulence, *NASA Tech. Memo 100022.*

MORTENSEN, N. G., HOJSTRUP, J. [1995]: Annex 4: The Solent Sonic Response and Associated Problems, *Procs. Ninth Symposium on Meteorological Observations and Instrumentation*, pp. 18-28.

MORTON, B. R., TAYLOR, G. F. R. S., TURNER, J. S. [1956]: Turbulent Gravitational Convection from Maintained and Instantaneous Sources, *Procs. Royal Society London*, Vol. 234-A, pp. 1-23.

MUKARAMI, S., MOCHIDA, A., HAYASHI, Y., SAKAMOTO, S. [1992]: Numerical Study on Velocity-Pressure Fields and Wind Forces for Bluff Bodies by k-ε, ASM, LES, *Journal of Wind Engineering and Industrial Aerodynamics*, Vol. 41-44, pp.2841-2852.

MULLER, D., RENZ, U. [1996]: Determination of All Airflow Velocity Components by a Particle Image Velocimetry System (PIV), *Procs. 5th International Conference on Air Distribution in Rooms (ROOMVENT)*, pp. 413-419.

MULLER, D., RENZ, U. [1998]: Measurement and Prediction of Room Airflow Patterns Using Different Turbulence Models, *Procs. 8th International Conference on Air Distribution in Rooms (ROOMVENT)*, Vol. 1, pp. 109-116.

MUSSER, A., MCGRATTAN, K., PALMER, J. [2001]: Evaluation of a Fast, Simplified Computational Fluid Dynamics Model for Solving Room Airflow Problems, *Paper NISTIR 6760*, National Institute of Standards and Technology, Interagency Report.

NEVES, K. W. [1988]: Supercomputer Architecture. Computational Fluid Dynamics: Algorithms and Supercomputers, *AGARDOGRAPH*, No. 311.

NEGRAO, O. R. [1997]: Integration of Computational Fluid Dynamics and Building Thermal and Mass Flow Simulations, *Energy and Buildings*, Vol. 27, pp. 155-165.

NIELSEN, P. V., RESTIVO, A., WHITELAW, J. H. [1979]: Buoyancy-Affected Flows in Ventilated Rooms, *Numerical Heat Transfer*, Vol. 2, pp. 115-127.

NIELSEN, P. V. [1998a]: Airflow in a World Exposition Pavilion Studied by Scale-Model Experiments and Computational Fluid Dynamics, *ASHRAE Transactions*, Vol. 101 (2), pp. 1118-1126.

NIELSEN, P. V. [1998b]: The Selection of Turbulence Models for Prediction of Room Airflows, *ASHRAE Transactions*, Vol. 104, Part 1B, pp. 1119-1127.

NIEUWSTADT, F. T. M. [1993]: *Advances in Turbulence IV: Proceedings of the Fourth European Turbulence Conference*, European Turbulence Conference, Delft 30th June-3rd July 1992, Kluwer Academic Publisher, ISBN 0792322827.

NOBILE, E., ONESTI, L. [1995]: Numerical Simulation of Three-Dimensional Time-Dependent Buoyant Flows on the Cray T3D, *Supercomputing Review, Numerical Simulation for Science and Technology*, No. 7, November.

OLSON, D. A., GLICKSMAN, L. R., FERM, H. M. [1990]: Steady-State Natural Convection in Empty and Partitioned Enclosures at High Rayleigh Numbers, *Transactions of the ASME*, Vol. 112, pp. 640-647.

OLSON, D. A., GLICKSMAN, L. R. [1991]: Transient Natural Convection in Enclosures at High Rayleigh Numbers, *ASME Journal of Heat Transfer*, Vol. 113, pp. 635-641.

PAPAKONSTANTINOU, K., CHALOULAKOU, A., DUCI, A., VLACHAKIS, N., MARKATOS, N. [2003]: Air Quality in an Underground Garage: Computational and Experimental Investigation of Ventilation Effectiveness, *Energy and Buildings*, Vol. 35(9), p. 933.

PATANKAR, S. V. [1980]: *Numerical Heat Transfer and Fluid Flow*, Hemisphere Publishing Co., McGraw-Hill, ISBN 0891165223.

PENG, S-H. [1998]: *Modelling of Turbulent Flow and Heat Transfer for Building Ventilation*, Ph.D. Thesis, Chalmers University of Technology, Gothenburg, Sweden.

PICKERING, C. J. D., HALLIWELL, N. A. [1984]: Speckle Photography in Fluid Flows: Signal Recovery with Two-Step Processing, *Applied Optics*, Vol. 23, pp. 1128-29.

PITKANEN, H., ESA, H., SALLINEN, P., LARJOLA, J., HEISKA, H., SIIKONEN, T. [1999]: Time-Accurate CFD Analysis of a Centrifugal Compressor, *Procs. 4th Int. Symposium on Experimental and Computational Aerothermodynamics of Internal Flows,* ISAIF.

POSNER, J. D. [2001]: *Laser Doppler Anemometry and Particle Image Velocimetry Measurements of Indoor Air Flows in a Model Room*, Master Thesis, University of California, U.S.A.

POSNER, J. D., BUCHANAN C. R., DUNN-RANKIN, D. [2003]: Measurement and Prediction of Indoor Air Flow in a Model Room, *Energy and Buildings*, Vol. 35, pp. 515-526.

PRASAD, A. K. [2000]: Particle Image Velocimetry, *Current Science*, Vol. 79 (1), pp. 51-60.

RAFFEL, M., WILLERT, C., KOMPENHHANS, J. [1998]: *Particle Image Velocimetry, a Practical Guide*, Springer-Verlag, Berlin Heidelberg.

RAIHTBY, G. D., HOLLANDS, K. G. T. [1998]: *Natural Convection*, IN: Roshsenow, W. M., Hartneet, J. P., Cho, Y. I.: *Handbook of Heat Transfer*, 3rd Edition, McGraw-Hill, New York. Chp. 4.

RAMESH, N., VENKATESHAN, S. P. [2001]: Experimental Study of Natural Convection in a Square Enclosure Using Differential Interferometer, *Int. Journal of Heat and Mass Transfer*, Vol. 44, pp. 1107-1117.

RAMOS, J. A. E., MARTINHO, N. A. G., PITARMA, R. A., CARVALHO M. G. [2002]: Three-Dimensional Natural Convection in Rooms Connected to the Outside Through Large Openings, *Procs. 8th Int. Conference Air Distribution in Rooms*, Denmark.

RASMUS, L. [1996]: Estimation of Airflow in Livestock Buildings Using Image Analysis, *Procs. 5th Conference on Air Distribution in Rooms (ROOMVENT)*, pp. 49-64.

RICARDO UK LTD [2000]: *Vehicle Thermal Management, VTHERM,* Internal Report.

RICARDO UK LTD [2004A]: VECTIS Computational Fluid Dynamics Release 3.8 - User's Guide, Ricardo Software, Client Confidential.

RICARDO UK LTD [2004B]: VECTIS Computational Fluid Dynamics Release 3.8 - Theory Manual, Ricardo Software, Client Confidential.

ROACHE, P. J. [1994]: Perspective: A Method for Uniform Reporting of Grid Refinement Studies, *ASME Journal of Fluid Engineering*, Vol. 116, pp. 405-413.

ROACHE, P. J. [1997]: Quantification of Uncertainty in Computational Fluid Dynamics, *Annual Review of Fluid Mechanics*, Vol. 29, pp. 123-160.

RODI, W. [1991]: Experience with Two-Layer Models Combining the k-Epsilon Model with a One-Equation Model Near The Wall, *29th Aerospace Sciences Meeting, Reno, NV, AIAA-1991-216*, p. 13.

SAMPATH, S. [2001]: *Sampling Theory and Methods*, Alpha Science, Pangbourne Publishers, ISBN 1842650505.

SASE, S., TAKAKURA, T., NARA, M. [1984]: Wind-Tunnel Testing on Airflow and Temperature Distribution of a Naturally Ventilated Greenhouse, *Acta Hort.*, Vol. 148, pp. 329.

SCHROFF, G. M., KELLER, B. [1993]: Stabilization of Unstable Procedures: The Recursive Projection Method, *SIAM Journal of Numerical Analysis*, Vol. 30 (4), pp. 1099-1120.

SCHUSTER, M. [2003]: Application of CFD as an Efficient Analysis Tool Supporting the Experimental Investigation of Underhood and Underbody Vehicle Flows, *Procs. 6th Vehicle Thermal Management Systems Conference, SAE Paper No. C599/056/2003.*

SEGAL, G., BIJL, H., VUIK, K., KUPPEN, W., ZIJLEMA, M. [1996]: *ISNaS – Incompressible Flow Solver Mathematical Manual*, Institute of Applied Mathematics, Delft University of Technology, Netherlands, [Online], Available: http://ta.twi.tudelft.nl/isnas/isnasmath manual/mathmanual.html, August 2005.

SKEA, A., JOLLIFFE, A., HARRISON, R., JONES, M. R., CARDANI, P., SMITH, L. [2003]: Integrated Underbonnet Thermal Management Simulation, *Procs. 6th Vehicle Thermal Management Systems Conference, SAE Paper No. C599/074/2003.*

SOLLER, C., WENSKUS, R. [1994]: Interferometric Tomography for Flow Visualization of Density Fields in Supersonic Jets and Connective Flow, *Applied Physics*, Vol. 33, Issue 14, pp. 2921–2932.

SOMARATHNE, S., SEYMOUR, M., KOLOKOTRONI, M. [2005]: Dynamic Thermal CFD Simulation of a Typical Office by Efficient Transient Solution Methods, *Building and Environment*, Vol. 40, pp. 887-896.

SORENSEN, D. N., NIELSEN, P. V. [2003]: Quality Control of Computational Fluid Dynamics in Indoor Environments, *Indoor Air*, Blackwell Publ., ISBN 0905-6947.

SOTIROPOULOS, F., VENTIKOS Y. [1998]: Prediction of Flow Through a 90 Deg Bend Using Linear and Non-Linear Two-Equation Models, *AIAA Journal*, Vol. 36(7), pp. 1256-1262.

SOUTH, J., WITTEN, T. [1998]: Turbulence in a Heated Fluid, *Materials Research Centre, University of Chicago,* [Online], Available: http://mrsec.uchicago.edu/Nuggets/Turbulence, October 2004.

SREBRIC, J., CHEN, Q., GLICKSMAN, L. R. [1999]: Validation of a Zero-Equation Turbulence Model for Complex Indoor Airflow Simulation, *ASHRAE Transactions,* Vol. 105(2), pp. 414-427.

SPALDING, D. B. [1972]: A Novel Finite-Difference Formulation for Differential Expressions Involving both First and Second Derivatives, *Int. Journal of Numerical Methods Eng.*, Vol. 4.

STANISLAS, M., KOMPENHANS, J., WESTERWEEL, J. [2000]: *Particle Image Velocimetry,* Kluwer Academic Publishers, ISBN 0-7923-6160-1.

STATHOPOULOS, T. [2002]: The Numerical Wind Tunnel for Industrial Aerodynamics: Real or Virtual in the New Millennium?, *Wind and Structures*, Vol. 5(2-4), pp. 193-208.

STERN, F., WILSON, R. V., COLEMAN, H. W., PATERSON, E. G. [1999]: Verification and Validation of CFD Simulations, *Iowa Institute of Hydraulic Research (IIHR), R # 407.*

STETSON, K. A. [1975]: A Review of Speckle Photography and Interferometry, *Optical Engineering*, Vol. 14, pp. 482-89.

STEVENS, S. P., BANCROFT T. G., SAPSFORD, S. M. [1999]: Improving the Effectiveness of Underhood Airflow Predictions, 4th *Vehicle Thermal Management Systems Conference, SAE paper No. C543/058/99.*

STICKLAND, M. T., SCANLON, T. J., OLDROYD, A., WADDELL, P., CRAWLEY, F., STUBBS, B. [1996]: An Experimental and Computational Analysis of Buoyancy Driven Flows by Laser Sheet Tomography, Particle Image Velocimetry and Computational Fluid Dynamics, *Symposium on Flow Visualization and Image Processing, Honolulu*, USA, Feb 23-26, Vol. 1, pp. 203-208.

TANASAWA, I. [1995]: Experimental Techniques in Natural Convection, *Experimental Thermal and Fluid Science*, Vol. 10, Issue 4, May, pp. 503-518.

TASKINEN, P. [2004]: Modelling of Spray Turbulence with Modified RNG k-epsilon Model, *International Multidimensional Engine Modeling User's Group Meeting 2005*, April 10, Detroit, U.S.A.

TENNEKES, H., LUMLEY, J. L. [1972]: *A First Course in Turbulence*, M.I.T. Press, Cambridge, Massachusetts, USA, ISBN 0-262-20019-8.

THERMOANALYTICS INC. [2003a]: RadTherm Transient CFD Input. Using Transient CFD Data with RadTherm, *Technical Bulletin #330 and #340*, [Online], Available: www.Thermo Analytics.com/support/bulletins, April 2003.

THERMOANALYTICS, INC. [2003b]: *RadTherm™ Version 7.1*, Technical Brochure, Copyright 1996-2004, [Online], Available: www.thermoanalytics.com/support/brochures /RadTherm-Brochure.pdf, August 2004.

VARGAS, M., SIERRA, F. Z., RAMOS, E., AVRAMENKO, A. A. [2002]: Steady Natural Convection in a Cavity, *Int. Comm. Heat Mass Transfer*, Vol. 29, No. 2, pp. 213-221.

WATKINS, S. V. [1989]: Three-Dimensional Modelling of Gas Flow and Spray in Diesel Engines, in *Computer Calculation of Fluid Flow, Heat and Mass Transfer and Combustion in Reciprocating Engines*, Hemispere, p. 193.

WEIDMANN, E. P., WIEDEMANN, J., BINNER, T., REISTER H. [2005]: Underhood Temperature Analysis in Case of Natural Convection, 7th *Vehicle Thermal Management Systems Conference, SAE Paper No. 2005-01-2045.*

WILCOX, D. C. [1988]: Reassessment of the Scale Determining Equation for Advanced Turbulence Models, *AIAA Journal*, Vol. 26, No. 11, p. 1299.

WESTERWEEL, J. [2000]: Theoretical Analysis of the Measurement Precision in Particle Image Velocimetry, *Experiments in Fluids*, S3-S12.

WISNIEWSKI, T. S., BLOGOWSKA, K., REBOW, M. [1998]: Infrared and Liquid Crystal Thermography in Natural Convection, *Procs. 8th Int. Symposium on flow visualisation*, Sorrento, Italy, ISBN 0953399109.

WOFAHRT, J. K., BAIER, W. B., WIESLER, B., RAULOT, A., RUGH, J. P., BHARATHAN, D., KUBMANN, C. [2005]: Aspects of Cabin Fluid Dynamics, Heat Transfer, and Thermal Comfort in Vehicle Thermal Management Simulations, *SAE paper No. 2005-01-2000.*

WORTHY, J. [2003]: *Large Eddy Simulation of Buoyant Plumes*, Ph.D. Thesis, Cranfield University, School of Mechanical Engineering, United Kingdom.

WOSNITZA, E. M. [2002]: Data Analysis in Thermomechanical Analogue Modelling, In: *Schellart, W. P., Passchier, C. W. [2002]*: Analogue Modelling of Large Scale Tectonic Processes, *Journal of the Virtual Explorer*, Vol. 7, pp. 97-122.

WOZNIAK, G., WOZNIAK, K. [1994]: Buoyancy and Thermocapillary Flow Analysis by the Combined Use of Liquid Crystals and PIV, *Experiments in Fluids*, Vol. 17, pp. 141-146.

YAKHOT, V., ORSZAG, S. A. [1986]: Renormalisation Group Analysis of Turbulence. I. Basic Theory, *Journal of Scientific Computing*, Vol. 1, No. 1, pp. 3-51.

YANG, T. [2004]: *CFD and Field Testing of a Naturally Ventilated Full-Scale Building*, Ph.D. Thesis, University of Nottingham, School of Civil Engineering, United Kingdom.

YANG, Z., BOZEMAN, J., SHEN, F. Z., ACRE, J. A. [2003]: CFRM Concept at Vehicle Idle Conditions, *SAE Paper No. 2003-01-0613.*

YANG, Z., BOZEMAN, J., SHEN, F. Z. [2004]: CFD for Flow Rate and Air Recirculation at Vehicle Idle Conditions, *SAE Paper No. 2004-01-0053.*

YAZHUO, Q. [2002]: Application of CFD for Indoor Airflow Simulation – A Zero-Equation Turbulence Model, [Online], Available: www.arche.psu.edu/courses /ae597J, April 2003.

YE, T., MITTAL, R., UDAYKUMAR, H. S., SHYY, W. [1999]: An Accurate Cartesian Grid Method for Viscous Incompressible Flows with Complex Immersed Boundaries, *Journal of Computational Physics,* Vol. 156, pp. 209-240.

ZHANG, Y., RUFF, G. A. [1994]: Three-Dimensional Temperature Measurements in Enclosures by Using Multiview Interferometric Tomography, *Measurement Science & Technology*, Vol. 5, No. 5, pp. 495-502.

ZHANG, G., SVIDT, K., BJERG, B., MORSING, S. [1999]: Buoyant Flow Generated by Thermal Convection of a Simulated Pig, *Transactions of the ASAE*, Vol. 42 (4), p. 1113.

ZHAO, L., ZHANG, Y., WANG, X., RISKOWSKI, G. L., CHRISTIANSON, L. L. [1999]: Development of Particle Image Velocimetry Techniques for Measurement of Room Airflow Patterns in Ventilated Airspaces, *ASHRAE Transactions*, Vol. 105, No. 2.

ZHOU, Y., MCCOMB W. D., VEHALA, G. [1997]: Renormalization Group (RG) in Turbulence: Historical and Comparative Perspective, *NASA Tech. Report ICASE 1997.*

SUPPLIERS OF INSTRUMENTATION AND EXPERIMENTAL PARTS

ATP INSTRUMENTATION LTD, Tournament Way, Ivanhoe Industrial Estate, Ashby De La Zouch, Leicestershire, LE65 2UU. Website: www.atp-instrumentation.co.uk.

CONTINUUM, 3150 Central Expressway, Santa Clara, CA, 95051, USA. Website: www.continuumlasers.com.

FARNELL ELECTRONIC COMPONENTS LTD, Casteleton Road, Leeds, LS12 2EN. Website: www.farnellinone.co.uk.

HAWCO DIRECT, 8 Cranfield Road, Lostcock Industrial Estate, Bolton, Lancs. BL6 4SB. Website: www.hawcodirect.co.uk.

INFINITY PHOTO-OPTICAL COMPANY, 706 Mohawk Dr., Suite 15, Bulder, CO 80303 USA. Website: www.infinity-usa.com.

INSTRUMENT GLASSES, 236-258 Alma Road, Ponders End, Enfield, Middlesex, EN3 7BB. Website: www.instrument-glasses.co.uk.

LAVISION GMBH, Anna-Vandenhoeck-Ring 19, D-37081 Goettingen, Germany. Website: www.LaVision.de.

MEASUREMENT SYSTEMS LTD, 16 Kingfisher Court, Newbury, Berkshire, RG14 5SJ. Website: www.measurementsystems.co.uk.

OMEGA ENGINEERING LTD, One Omega Drive, River Bend Technology Centre, Northbank, Irlam, Manchester, M44 5BD. Website: www.omega.co.uk.

PHOTONIC SOLUTIONS PLC, Gracemount Business Pavilions, 40 Captains Road, Units A2/A3, Edinburgh, EH17 8QF. Website: www.psplc.com.

RS COMPONENTS LTd, P.O. Box 99, Corby, Northants, NN17 9RS. Website: www.rswww.com.

SCITEK CONSULTANTS LTD, Unit 41 Derwent Business Centre, Derby, DE22 3TN. Website: www.scitekconsultants.co.uk.

Appendices

APPENDIX A

VECTIS STRUCTURE AND RADIATION MODULE

The following gives a brief overview of the structure of the VECTIS software package and its radiation module. The finite-volume formulation of the governing equations for radiation heat transfer is also presented. Further details can be found in the VECTIS manual [Ricardo Ltd. 2004b].

VECTIS, Code Structure – VECTIS is based on five individual but linked programs, referred to as *phases*, which are schematically shown in Figure A1. A CFD investigation requires a CAD model free of geometrical imperfections; it is the *Phase1* program that enables the correction of the CAD geometry provided for the simulation and then its conversion to a triangulated format for numerical analysis. The construction of the mesh grid, the mesh refinement and the specification of boundary conditions are also performed in *Phase1*. *Phase2* is the VECTIS mesh generator. It is fully automatic and produces a locally refined Cartesian mesh that is suitable for fluid analysis using the CFD solver. *Phase4* concludes the VECTIS mesh generation: it reads the output file of *Phase2* and assembles all connectivity information of the mesh (i.e. the number and the addresses of neighbours that a cell has in each of the six directions) as required by the solver (the *Phase3* module has been completely integrated into *Phase4* in a recent version of the software [Ricardo Ltd. 2004b] and thus it is not shown in Figure A1). Once the model is ready for the analysis, the user must prepare an "input" file containing all the modelling features for the numerical solution. This can be done graphically with *Phase5*, which is then

- *Phase5* reads the results of *radsolv* from the *outfile* and performs further iterations until the successive data exchange. The process is then repeated.

The *radpost* program can be used to visualise super-patches, view factors and the results of the radiation calculations. *Phase6* can be used to view both convection and radiation results.

Radiation Model, Mathematical and Numerical Formulation – The calculation of heat transfer is coupled to the energy equation with a heat source term. The governing equation for the heat transfer is given in a tensor notation as:

$$\rho c \frac{\partial T}{\partial t} = \nabla \cdot (k \nabla T) \tag{A.1}$$

The finite volume method is based on a flux balance: the sum of fluxes that enter the system must be equal the sum of fluxes that leave the system. Using Green's theorem, equation (A.1) can be transformed to:

$$\int_{\Omega} \rho c \frac{\partial T}{\partial t} d\Omega = \int k \frac{\partial T}{\partial n} d\Gamma \tag{A.2}$$

In this transformation, the volume integral was replaced by the integration over the boundary. There are several types of boundary conditions that the heat-transfer equation allows so that the different types of heat-transfer problems can be modelled:

$$-k \frac{\partial T}{\partial n} = k \frac{T - T_n}{r} = q_k \qquad \text{on boundary with specified heat flux, } \Gamma_1$$

$$-k \frac{\partial T}{\partial n} = h(T - T_\infty) = q_c \qquad \text{on boundary with specified convective heat loss, } \Gamma_2$$

$$-k \frac{\partial T}{\partial n} = h(T^4 - T_\infty^4) = q_r \qquad \text{on boundary with specified radiation, } \Gamma_3$$

Equation (A.2) can also be re-written as

$$\int_{\Omega} \rho c \frac{\partial T}{\partial t} d\Omega = \int_{\Gamma_1} q_k d\Gamma + \int_{\Gamma_2} q_c d\Gamma + \int_{\Gamma_3} q_r d\Gamma \tag{A.3}$$

Equation (A.3) cannot be solved directly but it needs to be discretised. Because the Finite Volume Method is used in *radsolv* the discreet points are the centre points of the patches or super patches. The equation system then looks like:

$$\boldsymbol{M}\dot{\boldsymbol{T}} + \boldsymbol{K}\boldsymbol{T} + \boldsymbol{C}\boldsymbol{T} + \boldsymbol{R}\boldsymbol{T}^4 = \boldsymbol{Q} + \boldsymbol{C}_\infty + \boldsymbol{R}_\infty \qquad \text{(A.4)}$$

where

$$\boldsymbol{M}\dot{\boldsymbol{T}} = \int_\Omega \rho c \frac{\partial T}{\partial t} d\Omega = \delta_{ij} \rho_i c_i V_i \dot{T}_i \qquad \text{- Mass matrix}$$

$$\boldsymbol{K}\boldsymbol{T} = \int_\Gamma k \frac{T - T_n}{r} d\Gamma = \sum_{j=1}^{nb_1} k_i \frac{A_{ij}}{r_{ij}} \left(T_i - T_j\right) \qquad \text{- Conduction matrix}$$

$$\boldsymbol{C}\boldsymbol{T} = \int_\Gamma h \cdot T d\Gamma = \sum_{j=1}^{nb_2} h_{ij} A_{ij} T_j \qquad \text{- Convection matrix}$$

$$\boldsymbol{R}\boldsymbol{T}^4 = \int_\Gamma \varepsilon \sigma T^4 d\Gamma = \sum_{j=1}^{nb_3} \varepsilon_{ij} \sigma A_{ij} T_j^4 \qquad \text{- Radiation matrix}$$

$$\boldsymbol{Q} = \int_\Gamma q d\Gamma = \sum_{j=1}^{nb_2} q_{kij} A_{ij} \qquad \text{- Conduction (heat flux) vector}$$

$$\boldsymbol{C}_\infty = \int_\Gamma h \cdot T_\infty d\Gamma = \sum_{j=1}^{nb_2} h_{ij} A_{ij} T_{\infty j} \qquad \text{- Convection vector}$$

$$\boldsymbol{R}_\infty = \int_\Gamma \varepsilon \sigma T_\infty^4 d\Gamma = \sum_{j=1}^{nb_3} \varepsilon_{ij} A_{ij} T_{\infty j}^4 \qquad \text{- Radiation vector}$$

APPENDIX B

CALCULATION OF RAYLEIGH NUMBER (*Ra*) AND CONVECTIVE HEAT TRANSFER COEFFICIENT (*h*)

The functional equation for the heat transfer coefficient, h, in natural convection is

$$h \text{ or } \bar{h} = fn\left(k, |T_s - T_\infty|, x \text{ or } L, \nu, \alpha, g, \beta\right) \tag{B.1}$$

where L is the length scale characteristic of the given problem. From dimensional analysis (and Buckingham's theorem), 4 pi-groups emerges from the 8 variables in [W], [m], [s], and [°C] (or [K]). These are:

$$\Pi_1 = \frac{\bar{h}L}{k} = \overline{Nu}_L, \qquad \Pi_2 = \frac{\nu}{\alpha} = Pr, \qquad \Pi_3 = \frac{L^3}{\nu^2}|g|, \qquad \Pi_4 = \beta|T_s - T_\infty| = \beta\Delta T$$

where all variables are defined in the nomenclature of this thesis.

$\overline{Nu}_L$ is the average Nusselt number and is inversely proportional to the thickness of the thermal boundary layer. From knowledge of the Nusselt number, the average heat transfer coefficient may be found. Π_3 characterises the importance of the buoyant forces relative to viscous forces. Π_4 characterises the thermal expansion of the fluid. The pi-groups Π_3 and Π_4 usually appear as a product, i.e. the Grashof number, Gr_L (where the subscript designates the characteristic length on which the dimensionless number is based on):

$$\Pi_3\Pi_4 \equiv Gr_L = \frac{g\beta\Delta TL^3}{\nu^2} \tag{B.2}$$

The Grashof number plays the same role in free convection that the Reynolds number plays in forced convection. In the dimensional analysis of natural convective flows the product of *Gr* and *Pr* is usually used. This product defines the Rayleigh number, *Ra*:

$$Ra_L \equiv Gr_L Pr = \frac{g\beta\Delta TL^3}{\alpha\nu} \tag{B.3}$$

The Rayleigh number is normally used to highlight the transition from laminar to turbulent flow. The critical Rayleigh number depends on the geometry of the model and the fluid properties. Usually, for Rayleigh numbers in the range of 10^5 to 10^7 the flow is characterised by instability or "soft" turbulence, as discussed in Chapter 1 (Section 1.2.3, *Dynamic Similarity*). Above Rayleigh numbers of 10^8-10^9, full turbulent motion begins. The correlation of natural convection gives:

$$Nu_L \equiv fn(Ra_L, Pr) \tag{B.4}$$

Generally, such correlation is of the form:

$$Nu_L \equiv C \cdot Ra_L^{\ n} \tag{B.5}$$

where C is a constant depending on geometry, n=1/4 for laminar flows and n=1/3 for turbulent flows.

Analytical calculations were performed during this study to determine the actual airflow regime around the heated components of the underhood model under analysis. The results are tabulated in Table B1. A sample set of calculations (for the engine block) are presented below.

Heat Transfer Characteristics, Engine Block – The Rayleigh number was calculated for both the horizontal and the vertical surfaces of the block. The airflow properties were determined from thermodynamic tables at the film temperature value.

$$T_{film} = \frac{T_s + T_\infty}{2} = \frac{130 + 70}{2} = 100°C = 373K$$

The volumetric expansion coefficient was approximated by

$$\beta = \frac{1}{T_\infty} = \frac{1}{70 + 273} = 2.92 \times 10^{-3} K^{-1}$$

For the vertical walls of the engine block, Equation (B.3) gave

$$Ra_{vertical} = \frac{9.81 \cdot 2.92 \times 10^{-3} \cdot (130 - 70) \cdot 0.25^3}{3.49 \times 10^{-5} \cdot 2.33 \times 10^{-5}} = 3.30 \times 10^7$$

The Rayleigh numbers for the upper and lower horizontal surfaces were determined in the same way but using the appropriate length scales. The area-weighted average of the *Ra* number for the block was then calculated:

$$Ra_{avg} = \frac{(Ra_{vertical} \times A_{vertical}) + (Ra_{upper} \times A_{upper}) + (Ra_{lower} \times A_{lower})}{(A_{vertical} + A_{upper} + A_{lower})} = 2.36 \times 10^7$$

The convective heat transfer coefficient was calculated from the average Nusselt number, which was determined using empirical correlations. The *Squire-Eckert* relation [Lienhard *et al.* 2002] was employed for calculating for the vertical walls, which were taken to be at isothermal condition:

$$\overline{Nu}_{vertical} = 0.678 Ra_L^{1/4} \left(\frac{Pr}{0.952 + Pr} \right)^{1/4}$$

where the Prandtl number was

$$Pr = \frac{\nu}{\alpha} = \frac{\rho C_p \nu}{k} = \frac{0.948 \cdot 1010.1 \cdot 2.33 \times 10^{-5}}{0.0316} = 7.06 \times 10^{-1}$$

Hence, $\underline{\overline{Nu}_{vertical} = 41.5}$

For heated horizontal surfaces facing up, with an area A and a perimeter P, Raihtby and Hollands [1998] suggested the following relation:

$$\overline{Nu}_{upper} = \frac{0.560 Ra_L^{1/4}}{\left[1 + (0.492/Pr)^{9/16}\right]^{4/9}}$$

where the characteristic length scale is taken as A/P. Consequently, $\overline{Nu}_{upper} = 9.56$.

However, for $\overline{Nu}_L \leq 10$, the boundary layer is relatively thick and the $\overline{Nu}$ value must be corrected [Raihtby and Hollands 1998]:

$$\overline{Nu}_{corrected} = \frac{1.4}{\ln\left(1+1.4/\overline{Nu}_L\right)} = 10.2$$

For the bottom surfaces of the block, the correlation given by Fuji and Himura [1972], $\overline{Nu}_{lower} = 0.58 Ra_L^{1/5}$ with L taken as the width of the block, was used. This resulted in $\underline{\overline{Nu}_{lower} = 13.6}$.

The convective heat transfer coefficient was determined from $\bar{h} = \frac{\overline{Nu} \cdot k}{L}$ [W/m^{2}K] and the convective heat flux from $q = \bar{h}\left(T_s - T_\infty\right)$ [W/m^2].

The results of the calculations for each block of the underhood model are presented in Table B1.

APPENDIX C

UNDERHOOD MODEL CAD DRAWINGS

Two-dimensional CAD drawing were prepared with the CAD software I-DEAS™ [Electronic Data System 2003] and used to support the manufacture and construction of the laboratory rig and the setup of the CFD model.

The following 2-D drawings are presented in the following pages:

1) Experimental apparatus (overview, first dimensioning sheet)
2) Experimental apparatus (overview, second dimensioning sheet)
3) Engine block
4) Turbocharger block
5) Gearbox block
6) Glass compartment

APPENDIX E

PIV SEEDING – TRACER PARTICLE DYNAMICS

The performance of trace particles as how closely they follow the flow streamlines is important since it is actually the velocity of the tracers that is measured by the PIV instrumentation. When the density of the seeding and fluid is different, this can be quantified by considering the effect of gravity on both the particles and the fluid motion. Stokes' drag law can be used to relate the terminal settling velocity of a smooth, rigid sphere (tracer particle) in a viscous fluid of known density and viscosity to the diameter of the sphere when subjected to a known force field (e.g. gravitational force). The drag force on the particle is written according to Stokes' law (i.e. assuming a fluid with a very small Reynolds number, where the viscous forces are much larger than the inertial forces) as [Massey 1998]:

$$F_d = 3\pi\mu V_{pt} d_{pt} \tag{E.1}$$

where V_{pt} is the particle velocity and d_{pt} is the particle diameter

The settling velocity is established by equating the drag force to the gravitational force, $F_g = mg$,

$$F_d = F_g, \quad \text{i.e. } 3\pi\mu_f V_{pt} d_{pt} = \frac{(\rho_{pt} - \rho_f)\pi d_{pt}^{\,3}}{6} g$$

The particle settling velocity is therefore written as:

$$V_{pt} = \frac{(\rho_{pt} - \rho_f)}{18\mu_f} g d_{pt}^{\,2} \tag{E.2}$$

where ρ_{pt} and ρ_f are the densities of the particle and the fluid, respectively, and μ_f is the fluid viscosity.

It is also useful to look at the seeding velocity as a function of time when a step in fluid velocity is imposed. The relaxation time, i.e. the time required for the tracer to adjust/relax its velocity to the fluid velocity can be expressed as,

$$\tau = d_p^2 \frac{\rho_p}{18\mu} \tag{E.3}$$

From Newton's Law

$$\begin{aligned} F_g - F_d &= mg - 3\pi\mu V(t) d_{pt} = m\frac{dV(t)}{dt} \\ \Rightarrow \tau g - V(t) &= \tau \frac{dV(t)}{dt} \end{aligned} \tag{E.4}$$

Accordingly, the step response of a particle injected at zero velocity in a flow with a velocity V_{TS} follows an exponential law if the density of the particle is much greater than the fluid density [Raffel *et al.* 2001].

$$V(t) = V_{TS}\left[1 - e^{-\frac{t}{\tau}}\right] \tag{E.5}$$

where t is time, and τ is the relaxation time.

The relaxation of the particle velocity with time is plotted in Figure E1. At t = 0, $V(t)$ = 0; when $t > 3\tau$ the gravitational force balances with the drag force and $V(t) = V_{TS}$. The equations of motion would be more complex if Stokes flow cannot be assumed (i.e. if $Re > 1$).

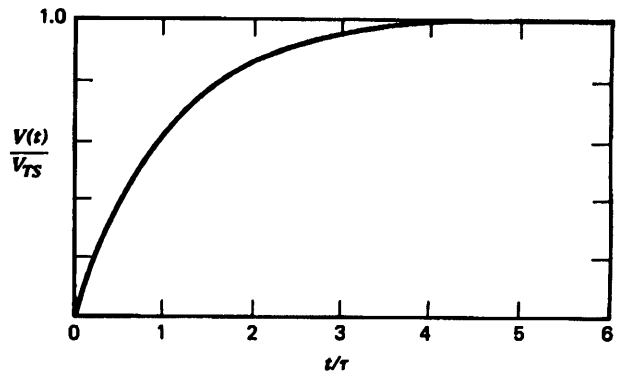

Figure E1 – Velocity relaxation of a particle with specific diameter.

Equations (E.2) and (E.5) provide good guidance for the selection of the optimal diameter for a PIV flow tracer particle. Some researches have proposed alternative methods to determine if the tracers would follow the flow streamlines, including describing the motion of particles relative to the flow as a function of the frequency response to an oscillating flow [Al-Taweel and Carley 1971].

For the present study, vegetable corn oil droplets were employed as seeding (density of 922 kg/m^3). Owing to large density difference with air, the oil was atomised in droplets of approximately 1μm in diameter. Considering the properties of air at 300K (i.e. ρ_f=1.16 kg/m^3, μ_f=1.87×10^{-5} kg/ms), the settling velocity of the tracers resulted from Equation (E.2) to be 0.026 mm/s (i.e. 2.6×10^{-5} m/s), thus, of a negligible magnitude compared to the mean velocity of the buoyant flow in the underhood.

APPENDIX H

MATLAB™ PROGRAM FOR CONTOUR PLOTS

The code written in Matlab™ [Mathworks 1999] was used to interpolate in 2-D planes the temperature values measured with thermocouples and extracted from the CFD solution. The program then produced contour maps of the temperature distribution for each investigated surfaces and air planes.

The temperature data and the thermocouple coordinate locations were written in input text files that were then processed by the program. The files contained also the logging time for each set of measurement point, which were written in successive rows (a sample input file is shown below). For each row, the code interpolated the data in space using a triangle-based linear function. The result was a contour plot varying with time but on a fixed temperature scale. The program enabled therefore to visualise the time-dependent changes in temperature distribution for each investigated plane, during both heating and cooling conditions. The following commands were used to write the code:

MESHGRID	Produces a uniform grid (XI x YI) from the matrix of X, Y coordinates of the thermocouples.
ZI = GRIDDATA(X,Y,T,XI,YI)	Fits a surface of the form T = F(X,Y) (temperature values) to the data in the non-uniformly spaced vectors (X, Y, T). The triangle-based linear interpolation of the surface is calculated at the points specified by (XI, YI).
C = INTERP2(ZI,2)	Two-dimensional expansion of ZI with interpolation between every element, working recursively two times.
CONTOURF(C)	Colour filled contour plot of matrix C. Calculations repeated and plot updated at each timestep specified in the input text file.

APPENDIX I

SAMPLING THEORY AND STANDARD ERRORS

Only a limited number of PIV images can be acquired to represent the mean flow field in a plane. Statistical sampling theory [Sampath 2001] was employed in this study to determine the margin of error (*confidence interval*) of the PIV samples in determining various flow parameters (e.g. the *population mean* – the theoretical mean of an infinite number of observations). A description of the statistical relations used in this study to determine the 95% confidence interval of the PIV data follows:

1) Assuming x_1, ..., x_n are n independent observations that are "normally" distributed with an expected value μ_p (*population mean*) and a deviation σ_p (*population deviation*), the first step of the statistical analysis consisted of calculating the *sample mean*, $\bar{x}_n$:

$$\bar{x}_n = (x_1 + \cdots + x_n)/n \tag{I.1}$$

2) The *sample deviation*, s_n was then calculated from:

$$s_n = \sqrt{\frac{1}{(n-1)}\sum_{i=1}^{n}(x_i - \bar{x}_n)^2} \tag{I.2}$$

3) The *Standard Error of the Mean* (SE_m), i.e. the variation of the sample mean around the true population mean, μ_p, was determined from:

$$SE_m = \frac{s_n}{\sqrt{n}} \tag{I.3}$$

4) The confidence level expresses the probability (usually percentage) that the confidence interval produced for a sample mean will contain the true values (i.e. the mean flow parameters of the population). Common choices are 90%, 95% and 99%. These levels correspond to percentages of the area under the standard

normal distribution curve. For example, a 95% confidence interval covers 95% of the distribution, i.e. there is a 95% confidence/certainty that the true mean parameter lies within a specific interval; the probability of observing a value outside this range is less than 5%.

The confidence interval is constructed from knowledge that the probability of the measurements falling within a specified range (i.e. $\pm\Delta x$) for a Gaussian population is statistically given by [Kirkup 1994]:

$$\text{Prob}(\Delta x) = \int_{\mu-\Delta x}^{\mu+\Delta x} \frac{1}{\sigma\sqrt{2\pi}} e^{-\left(\frac{(x-\mu_p)^2}{2\sigma^2}\right)} dx \qquad \text{(I.4)}$$

After normalisation, the integral of Equation (I.4) can be solved employing the *Student-t* distribution [Kirkup 1994]. The *Student-t* distribution is commonly used in place of a standard normal distribution for relatively small sample sizes. The distribution curve establishes the probability interval for a required confidence level, e.g. 95%:

$$Prob\left(\bar{x} - t \cdot SE_m \leq \mu_p \leq \bar{x} - t \cdot SE_m\right) = 0.95 \qquad \text{(I.5)}$$

For samples of the same size, the confidence interval increases as the confidence level is increased (i.e. the value of t is the largest for a 99% level). For a confidence interval of 95% and for relatively small samples, t is commonly taken to be equal to 1.96 [Kirkup 1994].

$$t \equiv \frac{\bar{x} - \mu_p}{S_n / \sqrt{n}} = 1.96 \qquad \text{(I.6)}$$

Consequently, the upper and lower limits of uncertainty of the population (the confidence interval) were calculated from the sample mean according to:

$$\mu_p(95\%) = \bar{x} \pm 1.96 \cdot SE_m \qquad \text{(I.7)}$$

APPENDIX J

AUTOMATED FAST TRANSIENT SIMULATION

J.1 BATCH FILE

SETUP

- The user specifies in the Batch file the location of the directories that contain the files of the CHT parts of the simulation.
- The user enters in the Batch file the commands to be then automatically written in the VECTIS input files for running the simulation (for each CHT part).
- Once saved with *.bat* extension, the program can be directly run from a Windows™ DOS shell.

Below is a sample Batch file for a simulation with two CHT parts. The code would need to be expanded for CFD computations modelling more than two CHT parts and should be modified accordingly to the simulation requirements.

SOURCE CODE (as written to run for SWITCH methodology on *ModelA*)

```
@echo off
cls
echo. ************************************************************
echo. AUTOMATIC BATCH FILE FOR RUNNING VECTIS TRANSIENT
SIMULATION
echo. Written by MATTEO FRANCHETTA
echo. ************************************************************

type nul >"%temp%\~YesOrNo.tmp"
echo.
echo. Delete all files in directory [y/n]?
del /p "%temp%\~YesOrNo.tmp" >nul
if not exist "%temp%\~YesOrNo.tmp" goto Yes
echo.
del %temp%\~YesOrNo.tmp
goto :SS
:Yes
for %%i IN (0 1 2 3 4 5 6 7 8 9) do del
"D:\Documents\PhD\VECTIS\METH_TESTA\3_BLOCK\*.*_00%%i"
for %%i IN (0 1 2 3 4 5 6 7 8 9) do del
"D:\Documents\PhD\VECTIS\METH_TESTA\3_AIR\*.*_00%%i"
for %%i IN (0 1 2 3 4 5 6 7 8 9) do del
"D:\Documents\PhD\VECTIS\METH_TESTA\3_BLOCK\*.*_01%%i"
for %%i IN (0 1 2 3 4 5 6 7 8 9) do del
"D:\Documents\PhD\VECTIS\METH_TESTA\3_AIR\*.*_01%%i"
goto :SS

:SS
set noSS=
set /p noSS= Type number of Steady-State iterations =
if %noSS% GTR 10000 (goto HIGH) else goto LOW
if %noSS% LSS 1 (goto LOW)
goto TR
:TR
set noTR=
echo.
set /p noiteTR= Type number of Transient timesteps =
echo.
set /p SizeTR= Type size of timesteps (seconds) =
set /a NoTR=%noiteTR%*%SizeTR%
goto end
:HIGH
ECHO. The number of iterations you have chosen is too large.
ECHO. Please try again
goto SS
:LOW
if %noSS% LSS 1 (ECHO. The number of iterations you have chosen is too low.
ECHO. Please try again
goto SS) else goto TR
:END
echo.
set /p ITE= Insert number of VECTIS runs =
set /p REP= Insert in different format (e.g. for 3 write "1 2 3") =
echo.
set /a SIMTIMEs=(%ITE%/2)*%NoTR%
set /a dec=100
set /a Hour=3600
set /a Minutes=60
set /a SIMTIMEh=%SIMTIMEs%/%Hour%
set /a SIMTIMEm=(%SIMTIMEs%/%Minutes%)-(%SIMTIMEh%*%minutes%)
set /a SIMTIMEs2=(%SIMTIMEs%)-(%SIMTIMEh%*%Hour%)-
(%SIMTIMEm%*%Minutes%)
echo. Simulated Time is %SIMTIMEs% second (%SIMTIMEh%hrs
%SIMTIMEm%min %SIMTIMEs2%sec)

type nul >"%temp%\~YesOrNo.tmp"
echo. Is this fine [y/n]?
del /p "%temp%\~YesOrNo.tmp" >nul
if not exist "%temp%\~YesOrNo.tmp" goto Yes
del %temp%\~YesOrNo.tmp
goto :SS
:Yes
goto :DIRECTORY

:: XXXXXXXXXXXXXXXXXXXXXXXXXXXXXXXXXXXXXXXXXXXXXXX
:RUN
echo.      DONE!
echo.
PAUSE
cls
```

```
D:
cd "%AIR%"
SET /a I=0
if %I%==%ITE% (
GOTO :PLOT
) ELSE (
copy /Y "D:%INPFOLDER%\BLOCK.INP1" "D:%BLOCK%\BLOCK.INP"
copy /Y "D:%INPFOLDER%\AIR.INP1" "D:%AIR%\AIR.INP"
call run_air
)
:
SET /a I=%I%+1
if %I%==%ITE% (
GOTO :PLOT
) ELSE (
copy /Y "D:%INPFOLDER%\BLOCK.INP16" "D:%BLOCK%\BLOCK.INP"
copy /Y "D:%INPFOLDER%\AIR.INP16" "D:%AIR%\AIR.INP"
call run_air
)
:: XXXXXXXXXXXXXXXXXXXXXXXXXXXXXXXXXXXXXXXXXXXXXX

:: XXXXXXXXXXXXXXXXXXXXXXXXXXXXXXXXXXXXXXXXXXXXXX
:DIRECTORY
SET HOME=\Documents and Settings\M_FRANCHETTA.MECHENG\Desktop
SET INPFOLDER=\Documents\PhD\VECTIS\METH_TESTA\INP
SET BLOCK=\Documents\PhD\VECTIS\METH_TESTA\3_BLOCK
SET AIR=\Documents\PhD\VECTIS\METH_TESTA\3_AIR
echo.
echo. HOME DIRECTORY   = C:%HOME%
echo. INP FILES DIR    = D:%INPFOLDER%
echo.
echo. MODEL1 FILES DIR = D:%AIR%
echo. MODEL2 FILES DIR = D:%BLOCK%
echo.
echo. PROCESSING INPUT FILES...
echo.
GOTO :AIRINP
:: XXXXXXXXXXXXXXXXXXXXXXXXXXXXXXXXXXXXXXXXXXXXXX

:: XXXXXXXXXXXXXXXXXXXXXXXXXXXXXXXXXXXXXXXXXXXXXX
:AIRINP
D:
cd "%INPFOLDER%"
del AIR.INP*
for %%i IN (%REP%) do echo !VECTIS_MAIN_INPUT MODULAR VERSION
3.400>>AIR.INP%%i
for %%i IN (1 3 5 7 9) do echo STEADY_STATE >>AIR.INP%%i
for %%i IN (1 3 5 7 9) do echo
#========================================== >>AIR.INP%%
for %%i IN (1 3 5 7 9) do echo EQUATIONS >>AIR.INP%%i
for %%i IN (1 3 5 7 9) do echo EQN_U_MOMENTUM >>AIR.INP%%i
for %%i IN (1 3 5 7 9) do echo EQN_V_MOMENTUM >>AIR.INP%%i
for %%i IN (1 3 5 7 9) do echo EQN_W_MOMENTUM >>AIR.INP%%i
for %%i IN (1 3 5 7 9 do echo EQN_PRESSURE >>AIR.INP%%i
for %%i IN (1 3 5 7 9) do echo EQN_TEMPERATURE >>AIR.INP%%i
for %%i IN (1 3 5 7 9) do echo
#========================================== >>AIR.INP%%i
for %%i IN (1 3 5 7 9) do echo U_MOMENTUM>>AIR.INP%%i
for %%i IN (1 3 5 7 9) do echo 100 2 0 2 -10 >>AIR.INP%%i
for %%i IN (1 3 5 7 9) do echo 8.0000e-001 8.0000e-001 8.0000e-001 8.0000e-
001 1.0000e+000 1.0000e+000 1.0000e+000 >>AIR.INP%%i
for %%i IN (1 3 5 7 9) do echo
#========================================== >>AIR.INP%%i
for %%i IN (1 3 5 7 9) do echo V_MOMENTUM>>AIR.INP%%i
for %%i IN (1 3 5 7 9) do echo 100 2 0 2 -10 >>AIR.INP%%i
for %%i IN (1 3 5 7 9) do echo 8.0000e-001 8.0000e-001 8.0000e-001 8.0000e-
001 1.0000e+000 1.0000e+000 1.0000e+000 >>AIR.INP%%i
for %%i IN (1 3 5 7 9) do echo
#========================================== >>AIR.INP%%i
for %%i IN (1 3 5 7 9) do echo W_MOMENTUM>>AIR.INP%%i
for %%i IN (1 3 5 7 9) do echo 100 2 0 2 -10 >>AIR.INP%%i
for %%i IN (1 3 5 7 9) do echo 8.0000e-001 8.0000e-001 8.0000e-001 8.0000e-
001 1.0000e+000 1.0000e+000 1.0000e+000 >>AIR.INP%%i
for %%i IN (1 3 5 7 9) do echo
#========================================== >>AIR.INP%%i
for %%i IN (1 3 5 7 9) do echo PRESSURE>>AIR.INP%%i
for %%i IN (1 3 5 7 9) do echo 100 1 3 2 -10 >>AIR.INP%%i
for %%i IN (1 3 5 7 9) do echo 9.5000e-001 9.5000e-001 9.5000e-001 9.5000e-
001 1.0000e+000 1.0000e+000 1.0000e+000 >>AIR.INP%%i
for %%i IN (1 3 5 7 9) do echo
#========================================== >>AIR.INP%%i
for %%i IN (1 3 5 7 9) do echo TEMPERATURE>>AIR.INP%%i
for %%i IN (1 3 5 7 9) do echo 100 1 0 2 -10 >>AIR.INP%%i
for %%i IN (1 3 5 7 9) do echo 1.0000e+000 1.0000e+000 1.0000e+000
1.0000e+000 1.0000e+000 1.0000e+000 1.0000e+000 >>AIR.INP%%i
for %%i IN (1 3 5 7 9) do echo
#========================================== >>AIR.INP%%i
for %%i IN (1 3 5 7 9) do echo SOLUTION_CONTROL_2 >>AIR.INP%%i
for %%i IN (1 3 5 7 9) do echo F >>AIR.INP%%i
for %%i IN (1 3 5 7 9) do echo -6 1.000000e-006 >>AIR.INP%%i
for %%i IN (1 3 5 7 9) do echo 0.000000e+000 %NoSS%.0e+000 1.000000e+000
>>AIR.INP%%i
for %%i IN (1 3 5 7 9 11 13 15) do echo 5 1.000000e+000 %NoSS%.0e+000
>>AIR.INP%%i
for %%i IN (2 4 6 8 10) do echo EQUATIONS>>AIR.INP%%i
for %%i IN (2 4 6 8 10) do echo EQN_TEMPERATURE>>AIR.INP%%i
for %%i IN (2 4 6 8 10) do echo
#========================================== >>AIR.INP%%i
for %%i IN (2 4 6 8 10) do echo TEMPERATURE>>AIR.INP%%i
for %%i IN (2 4 6 8 10) do echo 100 1 0 2 -10 >>AIR.INP%%i
for %%i IN (2 4 6 8 10) do echo 1.0000e+000 1.0000e+000 1.0000e+000
1.0000e+000 1.0000e+000 1.0000e+000 1.0000e+000 >>AIR.INP%%i
for %%i IN (2 4 6 8 10) do echo
#========================================== >>AIR.INP%%i
for %%i IN (2 4 6 8 10) do echo SOLUTION_CONTROL_2>>AIR.INP%%i
for %%i IN (2 4 6 8 10) do echo F>>AIR.INP%%i
for %%i IN (2 4 6 8 10) do echo -6 1.000000e-006>>AIR.INP%%i
for %%i IN (2 4 6 8 10) do echo 0.000000e+000 %NoTR%.0e+000 1.000000e+000
>>AIR.INP%%i
for %%i IN (2 4 6 8 10) do echo 2 %SizeTR%.0e+000 %NoTR%.0e+000
>>AIR.INP%%i
for %%i IN (%REP%) do echo
#========================================== >>AIR.INP%%i
for %%i IN (%REP%) do echo ALGORITHM>>AIR.INP%%i
for %%i IN (1 3 5 7 9) do echo SIMPLE>>AIR.INP%%i
for %%i IN (2 4 6 8 10) do echo PISO>>AIR.INP%%i
for %%i IN (%REP%) do echo
#========================================== >>AIR.INP%%i
for %%i IN (%REP%) do echo REFERENCE_POINT>>AIR.INP%%i
for %%i IN (%REP%) do echo  4 3 4 >>AIR.INP%%i
for %%i IN (%REP%) do echo
#========================================== >>AIR.INP%%i
for %%i IN (%REP%) do echo MONITORING_POINT_IJK>>AIR.INP%%i
for %%i IN (%REP%) do echo 9 3 14 >>AIR.INP%%i
for %%i IN (%REP%) do echo top >>AIR.INP%%i
for %%i IN (%REP%) do echo MONITORING_POINT_IJK>>AIR.INP%%i
for %%i IN (%REP%) do echo 9 3 8 >>AIR.INP%%i
for %%i IN (%REP%) do echo bottom >>AIR.INP%%i
for %%i IN (%REP%) do echo MONITORING_POINT_IJK>>AIR.INP%%i
for %%i IN (%REP%) do echo 12 3 11 >>AIR.INP%%i
for %%i IN (%REP%) do echo right >>AIR.INP%%i
for %%i IN (%REP%) do echo MONITORING_POINT_IJK>>AIR.INP%%i
for %%i IN (%REP%) do echo 6 3 11 >>AIR.INP%%i
for %%i IN (%REP%) do echo left >>AIR.INP%%i
for %%i IN (%REP%) do echo
#==========================================>>AIR.INP%%i
for %%i IN (%REP%) do echo CHECKPOINT >>AIR.INP%%i
for %%i IN (1 3 5 7 9) do echo F F T %NoSS% F F >>AIR.INP%%i
for %%i IN (2 4 6 8 10) do echo F F T %noiteTR% F F >>AIR.INP%%i
for %%i IN (%REP%) do echo T>>AIR.INP%%i
for %%i IN (%REP%) do echo
#==========================================>>AIR.INP%%i
for %%i IN (%REP%) do echo
PARALLEL_POSTPRO_FORMAT>>AIR.INP%%i
for %%i IN (%REP%) do echo  0 >>AIR.INP%%i
for %%i IN (%REP%) do echo
#==========================================>>AIR.INP%%i
for %%i IN (%REP%) do echo OUTPUT_WALL_DATA>>AIR.INP%%i
for %%i IN (%REP%) do echo  T>>AIR.INP%%i
for %%i IN (%REP%) do echo
#==========================================>>AIR.INP%%i
for %%i IN (%REP%) do echo WALL_BOUNDARY>>AIR.INP%%i
for %%i IN (%REP%) do echo  3 >>AIR.INP%%i
for %%i IN (%REP%) do echo  4.730000e+002 0.000000e+000>>AIR.INP%%i
for %%i IN (%REP%) do echo WALL_BOUNDARY>>AIR.INP%%i
for %%i IN (%REP%) do echo  4 >>AIR.INP%%i
for %%i IN (%REP%) do echo  5.000000e+002 0.000000e+000>>AIR.INP%%i
for %%i IN (%REP%) do echo WALL_BOUNDARY>>AIR.INP%%i
for %%i IN (%REP%) do echo  5 >>AIR.INP%%i
for %%i IN (%REP%) do echo  5.000000e+002 0.000000e+000>>AIR.INP%%i
for %%i IN (%REP%) do echo WALL_BOUNDARY>>AIR.INP%%i
for %%i IN (%REP%) do echo  6 >>AIR.INP%%i
for %%i IN (%REP%) do echo  5.000000e+002 0.000000e+000>>AIR.INP%%i
for %%i IN (%REP%) do echo WALL_BOUNDARY>>AIR.INP%%i
for %%i IN (%REP%) do echo  7 >>AIR.INP%%i
for %%i IN (%REP%) do echo  5.000000e+002 0.000000e+000>>AIR.INP%%i
for %%i IN (%REP%) do echo
#==========================================>>AIR.INP%%i
for %%i IN (%REP%) do echo EXT_TEMPERATURE_HTC_BC>>AIR.INP%%i
for %%i IN (%REP%) do echo  4 3.000000e+002 0.000000e+000 >>AIR.INP%%i
for %%i IN (%REP%) do echo EXT_TEMPERATURE_HTC_BC>>AIR.INP%%i
for %%i IN (%REP%) do echo  5 3.000000e+002 0.000000e+000 >>AIR.INP%%i
for %%i IN (%REP%) do echo EXT_TEMPERATURE_HTC_BC>>AIR.INP%%i
for %%i IN (%REP%) do echo  6 3.000000e+002 0.000000e+000 >>AIR.INP%%i
for %%i IN (%REP%) do echo EXT_TEMPERATURE_HTC_BC>>AIR.INP%%i
for %%i IN (%REP%) do echo  7 3.000000e+002 0.000000e+000 >>AIR.INP%%i
for %%i IN (%REP%) do echo
#==========================================>>AIR.INP%%i
for %%i IN (%REP%) do echo INITIAL_CONDITION>>AIR.INP%%i
for %%i IN (%REP%) do echo 0.000000e+000 0.000000e+000
0.000000e+000>>AIR.INP%%i
for %%i IN (%REP%) do echo 1.000e+000 0.000e+000 0.000e+000 0.000e+000
0.000e+000 0.000e+000 0.000e+000>>AIR.INP%%i
for %%i IN (%REP%) do echo 1.000e-001 5.000e-004 1.000000e+005 2.730e+002
0.000e+000>>AIR.INP%%i
for %%i IN (%REP%) do echo 0.000e+000 1.000e+000 0.000e+000
0.000e+000>>AIR.INP%%i
for %%i IN (%REP%) do echo
#==========================================>>AIR.INP%%i
for %%i IN (%REP%) do echo CHT_WALL_BOUNDARY>>AIR.INP%%i
for %%i IN (%REP%) do echo  4 1.000e-003 >>AIR.INP%%i
for %%i IN (%REP%) do echo CHT_WALL_BOUNDARY>>AIR.INP%%i
for %%i IN (%REP%) do echo  5 1.000e-003 >>AIR.INP%%i
for %%i IN (%REP%) do echo CHT_WALL_BOUNDARY>>AIR.INP%%i
for %%i IN (%REP%) do echo  6 1.000e-003 >>AIR.INP%%i
for %%i IN (%REP%) do echo CHT_WALL_BOUNDARY>>AIR.INP%%i
for %%i IN (%REP%) do echo  7 1.000e-003 >>AIR.INP%%i
for %%i IN (%REP%) do echo
#==========================================>>AIR.INP%%i
for %%i IN (%REP%) do echo CHT_LINK>>AIR.INP%%i
for %%i IN (%REP%) do echo block 0 >>AIR.INP%%i
for %%i IN (%REP%) do echo CHT_LINK>>AIR.INP%%i
for %%i IN (%REP%) do echo block 0 >>AIR.INP%%i
for %%i IN (%REP%) do echo CHT_LINK>>AIR.INP%%i
for %%i IN (%REP%) do echo block 0 >>AIR.INP%%i
for %%i IN (%REP%) do echo CHT_LINK>>AIR.INP%%i
for %%i IN (%REP%) do echo block 0 >>AIR.INP%%i
for %%i IN (%REP%) do echo
#==========================================>>AIR.INP%%i
for %%i IN (%REP%) do echo PRANDTL_NUMBER>>AIR.INP%%i
for %%i IN (%REP%) do echo 7.000e-001 >>AIR.INP%%i
for %%i IN (%REP%) do echo
#==========================================>>AIR.INP%%i
for %%i IN (%REP%) do echo SPECIES_DATA>>AIR.INP%%i
for %%i IN (%REP%) do echo  1.604e+001 >>AIR.INP%%i
for %%i IN (%REP%) do echo  1.7450e+003 1.5900e-001 0.0000e+000
0.0000e+000 0.0000e+000 >>AIR.INP%%i
for %%i IN (%REP%) do echo  6.7055e-006 4.5297e-008 -1.2064e-011 1.6092e-
015 0.0000e+000 >>AIR.INP%%i
for %%i IN (%REP%) do echo
#==========================================>>AIR.INP%%i
for %%i IN (%REP%) do echo SPECIES_DATA>>AIR.INP%%i
for %%i IN (%REP%) do echo  2.897e+001 >>AIR.INP%%i
for %%i IN (%REP%) do echo  1.0470e+003 -1.3417e-001 2.7578e-004 -1.5304e-
007 3.8210e-011 >>AIR.INP%%i
for %%i IN (%REP%) do echo  6.7055e-006 4.5297e-008 -1.2064e-011 1.6092e-
015 0.0000e+000 >>AIR.INP%%i
```

```
for %%i IN (%REP%) do echo
#=========================================>>AIR.INP%%i
for %%i IN (%REP%) do echo SPECIES_DATA>>AIR.INP%%i
for %%i IN (%REP%) do echo  2.918e+001 >>AIR.INP%%i
for %%i IN (%REP%) do echo  1.0470e+003 -1.3417e-001 2.7578e-004 -1.5304e-
007 3.8210e-011 >>AIR.INP%%i
for %%i IN (%REP%) do echo  6.7055e-006 4.5297e-008 -1.2064e-011 1.6092e-
015 0.0000e+000 >>AIR.INP%%i
for %%i IN (%REP%) do echo
#=========================================>>AIR.INP%%i
for %%i IN (%REP%) do echo SPECIES_DATA>>AIR.INP%%i
for %%i IN (%REP%) do echo  2.800e+001 >>AIR.INP%%i
for %%i IN (%REP%) do echo  1.0470e+003 -1.3417e-001 2.7578e-004 -1.5304e-
007 3.8210e-011 >>AIR.INP%%i
for %%i IN (%REP%) do echo  6.7055e-006 4.5297e-008 -1.2064e-011 1.6092e-
015 0.0000e+000 >>AIR.INP%%i
for %%i IN (%REP%) do echo
#=========================================>>AIR.INP%%i
for %%i IN (%REP%) do echo BODY_FORCE>>AIR.INP%%i
for %%i IN (%REP%) do echo  0.000e+000 0.000e+000 -1.000e+000 9.810e+000 -
1.000e+000>>AIR.INP%%i
for %%i IN (2 3 4 5..) do echo
#=========================================>>AIR.INP%%i
for %%i IN (2 3 4 5 6 7 8 9 10) do echo RESTART_INITIAL_CONDITION
>>AIR.INP%%i
for %%i IN (2 3 4 5 6 7 8 9 10) do echo  1 0 0 >>AIR.INP%%i
echo D:%AIR%\AIR.RST1_001 >>AIR.INP2
echo D:%AIR%\AIR.RST1_002 >>AIR.INP3
..
echo D:%AIR%\AIR.RST1_015 >>AIR.INP16
for %%i IN (%REP%) do echo
#=========================================>>AIR.INP%%i
for %%i IN (%REP%) do echo EXTCFD_MODEL>>AIR.INP%%i
for %%i IN (%REP%) do echo run_block >>AIR.INP%%i
for %%i IN (%REP%) do echo
#=========================================>>AIR.INP%%i
for %%i IN (%REP%) do echo SCALE_RESTART>>AIR.INP%%i
for %%i IN (%REP%) do echo  1.000e+000 >>AIR.INP%%i
for %%i IN (%REP%) do echo
#=========================================>>AIR.INP%%i
for %%i IN (%REP%) do echo BOUNDARY_NAME>>AIR.INP%%i
for %%i IN (%REP%) do echo  3 300K_SURF >>AIR.INP%%i
for %%i IN (%REP%) do echo BOUNDARY_NAME>>AIR.INP%%i
for %%i IN (%REP%) do echo  4 BLOCK_TOP >>AIR.INP%%i
for %%i IN (%REP%) do echo BOUNDARY_NAME>>AIR.INP%%i
for %%i IN (%REP%) do echo  5 BLOCK_BOTTOM >>AIR.INP%%i
for %%i IN (%REP%) do echo BOUNDARY_NAME>>AIR.INP%%i
for %%i IN (%REP%) do echo  6 BLOCK_LEFT >>AIR.INP%%i
for %%i IN (%REP%) do echo BOUNDARY_NAME>>AIR.INP%%i
for %%i IN (%REP%) do echo  7 BLOCK_RIGHT >>AIR.INP%%i
for %%i IN (%REP%) do echo
#=========================================>>AIR.INP%%i
GOTO :BLOCKINP
:: XXXXXXXXXXXXXXXXXXXXXXXXXXXXXXXXXXXXXXXXX
:: XXXXXXXXXXXXXXXXXXXXXXXXXXXXXXXXXXXXXXXXX
:BLOCKINP
D:
cd "%INPFOLDER%"
del BLOCK.INP*
for %%i IN (%REP%) do echo !VECTIS_MAIN_INPUT MODULAR VERSION
3.400 >>BLOCK.INP%%i
for %%i IN (1 3 5 7 9) do echo STEADY_STATE>>BLOCK.INP%%i
for %%i IN (1 3 5 7 9) do echo
#=========================================>>BLOCK.INP%%i
for %%i IN (%REP%) do echo EQUATIONS>>BLOCK.INP%%i
for %%i IN (2 4 6 8 10) do echo EQN_TEMPERATURE>>BLOCK.INP%%i
for %%i IN (2 4 6 8 10) do echo
#=========================================>>BLOCK.INP%%i
for %%i IN (2 4 6 8 10) do echo TEMPERATURE>>BLOCK.INP%%i
for %%i IN (2 4 6 8 10) do echo  100 1 0 2 -10>>BLOCK.INP%%i
for %%i IN (2 4 6 8 10) do echo  1.0000e+000 1.0000e+000 1.0000e+000
1.0000e+000 1.0000e+000 1.0000e+000 1.0000e+000>>BLOCK.INP%%i
for %%i IN (%REP%) do echo
#=========================================>>BLOCK.INP%%i
for %%i IN (%REP%) do echo SOLUTION_CONTROL_2>>BLOCK.INP%%i
for %%i IN (%REP%) do echo F>>BLOCK.INP%%i
for %%i IN (%REP%) do echo -6 1.000000e-006>>BLOCK.INP%%i
for %%i IN (1 3 5 7 9) do echo 0.000000e+000 %NoSS% 0e+000
1.000000e+000>>BLOCK.INP%%i
for %%i IN (1 3 5 7 9) do echo 5 1.000000e+000
%NoSS% 0e+000>>BLOCK.INP%%i
for %%i IN (2 4 6 8 10) do echo 0.000000e+000 %NoTR% 0e+000
1.000000e+000>>BLOCK.INP%%i
for %%i IN (2 4 6 8 10) do echo 2 %SizeTR% 0e+000
%NoTR% 0e+000>>BLOCK.INP%%i
for %%i IN (%REP%) do echo
#=========================================>>BLOCK.INP%%i
for %%i IN (%REP%) do echo ALGORITHM>>BLOCK.INP%%i
for %%i IN (%REP%) do echo SIMPLE>>BLOCK.INP%%i
for %%i IN (%REP%) do echo
#=========================================>>BLOCK.INP%%i
for %%i IN (%REP%) do echo REFERENCE_POINT>>BLOCK.INP%%i
for %%i IN (%REP%) do echo  2 2 2 >>BLOCK.INP%%i
for %%i IN (%REP%) do echo
#=========================================>>BLOCK.INP%%i
for %%i IN (%REP%) do echo MONITORING_POINT_IJK>>BLOCK.INP%%i
for %%i IN (%REP%) do echo 8 2 7 >>BLOCK.INP%%i
for %%i IN (%REP%) do echo block>>BLOCK.INP%%i
for %%i IN (%REP%) do echo
#=========================================>>BLOCK.INP%%i
for %%i IN (%REP%) do echo CHECKPOINT>>BLOCK.INP%%i
for %%i IN (1 3 5 7 9) do echo F F T %NoSS% F F>>BLOCK.INP%%i
for %%i IN (2 4 6 8 10) do echo F F T %noiteTR% F F>>BLOCK.INP%%i
for %%i IN (%REP%) do echo T>>BLOCK.INP%%i
for %%i IN (%REP%) do echo
#=========================================>>BLOCK.INP%%i
for %%i IN (%REP%) do echo
PARALLEL_POSTPRO_FORMAT>>BLOCK.INP%%i
for %%i IN (%REP%) do echo  0 >>BLOCK.INP%%i
for %%i IN (%REP%) do echo
#=========================================>>BLOCK.INP%%i
for %%i IN (%REP%) do echo OUTPUT_WALL_DATA>>BLOCK.INP%%i
for %%i IN (%REP%) do echo  T>>BLOCK.INP%%i
for %%i IN (%REP%) do echo
#=========================================>>BLOCK.INP%%i
for %%i IN (%REP%) do echo WALL_BOUNDARY>>BLOCK.INP%%i
for %%i IN (%REP%) do echo  3 >>BLOCK.INP%%i
for %%i IN (%REP%) do echo  5.000000e+002
0.000000e+000>>BLOCK.INP%%i
for %%i IN (%REP%) do echo WALL_BOUNDARY>>BLOCK.INP%%i
for %%i IN (%REP%) do echo  4 >>BLOCK.INP%%i
for %%i IN (%REP%) do echo  5.000000e+002
0.000000e+000>>BLOCK.INP%%i
for %%i IN (%REP%) do echo WALL_BOUNDARY>>BLOCK.INP%%i
for %%i IN (%REP%) do echo  5 >>BLOCK.INP%%i
for %%i IN (%REP%) do echo  5.000000e+002
0.000000e+000>>BLOCK.INP%%i
for %%i IN (%REP%) do echo WALL_BOUNDARY>>BLOCK.INP%%i
for %%i IN (%REP%) do echo  6 >>BLOCK.INP%%i
for %%i IN (%REP%) do echo  5.000000e+002
0.000000e+000>>BLOCK.INP%%i
for %%i IN (%REP%) do echo
#=========================================>>BLOCK.INP%%i
for %%i IN (%REP%) do echo
EXT_TEMPERATURE_HTC_BC>>BLOCK.INP%%i
for %%i IN (%REP%) do echo  3 3.000000e+002
0.000000e+000>>BLOCK.INP%%i
for %%i IN (%REP%) do echo
EXT_TEMPERATURE_HTC_BC>>BLOCK.INP%%i
for %%i IN (%REP%) do echo  4 3.000000e+002
0.000000e+000>>BLOCK.INP%%i
for %%i IN (%REP%) do echo
EXT_TEMPERATURE_HTC_BC>>BLOCK.INP%%i
for %%i IN (%REP%) do echo  5 3.000000e+002
0.000000e+000>>BLOCK.INP%%i
for %%i IN (%REP%) do echo
EXT_TEMPERATURE_HTC_BC>>BLOCK.INP%%i
for %%i IN (%REP%) do echo  6 3.000000e+002
0.000000e+000>>BLOCK.INP%%i
for %%i IN (%REP%) do echo
#=========================================>>BLOCK.INP%%i
for %%i IN (%REP%) do echo INITIAL_CONDITION>>BLOCK.INP%%i
for %%i IN (%REP%) do echo 0.000000e+000 0.000000e+000
0.000000e+000>>BLOCK.INP%%i
for %%i IN (%REP%) do echo 1.000e+000 0.000e+000 0.000e+000 0.000e+000
0.000e+000 0.000e+000 0.000e+000>>BLOCK.INP%%i
for %%i IN (%REP%) do echo 1.000e-001 5.000e-004 1.000000e+005 2.730e+002
0.000e+000>>BLOCK.INP%%i
for %%i IN (%REP%) do echo 0.000e+000 1.000e+000 0.000e+000
0.000e+000>>BLOCK.INP%%i
for %%i IN (%REP%) do echo
#=========================================>>BLOCK.INP%%i
for %%i IN (%REP%) do echo SOLID>>BLOCK.INP%%i
for %%i IN (%REP%) do echo  1.000e+003 >>BLOCK.INP%%i
for %%i IN (%REP%) do echo  5.000e+001 0.000e+000 0.000e+000 0.000e+000
0.000e+000 >>BLOCK.INP%%i
for %%i IN (%REP%) do echo  5.000e+001 0.000e+000 0.000e+000 0.000e+000
0.000e+000 >>BLOCK.INP%%i
for %%i IN (%REP%) do echo
#=========================================>>BLOCK.INP%%i
for %%i IN (%REP%) do echo CHT_WALL_BOUNDARY>>BLOCK.INP%%i
for %%i IN (%REP%) do echo  3 1.000e-003 >>BLOCK.INP%%i
for %%i IN (%REP%) do echo CHT_WALL_BOUNDARY>>BLOCK.INP%%i
for %%i IN (%REP%) do echo  4 1.000e-003 >>BLOCK.INP%%i
for %%i IN (%REP%) do echo CHT_WALL_BOUNDARY>>BLOCK.INP%%i
for %%i IN (%REP%) do echo  5 1.000e-003 >>BLOCK.INP%%i
for %%i IN (%REP%) do echo CHT_WALL_BOUNDARY>>BLOCK.INP%%i
for %%i IN (%REP%) do echo  6 1.000e-003 >>BLOCK.INP%%i
for %%i IN (%REP%) do echo
#=========================================>>BLOCK.INP%%i
for %%i IN (%REP%) do echo CHT_LINK>>BLOCK.INP%%i
for %%i IN (%REP%) do echo air 0 >>BLOCK.INP%%i
for %%i IN (%REP%) do echo CHT_LINK>>BLOCK.INP%%i
for %%i IN (%REP%) do echo air 0 >>BLOCK.INP%%i
for %%i IN (%REP%) do echo CHT_LINK>>BLOCK.INP%%i
for %%i IN (%REP%) do echo air 0 >>BLOCK.INP%%i
for %%i IN (%REP%) do echo CHT_LINK>>BLOCK.INP%%i
for %%i IN (%REP%) do echo air 0 >>BLOCK.INP%%i
for %%i IN (%REP%) do echo
#=========================================>>BLOCK.INP%%i
for %%i IN (%REP%) do echo POSTPROCESSING_DATA>>BLOCK.INP%%i
for %%i IN (%REP%) do echo LPP_PATCH_DISTANCE = ON
>>BLOCK.INP%%i
for %%i IN (%REP%) do echo
#=========================================>>BLOCK.INP%%i
for %%i IN (%REP%) do echo BODY_FORCE>>BLOCK.INP%%i
for %%i IN (%REP%) do echo  0.000e+000 0.000e+000 -1.000e+000 9.810e+000
1.160e+000 >>BLOCK.INP%%i
for %%i IN (%REP%) do echo
#=========================================>>BLOCK.INP%%i
for %%i IN (2 3 4 5 6 7 8 9 10) do echo RESTART_INITIAL_CONDITION
>>BLOCK.INP%%i
for %%i IN (2 3 4 5 6 7 8 9 10) do echo  1 0 0 >>BLOCK.INP%%i
echo D:%BLOCK%\BLOCK.RST1_001 >>BLOCK.INP2
echo D:%BLOCK%\BLOCK.RST1_002 >>BLOCK.INP3
..
echo D:%BLOCK%\BLOCK.RST1_015 >>BLOCK.INP16
for %%i IN (%REP%) do echo SCALE_RESTART >>BLOCK.INP%%i
for %%i IN (%REP%) do echo  1.000e+000 >>BLOCK.INP%%i
for %%i IN (%REP%) do echo
#=========================================>>BLOCK.INP%%i
for %%i IN (%REP%) do echo BOUNDARY_NAME >>BLOCK.INP%%i
for %%i IN (%REP%) do echo  3 TOP >>BLOCK.INP%%i
for %%i IN (%REP%) do echo BOUNDARY_NAME >>BLOCK.INP%%i
for %%i IN (%REP%) do echo  4 BOTTOM >>BLOCK.INP%%i
for %%i IN (%REP%) do echo BOUNDARY_NAME >>BLOCK.INP%%i
for %%i IN (%REP%) do echo  5 RIGHT >>BLOCK.INP%%i
for %%i IN (%REP%) do echo BOUNDARY_NAME >>BLOCK.INP%%i
for %%i IN (%REP%) do echo  6 LEFT >>BLOCK.INP%%i
for %%i IN (%REP%) do echo
#=========================================>>BLOCK.INP%%i
GOTO :RUN
:: XXXXXXXXXXXXXXXXXXXXXXXXXXXXXXXXXXXXXXXXX
```

J.2 JAVA™ PROGRAM

SETUP

The user must create a new directory for each individual CHT model and name it as the INP file of the corresponding CHT part being modelled (e.g. for BLOCK.INP, the related files will be stored in a new directory called BLOCK). Furthermore:

- In each directory the user must create a directory called *store*.
- The user must write the input files for both the steady and transient computations of each CHT model.

The input file for the transient computations (TR runs) must be setup with the Restart Initial Condition (RIC) specification (i.e. set to re-start the solution from the thermal and flow conditions calculated by the previous run). The steady-state computations (SS) do not require the RIC specification since will have this automatically added to the code once the first cycle is completed. (NB. If the simulation needs to be restarted, the RIC specification must be removed from the SS input file).

RUN COMMAND

java cfd/utils/RunPseudoTrans startNo endNo Rstfreq MOD1 MOD2

e.g. *java cfd/utils/RunPseudoTrans 0 10 2 AIR BLOCK* will start a new simulation (with AIR as the master CHT domain and BLOCK as the second and only other CHT domain), will run 10 methodology cycles and save restarts every 2 cycles.

SOLUTION PROCEDURE

1. The SS runs are started from the transient restart files.
2. The SS post files are copied to the *store* directory with an incrementing suffix (the restart file is copied only if this is a *n* iteration).
3. All the TR files that are in the working directory are deleted.
4. The TR runs are started from the steady-state restart files.
5. The TR post files are copied to the *store* directory with an incrementing suffix (the restart file is copied only if this is a *n* iteration).
6. All the SS files in the working directory are deleted.

SOURCE CODE

```
PACKAGE CFD.UTILS;

IMPORT JAVA.IO.*;
IMPORT CFD.GUIUTILS.*;

PUBLIC CLASS RUNPSEUDOTRANS {

  PUBLIC RUNPSEUDOTRANS() {
  }

  PUBLIC STATIC VOID MAIN(STRING[] ARGS) {
    IF (ARGS.LENGTH < 4) {
      SYSTEM.OUT.PRINTLN("USAGE RUNPSEUDOTRANS START END RSTFREQ
PART1 PART2 .....");
      SYSTEM.EXIT(-1);
    }
    INT START = 0;
    INT END = 0;
    INT RSTFREQ = 0;
    TRY {
      START = INTEGER.PARSEINT(ARGS[0]);
      END = INTEGER.PARSEINT(ARGS[1]);
      RSTFREQ = INTEGER.PARSEINT(ARGS[2]);
    } CATCH (NUMBERFORMATEXCEPTION E) {
      SYSTEM.OUT.PRINTLN("USAGE RUNPSEUDOTRANS START END RSTFREQ
PART1 PART2 .....");
      SYSTEM.OUT.PRINTLN("CHECK START END AND RSTFREQ ARE INTEGERS");
    }

    STRING FILENAME;
    INT NOOFPARTS = ARGS.LENGTH - 3;
    STRING[] DIRNAMES = NEW STRING[NOOFPARTS];
    STRING[] TRNAMES = NEW STRING[NOOFPARTS];
    STRING[] SSNAMES = NEW STRING[NOOFPARTS];
    FOR (INT I = 0 ; I < NOOFPARTS ; I++) {
      DIRNAMES[I] = ARGS[I+3];
      TRNAMES[I] = ARGS[I+3]+"_TR.INP";
      SSNAMES[I] = ARGS[I+3]+"_SS.INP";
    }
    RUNTIME RT = RUNTIME.GETRUNTIME();
    PROCESS P;
    BOOLEAN FIRSTRUN = TRUE;
    IF (START != 0) FIRSTRUN = FALSE;
    TRY {
      FOR (INT I = START ; I < END+1 ; I++) {
        IF (FIRSTRUN && I !=0) {
          FIRSTRUN = FALSE;
          // AFTER THE FIRST ITERATION NEED TO ADD RST SPECS INTO
          // INPUT FILES
          ADDRST(DIRNAMES);
        }
        P = RT.EXEC("CMD /C START /D"+DIRNAMES[0]+"/WAIT CMD /C PHASE5
"+SSNAMES[0]);
        P.WAITFOR();
        MOVEFILES(DIRNAMES, "_TR.", I, RSTFREQ);
        P = RT.EXEC("CMD /C START /D"+DIRNAMES[0]+"/WAIT CMD /C PHASE5
"+TRNAMES[0]);
        P.WAITFOR();
        MOVEFILES(DIRNAMES, "_SS.", I, RSTFREQ);
        SYSTEM.OUT.PRINTLN(""+P.EXITVALUE());
      }
    } CATCH (EXCEPTION E) {
      SYSTEM.OUT.PRINTLN(""+E);
      E.PRINTSTACKTRACE();
      SYSTEM.OUT.PRINTLN("PROBLEM RUNNING COMMANDS");
    }
  }

  STATIC PRIVATE VOID ADDRST(STRING[] DIRS) {
    STRING ANALYSIS;
    //    FOR (INT AN = 0 ; AN < 2 ; AN++) {
    //      IF (AN == 0) ANALYSIS = "SS";
    //    ELSE ANALYSIS = "TR";
    ANALYSIS = "SS";
    PARTLOOP : FOR (INT PART = 0 ; PART < DIRS.LENGTH ; PART++) {
      FILE DIR = NEW FILE(DIRS[PART]);
      FILE FILE = NEW FILE(DIR, DIRS[PART]+"_"+ANALYSIS+".INP");
      STRING TOKEN;
      STREAMTOKENIZER INTEXT;
      TRY {
        FILEINPUTSTREAM FI = NEW FILEINPUTSTREAM(FILE);
        INTEXT = NEW STREAMTOKENIZER(NEW BUFFEREDREADER(NEW
INPUTSTREAMREADER(NEW BUFFEREDINPUTSTREAM(FI, 10000000)), 1000000));
        INTEXT.RESETSYNTAX();
        INTEXT.EOLISSIGNIFICANT(TRUE);
        INTEXT.WORDCHARS('\U0000', '\UFFFF');
        INTEXT.WHITESPACECHARS('\U0000','\U0020');
        TOKENLOOP : WHILE(TRUE) {
          INTEXT.NEXTTOKEN();
          IF (INTEXT.SVAL != NULL &&
INTEXT.SVAL.COMPARETOIGNORECASE("RESTART_INITIAL_CONDITION")
== 0) {
            // ALREADY HAS A RST SPEC
            CONTINUE PARTLOOP;
          }
          IF (INTEXT.TTYPE == INTEXT.TT_EOF) BREAK;
        }
        FI.CLOSE();
      } CATCH (IOEXCEPTION E) {
        SYSTEM.OUT.PRINTLN("ERROR READING FILE = "+FILE);
        SYSTEM.EXIT(-1);
      }
      FILEWRITER FW = NULL;
      FILE TEMP = NULL;
      TRY {
        TEMP = FILE.CREATETEMPFILE("PTM",NULL);
        TEMP.DELETEONEXIT();
        FW = NEW FILEWRITER(TEMP);
      }
      CATCH (IOEXCEPTION E) {
        SYSTEM.OUT.PRINTLN("CAN'T OPEN TEMP FILE = ");
        SYSTEM.EXIT(-1);
      }

      TRY {
        FILEINPUTSTREAM FI = NEW FILEINPUTSTREAM(FILE);
        INTEXT = NEW STREAMTOKENIZER(NEW BUFFEREDREADER(NEW
INPUTSTREAMREADER(NEW BUFFEREDINPUTSTREAM(FI, 10000000)), 1000000));
        INTEXT.RESETSYNTAX();
        INTEXT.EOLISSIGNIFICANT(TRUE);
        INTEXT.WORDCHARS('\U0000', '\UFFFF');
        // INTEXT.WHITESPACECHARS('\U0000','\U0020');
        TOKENLOOP : WHILE(TRUE) {
          INTEXT.NEXTTOKEN();
          IF (INTEXT.TTYPE == INTEXT.TT_EOL) {
            FW.WRITE("\N");
            CONTINUE TOKENLOOP;
          }
          IF (INTEXT.TTYPE == INTEXT.TT_EOF) BREAK;
          FW.WRITE(INTEXT.SVAL);
        }

FW.WRITE("#================================================\N");
        FW.WRITE("RESTART_INITIAL_CONDITION\N");
        FW.WRITE(" 1 0 0\N");
        FW.WRITE(DIRS[PART]+"_TR.RST1_001\N");

FW.WRITE("#================================================\N");
        FI.CLOSE();
      } CATCH (IOEXCEPTION E) {
        SYSTEM.OUT.PRINTLN("ERROR READING FILE = "+FILE);
        SYSTEM.EXIT(-1);
      }

      TRY {
        FW.CLOSE();
      } CATCH (IOEXCEPTION E) {
        SYSTEM.OUT.PRINTLN("COULDN'T CLOSE OUTPUT FILE");
      }
      IF (FILE.DELETE() == FALSE) {
        SYSTEM.OUT.PRINTLN("CAN'T DELETE INPUT FILE = "+FILE);
      }
      IF (TEMP.RENAMETO(FILE) == FALSE) {
        SYSTEM.OUT.PRINTLN("FILE RENAME FAILED = "+FILE);
      }
    }
    // }
  }

  STATIC PRIVATE VOID MOVEFILES(STRING[] DIRS, STRING FILTER, INT COUNT,
INT RSTFREQ) {
    // FIND ALL FILES WITH 001 EXTENSION AND MOVE THEM TO ANOTHER
DIRECTORY
    // AND CHANGE THE EXTENSION TO THE NEXT IN AN INCREMENTING SERIES
    STRING EXTENSION;
    IF (COUNT < 10) EXTENSION = "00"+COUNT;
    ELSE IF (COUNT < 100) EXTENSION = "0"+COUNT;
    ELSE EXTENSION = ""+COUNT;
    FOR (INT PART = 0 ; PART < DIRS.LENGTH ; PART++) {
      FILE DIR = NEW FILE(DIRS[PART]);
      WILDCARDFILTER WCF = NEW WILDCARDFILTER("*001");
      STRING[] FILES = DIR.LIST(WCF);
      STRING[] TEXT = WCF.GETWILDCARDTEXTS();
      FILE OLDFILE;
      FILE NEWFILE;

      FOR (INT I=0; I<FILES.LENGTH; I++) {
        IF (TEXT[I].INDEXOF(FILTER) == -1) CONTINUE;
        SYSTEM.OUT.PRINTLN("TEXT = "+TEXT[I]);
        OLDFILE = NEW FILE(DIR, FILES[I]);
        NEWFILE = NEW FILE(DIR, "STORE/"+TEXT[I]+EXTENSION);
        SYSTEM.OUT.PRINTLN("OLDFILE = "+OLDFILE);
        SYSTEM.OUT.PRINTLN("NEWFILE = "+NEWFILE);
        SYSTEM.OUT.PRINTLN("MOVE = "+OLDFILE.RENAMETO(NEWFILE));
        IF (OLDFILE.GETNAME().INDEXOF("RST") != -1) {
          // IF A RST CHECK IF THERE IS A PREVIOUS VERSION THAT CAN BE
          // DELETED
          IF ((COUNT-1)%RSTFREQ != 0) {
            // DELETE THE FILE
            STRING EXTENSIOND;
            IF ((COUNT-1) < 10) EXTENSIOND = "00"+(COUNT-1);
            ELSE IF ((COUNT-1) < 100) EXTENSIOND = "0"+(COUNT-1);
            ELSE EXTENSIOND = ""+(COUNT-1);
            NEWFILE = NEW FILE(DIR, "STORE/"+TEXT[I]+EXTENSIOND);
            IF (NEWFILE.DELETE() == FALSE) {
              SYSTEM.OUT.PRINTLN("CAN'T DELETE FILE "+NEWFILE);
            }
          }
        }
      }
    }
  }
}
```

J.3 JAVA™ PROGRAM FOR JOINING OUTPUT FILES

The program was written to concatenate the output files written by VECTIS during a simulation carried out with the transient methodology devised in this study, enabling the post-processing of the complete set of CFD results generated.

SETUP INSTRUCTIONS

No setup is required to run the code providing that the files to be concatenated do exist, have a numbered extension (e.g., _001, _002) and they are placed in the same directory.

RUN COMMAND

java cfd/utils/Concat SizeStep Files_wilcard out.name

e.g., *java cfd/utils/Concat 5 AIR_TR.GLO_* GLO.OUT* will concatenate all the transient global files of the AIR part into the GLO.OUT file, re-writing the time progression of the solution based on timesteps of 5 seconds (**SizeStep** should not specified to conserve the original timescale of the solution).

SOURCE CODE

```
package cfd.utils;

import java.io.*;
import java.util.*;

public class Concat {

   public Concat() {
   }

   public static void main(String[] args) {
      if (args.length < 3) {
         System.out.println("usage Concat SizeSteps Files out.file");
         System.exit(-1);
      }
               System.out.println("Size Timestep = "+args[0]);
      for (int i = 1 ; i < args.length - 1 ; i++) {
         System.out.println("Cat file = "+args[i]);
      }
               System.out.println("Output file = "+args[args.length - 1]);
      StreamTokenizer inText;
      int count = 0;
               int step = 0;
               step = Integer.parseInt(args[0]);
      FileWriter fw = null;
      try {
         fw = new FileWriter(args[args.length - 1]);
      }
      catch (IOException e) {
         System.out.println("Can't open output file = "+args[args.length - 1]);
         System.exit(-1);
      }
      Vector tokens = new Vector();
      String token;
      for (int i = 1 ; i < args.length - 1 ; i++) {

         try {
            File inputFile = new File(args[i]);
            inText = new StreamTokenizer(new BufferedReader(new
InputStreamReader(new BufferedInputStream(new
FileInputStream(inputFile), 10000000)), 1000000));
            inText.resetSyntax();
      }
            inText.eolIsSignificant(true);
            inText.wordChars('\u0021', '\uFFFF');
            inText.whitespaceChars('\u0000','\u0020');
            tokenLoop : while(true) {
               inText.nextToken();
               if (inText.ttype == inText.TT_EOL) {
                  count++;
                  try {
                     Iterator tokensIt = tokens.iterator();
                     int size= count * step;
                     tokensIt.next(); // throw away the first column
                      fw.write(size+" "); // write count instead
                     while (tokensIt.hasNext()) {
                        token = (String)tokensIt.next();
                        fw.write(token);
                        fw.write(" ");
                     }
                      fw.write("\n");
                  } catch (IOException e) {
                     System.out.println(""+e);
                     System.out.println("Error writing to output file =
"+args[args.length - 1]);
                     System.exit(-1);
                  }
                  if (inText.ttype == inText.TT_EOF) break;
                  //inText.nextToken();
                  tokens.clear();
                  continue tokenLoop;
               }
               if (inText.ttype == inText.TT_EOF) break;
               tokens.add(inText.sval);
            }
         } catch (IOException e) {
            System.out.println("error reading file = "+args[i]);
            System.exit(-1);
         }
      }
      try {
      fw.close();
      } catch (IOException e) {
         System.out.println("Couldn't close output file");
```